Journal of the Serbian Chemical Society

*e*Version
*e*lectronic

Available on line at

СХД
1897

www.shd.org.rs/JSCS/

CONTENTS*

* For colored figures in this issue please see electronic version at the Journal Home Page: http://www.shd.org.rs/JSCS/

The synthesis, characterization, antioxidant and antimicrobial activity of some novel amides of the esters of substituted 1,4-dihydropyridines

JASMINA B. NIKOLIĆ[1#], NEVENA Ž. PRLAINOVIĆ[1], GAVRILO M. ŠEKULARAC[2#],
LUKA R. MATOVIĆ[3#], ANITA M. LAZIĆ[3#] and SAŠA Ž. DRMANIĆ[1*#]

[1]*Department of Organic Chemistry, Faculty of Technology and Metallurgy, University of Belgrade, Belgrade, Serbia,* [2]*Institute of Chemistry, Technology and Metallurgy, University of Belgrade, Belgrade, Serbia and* [3]*Innovations Center of Faculty of Technology and Metallurgy, University of Belgrade, Belgrade, Serbia*

Abstract: The esters of substituted 1,4-dihydropyirdines (1,4-DHP) are formed in the reaction of an appropriate aldehyde and ethyl acetoacetate in the presence of concentrated water solution of ammonia. The esters form the amides by the reaction with primary amines. The series of the amides has been synthesized with the aim to analyze their chemical characteristics, antioxidant and antimicrobial activity. The amine used in this research is 2-aminothiazole. The antioxidant activity is analysed by 2,2-diphenyl-1-picrylhydrazyl (DPPH) and 2,2'-Azino-bis(3-ethylbenzthiazoline-6-sulfonic acid) (ABTS) methods and the antimicrobial activity screening was performed by broth microdilution method, using different microbial strains. The characterization of the obtained amides was done by melting points, FTIR, NMR and elemental analysis. The possibilities for further research was suggested, which could lead to the application of selected compounds.

Keywords: biologically active compounds; DPPH analysis; ABTS analysis; broth microdilution method.

INTRODUCTION

The derivatives of substituted 1,4-dihydropyirdines (1,4-DHP), such as esters (Fig. 1), have lately drawn attention because of their significant biological activity.

Various medicines containing the esters of substituted 1,4-DHP are used as calcium antagonists, or cardiovascular agents (antihypertensive drugs) as it is stated in literature[1] by Debache *et. al*. Furthermore, the interest for the various

---

141

derivatives of 1,4-DHP becomes even greater because of its similarity to nicotin-amide dinucleotide, the coenzyme which is involved in a lot of metabolic processes.
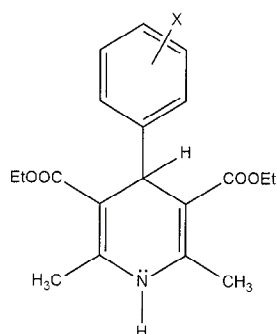
Fig. 1. The general formula of substituted esters of 1,4-DHP.

The methods for the synthesis of the esters of 1,4-DHP originate from 1882 when Hantzsch developed his synthesis.[2] By today the variations of the method mentioned above have been created, depending on the demand for the production speed and yield.

As it is mentioned already, this group of compounds is known as the active compounds of the medicines for the calcium channel blocking and for the insufficient heart activity. The aim of the therapy in which the drugs based on them are used is to provide reliable and healthy work of the body muscles, especially of the heart muscle[3] and also as vasodilators.[4]

The amide bond is among the most significant functional groups in chemistry and biochemistry, a part of protein and peptide molecules and also a part of an active substance of many medicines[5] and 1,4-DHP molecule is an usual base for it.

The antioxidant activity of the 1,4-DHP derivatives has already been examined.[6,7] Ahamed *et.al.*[8] synthesized 18 amides of the esters 1,4-DHP with the aim to study their antimicrobial and anticoagulant activity, using differently substituted esters of 1,4-DHP and 3 amines: 2-amino-4-phenylthiazole, 5-phenyl--1,3,4-tiadiazole-2-amine and 5-phenyl-1,3,4-oxadiazole-2-amine. The products synthesized from chlorophenyl and nitrophenyl esters of 1,4-DHP, with 2-amino--4-phenylthiazole displayed significant activity against *Escherischia coli* and *Candida albicans*, respectively. (Fig. 2a and b).[8] Furthermore, the amide with the hydroxyphenyl substituent, synthesized with 5-phenyl-1,3,4-tiadiazole-2-amine showed rather prominent anticoagulant activity in comparison to the referent compound heparine (Fig.2c).[8]

Based on this study,[8] the synthesis of amides of the esters substituted 1,4--DHP was performed in this research. The amine used was 2-amino-thiazole (Fig. 3).
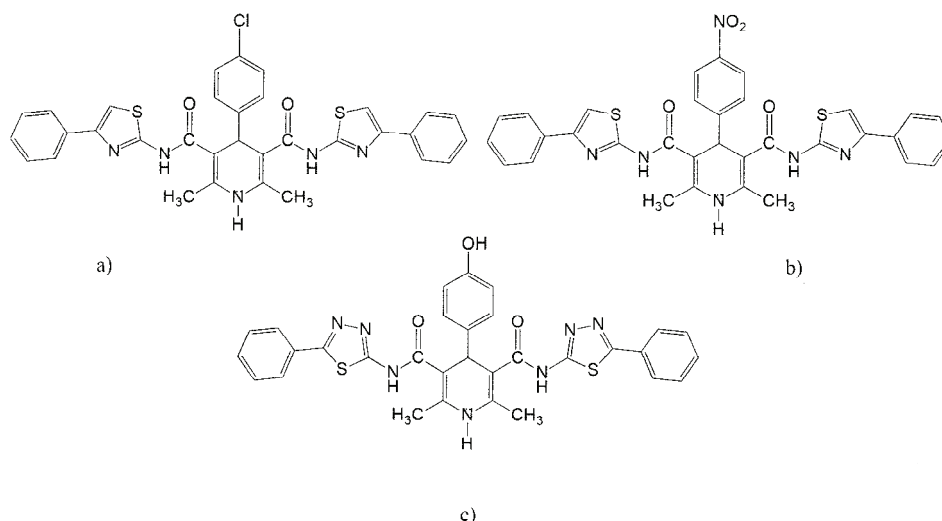
Fig. 2. The formulas of synthesized amides of the esters of 1,4-DHP.[8]
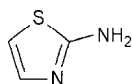
Fig. 3. The formula of 2-aminothiazole.

Substituted 2-aminothiazoles can be used as base reactants for the synthesis of biocides, fungicides, dyes and medicines for the treatment of hyperthyroidism.[9]

EXPERIMENTAL

The synthesis of esters 1,4-DHP[6]

The reaction mixture of 0.01 mole of the aldehyde which was used, 0.02 mol of ethyl acetoacetate, 0.01 mol of concentrated water solution of ammonia and 20 mL of methanol was refluxed for 6 h with mixing, at 65 °C (Fig. 4). After that, the mixture was poured into the beaker and intensively stirred at room temperature. It was then left overnight to crystallise. The obtained white crystals were washed in methanol and recrystallised in the same solvent. The list of the synthesized compounds is given in Table I.

Synthesis of the amides of the esters 1,4-DH[8]

The mixture of each of the esters of 1,4-DHP (0.005 mole) and 2-aminothiazole (0.01 mol) was dissolved in ethanol and then kept for 5 min in an ultrasonic bath. It was afterwards washed by distilled water and recrystallised from ethyl acetate. The reaction scheme is presented in Fig. 4 and the list of synthesized compounds is given in Table II.

DPPH assay[16]

The examined amides were diluted in DMSO in 10 different concentrations. A stable free radical DPPH• (Fluka Chemie AG Buchs) was diluted in methanol, at the concentration of 6.58×10^{-5} M. 140 μL of DPPH• solution was poured into 96 wells on the microtiter plate, as well as 110 μL of DMSO solutions of tested compounds and also pure DMSO (10 μL) as control specimen. It was left for 30 min in the dark, at room temperature and then the absorb-

ance at 517 nm was measured using Shimadzu 1700 UV–Vis spectrophotometer. All measurements were repeated 3 times. Ascorbic acid was used as reference substance in the concentrations from 50 up to 500 mg mL^{-1}. IC_{50} was calculated based on the percentage of neutralised DPPH$^\bullet$.
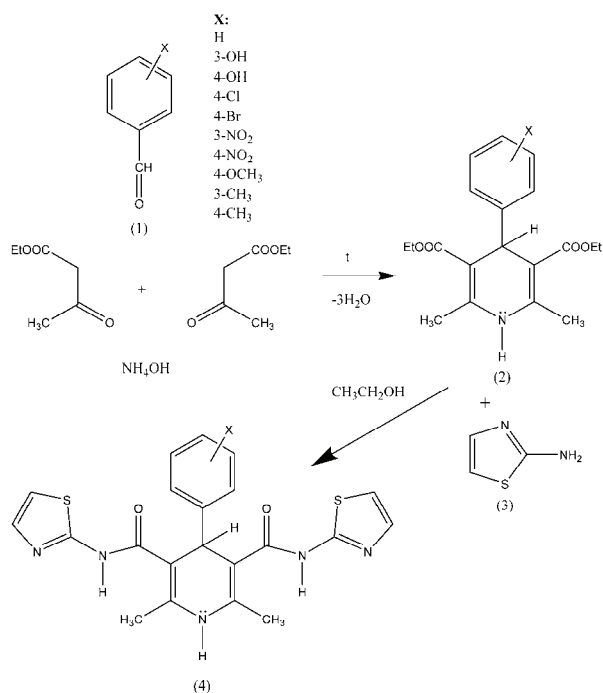
Fig. 4. The synthesis of the amides of the esters of 1,4-DHP (**4**) with 2-aminothiazole (**3**) *via* esters of 1,4-DHP (**2**) that are produced from the corresponding substituted benzaldehydes (**1**).

TABLE I. The synthesized esters of 1,4-DHP

No.	Compound	X
1a[10]	4-Phenyl-2,6-dimethyl-3,5-dicarboetoxy-1,4-dihydropiridine	H
2a[11]	4-(3'-Hydroxyphenyl)-2,6-dimethyl-3,5-dicarboetoxy-1,4-dihydropiridine	3-OH
3a[12]	4-(4'-Hydroxyphenyl)-2,6-dimethyl-3,5-dicarboetoxy-1,4-dihydropiridine	4-OH
4a[10]	4-(4'-Chlorophenyl)-2,6-dimethyl-3,5-dicarboetoxy-1,4-dihydropiridine	4-Cl
5a[13]	4-(4'-Bromophenyl)-2,6-dimethyl-3,5-dicarboetoxy-1,4-dihydropiridine	4-Br
6a[11]	4-(3'-Nitrophenyl)-2,6-dimethyl-3,5-dicarboetoxy-1,4-dihydropiridine	3-NO$_2$
7a[10]	4-(4'-Nitrophenlyl)-2,6-dimethyl-3,5-dicarboetoxy-1,4-dihydropiridine	4- NO$_2$
8a[10]	4-(4'-Metoxyphenyl)-2,6-dimethyl-3,5-dicarboetoxy-1,4-dihydropiridine	4-OCH$_3$
9a[14]	4-(3'-Methylphenyl)-2,6-dimethyl-3,5-dicarboetoxy-1,4-dihydropiridine	3-CH$_3$
10a[15]	4-(4'-Methylphenyl)-2,6-dimethyl-3,5-dicarboetoxy-1,4-dihydropiridine	4-CH$_3$

ABTS assay[17]

Bisradical cation ABTS$^{\bullet+}$ was obtained by the reaction of potassium persulfate (2.5 mM) and ABTS (7 mM) of 16 h in the dark. After ABTS$^{\bullet+}$ was stabilised, it was diluted by meth-

anol up to the absorbance of 0.700±0.02 at 734 nm, measured using Shimadzu 1700 UV–Vis spectrophotometer. Then 20 μL of each specimen (solutions of 3 mmol L^{-1} of tested compounds in DMSO) was added into 2 mL of the prepared ABTS$^{•+}$ solution and the noted above absorbance was measured. The solution of ABTS with 20 μL was used as control specimen. Ascorbic acid was used as a reference substance and the antioxidant activity of the tested compounds was compared to it. IC_{50} was calculated based on the percentage of neutralised ABTS$^{•+}$.

TABLE II. The synthesized amides of the esters of 1,4-DHP

No.	Compound	X
1b	1,4-Dihydro-2,6-dimethyl-N^3,N^5-bis(2-thiazolyl)-4-phenyl-3,5-pyridine-dicarboxamide	H
2b	1,4-Dihydro-2,6-dimethyl-N^3,N^5-bis(2-thiazolyl)-4-(3-hydroxyphenyl)-3,5-pyridinedicarboxamide	3-OH
3b	1,4-Dihydro-2,6-dimethyl-N^3,N^5-bis(2-thiazolyl)-4-(4-hydroxyphenyl)-3,5-pyridinedicarboxamide	4-OH
4b	1,4-Dihydro-2,6-dimethyl-N^3,N^5-bis(2-thiazolyl)-4-(4-chlorophenyl)-3,5-pyridinedicarboxamide	4-Cl
5b	1,4-Dihydro-2,6-dimethyl-N^3,N^5-bis(2-thiazolyl)-4-(4-bromophenyl)-3,5-pyridinedicarboxamide	4-Br
6b	1,4-Dihydro-2,6-dimethyl-N^3,N^5-bis(2-thiazolyl)-4-(3-nitrophenyl)-3,5-pyridinedicarboxamide	3-NO$_2$
7b	1,4-Dihydro-2,6-dimethyl-N^3,N^5-bis(2-thiazolyl)-4-(4-nitrophenyl)-3,5-pyridinedicarboxamide	4-NO$_2$
8b	1,4-Dihydro-2,6-dimethyl-N^3,N^5-bis(2-thiazolyl)-4-(4-metoxyphenyl)-3,5-pyridinedicarboxamide	4-OCH$_3$
9b	1,4-Dihydro-2,6-dimethyl-N^3,N^5-bis(2-thiazolyl)-4-(3-methylphenyl)-3,5-pyridinedicarboxamide	3-CH$_3$
10b	1,4-Dihydro-2,6-dimethyl-N^3,N^5-bis(2-thiazolyl)-4-(4-methylphenyl)-3,5-pyridinedicarboxamide	4-CH$_3$

In vitro *antimicrobial activity*[18]

The antimicrobial activity of all synthesized compounds was determined on a wide range of different microorganisms by broth microdilution method.[12] The advantage of this method is its capability to quantitatively determine antimicrobial activity and gives precise insight into the effect of every examined compound on the applied bacterial strains.

The broth microdilution method[18] was applied to determine the minimal inhibitory concentrations (*MIC*) of the investigated compounds against nine American Type Cell Collection (ATCC) bacterial strains and one strain of yeast, *Candida albicans* (Table III). The method was performed in agreement with Clinical and Laboratory Standard Institute (CLSI 2005).

The active microbial cultures were prepared from lyophilized standard strains by transferring them to test tubes with the appropriate broth. The nutrient broth was used for bacterial strains, except for *L. monocytogenes*, for which the soya tryptone broth was used.

The malt broth was used for *C. albicans*. All bacterial strains were incubated for 24 h at 37 °C while *C. albicans* was incubated at 32 °C. The density of microbial suspensions was set approximately at 10^5 CFU (colony forming units), using the appropriate broth.

TABLE III. The examined bacteria and fungi types

No.	Microorganism	ATCC No.
1	*Staphylococcus aureus* (G+)	6538
2	*Lysteria monocytogenes* (G+)	19115
3	*Enterococcus faecalis* (G+)	29212
4	*Shigella sonnei* (G–)	29930
5	*Salmonella enteritidis* (G–)	13076
6	*Yersinia enterolitica* (G–)	27729
7	*Escherichia coli* (G–)	35150
8	*Proteus hauseri* (G–)	13315
9	*Pseudomonas aeruginosa* (G–)	27853
10	*Candida albicans*	10259

All examined compounds were first dissolved in 5 % dimethyl sulfoxide to the concentration of 2.5 mg mL^{-1}, and then series of concentrations were prepared by two-fold dilution, using the appropriate broth. The serial concentrations were prepared directly in microtiter plates and the final volume of specimens was 50 µL. The investigated concentrations were in the range from 0.0024 to 1.25 mg mL^{-1}. In the last column only the appropriate broth was added. Then 50 µL of each microbial suspension were added in each well, so that the final concentrations of the examined extracts were half of those at the beginning, and the final volume was 100 µL in each well. Triphenyltetrazoliumchloride (TTC), in concentration of 0.75 vol. % was used as the growth indicator. If the growth of the microbial strain occurs, this indicator gives the rosy-red colour to the broth. The plates with bacteria were incubated at 37 °C, and with *C. albicans* on 32 °C, for 24 h. The results were read the following day and for *MIC* value of each compound on every strain was taken the concentration at which there was no development of red colour. All tests were performed in triplicate and the *MIC* values were constant.

Characterization of synthesised compounds.

FTIR spectra were recorded on Thermo Scientific Nicolet iS10, elemental analysis was done on Vario EL III CHNOS and ^{1}H- and ^{13}C-NMR were recorded on Bruker Ascend 400 MHz (^{1}H 400 MHz, ^{13}C 100 MHz). The resulting data are given in Supplementary material to this paper.

RESULTS AND DISCUSSION

Antioxidant activity – DPPH

Based on the interaction of the synthesized compounds with the DPPH free radical the capability of a compound to transfer a hydrogen atom can be determined. The greater above-mentioned capability the compound possess the higher antioxidant activity it has. The stability of DPPH radical is based on the analysed compound structure and the solvent which is used. The results of the DPPH test for 10 analysed amides of the esters of 1,4-DHP are given in Table IV, in the form of IC_{50} values. The relationship between the structure of the examined compounds and their antioxidant activity can be related to the present substituents on the aromatic ring and their position. Some of the compounds showed con-

siderable antioxidant activity, namely the one with the 3-OH group (**2b**) displays the most prominent activity, while the 4-OH (**3b**) compounds show it also, but it is somewhat weaker. Furthermore **3b** displayed even lower activity than **2b**, which points to the effect of shifting the position of OH group along the aromatic ring, in other words the increase of its distance from the side chain decreases the antioxidant activity. Apart from the OH-substituted derivatives, the only one with certain, but considerably weak antioxidant activity is the 4-NO$_2$ (**7b**) one and all the rest of them showed no activity, according to DPPH method.

TABLE IV. IC_{50} values of the analysed compounds determined by DPPH method

Compound	IC_{50} / mM
1b	–
2b	0.578
3b	1.377
4b	–
5b	–
6b	–
7b	1.848
8b	–
9b	–
10b	–

Antioxidant activity – ABTS

The same amides were examined by ABTS test and the results are displayed in Table V.

TABLE V. The results of the ABTS antioxidant activity of the analysed compounds

Compound	IC_{50} / mM
1b	2.95
2b	1.21
3b	1.25
4b	-
5b	2.65
6b	-
7b	2.5
8b	-
9b	-
10b	-

The strongest antioxidant activity by the ABTS method was again shown in the case of OH-substituted compounds, in the same order (from the stronger **2b** to the weaker **3b**), and even slighter for the 4-NO$_2$ compound (**7b**), confirming the previously used DPPH method. However, when ABTS method is used, some activity is also detected for the unsubstituted derivative **1b** and the 4-Br derivate-

ive (**5b**), which does not show activity with DPPH. It can be concluded that ABTS method is more sensitive to the antioxidant activity for the examined type of compound.

Antimicrobial screening

Only some amides showed considerable activity against the tested strains of microorganisms, mostly the same which had also shown antioxidant activity, but also the unsubstituted amide. Hydroxyl substituted amides (**2b** and **3b**) proved to be the most active against both G+ (*S. aureus*, *L. monocytogenes*) and G– bacterial strains (*S. sonnei*, *Y. enterolytica*, *P. hauseri*), but not as well against *C. albicans*. The unsubsstitued amide **1b** displayed some activity towards G– (*S. sonnei*, *Y. enterolytica)* and rather a weak one against G+ (*L. monocytogenes*) and *C. albicans*. 4-Br (**5b**) showed some activity against G+ (*S. aureus*, *L. monocytogenes*) and 4-NO$_2$ only some against *S. aureus.*

The overall results of the antimicrobial screening are given in Table VI.

TABLE VI. Antimicrobial activity of examined compounds (mM)

Cmpd.	Microbe									
	S. aureus	*L. monocy-togenes*	*E. fae-calis*	*S. sonnei*	*S. enteri-tidis*	*Y. ent-erolytica*	*E. coli*	*P. hau-seri*	*P. aeru-ginosa*	*C. albi-cans*
1b	4.44	1.80	4.55	0.79	5.10	0.87	5.25	1.22	2.35	1.18
2b	0.18	0.36	2.54	1.24	2.54	0.58	2.54	0.62	5.10	2.44
3b	0.21	0.41	2.64	1.38	2.72	0.62	2.82	0.75	5.12	2.81
4b	>5.06	>5.06	>5.06	>5.06	>5.06	>5.06	>5.06	>5.06	>5.06	>5.06
5b	0.63	0.98	5.12	3.01	5.12	0.77	3.05	1.02	5.12	4.45
6b	>5.06	>5.06	>5.06	>5.06	>5.06	>5.06	>5.06	>5.06	>5.06	>5.06
7b	0.89	1.12	3.07	2.72	2.95	0.88	3.01	1.11	3.89	2.99
8b	>5.06	>5.06	>5.06	>5.06	>5.06	>5.06	>5.06	>5.06	>5.06	>5.06
9b	>5.06	>5.06	>5.06	>5.06	>5.06	>5.06	>5.06	>5.06	>5.06	>5.06
10b	>5.06	>5.06	>5.06	>5.06	>5.06	>5.06	>5.06	>5.06	>5.06	>5.06

Overall activity can be described as weak to moderate against G+ or G– strains of bacteria, or yeast *C. albicans.* The activity cannot be specified as selective towards G+ or G– strains, as it is not very strong however the obtained data can be used to direct the further investigation.

CONCLUSIONS

The synthesized amides were characterized by FTIR, NMR, melting points and elemental analysis (the data are given in Supplementary material). The antioxidant activity was analysed by two similar methods, DPPH and ABTS. When DPPH method was used it was shown that the hydroxyphenyl substituted compounds were the most efficient. Some weaker activity was also displayed by the 4-nitrophenyl substituted derivative, while 3-nitrophenyl derivative and the unsubstituted compound showed no antioxidant activity at all. In agreement with

that, the ABTS method also displayed the hydroxyphenyl substituted derivatives as active and the 4-nitrophenyl derivative as weakly active, but also detects some slight activity in the case of the 4-bromo substituted compound, which makes this method more suitable for further analysis, when the antioxidant activity of the given type of compound is examined.

The results of antimicrobial screening were moderately significant and pointed to the compounds with antioxidant activity as well.

The conclusion can be derived that the amides of the hydroxyl substituted esters of 1,4-dihydropyridines should be considered for further research and that perhaps some attention should be paid to nitro and halogen substituted also.

SUPPLEMENTARY MATERIAL

Additional data and information are available electronically at the pages of journal website: https://www.shd-pub.org.rs/index.php/JSCS/article/view/12635, or from the corresponding author on request.

ИЗВОД

СИНТЕЗА, КАРАКТЕРИЗАЦИЈА, АНТИОКСИДАТИВНА И АНТИМИКРОБНА АКТИВНОСТ НЕКИХ НОВИХ АМИДА ЕСТАРА 1,4-ДИХИДРОПИРИДИНА

ЈАСМИНА Б. НИКОЛИЋ[1], НЕВЕНА Ж. ПРЛАИНОВИЋ[1], ГАВРИЛО М. ШЕКУЛАРАЦ[2], ЛУКА Р. МАТОВИЋ[3], АНИТА М. ЛАЗИЋ[3] и САША Ж. ДРМАНИЋ[1]

[1]Катедра за Органску хемију, Технолошко–металрушки факултет Универзитета у Београду, Београд, [2]Институт за хемију, технологију и металургију Универзитета у Београду, Београд и [3]Иновациони центар Технолошко–металуршког факултета Универзитета у Београду, Београд

Естри супституисаних 1,4-дихидропиридина се формирају у реакцији одговарајућег алдехида и етил-ацетоацетата у присуству амонијум-хидроксида. Наведени естри прелазе у амиде реакцијом са примарним аминима. Серија оваквих амида је синтетисана са циљем да се испита њихова антиоксидативна и антимиркобна активност, као и хемијске карактеристике. Амин употребљен за синтезу је 2-аминотиазол. Антиоксидативна активност је анализирана DPPH и ABTS методама, а антимикробна бујон микродилуционом методом. Карактеризација добијених једињења урађена је помоћу тачака топљења, FTIR, NMR и елементалном анализом. Предложене су могућности за наставак истраживања, који бу водио њиховој примени одређених испитиваних једињења.

REFERENCES

1. A. Debache, W. Ghalem, R. Boulcina, A. Belfaitah, S. Rhouati, B. Carboni, *Tetrahedron Lett.* **50** (2009) 5248 (https://doi.org/10.1016/j.tetlet.2009.07.018)
2. U. Eisner, J. Kuthan, *Chem. Rev.* **72** (1972) 1 (https://doi.org/10.1021/cr60275a001)
3. A. Velena, N. Zarkovic, K. Gall Troselj, E. Bisenieks, A. Krauze, J. Poikans, G. Duburs, *Oxid. Med. Cell. Longev.* **2016** (2016) (https://doi.org/10.1155/2016/1892412)

4. Y. Wei1 , Y. Lu, Y. Zhu, W. Zheng, F. Guo, Be. Yao, S. Xu, Y. Wang, L. Jin , Y. Li, *Biochim. Biophys. Acta – Gen. Subj.* **1862** (2018) 2261 (https://doi.org/10.1016/j.bbagen.2018.07.022)

5. E. D. Funder, J. B. Trads, K. V. Gothelf, *Org. Biomol. Chem.* **13** (2015) 185 (https://doi.org/10.1039/C4OB01931H)

6. A. E. Sausins, G. Duburs, *Chem. Heterocycl. Compd.* **28** (1992) 363 (https://doi.org/10.1007/bf00766993)

7. A. Kumar, R. A. Maurya, S. Sharma, M. Kumar, G. Bhatia, *Eur. J. Med. Chem.* **45** (2010) 501 (https://doi.org/10.1016/j.ejmech.2009.10.036)

8. A. Ahamed, I. A. Arif, M. Mateen, R. Surendra Kumar, A. Idhayadhulla, *Saudi J. Biol. Sci.* **25** (2018) 1227 (https://doi.org/10.1016/j.sjbs.2018.03.001)

9. A. Gallardo-Godoy, J. Gever, K. L. Fife, B. M. Silber, S. B. Prusiner, A. R. Renslo, *J. Med. Chem.* **54** (2011) 1010 (https://doi.org/10.1021/jm101250y)

10. J. V. Urošević, S. Ž. Drmanić , J. B. Nikolić, I. O. Juranić, B. Ž. Jovanović, *J. Serb. Chem. Soc*. **78** (2013) 1963 (https://doi.org/10.2298/JSC131120139U)

11. V. Sivamurugan, R. Suresh Kumar, M. Palanichamy, V. Murugesan, *J. Heterocycl. Chem.* **42** (2005) 743 (https://doi.org/10.1002/jhet.5570420534)

12. H. N. De Armas, N. Blaton, O. M. Peeters, C. De Ranter, M. Suárez, E. Rolando, Y. Verdecia, E. Ochoa, N. Martín, M. Quinteiro, C. Seoane, J. L. Soto, *J. Heterocycl. Chem.* **37** (2000) 1575 (https://doi.org/10.1002/jhet.5570370627)

13. B. Palakshi Reddy, K. Rajesh, V. Vijayakumar, *Arab. J. Chem.* **8 (**2015) 138 (https://doi.org/10.1016/j.arabjc.2011.01.027)

14. D. B. Shinde, N. D. Shinde, M. S. Shingare, M. P. Dubey, G. K. Patnaik, *Indian J. Chem., B* **34** (1995) 920

15. J. Ramchander, Gajula Raju, N. Rameshwar, T. Sheshashena Reddy, A. Ram Reddy, *Spectrochim. Acta, A* **85** (2012) 210 (https://doi.org/10.1016/j.saa.2011.09.062)

16. S. Kedare, R. Singh, *JFST* **48** (2011) 412 (https://doi.org/10.1007/s13197-011-0251-1)

17. R. Walker, J. D. Everette, *J. Agric. Food Chem.* **57** (2009) 1156 (https://doi.org/10.1021/jf8026765)

18. A. Espinel-Ingroff, A. Fothergill, M. Ghannoum, E. Manavathu, L. Ostrosky-Zeichner, M. Pfaller, M. Rinaldi, W. Schell, T. Walsh, *J. Clin. Microbiol.* **43** (2005) 5243 (https://doi.org/10.1128/JCM.43.10.5243-5246.2005).

SUPPLEMENTARY MATERIAL TO

The synthesis, characterization, antioxidant and antimicrobial activity of some novel amides of the esters of substituted 1,4-dihydropyridines

JASMINA B. NIKOLIĆ[1#], NEVENA Ž. PRLAINOVIĆ[1], GAVRILO M. ŠEKULARAC[2#], LUKA R. MATOVIĆ[3#], ANITA M. LAZIĆ[3#] and SAŠA Ž. DRMANIĆ[1*#]

[1]Department of Organic Chemistry, Faculty of Technology and Metallurgy, University of Belgrade, Belgrade, Serbia, [2]Institute of Chemistry, Technology and Metallurgy, University of Belgrade, Belgrade, Serbia and [3]Innovations Center of Faculty of Technology and Metallurgy, University of Belgrade, Belgrade, Serbia

CHARACTERIZATION OF SYNTHESISED COMPOUNDS

1a

Yield: 72%. M.P. 157 °C.

Elemental: $C_{19}H_{23}NO_4$ (M_w=329.40 gmol^{-1}): C. 69.28; H. 7.04; N. 4.25; O. 19.43 %. Found: C. 69.30; H. 7.02; N. 4.20; O. 19.48 %.

IR(KBr. cm^{-1}) ν_{max}: 3339.60 (N-H); 3033.27 (Ar-H); 2981.98 (C-H); 1685.90 (C=O).

2a

Yield: 53%. M.P. 184 °C.

Elemental: $C_{19}H_{23}NO_5$ (M_w=345.16 gmol^{-1}): C. 66.07; H. 6.71; N. 4.06; O. 23.16 %. Found: C. 66.00; H. 6.78; N. 4.09; O. 23.13 %.

IR(KBr. cm^{-1}) ν_{max}: 3348.23 (N-H); 3027.11 (Ar-H); 2978.54 (C-H); 1702.04 (C=O); 1443.47 (C–OH); 818.27 (Ar-H).

3a

Yield: 81%. M.P. 230 °C.

Elemental: $C_{19}H_{23}NO_5$ (M_w=345.16 gmol^{-1}); C. 66.07; H. 6.71; N. 4.06; O. 23.16 %. Found: C. 66.10; H. 6.68; N. 4.05; O. 23.17 %.

IR(KBr. cm^{-1}) ν_{max}: 3341.89 (N-H); 3107.12 (Ar-H); 2988.47 (C-H); 1701.75 (C=O). 1485.22 (C–OH); 826.31 (Ar-H).

4a

Yield: 65% M.P. 111 °C.

Elemental: $C_{19}H_{22}NO_4Cl$ (M_w=363.5 gmol^{-1}) C. 63; H. 5.8; N. 3.9; O. 17.6; Cl. 9.7 %. Found: C. 63.5; H. 5.6; N. 3.6; O. 17.5; Cl. 9.8 %.

---

* Corresponding author. E-mail: drmana@tmf.bg.ac.rs

IR(KBr. cm^{-1}) v_{max}: 3339.60 (N-H); 3031.3 (Ar-H). 2981.98 (C-H); 1685.90 (C=O); 827.13 (Ar-H); 701.67 (C-Cl)

5a

   4-(4'-bromfenil)-2.6-dimetil-3.5-dikarboetoksi-1.4-dihidropiridin

Yield: 61% M.P. 95 °C.

Elemental: $C_{19}H_{22}NO_4Br$ (Mw=408 gmol^{-1}) C. 56; H. 5.1; N. 3.5; O. 15.8; Br. 19.6 %. Found: C. 56.5; H. 5.2; N. 3.2; O. 15.6; Br. 19.5 %.

IR(KBr. cm^{-1}) vmax: 3342.76 (N-H); 3102.3 (Ar-H). 2990.79 (C-H); 1703.28 (C=O); 808.57 (Ar-H); 682.52 (C-Br)

6a

Yield: 52%. M.P. 163 °C.

Elemental: $C_{19}H_{22}N_2O_6$ (M_w=374.39 gmol^{-1}): C. 60.95; H. 5.92; N. 7.48; O. 25.65 %. Found: C. 60.90; H. 5.97; N. 7.50; O. 25.63 %.

IR(KBr. cm^{-1}) v_{max}: 3342.76 (N-H); 3102.27 (Ar-H); 2990.79 (C-H); 1703.28 (C=O); 1643.16 (C-NO$_2$); 826.35 (Ar-H).

7a

Yield: 84%. M.P. 120 °C.

Elemental: $C_{19}H_{22}N_2O_6$ (M_w=374.39 gmol^{-1}): C. 60.95; H. 5.92; N. 7.48; O. 25.65 %. Found: C. 60.88; H. 5.99; N. 7.45; O. 25.68 %.

IR (KBr. cm^{-1}) v_{max}: 3316.31 (N-H); 3100.27 (Ar-H); 2978.05 (C-H); 1699.76 (C=O); 1644.22 (C-NO$_2$); 823.29 (Ar-H).

8a

Yield: 70% M.P. 93 °C.

Elemental: $C_{20}H_{25}NO_5$ (Mw=359 gmol^{-1}) C. 67; H. 6.8; N. 3.9; O. 22.3 %. Found: C. 67.2; H. 6.5; N. 3.9; O. 22.4 %.

IR(KBr. cm^{-1}) v_{max}: 3341.52 (N-H); 3027.11 (Ar-H); 2991.97 (C-H); 1720.79 (C=O); 1211.44 (C–OCH$_3$); 809.15 (Ar-H).

9a

Yield: 68% M.P. 90 °C.

Elemental: $C_{20}H_{25}NO_4$ (Mw=343 gmol^{-1}) C. 70; H. 7; N. 4; O. 19 %. Found: C. 69.9; H. 7.2; N. 3.9; O. 21 %.

IR(KBr. cm^{-1}) v_{max}: 3348.23 (N-H); 3030.11 (Ar-H); 2978.54 (C-H); 1646.90 (C=O). 1368.29 (CH$_3$); 818.27 (Ar-H).

10a

Yield: 71% M.P. 98 °C.

Elemental: $C_{20}H_{25}NO_4$ (Mw=343 gmol^{-1}) C. 70; H. 7; N. 4; O. 19 %. Found: C. 70.1; H. 6.9; N. 4.1; O. 18.9 %.

IR(KBr. cm^{-1}) v_{max}: 3341.89 (N-H); 3100.40 (Ar-H); 2988.47(C-H); 1655.47 (C=O). 1485.22 (CH$_3$); 840.95 (Ar-H).

1b

Yield: 72%. M.P. 124 °C.

Elemental: $C_{21}H_{19}N_5O_2S_2$ (M_w=437.54 gmol^{-1}): C. 57.65; H. 4.38; N. 16.01; O. 7.31; S. 14.65 %. Found: C. 55.65; H. 4.38; N. 18.01; O. 7.01; S. 14.95 %.

IR(KBr. cm^{-1}) ν_{max}: 3339.34 (N-H); 1649.04 (HNCO); 737.54 (C-S-C); 1486.63 (C=N); 3085.82 (C-H aromatic).

^{1}H NMR: (400 MHz, CDCl$_3$, δ/ppm): 7.296 – 7.270 (2H, m, C$_6$H$_4$), 7.210 (1H, t, $J_1 = J_2$ = 7.6 Hz, C$_6$H$_4$), 7.144 – 7.091 (6H, m, C$_6$H$_4$, C$_3$H$_2$NS, NH), 6.552 (2H, d, J = 3.6 Hz, C$_3$H$_2$NS), 5.625 (1H, s, C$_5$H$_2$N), 2.338 (6H, s, CH$_3$).

^{13}C NMR: (100 MHz, CDCl$_3$, δ/ppm): 167.60 (2C, C=O), 147.74 (1C, C$_6$H$_4$), 143.75 (2C, C$_3$H$_2$NS), 138.90 (2C, C$_3$H$_2$NS), 128.00 (2C, C$_6$H$_4$), 127.82 (2C, C$_6$H$_4$), 126.08 (1C, C$_6$H$_4$), 108.95 (2C, C$_3$H$_2$NS), 104.23 (2C, C$_5$H$_2$N), 59.70 (2C, C$_5$H$_2$N), 39.63 (1C, C$_5$H$_2$N), 14.24 (2C, CH$_3$).
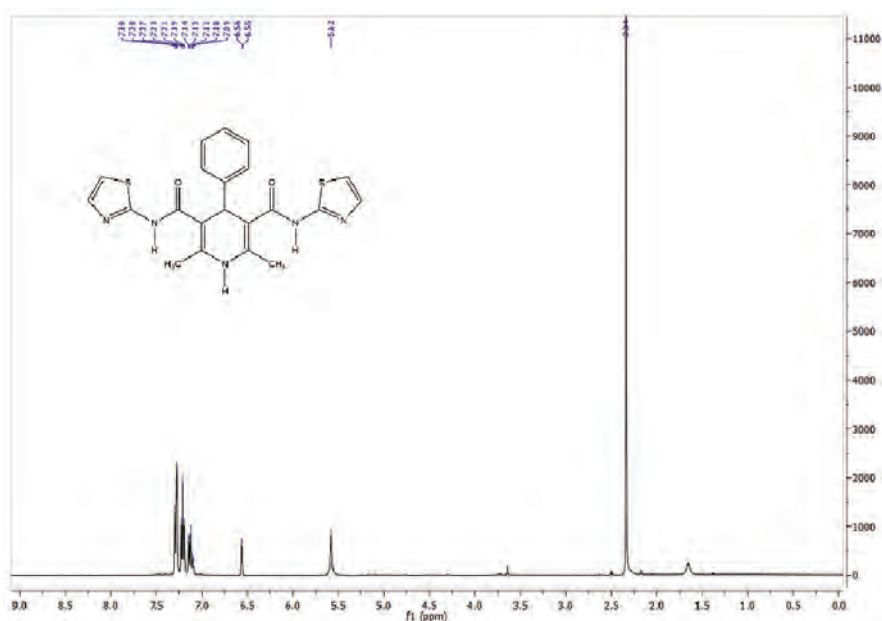
Fig S-1. The ^{1}H NMR spectrum of compound **1b**

NIKOLIĆ *et al.*
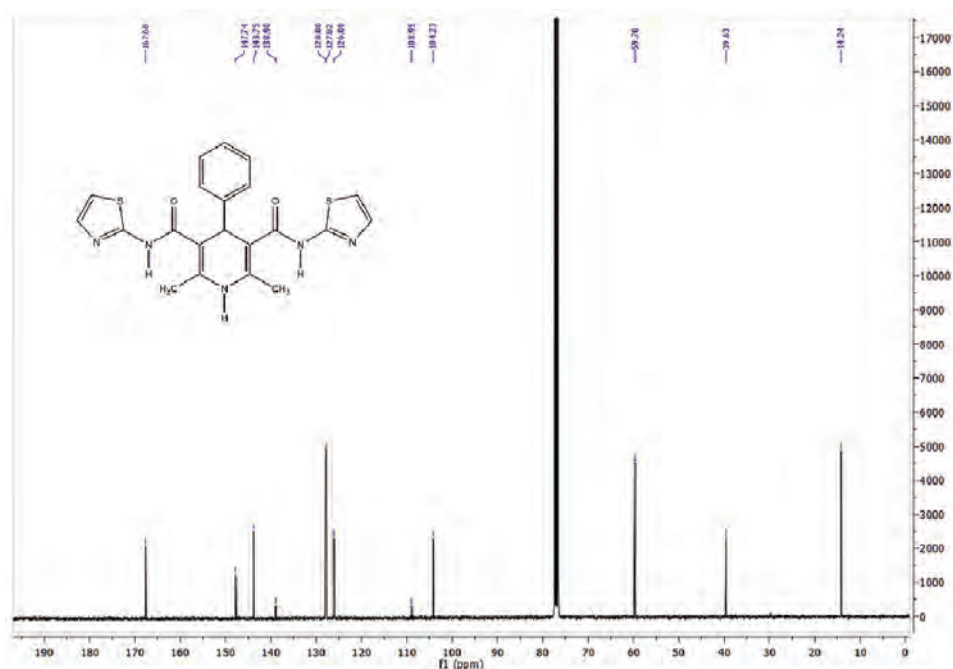
Fig S-2. The ^{13}C NMR spectrum of compound **1b**

2b

Yield: 53%. M.P. 141 °C.

Elemental: $C_{21}H_{19}N_5O_3S_2$ (M_w=453.54 gmol^{-1}): C. 55.61; H. 4.22; N. 15.44; O. 10.58; S. 14.14%. Found: C. 54.25; H. 5.59; N. 15.50; O. 10.57; S. 14.09 %.

IR(KBr. cm^{-1}) ν_{max}: 3348.94 (N-H); 1647.21 (HNCO); 736.52 (C-S-C); 1479.70 (C=N); 3085.57 (C-H aromatic).

^{1}H NMR: (400 MHz, DMSO-d_6, δ/ppm): 6.953 (1H, t, J_1 = 8.0 HZ, J_2 = 7.6 Hz, C_6H_4), 6.915 (2H, d, *J*= 3.6 Hz, C_3H_2NS), 6.846 (2H, s, NH), 6.572 (2H, d, *J*= 7.2 Hz, C_6H_4), 6.528 (2H, d, *J* = 3.6 Hz, C_3H_2NS), 6.474 (1H, d, *J*=8.8 Hz, C_6H_4), 4.794 (1H, s, C_5H_2N), 2.237 (6H, s, CH_3).

^{13}C NMR: (100 MHz, DMSO-d_6, δ/ppm): 167.50 (2C, C=O), 157.40 (1C, C_6H_4), 149.86 (1C, C_6H_4), 145.56 (2C, C_3H_2NS), 139.07 (2C, C_3H_2NS), 129.04 (1C, C_6H_4), 118.48 (1C, C_6H_4), 114.81 (1C, C_6H_4), 113.27 (1C, C_6H_4), 106.95 (2C, C_3H_2NS), 102.24 (2C, C_5H_2N), 59.42 (2C, C_5H_2N), 39.07 (1C, C_5H_2N), 14.65 (2C, CH_3).

Fig S-3. The ^{1}H NMR spectrum of compound **2b**
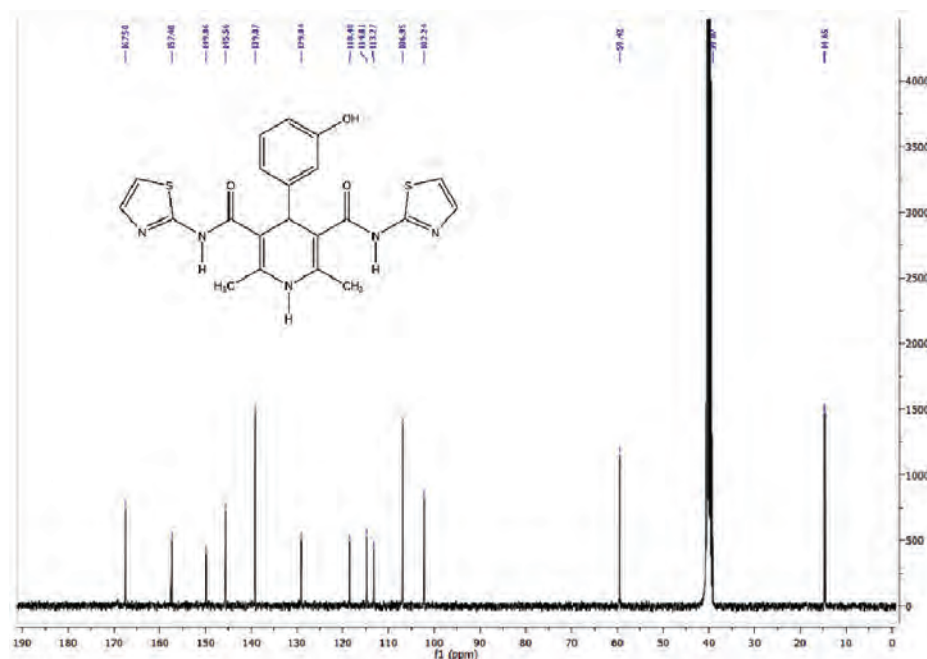
Fig S-4. The ^{13}C NMR spectrum of compound **2b**

NIKOLIĆ *et al.*

3b

Yield: 81%. M.P. 164 °C.

Elemental: $C_{21}H_{19}N_5O_3S_2$ (M_w=453.54 gmol^{-1}): C. 55.61; H. 4.22; N. 15.44; O. 10.58; S. 14.14%. Found: C. 53.21; H. 6.62; N. 15.57; O. 10.45; S. 14.15 %.

IR(KBr. cm^{-1}) v_{max}: 3343.03 (N-H); 1655.40 (HNCO); 739.38 (C-S-C); 1485.29 (C=N); 3074.12 (C-H aromatic).

^{1}H NMR: (400 MHz, CDCl$_3$, δ/ppm): 7.137 (2H, d, *J* = 8.4 Hz, C_6H_4), 7.092 (2H, d, *J* = 3.6 Hz, C_3H_2NS), 6.659 (2H, d, *J* = 8.4 Hz, C_6H_4), 6.548 (2H, d, *J* = 4.0 Hz, C_3H_2NS), 5.513 (1H, s, C_5H_2N), 4.913 (2H, s, NH), 2.325 (6H, s, CH$_3$);

^{13}C NMR: (100 MHz, CDCl$_3$, δ/ppm): 167.67 (2C, C=O), 153.83 (1C, C_6H_4), 143.40 (2C, C_3H_2NS), 140.41 (1C, C_6H_4), 138.82 (2C, C_3H_2NS), 129.20 (2C, C_6H_4), 114.63 (2C, C_6H_4), 108.94 (2C, C_3H_2NS), 104.49 (2C, C_3H_2NS), 59.70 (2C, C_5H_2N), 38.79 (1C, C_5H_2N), 14.26 (2C, CH$_3$).

Fig S-5. The ^{1}H NMR spectrum of compound **3b**
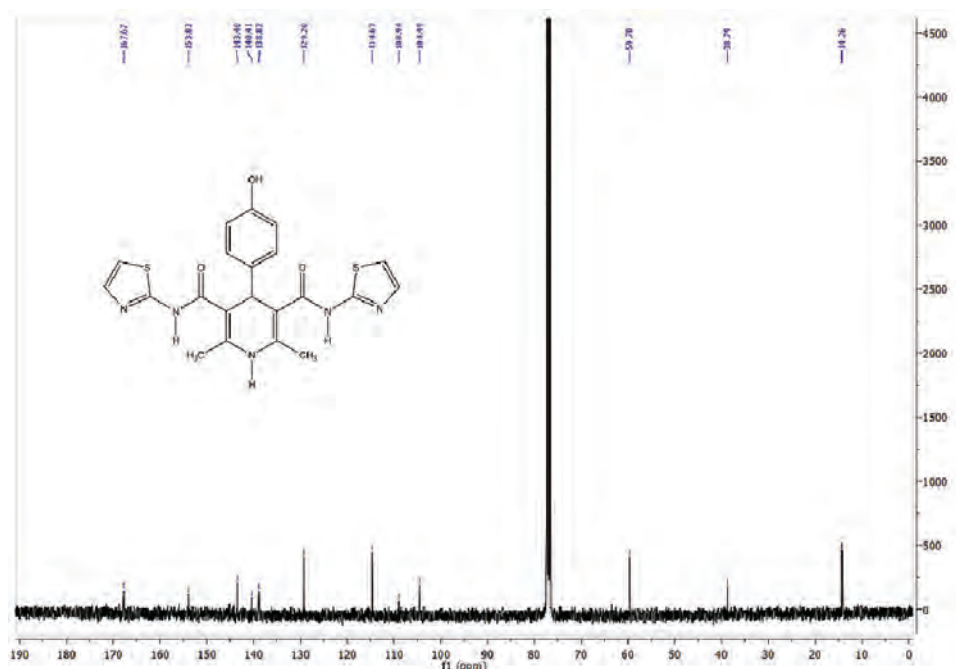
Fig S-6. The ^{13}C NMR spectrum of compound **3b**

4b

Yield: 79% M.P. 124 °C.

Elemental: $C_{21}H_{18}N_5O_2S_2Cl$ (M_w=471.5 gmol^{-1}) C. 53.4; H. 3.8; N. 14.8; O. 6.8; S. 13.6; Cl. 7.5 % Found: C. 53.5; H. 3.9; N. 14.9; O. 6.7; S. 13.4; Cl. 7.5 %

IR(KBr. cm^{-1}) ν_{max}: 3339.34 (N-H); 1649.04 (HNCO); 701.52 (C-S-C); 1486.63 (C=N); 3085.82 (C-H aromatic); 737.57 (C-Cl).

^{1}H NMR: (400 MHz, DMSO-d_6, δ/ppm): 7.251 (2H, d, J = 8.4 Hz, C_6H_4), 7.143 (2H, d, J = 8.4 Hz, C_6H_4), 6.848 (2H, s, NH), 6.752 (2H, d, J = 3.6 Hz, C_3H_2NS), 6.694 (2H, d, J = 3.6 Hz, C_3H_2NS), 4.829 (1H, s, C_5H_2N), 2.246 (6H, s, CH_3);

^{13}C NMR: (100 MHz, DMSO-d_6, δ/ppm): 167.22 (2C, C=O), 147.55 (1C, C_6H_4), 146.08 (2C, C_3H_2NS), 130.86 (1C, C_6H_4), 129.65 (2C, C_6H_4), 128.26 (2C, C_6H_4), 114.25 (2C, C_3H_2NS), 108.92 (2C, C_3H_2NS), 101.96 (2C, C_5H_2N), 59.52 (2C, C_5H_2N), 39.01 (1C, C_5H_2N), 14.60 (2C, CH_3).
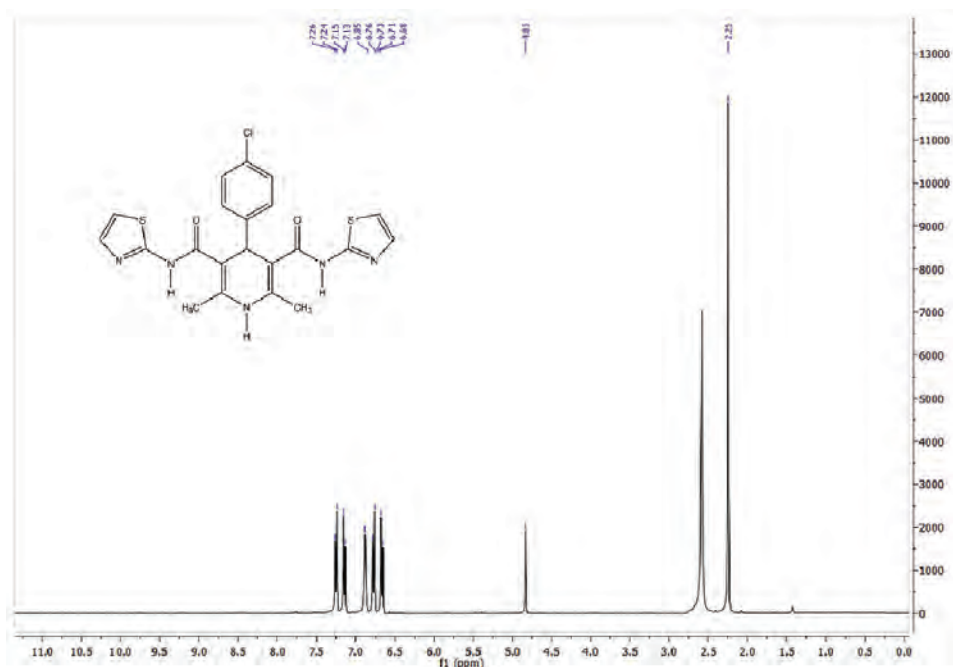
Fig S-7. The ^{1}H NMR spectrum of compound **4b**
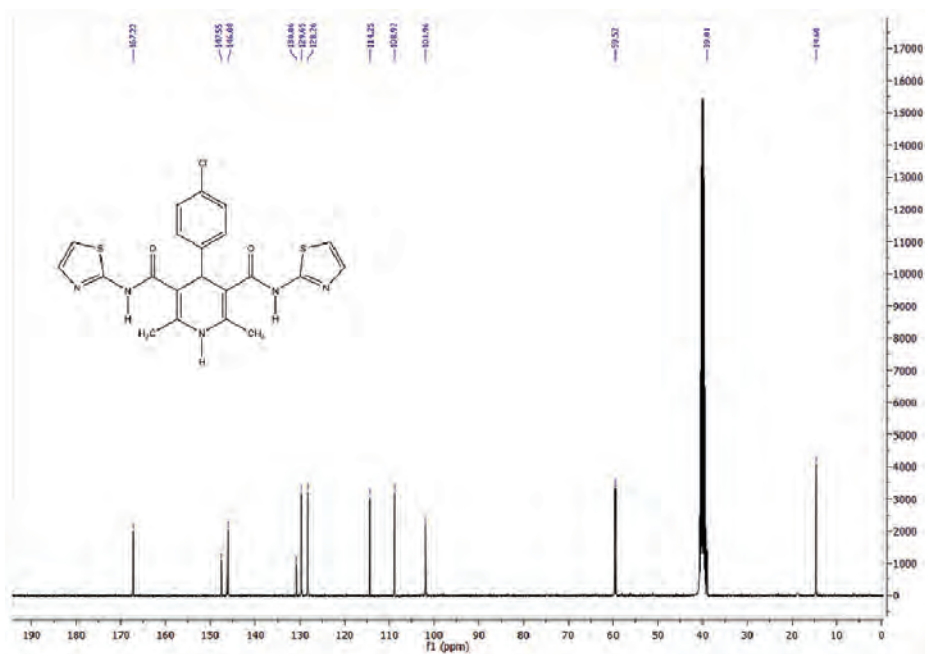
Fig S-8. The ^{13}C NMR spectrum of compound **4b**

5b

Yield: 83% M.P. 105 °C.

Elemental: $C_{21}H_{18}N_5O_2S_2Br$ (M_w=516 gmol^{-1}) C. 48.8; H. 3.5; N. 13.5; O. 6.2; S. 12.4; Br. 15.5 % Found: C. 48.9; H. 3.4; N. 13.6; O. 6.3; S. 12.4; Br. 15.4 %

IR (KBr. cm^{-1}) v_{max}: 3315.23 (N-H); 1681.10 (HNCO). 705.45 (C-S-C); 1483.35 (C=N) i 3104.06 (C-H aromatic); 2978.34 (C-H strech); 629.35 (C-Br)

^{1}H NMR: (400 MHz, DMSO-d_6, δ/ppm): 7.383 (2H, d, J = 8.0 Hz, C_6H_4), 7.089 (2H, d, J = 8.4 Hz, C_6H_4), 6.916 (2H, d, J = 3.6 Hz, C_3H_2NS), 6.862 (2H, s, NH), 6.523 (2H, d, J = 3.6 Hz, C_3H_2NS), 4.817 (1H, s, C_5H_2N), 2.246 (6H, s, CH_3);

^{13}C NMR: (100 MHz, DMSO-d_6, δ/ppm): 167.24 (2C, C=O), 147.97 (1C, C_6H_4), 146.13 (2C, C_3H_2NS), 139.03 (2C, C_3H_2NS), 131.19 (2C, C_6H_4), 130.09 (2C, C_6H_4), 119.39 (1C, C_6H_4), 106.99 (2C, C_3H_2NS), 101.89 (2C, C_5H_2N), 59.55 (2C, C_5H_2N), 39.10 (1C, C_5H_2N), 14.61 (2C, CH_3).
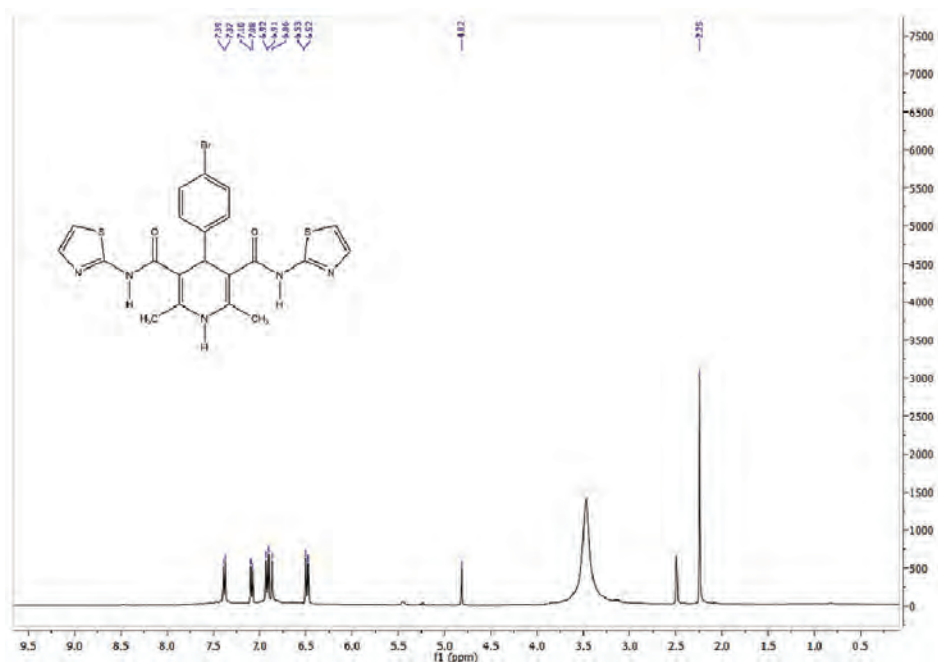
Fig S-9. The ^{1}H NMR spectrum of compound **5b**
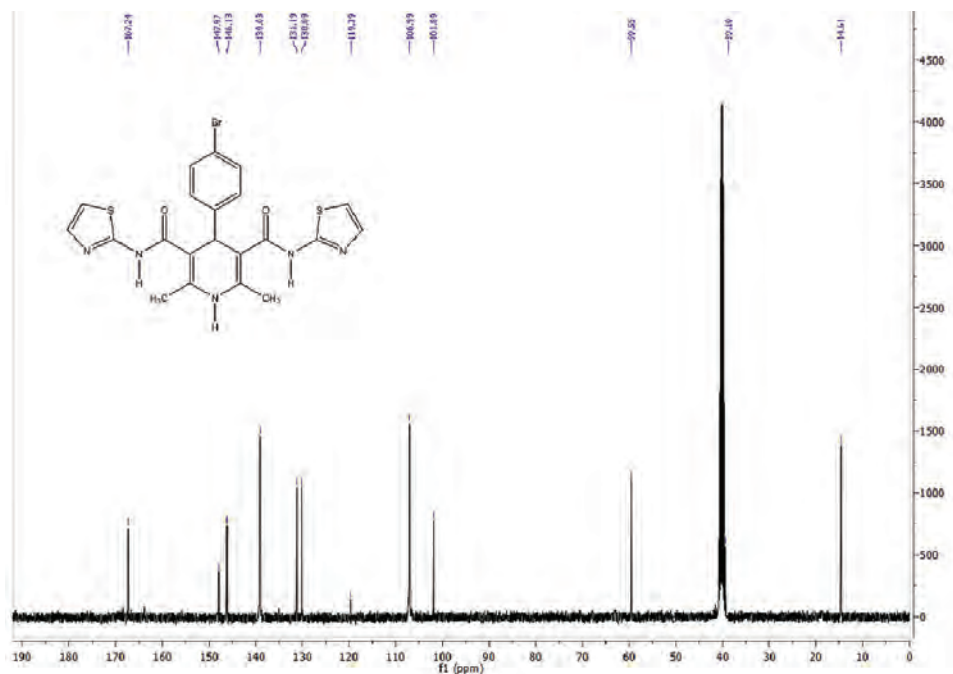
Fig S-10. The ^{13}C NMR spectrum of compound **5b**

6b

Yield: 52%. M.P.128 °C.

Elementalna: $C_{21}H_{18}N_6O_4S_2$ (M_w=482.53 gmol^{-1}): C. 52.27; H. 3.76; N. 17.42; O. 13.26; S. 13.29 %. Found: C. 52.00; H. 4.03; N. 17.01; O. 13.76; S. 13.20 %.

IR(KBr. cm^{-1}) ν_{max}: 3180.01 (N-H); 1643.61 (HNCO); 740.59 (C-S-C); 1484.01 (C=N); 3074.47 (C-H aromatic).

^{1}H NMR: (400 MHz, DMSO-d_6, δ/ppm): 8.002 – 7.969 (2H, m, C_6H_4), 7.599 (1H, d, J= 7.6 Hz, C_6H_4), 7.533 (1H, t, J_1 = 8.0 HZ, J_2 = 7.2 Hz, C_6H_4), 6.913 (2H, d, J=4,0 Hz, C_6H_4), 6,855 (2H, s, NH), 6.527 (2H, d, J = 3.6 Hz, C_3H_2NS), 4.954 (1H, s, C_5H_2N), 2.275 (6H, s, CH_3).

^{13}C NMR: (100 MHz, DMSO-d_6, δ/ppm): 166.96 (2C, C=O), 150.72 (1C, C_6H_4), 147.87 (1C, C_6H_4), 146.82 (2C, C_3H_2NS), 139.06 (2C, C_3H_2NS), 134.69 (1C, C_6H_4), 130.06 (1C, C_6H_4), 122.35 (1C, C_6H_4), 121.54 (1C, C_6H_4), 106.94 (2C, C_3H_2NS), 101.51 (2C, C_5H_2N), 59.67 (2C, C_5H_2N), 18.68 (1C, C_5H_2N), 14.52 (2C, CH_3).
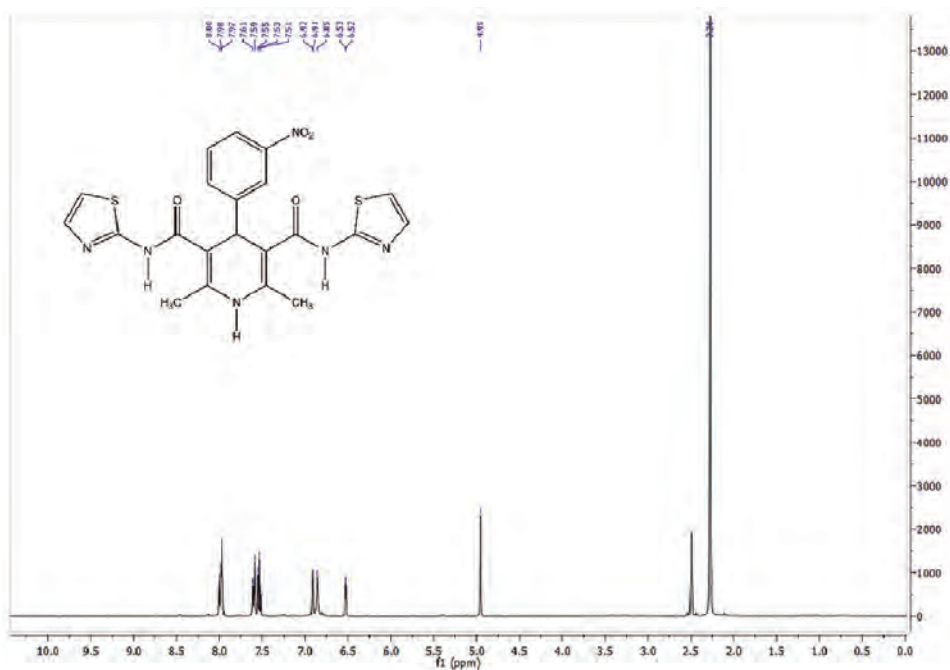
Fig S-11. The ^{1}H NMR spectrum of compound **6b**
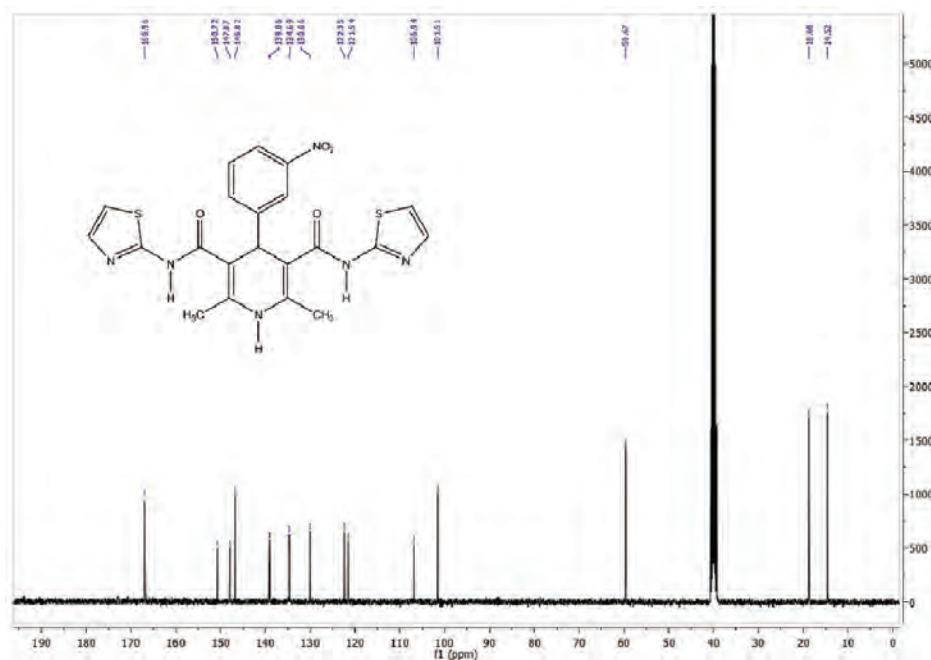
Fig S-12. The ^{13}C NMR spectrum of compound **6b**

7b

Yield 84%. M.P.105 °C.

Elemental: $C_{21}H_{18}N_6O_4S_2$ (M_w=482.53 gmol^{-1}): C. 52.27; H. 3.76; N. 17.42; O. 13.26; S. 13.29 %. Found: C. 53.27; H. 2.76; N. 17.72; O. 13.26; S. 12.99 %.

IR (KBr. cm^{-1}) v_{max}: 3304.06 (N-H); 1643.97 (HNCO); 746.11 (C-S-C); 1483.35 (C=N); 2978.34 (C-H aromatic).

^{1}H NMR: (400 MHz, CDCl$_3$, δ/ppm): 8.083 (2H, d, J = 8.4 Hz, C_6H_4), 7.449 (2H, d, J = 8.8 Hz, C_6H_4), 7.084 (2H, d, J = 3.6 Hz, C_3H_2NS), 6.544 (2H, d, J = 3.6 Hz, C_3H_2NS), 5.703 (1H, s, C_5H_2N), 5.093 (2H, s, NH), 2.358 (6H, s, CH$_3$);

^{13}C NMR: (100 MHz, CDCl$_3$, δ/ppm): 167.02 (2C, C=O), 155.04 (1C, C_6H_4), 146.37 (1C, C_6H_4), 144.52 (2C, C_3H_2NS), 138.76 (2C, C_3H_2NS), 128.89 (2C, C_6H_4), 123.29 (2C, C_6H_4), 108.89 (2C, C_3H_2NS), 103.27 (2C, C_5H_2N), 59.99 (2C, C_5H_2N), 40.13 (1C, C_5H_2N), 14.25 (2C, CH$_3$).
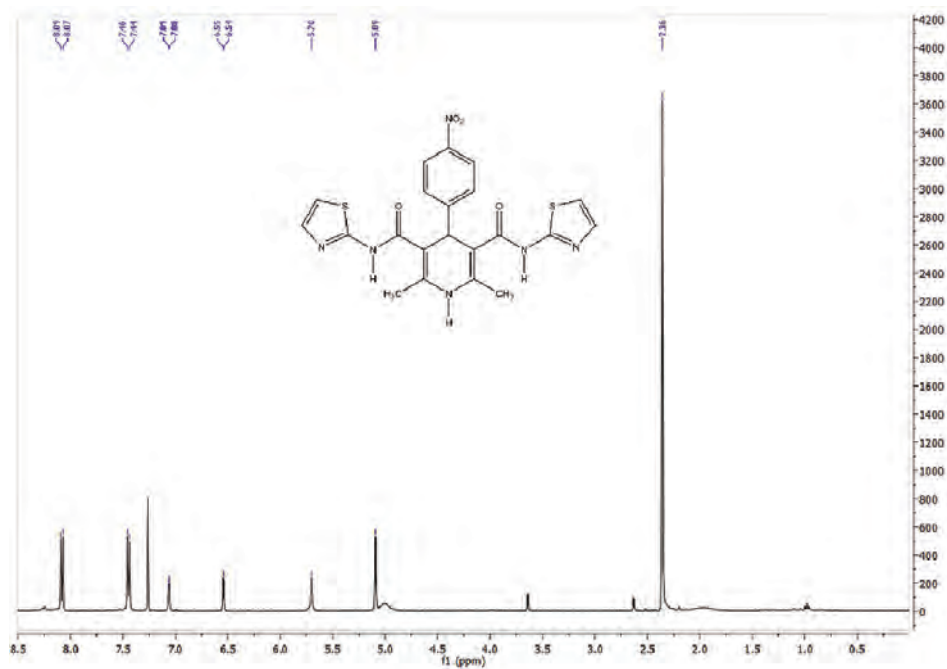
Fig S-13. The ^{1}H NMR spectrum of compound **7b**
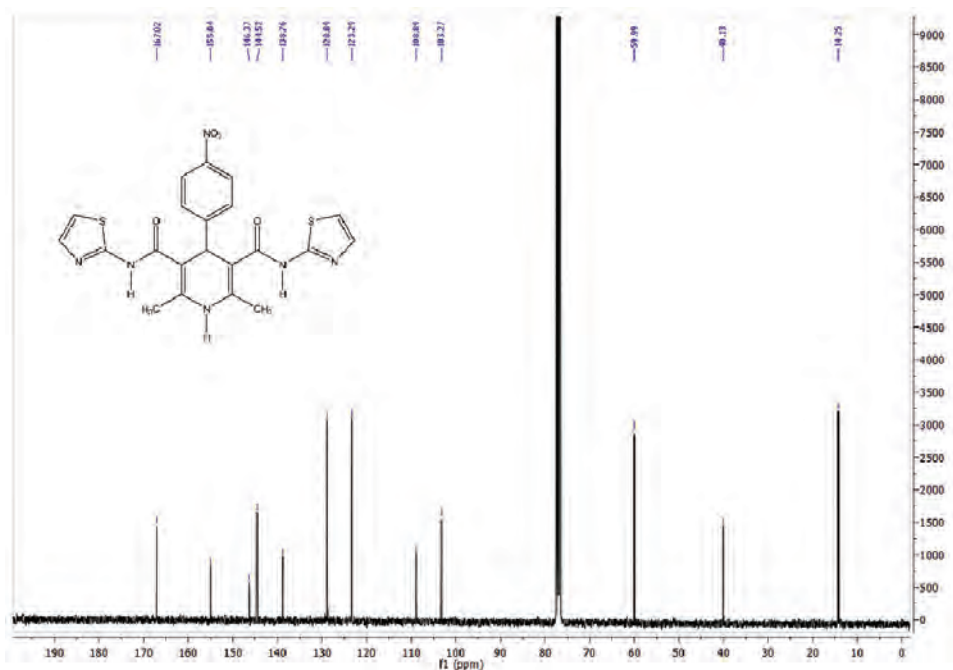
Fig S-14. The ^{13}C NMR spectrum of compound **7b**

8b

Yield: 78% M.P. 141 °C.

Elemental: $C_{21}H_{21}N_5O_3S_2$ (M_w=467 gmol^{-1}) C. 56.5; H. 4.5; N. 15; O. 10.3; S. 13.7 %. Found: C. 56.6; H. 4.6; N. 14.8; O. 10.4; S. 13.6 %.

IR(KBr. cm^{-1}) ν_{max}: 3348.94 (N-H); 1647.21 (HNCO); 736.52 (C-S-C); 1479.70 (C=N); 3085.57 (C-H aromatic); 1221.1 (C–OCH$_3$); 2978.75 (C-H stretch).

^{1}H NMR: (400 MHz, DMSO-d_6, δ/ppm): 7.037 (2H, d, J = 8.4 Hz, C_6H_4), 6.915 (2H, d, J = 3.6 Hz, C_3H_2NS), 6.849 (2H, s, NH), 6.746 (2H, d, J = 8.4 Hz, C_6H_4), 6.528 (2H, d, J = 3.6 Hz, C_3H_2SN), 4.781 (1H, s, C_5H_2N), 3.665 (3H, s, OCH$_3$), 2.284 (6H, s, CH$_3$).

^{13}C NMR: (100 MHz, DMSO-d_6, δ/ppm): 167.48 (2C, C=O), 157.90 (1C, C_6H_4), 145.42 (2C, C_3H_2NS), 140.96 (1C, C_6H_4), 139.06 (2C, C_6H_4), 128.74 (2C, C_3H_2NS), 113.66 (2C, C_3H_2NS), 106.96 (2C, C_6H_4), 102.56 (2C, C_5H_2N), 55.34 (1C, OCH$_3$), 38.40 (1C, C_6H_4N), 14.65 (2C, CH$_3$).

NIKOLIĆ *et al.*
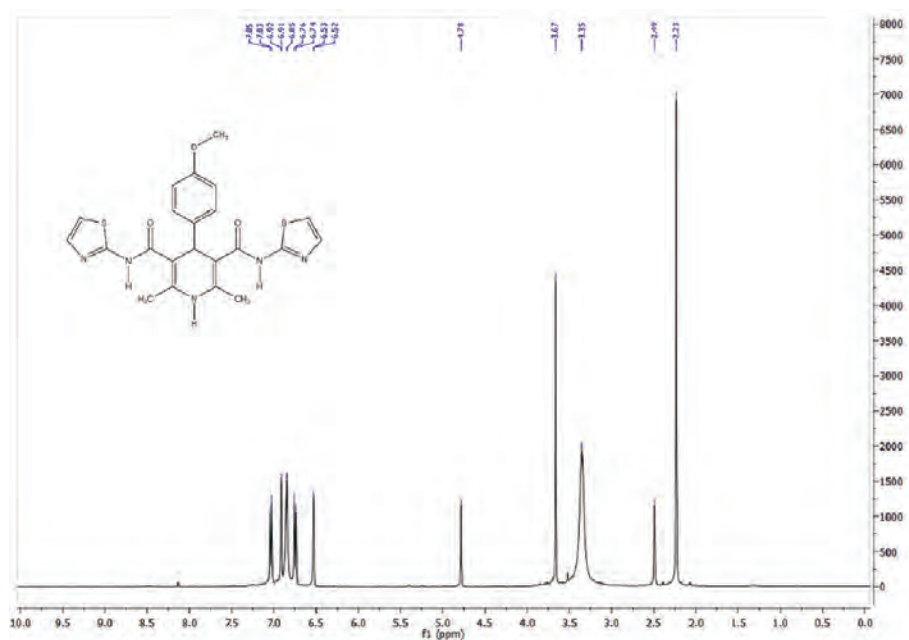
Fig S-15. The ^{1}H NMR spectrum of compound **8b**
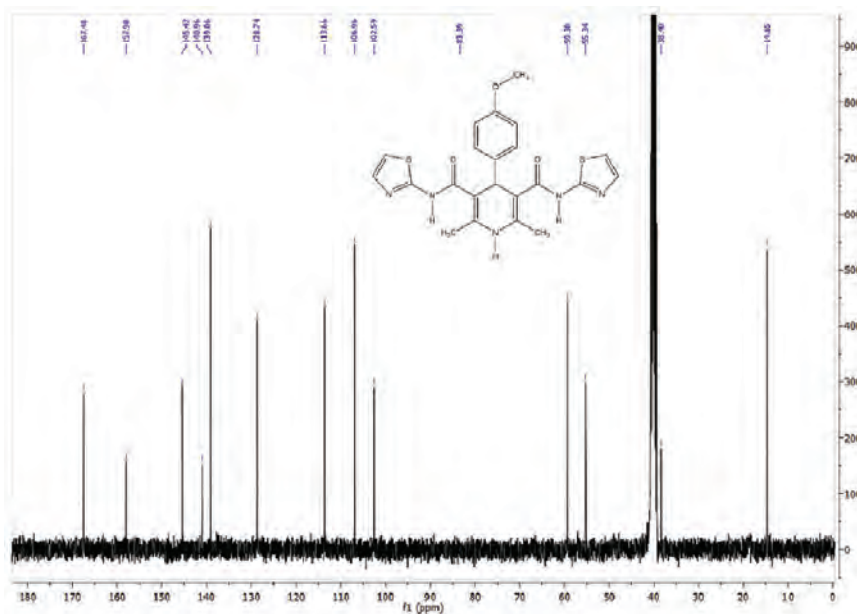
Fig S-16. The ^{13}C NMR spectrum of compound **8b**

9b

Yield: 77% M.P. 251 °C.

Elemental: $C_{22}H_{21}N_5O_2S_2$ (M_w=451 gmol^{-1}) C. 58.5; H. 4.6; N. 15.5; O. 7.1; S. 14.2 %. Found: C. 58.6; H. 4.4; N. 15.7; O. 6.9; S. 14.4 %.

IR(KBr. cm^{-1}) ν_{max}: 3310.35 (N-H); 1707.02 (HNCO); 781.65 (C-S-C); 1470.59 (C=N); 3022.21 (C-H aromatic).

^{1}H NMR: (400 MHz, DMSO-d_6, δ/ppm): 7.066 (1H, t, $J_1 = J_2 = 7.6$ Hz, C_6H_4), 6.950 – 6.854 (7H, m, C_6H_4, NH, C_3H_2NS), 6.525 (2H, d, $J = 3.6$ Hz, C_3H_2NS), 4.819 (1H, s, C_5H_2N), 2.245 (6H, s, CH_3), 2.210 (3H, s, CH_3).

^{13}C NMR: (100 MHz, DMSO-d_6, δ/ppm): 167.43 (2C, C=O), 148.56 (1C, C_6H_4), 145.67 (2C, C_3H_2NS), 136.97 (2C, C_6H_4), 128.49 (1C, C_6H_4), 128.23 (1C, C_3H_2NS), 126.97 (1C, C_6H_4), 124.94 (1C, C_3H_2NS), 106.95 (2C, C_3H_2NS), 102.32 (2C, C_5H_2N), 59.39 (2C, C_5H_2N), 39.26 (1C, C_5H_2N), 21.65 (1C, CH_3), 14.62 (2C, CH_3).
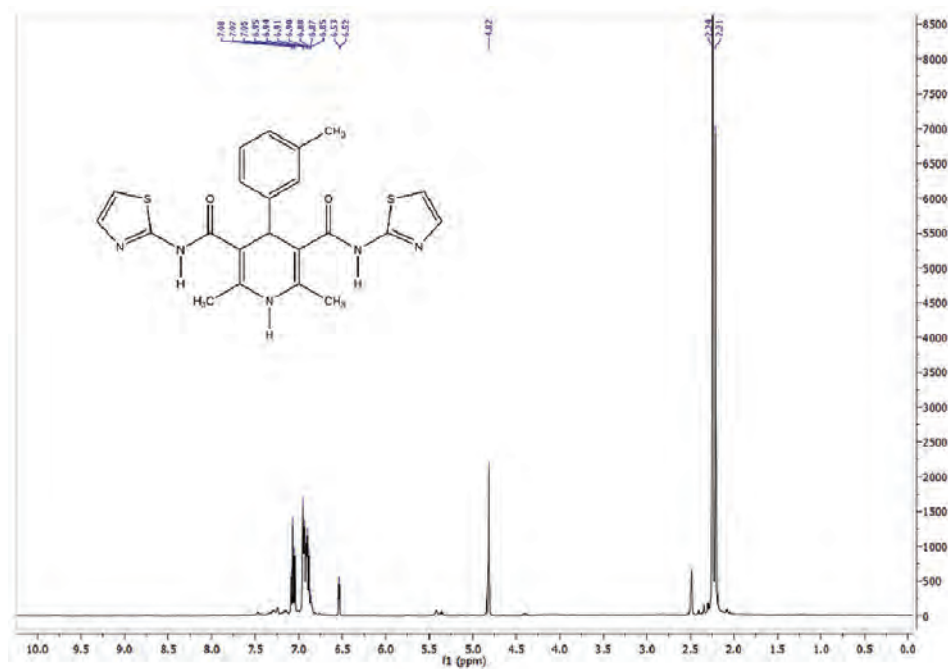
Fig S-17. The ^{1}H NMR spectrum of compound **9b**
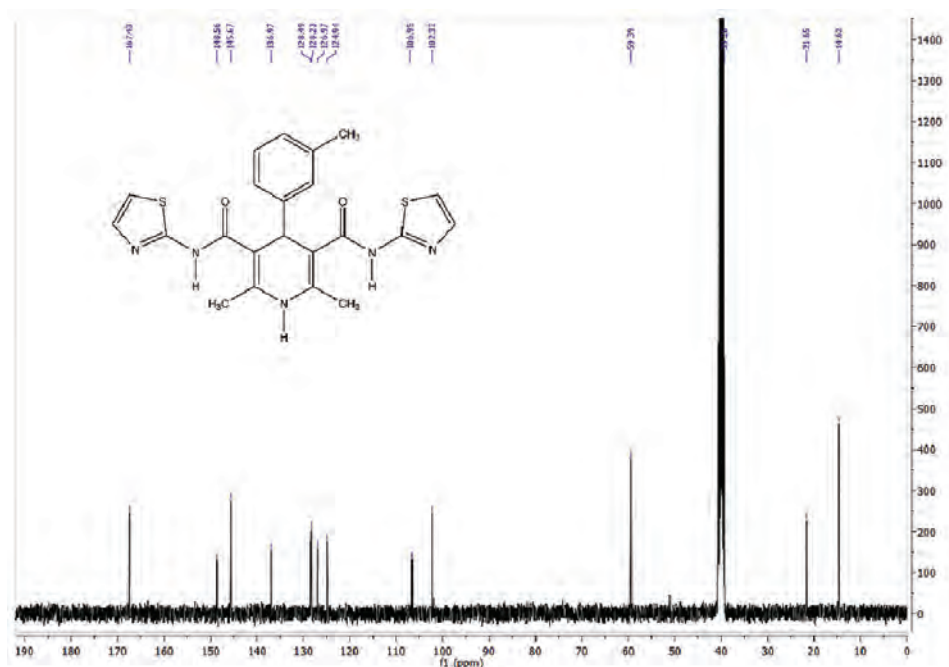
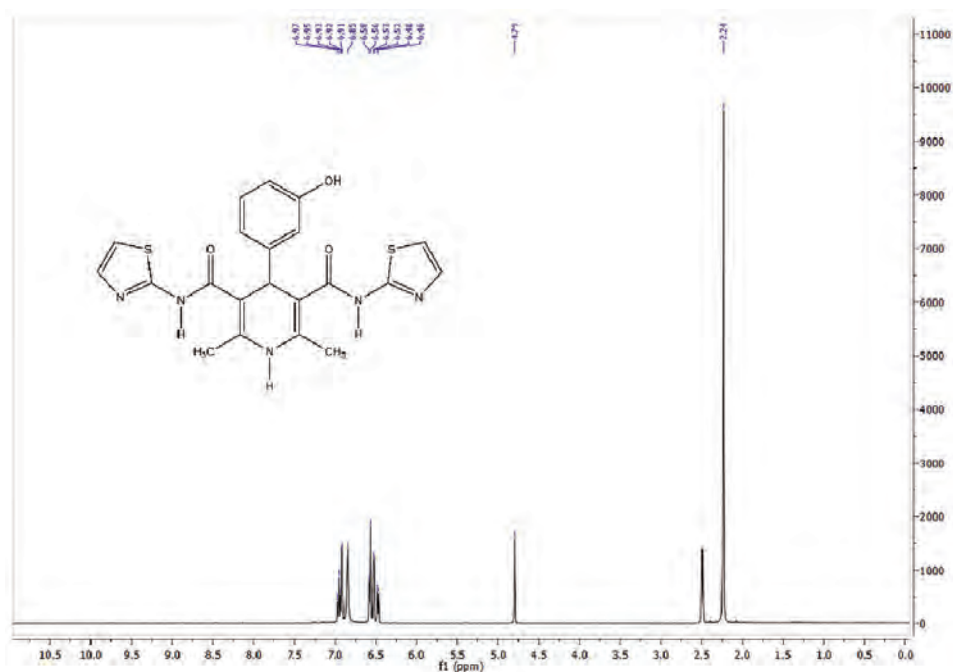Fig S-18. The ^{13}C NMR spectrum of compound **9b**

10b

Yield: 80% M.P. 164 °C.

Elemental: $C_{22}H_{21}N_5O_2S_2$ (M_w=451 gmol^{-1}) C. 58.5; H. 4.6; N. 15.5; O. 7.1; S. 14.2 %. Found: C. 58.7; H. 4.5; N. 15.6; O. 7.2; S. 14 %.

IR(KBr. cm^{-1}) ν_{max}: 3343.03 (N-H); 1695.40 (HNCO); 779.38 (C-S-C); 1477.29 (C=N); 3027.12 (C-H aromatic).

^{1}H NMR: (400 MHz, DMSO-d_6, δ/ppm): 7.026 (2H, d, J = 8.0 Hz, C_6H_4), 6.978 (2H, d, J = 8.0 Hz, C_6H_4), 6.920 (2H, d, J = 3.6 Hz, C_3H_2NS), 6.858 (2H, s, NH), 6.522 (2H, d, J = 3.6 Hz, C_3H_2NS), 4.814 (1H, s, C_5H_2N), 2.243 (6H, s, CH_3), 2.190 (3H, s, CH_3);

^{13}C NMR: (100 MHz, DMSO-d_6, δ/ppm): 167.45 (2C, C=O), 145.74 (1C, C_6H_4), 145.57 (2C, C_3H_2NS), 139.02 (2C, C_3H_2NS), 135.19 (1C, C_6H_4), 128.84 (2C, C_6H_4), 127.68 (2C, C_6H_4), 106.94 (2C, C_3H_2NS), 102.45 (2C, C_5H_2N), 59.38 (2C, C_5H_2N), 38.87 (1C, C_5H_2N), 21.01 (1C, CH_3), 14.61 (2C, CH_3).
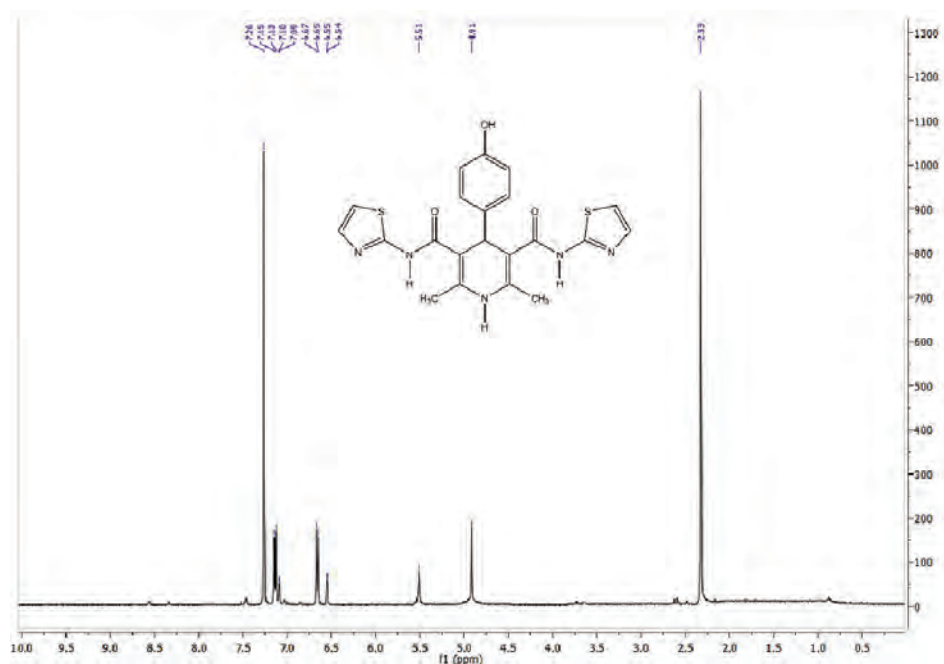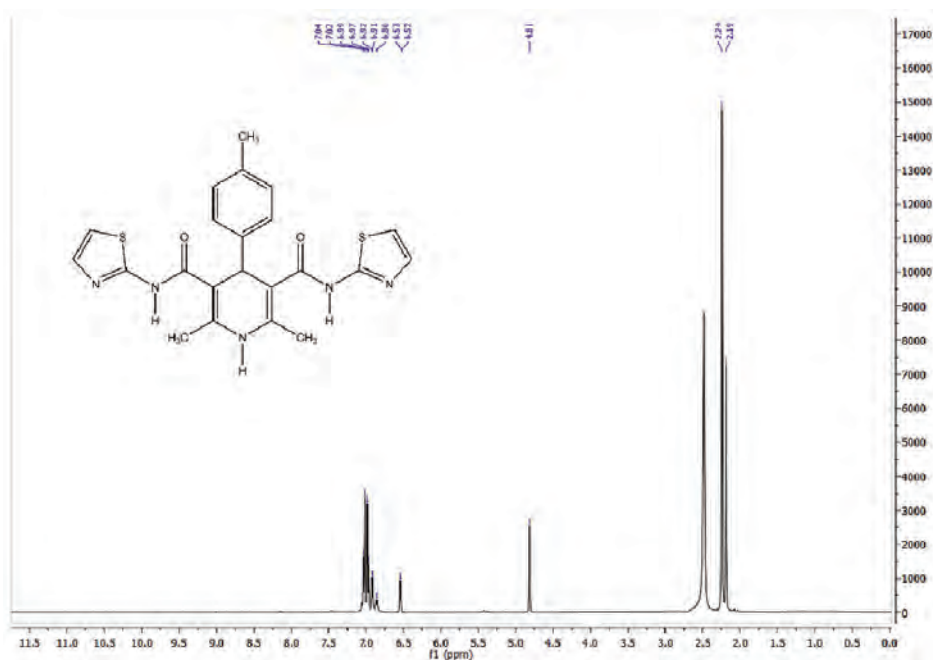
Fig S-19. The ^{1}H NMR spectrum of compound **10b**
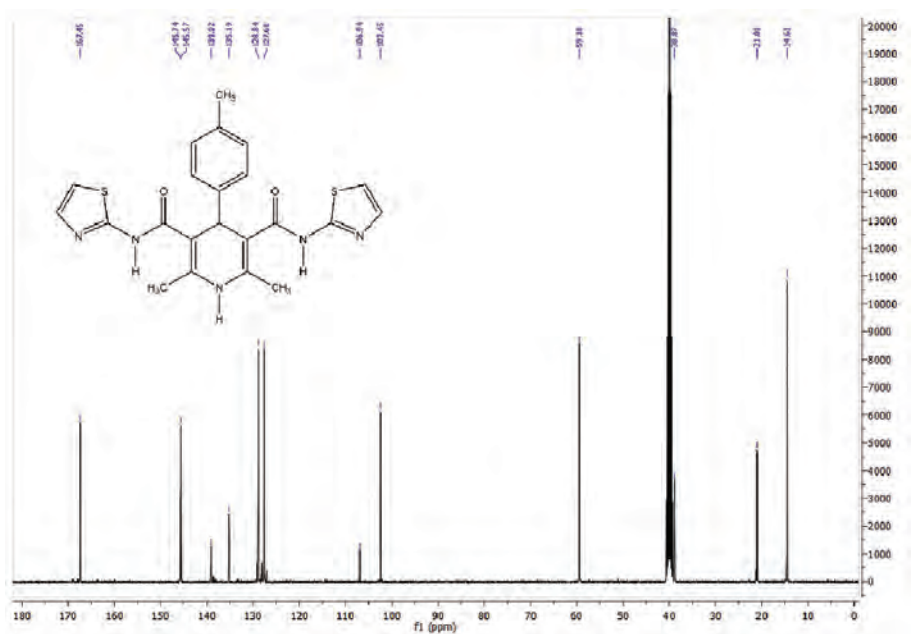
Fig S-20. The ^{13}C NMR spectrum of compound **10b**.

Oxidation of 1,5-benzodiazepine oximes catalysed by peroxidases

LIDIJA KOSYCHOVA*, LINA REKOVIC, IRINA BRATKOVSKAJA,
INGRIDA RADVEIKIENE and REGINA VIDŽIŪNAITĖ**

*Institute of Biochemistry, Life Sciences Center, Vilnius University, Saulėtekio al. 7,
Vilnius 10223, Lithuania*

Abstract: Oxidation of 1,3,4,5-tetrahydro-2*H*-1,5-benzodiazepine oximes catalysed by horseradish peroxidase (HRP) and recombinant *Coprinus cinereus* peroxidase (rCiP) was studied spectrophotometrically. The reaction rate dependences on the substrate and hydrogen peroxide concentrations were investigated; the values of apparent K_M and V_{max}, catalytic, oxidation and reduction constants (k_{cat}, k_{ox} and k_{red}, respectively) were calculated. The reactivity constants for the reactions catalysed by rCiP were higher than those for the HRP. Since oximes can have different structures depending on pH, the influence of pH on the rate of oxidation of compounds was studied. The dependences of the oxidation rate of the investigated oximes on the pH of the buffer solution were determined, and the pKa values of the amino acids of peroxidases responsible for the rate of catalysis were obtained. The HRP activity dependence on pH has a classical bell-shaped character, while rCiP dependence has a complex character.

Keywords: HRP; rCiP; 1,3,4,5-tetrahydro-2*H*-1,5-benzodiazepines.

INTRODUCTION

Nitrogen-containing heterocyclic compounds are widely distributed in nature. Both exocyclic and endocyclic organic nitrogen of heterocycles, as molecular centers, can participate in various metabolic transformations, one of which is biological oxidation. Biological nitrogen oxidation as a metabolic pathway was identified by Keese in 1959.[1] N-hydroxy compounds are biologically active secondary metabolites that can be further oxidised *in vivo* and are often sources of NO. The importance of such compounds and the mechanism of their effect on living organisms became particularly evident at the end of the last century, when R. F. Furchgott, L. J. Ignarro and F. Murad received the Nobel Prize in 1998. It should be noted that the synthesis of the first cyclic hydroxamic acid 2-hydroxy-

---

-2-pyridone was published by Shaw in 1951, and later in 1956 Clauson-Kaas synthesised derivatives of this compound that had antimicrobial properties.[2,3] The N-hydroxy group is the pharmacophore required for the biological activity of the entire drug molecule. This group significantly changes the properties of the molecule – solubility, acid–base properties and binding to the target protein. Such compounds are characterized by a wide spectrum of biological activity.[4,5]

Due to the widespread use of these compounds in medicine, the chemistry of these materials has expanded over the past few decades, producing a series of structurally novel compounds with a wide range of reactivity and stability.

Among these compounds are the pharmacologically active drugs benzodiazepines (BZDs) and their derivatives.[6] They are widely used as anti-inflammatory, analgesic, hypnotic, sedative and antidepressant agents.[6,7] Benzodiazepines bind to γ-aminobutyric acid (GABA$_A$) receptors, enhance the inhibitory effect of the neurotransmitter GABA$_A$ by removing benzodiazepine metabolites. In the liver benzodiazepines are metabolized by the action of cytochrome P450 enzymes and excreted in the urine.[8]

The 1,5-BZDs have received a lot of attention in medical research, as fewer side effects of new derivatives with enhanced pharmacological activity have been reported. These derivatives are a poorly studied class of compounds.[9] Data on their oxidation are inconsistent in the literature. Therefore, intensive transformation studies of such compounds are currently underway. One of the strategies for improving the properties of ketone drugs is the development of prodrugs by synthesising oxime precursors.[10,11] However, NO binding in the molecule to be used as a drug is known to be a risk factor, as most drugs containing amino and/or nitro groups generate reactive N–OH metabolites.[12] The high reactivity of N–OH metabolites towards nucleophiles is further enhanced by interaction with inorganic sulphate to form the o-sulphate esters, which are further ionized to form electrophilic reactive nitrene ions that covalently bind to various cellular components. The primary N-hydroxy metabolites of drugs with increased electronic density on the nitrogen atom are chemically unstable and can be further converted to secondary metabolites – nitrons, nitroses and nitro compounds.[12] Therefore, the characterization of 1,5-benzodiazepines with an iminoxy group and studies of their oxidative conversion are currently very relevant, since the resulting products can be toxic and the intensive use of these compounds can pose a danger to the environment.[13,14] Data from studies on the biodegradation of this type of compound using microorganisms and/or their enzymes have emerged recently.[15–18] Whereas, due to their chemical structure these N-hydroxyimines will have a spatially stable oxamide moiety that is likely to facilitate interaction with the enzymes. Benzodiazepine-containing drugs or other similar compounds can be oxidised not only by cytochrome P450 but also by human peroxidases (myeloperoxidases, eosinophil peroxidases, catalases). Peroxidases can

be found in all life domains.[19] Evolutionarily related heme-containing peroxidases are found in bacteria and organelles of prokaryotic origin (class I), fungi (class II) and plants (class III).[20] In the view of the wide applications of peroxidases in the key areas of biotechnology and bioremediation of contaminating environmental pollutants and industry, they are considered as one of the important industrial enzymes.

Horseradish peroxidase (HRP) is well known for its high catalytic activity and broad specificity for electron donors.[21] A fungal peroxidase from *Coprinus cinereus* (CiP; identical to *Arthromyces ramosus* peroxidase), has attained much attention because of its high specific activity, and broad substrate specificity similar to that of the HRP.[22] Notably, CiP consists of a single species of enzyme, whereas HRP consists of at least 12 isozymes possessing different catalytic properties. The mutants of recombinant CiP (rCiP) demonstrate an elevated stability compared with CiP and/or HRP.[23] For these reasons rCiP was selected for our study and HRP was used for comparison as in investigation of other scientists.[24]

The aim of this work was to investigate and compare the oxidation of 1,5--benzodiazepine oximes catalysed by these peroxidases, to determine the main kinetic parameters, oxidation and reduction constants and the influence of pH on these transformations, since such studies are relevant, but no similar studies were found in the literature.

EXPERIMENTAL

Enzymes and chemicals

Peroxidase (EC 1.11.1.7) from horseradish (HRP, type 1) was obtained from "Reanal" (Hungary). Recombinant peroxidase from the basidiomycete *Coprinus cinereus* (rCiP) was received from "Novozymes A/S" (Denmark).

The 1,3,4,5-tetrahydro-2*H*-1,5-benzodiazepine oximes **1**–**3** (Fig. 1) synthesis was performed as described.[25]
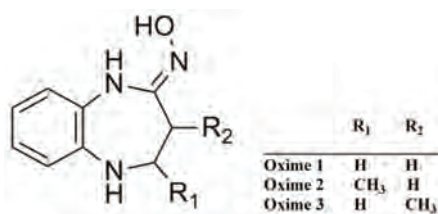
Fig. 1. Chemical structures of 1,3,4,5-tetra-hydro-2*H*-1,5-benzodiazepine oximes **1**–**3**.

96 % Ethanol was received from "Sigma Chemical Co". Acetic acid, sodium acetate, boric acid, potassium dihydrophosphate and potassium hydroxide were of analytical grade and received from "Sigma". Britton–Robinson buffer solution was obtained by titrating mixture of 20 mM H_3BO_3, 20 mM KH_2PO_4, 20 mM CH_3COOH with 0.3 M NaOH until necessary pH.

The hydrogen peroxide (30 %) was from "Roth" (Germany). Buffer solutions, solutions of enzymes and hydrogen peroxide were prepared in double distilled water. The concentrations of enzymes and hydrogen peroxide were determined spectrophotometrically.[26-28]

Samples of oximes **1**–**3** were weighed and dissolved in ethanol. The final concentration of ethanol in the solutions for kinetic measurements was 2 vol. %. pH of buffer solutions was determined by using universal pH-meter WTW GmbH (Germany).

Kinetic measurements and calculations

Spectrophotometric measurements were performed using computer-controlled "Nicolet evolution 300" spectrophotometer (Thermo electron Corporation, USA) in Britton–Robinson buffer solution, pH 7.0, at 298 K. Absorbance spectra changes were registered in the interval from 210 to 650 nm. The kinetics of substrate and product concentrations were calculated by using extinction coefficients at 225 and 550 nm, respectively. The extinction coefficients were determined experimentally, and the values are 9.6, 11.0 and 10.5 mM^{-1} cm^{-1} at 225 nm and 3.1, 2.5 and 3.2 mM^{-1} cm^{-1} at 550 nm, for oximes **1**, **2** and **3**, respectively.

The rate of substrate oxidation (V) was calculated by substrate concentration kinetic curve fitting. In the case of exponential function (decrease or increase): $V = kc_0$; k is the first order reaction constant and c_0 is the initial concentration of a substrate. For the linear dependence the initial rate was calculated as a slope. To analyze the rate dependence on the substrate concentration and determine the apparent kinetic parameters V_{max} and K_M of the reactions, the Michaelis–Menten equation was used. Catalytic constants were calculated as $k_{cat} = V_{max}/[E]$, whereas bimolecular enzyme and substrate reactivity constants (k_{ox} and k_{red}) were calculated as $k_{ox/red} = k_{cat}/K_M$.

The influence of buffer solution pH on the oxidation rate of oximes **1**–**3** catalysed by HRP or rCiP was investigated using spectrophotometric method by following spectral changes at 225 and 550 nm. The dependence of the reaction rate on buffer solution pH was studied using Britton–Robinson buffer solution in pH interval 3.5–12.0, at 298 K.

For data fittings the programs GraFit (Erithacus Software Ltd.), SigmaPlot 12.0 and MathCad 2001 (MathSoft, Inc.) were used.

RESULTS AND DISCUSSION

*Determination of kinetic parameters of peroxidase-catalysed oxidation of oximes **1**–**3***

The 1,5-benzodiazepine oximes (oximes **1**–**3**) were enzymatically oxidised by recombinant *Coprinus cinereus* (rCiP) and horseradish (HRP) peroxidases. The synthesised oximes **1**–**3** had similar absorbance spectra in the UV region with maxima at 225, 255 and 290 nm (Fig. 2). During the oxidation process the decrease of absorbance was observed at 225 and 255 nm while moderate changes were observed at 290 nm. At the same time, the new absorbance maxima appeared at 360 and 550 nm. This is supposedly related to the formation of an intermediate which is further converted to the final product. This assumption was supported by the initial increase and further decrease of absorbance at 360 and 550 nm during the oxidation of the studied oximes.

Results presented in Fig. 2 show changes of optical density, when oxime **1** is oxidised by rCiP. Analogous changes in optical density and oxidation reaction rate were observed in all studied cases and are dependent on the structure of oximes **1**–**3**, the concentrations of enzymes HRP and rCiP, hydrogen peroxide and oximes, as well as buffer pH solution.
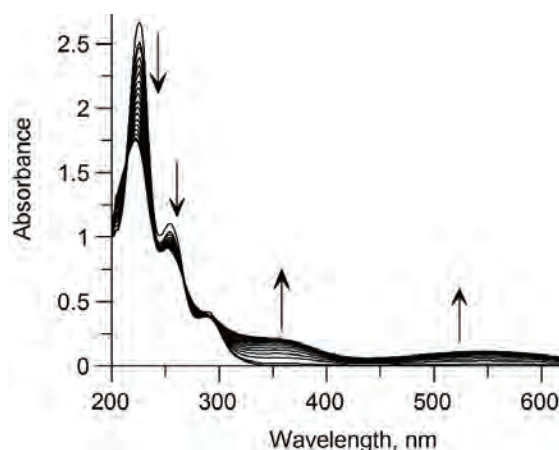
Fig. 2. The change in the absorbance spectra of oxime **1** during the oxidation catalysed by
rCiP peroxidase. Conditions: 100 µM H$_2$O$_2$, rCIP 1.0 nM, 100 µM oxime **1**.
0.06 M Britton–Robinson buffer solution, pH 7.0, 298 K.

*The dependence of the oxidation rate on the concentration of oximes **1–3** and on
hydrogen peroxide concentration*

The HRP- and rCiP-catalysed oxidation of oximes **1–3** in the presence of
H$_2$O$_2$ was performed at pH 7.0. The substrate consumption was followed at 225
nm, and the formation of an intermediate product at 550 nm. The rate of oximes
oxidation was directly proportional to rCiP or HRP concentrations.

The determined dependences of the oxidation rate on the concentrations of
oximes **1–3** are shown on Fig. 2. The oxidation rate was determined by fitting the
kinetic curves using an exponential decay function and it was found that the dep-
endence of the oxidation rate of oximes **1–3** on the concentration of these sub-
strates is hyperbolic and corresponds to the Michaelis–Menten equation. The
apparent values of the parameters K_M and V_{max} were determined, and also the
catalytic and oxidation constants were calculated and are presented in Table I.
Although the parameters obtained during the formation of the primary product
are similar to those of the disappearance of the oxime, evaluating and comparing
the obtained kinetic parameters is not completely correct, because during the
formation of the primary product its transformation into the final product also
takes place.

TABLE I. Kinetic parameters of oximes **1–3** oxidation at 225 nm

Oxime	HRP			rCIP		
	K_M / µM	k_{cat} / s^{-1}	k_{ox} / µM^{-1} s^{-1}	K_M / µM	k_{cat} / s^{-1}	k_{ox} / µM^{-1} s^{-1}
1	200.0±20.0	250.0±25.0	1.2±0.2	160.0±40.0	3500.0±900.0	10.0±1.0
2	250.0±25.0	26.0±8.0	0.14±0.03	120.0±25.0	230.0±25.0	1.9±0.2
3	50.0±10.0	150.0± 20.0	3.1±0.2	80.0±20.0	640.0±100.0	8.0±1.4

As can be seen from the data in Table I, peroxidases exhibit different affinity and reactivity to the oximes **1**–**3**. The lowest K_M values were obtained for oxime **3** during both the HRP-catalysed and rCiP-catalysed oxidation, 50 and 80 µM, respectively.

The highest oxidation (k_{ox}) and catalytic (k_{cat}) constants were obtained during the oxidation of oxime **1**, whereas they were slightly lower for oxime **3.** The oxidation constants of oxime **2** by both HRP and rCiP were significantly lower. In addition, the values of the constants k_{cat} and k_{ox} obtained with rCiP are significantly higher than those obtained with HRP, which allows us to conclude that rCiP catalyses oxidation processes more efficiently. These results are in good agreement with the literature data on the oxidative capacity of heme-containing peroxidases. It is known that rCiP has better oxidizing power than HRP[29] and the data obtained confirm this.

The investigation of the oximes oxidation rate on the concentration of H_2O_2 showed that the concentrations of H_2O_2 higher than 100 µM were inhibiting the reaction rate, thus they were not used for the calculation of the kinetic constants. The apparent values of the K_M and V_{max} were determined from obtained dependences and the catalytic and reduction constants were calculated and are presented in Table II.

TABLE II. Kinetic parameters of H_2O_2 reduction at 225 nm

Oxime	HRP			rCIP		
	K_M / µM	k_{cat} / s^{-1}	k_{red} / µM^{-1} s^{-1}	K_M / µM	k_{cat} / s^{-1}	k_{red} / µM^{-1} s^{-1}
1	15.0±4.0	110.0±10.0	7.0 ±2.0	38.0±16.0	460.0±80.0	12.1±3.3
2	8.5±0.8	12.5 ±2.0	1.5±0.3	37.0±21.0	220.0±50.0	6.1±2.3
3	25.0±7.0	130.0±15.0	5.2±1.0	51.0±17.0	450.0±60.0	8.8±1.7

As can be seen from the data in Table II, the reactivity constants for the reactions catalysed by rCiP were higher than those for the HRPs in all cases analysed. This indicates that rCiP oxidises 1,5-benzodiazepine oximes significantly more efficiently than HRP.

*The pH dependence of oximes **1**–**3** oxidation rates*

The changes of absorption spectra during the oxidation of oxime **1** catalysed by rCiP at different buffer solution pH are presented in Fig. 3. Similar spectral changes were observed during oxidations of oximes **2** and **3** catalysed by both peroxidases used in this work.

The decrease of absorbance was observed at 225 and 255 nm while two new absorbance maxima at 360 and 550 nm appeared during the oxidation of oxime **1** catalysed by rCiP at pH 7.0 (Fig. 3d). Similar changes were registered at pH 9.0 (Fig. 3e). Conversely, the expected maxima in the long wave region (550 nm) were diminished at pH 10.0 (Fig. 3f). In the acidic media at pH 3.5–4.5 and 5.5

both of the absorbance maxima at 360 and 550 nm were absent (Fig. 3a and b) or insignificant (Fig. 3c), instead noticeable increase of the absorbance was observed at 240–260 nm and 280–340 nm regions.
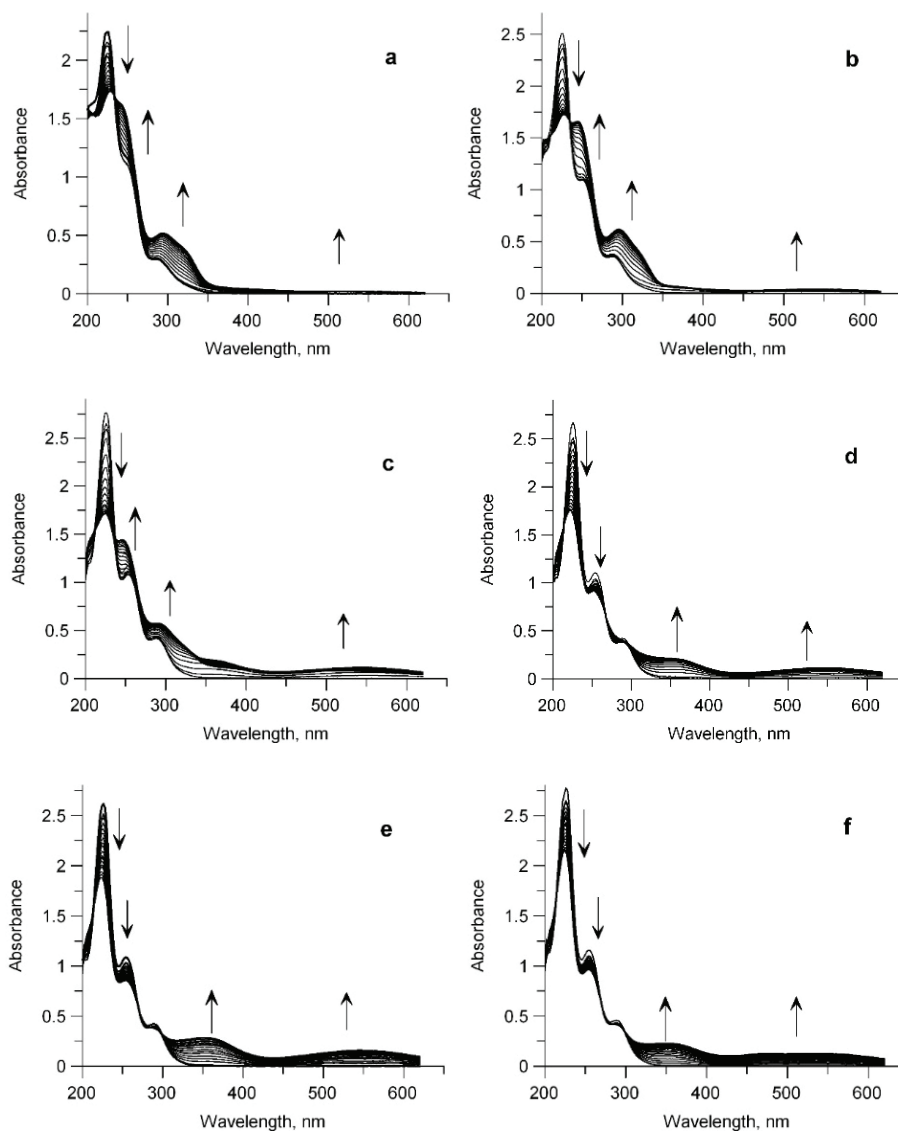
Fig. 3. The changes in the absorbance spectra during the oxidation of oxime **1** catalysed by rCiP at different buffer solution pH. Experimental conditions: oxime **1** – 100 μM; H_2O_2 – 100 μM; pH – 3.5 (a), 4.5 (b), 5.5 (c), 7.0 (d), 9.0 (e) and 10.0 (f); 0.06 M Britton–Robinson buffer solution, 298 K.

Based on the data from the literature[30] and the obtained results, the spectral changes can be explained by the formation of the initial reactive product during the enzymatic oxidation of oximes **1**–**3**. Presumably radical species which absorb UV light in the long wave region transform further into the final product during secondary non-enzymatic conversion step. This is in agreement with Fukunishi *et al.*, who showed that the iminoxical radicals capable of recombining through O–N, O–C, and N–N bonds to form the corresponding dimers are generated by oxidation of substituted benzaldehyde oximes with H_2O_2 and HRP.[31] Moreover, Aveline *et al.* showed that *N*-hydroxy-2(1*H*)-pyridone (N-HP) was capable of forming poorly reactive radicals.[30]

Our obtained results coincide with the data presented in work by Aveline *et al.* These results also confirm the presumption that initial product, which formed during peroxidase-catalysed oxidation of oximes **1**–**3**, can be radical.[30] If the radicals of investigated **1**–**3** oximes are protonized, positive charge from oxygen can be delocalized to the tertiary carbon. Since the reactivity of the formed radical is low, its disappearance is predetermined by radical recombination reactions. In acidic region, at pH 4.5–5.5, pronounced maxima at 360 and 550 nm were not observed, but intensive absorbance increases at 240–260 nm and 280–340 nm was registered. Probably an intermediate compound was formed during the oxidation reaction, which was further converted to the final product. These compounds are believed to be unstable in acidic buffer solutions because no distinct absorption maxima at 360 and 550 nm were observed.

The results obtained during the oxidation of oximes at neutral pH and basic buffer solutions (pH 7.0–9.0) also agree with the data presented in the literature.[30] In the beginning there was an increase in absorption during the oxidation of the oxime and a further decrease at 360 and 550 nm. It has also been observed that the compounds formed in alkaline solutions are converted to the final product more slowly than in acidic solutions. The intermediate compound probably is more stable and less reactive in alkaline solutions. It should be mentioned that the absorbance maximum at 550 nm was absent while a new one at 460 nm was registered in extremely basic medium (pH 11.0). It is possible that the studied oximes **1**–**3** could have been deoximated into their carbonyl form.[4,32] Similar spectral changes were also registered during the oxidation of oximes **2** and **3** catalysed by both peroxidases.

The rate of oxidation of oximes **1**–**3**, as well as intermediate compounds formed during the enzymatic reaction and their further transformation into the final product depended on the pH of the buffer solution (Fig. 4). As can be seen from results presented in Fig. 4 a and b, the pH dependence of HRP activity upon oxidation of oximes **1**–**3** was classically bell-shaped. For oximes **1** and **3**, the maximum HRP activity was observed in the pH range from 5.5 to 8.0, while the pH optimum for oxime **2** was shifted to a more acidic range from 4.5 to 7.0. A

similar trend was observed for the rate of formation of intermediate product at 550 nm at the same pH of the buffer solution (Fig. 4 b).
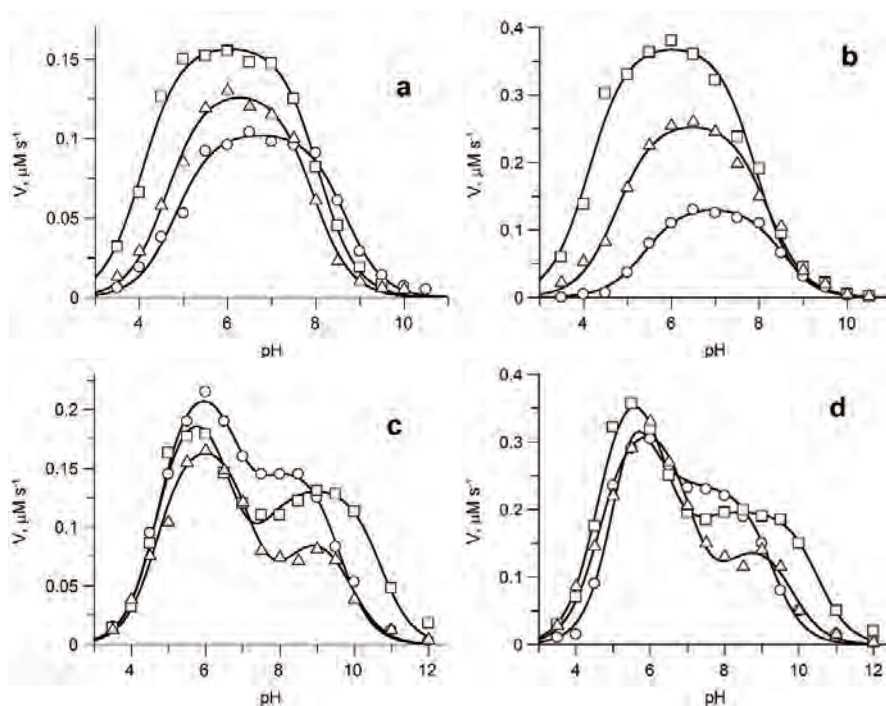
Fig. 4. The pH effect on the oxidation rates of oximes **1**–**3** catalysed by HRP and rCiP. The disappearance of substrate was followed at 225 nm (a, c); the formation of initial product was followed at 550 nm (b, d). Conditions: oximes – **1** (○), **2** (□) and **3** (△) – 100–110 μM; H_2O_2 – 100–110 μM; 0.06 M Britton–Robinson buffer solution, 298 K.

Determined reaction rate dependences on the buffer solution pH were complex when reaction was catalysed by rCiP Fig. 4 c and d. The dependences of oxidation rates of oximes **1**–**3** on the buffer solution pH, characterized by disappearance (225 nm) and appearance of intermediate product (550 nm), showed that rCiP is able to oxidise oximes **1**–**3** in a broader pH range from 3.5 to 11.0 with the highest rate observed in pH 5.5–6.5 interval. In highly acidic or basic buffer solutions the reaction rate decreased, and the pH curve shape differed from the classic bell form. To calculate the pKa values, the resulting curves were decomposed into individual peaks (deconvolution) and the resulting peaks were smoothed to a bell shape using a theoretical model. The determined pKa values of rCiP- and HRP-catalysed oxidation of oximes **1**–**3** are presented in Table III.

Peroxidases share a common catalytic mechanism for the degradation of H_2O_2.[33] The peroxidase reaction is a two-electron oxidation–reduction with three distinct steps.[34] The peroxidase catalytic cycle is described by the equations else-

where.[22] During this reaction, radicals are formed, which then disproportionate or initiate various non-enzymatic reactions, including degradation or polymerization processes.

TABLE III. The pKa values determined from the pH dependences of oximes **1**–**3** oxidation rate for HRP and rCiP catalysed reactions

Oxime	HRP		rCIP			
	pKa1	pKa2	pKa1	pKa2	pKa3	pKa4
1	4.8±0.04	8.6±0.04	4.7±0.02	7.0±0.04	7.4±0.03	9.7±0.02
2	4.0±0.10	8.0±0.10	4.7±0.02	6.6±0.02	7.3±0.02	10.7±0.02
3	4.6±0.03	8.4±0.03	4.7±0.03	7.2±0.06	8.2± 0.01	9.9±0.01

It is known that the rate of formation of an intermediate compound (radical) is independent of pH in the range of 6–10. However, in an acidic medium, the formation of an intermediate compound is determined by another titratable group with pKa 5.0 located in the catalytic center of the enzyme. Abelskov and Smulevich with co-autors concluded that this titratable group is the proximal His183, but not as expected the distal His55, and the latter is responsible for conversion of the Fe–OOH complex to intermediate compound (radical).[22,35]

In this work, the oxidation of oximes **1**–**3** with rCiP yielded pKa 4.7 and with HRP yielded pKa 4.0–4.8 for the first titratable group. It is as the protonated substrate, since the analysed substrates may have a different form in over the entire pH range (Fig. 5).
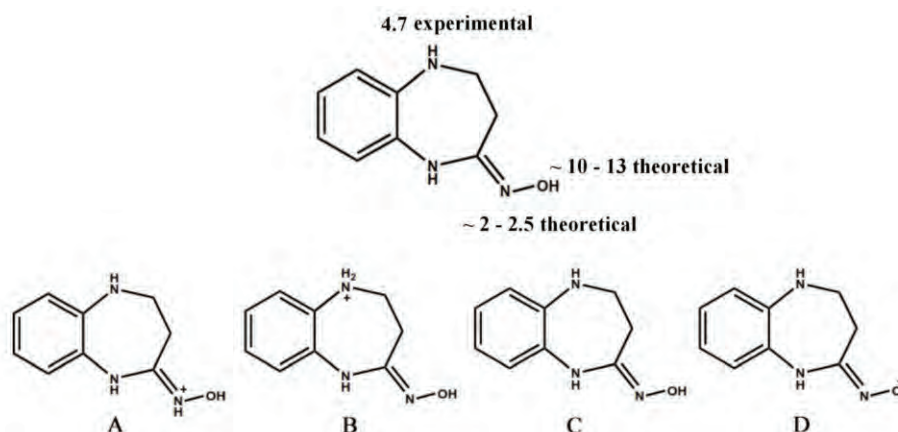
Fig. 5. Structures of oxime **1** that can be formed at different pH of the buffer solution.

Thus, oxime **1** has four potential ionization forms. In a strongly acidic medium, the nitrogen protonation of the =NH$^+$–OH group (form A) takes place. When the medium is acidified, one of the nitrogen atoms is protonated (form B), for which the pKa value is experimentally determined in this work to be 4.7. In

neutral media, oxime **1** exists in the C form. According to the literature, the anion in aqueous solutions has the pKa 10–13, so in a strongly alkaline medium the oxime =N–OH group is deprotonated, *i.e.*, the =N–O⁻ anion (D form) is formed.[4,36] But the strongly acidic (pH < 3) and alkaline (pH > 11) regions are outside the limits of the studied pH dependences and therefore may not be analysed.

The obtained pKa 4.7 of the first titratable group in the reaction with rCiP was very close to the values determined for oximes **1–3** by spectroscopic methods, 4.56, 4.60 and 4.51 (fluorescence data), respectively.[25] Therefore, it cannot be unambiguously determined whether this titratable group belongs to the enzyme or to the substrate, since the enzyme has distal His55 (pKa = 5.1) or proximal His183 (pKa= 5.0).[22] However, it turned out that the pKa of the first titratable group is 4.6–4.8 in both HRP- and rCiP-catalysed oxidation. The fact that the pKa of this group is independent of the enzyme used is a possible proof that the first titratable group belongs to the substrate. pKa values are very sensitive to the environment, and the catalytic centers of HRP and rCiP have their own differences, although they consist of the same amino acids. The second titratable group was found to have pKa 8.6 (1), 8.0 (2) and 8.4 (3), Table III. It is well known from the literature that the properties of HRP are unambiguously related to the distal histidine with pKa of 8.6, 8.8, which is capable of forming a hydrogen bond with ferrile oxygen [Fe(IV)=O] in compound II.[37,38] The obtained pKa values of the second titratable group were slightly different depending on the compound being oxidised. Therefore, it can be assumed that the substrate could influence the distribution of electron density in the His+–H–O–Fe group of atoms. The third titratable group (for rCiP) obtained in this work has pKa 9.7 and pKa 10.5–10.7 for the oxidation of oxime **2** with hydrogen peroxide and rCiP. It is known that the nitrogen of distal arginine in the catalytic center of HRP, HRP C, CiP and CCP heme peroxidases in the case of cpd I and II is capable of forming hydrogen bond with oxygen of Fe(IV)=O group of enzyme. In CiP peroxidase distal Arg has pKa ≈ 10.[22] In order to complete the peroxidase catalytic cycle the hydroxyl or one water molecule must dissociate and the ferric oxygen must take up one or two protons. In the case when Arg is deprotonated, the proton transfer becomes impossible and the rate decreases.

It should be mentioned that the deprotonation pKa of the =N–OH group of oximes **1–3** was not determined experimentally. If the obtained pKa 9.7 and pKa 10.5–10.7 are the conversion of the substrate to the anionic form, the rate may decrease due to the fact that the anionic form is not a peroxidase substrate. This is shown in the literature in studies with phenolic substrates (*p*-methoxyphenol) and HRP C.[22]

CONCLUSIONS

Spectrophotometric investigations of oxidation of oximes **1**–**3** catalysed by horseradish peroxidase (HRP) and fungal peroxidase (rCiP) showed how the rate of oxidation depends on the concentration of oximes and hydrogen peroxide, the nature of the enzymes, the structure of the oximes as well as from the pH of the buffer solution.

Based on the dependences of the reaction rates on the concentrations of oximes **1**–**3** and hydrogen peroxide, the apparent K_M and V_{max} values were determined, and the catalytic, oxidation and reduction constants were calculated. Determined reactivity constants indicate that rCiP oxidises 1,5-benzodiazepine oximes significantly more efficiently than HRP. The highest catalytic, oxidative and reduction constants were obtained in the oxidation of oxime **1**, and the lowest in the oxidation of oxime **2**. It was established that hydrogen peroxide concentrations higher than 100 μM inhibit reactions catalysed by peroxidases. Apparently, the reactivity of oximes depends on their structure, the position of the $-CH_3$ group in the oxime molecule, and interaction with the enzyme.

The dependences of the oxidation rates of oximes and the resulting intermediate products on the pH of the buffer solution, as well as the pKa values of the amino acids of the enzymes involved in catalysis, were obtained. It was determined that if the dependence of HRP activity on pH is classically bell-shaped, then the dependence of rCiP is complex. rCiP oxidises 1,5-benzodiazepine oximes over a wider pH range than HRP. Such pH dependencies are likely determined by the ionization forms of the oximes at various pHs, their pKa values, and the properties of the enzyme.

The results show that for practical applications in the oxidation of benzodiazepine oximes, rCiP is preferable to HRP because it oxidises more efficiently, works in a wider pH range, and can be synthesised cheaper, in large quantities, and with suitable activity.

И З В О Д

ОКСИДАЦИЈА ОКСИМА 1,5-БЕНЗОДИАЗЕПИНА КАТАЛИЗОВАНА ПЕРОКСИДАЗАМА

LIDIJA KOSYCHOVA, LINA REKOVIC, IRINA BRATKOVSKAJA, INGRIDA RADVEIKIENE
и REGINA VIDŽIŪNAITĖ

Institute of Biochemistry, Life Sciences Center, Vilnius University, Saulėtekio al. 7, Vilnius 10223, Lithuania

Спектрофотометријски је испитивана оксидација оксима 1,3,4,5-тетрахидро-2*H*--1,5-бензодиазепина катализована пероксидазом из рена (HRP) и рекомбинантном пероксидазом гљиве *Coprinus cinereus* (rCiP). Анализиран је утицај концентрације супстрата и водоник пероксида на брзину реакције. Израчунате су вредности K_M и V_{max}, као и константе каталитизе, оксидације и редукције (k_{cat}, k_{ox} и k_{red}). Константе реактивности за реакцију катализовану ензимом rCiP су биле веће него са HRP. Пошто се структура оксима мења у зависности од pH, даље је испитиван утицај pH на брзину оксидације испитиваних једињења. Утврђена је зависност брзине оксидације оксима од pH пуфера и

добијене pK_a вредности амино киселина пероксидаза које су одговорне за брзину ката-
лизе. Зависност активности HRP од pH прати класични облик звона, док је зависност
rCiP комплекснија.

REFERENCES

1. W. B. Jakoby, *Metabolic Basis of Detoxication: Metabolism of Functional Groups*,
   Elsevier Science, Amsterdam, 1982 (ISBN: 9780323137997)
2. E. N. Shaw, *2-hydroxy-pyridine-N-oxide and process for preparing same*, 1951
   (http://www.google.com/patents/US2540218) Accessed May 8, 2023
3. N. K. F. W. Clauson-Kaas, N. Elming, J. Tormod Nielsen, *Derivatives of N-hydroxy
   pyridines and process of production*, 1956 (http://www.google.ch/patents/US2748142)
   Accessed May 8, 2023.
4. S. B. King, *C-Nitroso Compounds, Oximes,* N-*Hydroxyguanidines and* N-*Hydroxyureas*,
   John Wiley & Sons, Ltd., New York, 2005 (https://doi.org/10.1002/3527603751.CH7)
5. R. Rani, C. Granchi, *Eur. J. Med. Chem.* **97** (2015) 505
   (https://doi.org/10.1016/J.EJMECH.2014.11.031)
6. P. Aastha, K. Navneet, A. Anshu, S. Pratima, K. Dharma, *Res. J. Chem. Sci.* **3** (2013) 90
   (http://www.isca.me/rjcs/Archives/v3/i7/14.ISCA-RJCS-2013-057.php)
7. P. Jara-Ulloa, S. Catalán-Caro, C. A. Escobar, *J. Chil. Chem. Soc.* **59** (2014) 2520
   (https://doi.org/10.4067/S0717-97072014000200027)
8. M. Whirl-Carrillo, R. Huddart, L. Gong, K. Sangkuhl, C. F. Thorn, R. Whaley, T. E.
   Klein, *Clin. Pharmacol. Ther.* **110** (2021) 563 (https://doi.org/10.1002/CPT.2350)
9. O. Mazimba, T. C. Molefe, *Int. J. Chem. Stud.* **3** (2015) 46
   (https://www.chemijournal.com/archives/2015/vol3issue3/PartA/3-2-9.1.pdf)
10. L. Kosychova, R. Vidziunaite, G. Mikulskiene, I. Bratkovskaja, R. Janciene, *Arkivoc*
    2015 (2015) 71 (https://doi.org/10.3998/ARK.5550190.P008.772)
11. S. Kumar, H. Kavitha, S. Arulmurugan, B. Venkatraman, *Mini. Rev. Org. Chem.* **9** (2012)
    285 (https://doi.org/10.2174/1570193X11209030285)
12. K. D. Krewulak, H. J. Vogel, *Biochim. Biophys. Acta – Biomembr.* **1778** (2008) 1781
    (https://doi.org/10.1016/J.BBAMEM.2007.07.026)
13. Y. Zhang, S. U. Geißen, C. Gal, *Chemosphere* **73** (2008) 1151
    (https://doi.org/10.1016/j.chemosphere.2008.07.086)
14. T. Kosjek, S. Perko, M. Zupanc, M. Zanoški Hren, T. Landeka Dragičević, D. Žigon, B.
    Kompare, E. Heath, *Water Res.* **46** (2012) 355
    (https://doi.org/10.1016/j.watres.2011.10.056)
15. T. Hata, H. Shintate, S. Kawai, H. Okamura, T. Nishida, *J. Hazard. Mater.* **181** (2010)
    1175 (https://doi.org/10.1016/J.JHAZMAT.2010.05.103)
16. E. Marco-Urrea, M. Pérez-Trujillo, C. Cruz-Morató, G. Caminal, T. Vicent, *Chemosphere*
    78 (2010) 474 (https://doi.org/10.1016/J.CHEMOSPHERE.2009.10.009)
17. A. Jelic, C. Cruz-Morató, E. Marco-Urrea, M. Sarrà, S. Perez, T. Vicent, M. Petrović, D.
    Barcelo, *Water Res.* **46** (2012) 955 (https://doi.org/10.1016/J.WATRES.2011.11.063)
18. S. Ostadhadi-Dehkordi, M. Tabatabaei-Sameni, H. Forootanfar, S. Kolahdouz, M. Ghazi-
    -Khansari, M. A. Faramarzi, *Bioresour. Technol.* **125** (2012) 344
    (https://doi.org/10.1016/J.BIORTECH.2012.09.039)

19. H. Kellner, P. Luis, M. J. Pecyna, F. Barbi, D. Kapturska, D. Kruğer, D. R. Zak, R. Marmeisse, M. Vandenbol, M. Hofrichter, *PLoS One* **9** (2014) e95557 (https://doi.org/10.1371/JOURNAL.PONE.0095557)
20. K. G. Welinder, J. M. Mauro, & L. Norskov-Lauritsen, *Biochem. Soc. Trans.* **20** (1992) 337 (https://doi.org/https://doi.org/10.1042/bst0200337)
21. S.-J. Kim, J.-A. Lee, Y.-H. Kim, & B.-K. Song, *J. Microbiol. Biotechnol.* **19** (2009) 966 (https://doi.org/10.4014/jmb.0901.018)
22. A. K. Abelskov, A. T. Smith, C. B. Rasmussen, H. B. Dunford, K. G. Welinder, *Biochemistry* **36** (1997) 9453 (https://doi.org/10.1021/BI970387R)
23. Y. Yao, L. Huang, Y. Xu, Q. X. Li, *J. Agric. Food Chem.* **70** (2022) 646 (https://doi.org/10.1021/acs.jafc.1c06261)
24. R. Ivanec-Goranina, J. Kulys, *Cent. Eur. J. Biol.* **3** (2008) 224 (https://doi.org/10.2478/S11535-008-0021-X)
25. L. Rekovic, L. Kosychova, I. Bratkovskaja, R. Vidziunaite, *J. Serb. Chem. Soc* **83** (2018) 343 (https://doi.org/10.2298/JSC180226090R)
26. L. X. Shannon, E. Kay, J. Y. Lew, *J. Biol. Chem.* **241** (1966) 2166 (https://doi.org/https://doi.org/10.1016/S0021-9258(18)96680-9)
27. Z. S. Farhangrazi, I. Yamazaki, L. S. Powers, B. R. Copeland, T. Nakayama, T. Amachi, *Biochemistry* **33** (1994) 5647 (https://doi.org/https://doi.org/10.1021/bi00184a038)
28. D. P. Nelson, L. A. Kiesow, *Anal. Biochem.* **49** (1972) 474 (https://doi.org/https://doi.org/10.1016/0003-2697(72)90451-4)
29. E. Torres, M. Ayala, *Biocatalysis based on heme peroxidases: Peroxidases as potential industrial biocatalysts*, Springer, Berlin, 2010 (https://doi.org/https://doi.org/10.1007/978-3-642-12627-7_3)
30. B. M. Aveline, I. E. Kochevar, R. W. Redmond, *J. Am. Chem. Soc.* **118** (1996) 10124 (https://doi.org/https://doi.org/10.1021/ja961989l)
31. K. Fukunishi, K. Kitada, I. Naito, *Synthesis (Stuttgart)* **3** (1991) 237 (https://doi.org/https://doi.org/10.1055/s-1991-26433)
32. S. Sahu, S. Sahu, S. Patel, S. Dash, B. K. Mishra, *Indian J. Chem.* **47** (2008) 259. (https://nopr.niscpr.res.in/handle/123456789/1410)
33. M. Nissum, A. Feis, G. Smulevich, *Biospectroscopy* **4** (1998) 355 (https://doi.org/https://doi.org/10.1002/(SICI)1520-6343(1998)4:6<355::AID-BSPY1>3.0.CO;2-I)
34. P. Tn, T. L. Poulos, J. Kraut, *J. Biol. Chem.* **255** (1980) 8199 (https://doi.org/https://doi.org/10.1016/S0021-9258(19)70630-9)
35. G. Smulevich, A. Feis, C. Focardi, J. Tams, K. G. Welinder, *Biochemistry* **33** (1994) 15425 (https://doi.org/https://doi.org/10.1021/BI00255A024)
36. S. Ramalingam, M. Karabacak, S. Periandy, N. Puviarasan, D. Tanuja, *Spectrochim. Acta, A* **96** (2012) 207 (https://doi.org/10.1016/j.saa.2012.03.090)
37. S. Hashimoto, Y. Tatsuno, T. Kitagawa, *Proc. Natl. Acad. Sci. U. S. A.* **83** (1986) 2417 (https://doi.org/https://doi.org/10.1073/PNAS.83.8.2417)
38. I. Yamazaki, M. Tamura, & R. Nakajima, *Mol. Cell. Biochem.* **40** (1981) 143 (https://doi.org/https://doi.org/10.1007/BF00224608).

Anticancer activity of Schiff base ligand (*E*)-4-((5-chloro-2--hydroxybenzylidene)amino)-1,5-dimethyl-2-phenyl-1*H*-pyrazol--3(2*H*)-one and its Co(II), Cu(II) and Zn(II) metal complexes

KULDEEP B. SAKHARE, KIRTI N. SARWADE, YOGESH N. BHARATE
and MAHADEO A. SAKHARE*

*Department of Chemistry, Balbhim Arts, Science & Commerce College,
Beed (MS) 431122, India*

Abstract: A series of transition metal complexes of Mn(II),Co(II), Ni(II), Cu(II), Zn(II) and VO(II) have been prepared by using the Schiff base ligand (L) derived from 4-aminoantipyrine and 5-chlorosalicylaldehyde. The structural properties of Schiff base ligand were characterized by mass, FT-IR, UV––Vis, ^{1}H-NMR spectroscopy, *etc*. Also, metal complexes were studied by P--XRD, elemental analysis, thermogravimetric studies along with various biological activities. The micro analytical data revealed that, the metal complexes have 1:1 stoichiometry composition of M:L. Generally, it is observed that prepared metal complexes show better antifungal, antibacterial and anticancer activities than its Schiff base ligand.

Keywords: Schiff base ligand; metal complexes; 5-chlorosalicylaldehyde; 4-aminoantipyrine.

INTRODUCTION

The Schiff bases can be synthesized by the condensation of the primary amines ($R–NH_2$) with carbonyl compounds ($>C=O$). Biological assessment of these Schiff base ligands is enhanced on undergoing complexation with transition metal ions.[1,2] The derivatives (metal complexes) which are synthesized by transition metals are known to play a vital biological role and can be used in chemotherapy.[3–5] Among the transition metal-supported drugs, the cisplatin (Cis-Pt $(NH_3)_2Cl_2$) was the inorganic compound which was firstly utilized in the medication or treatment of cancer. However, cisplatin was first inorganic compound but its clinical utilization had limitations due to rise of drug resistance.[6] Surplus limitation of platinum-supported drug comprised their cytotoxic assessment in blooming tissues.[7,8] As a result, compounds with more substantial discretion and

---

165

anti-proliferative assessment, than platinum-supported drugs are essential for the medication of solid tumours. Antithesis to platinum, copper is a trace element that is essential to human body. Numerous fundamental proteins and enzymes impose the activation and participation on trace amount of copper.[9,10]

Derivatives of 4-aminoantipyrine are known to exhibit analgesic,[11,12] anti-inflammatory effects,[13,14] antibacterial,[15] antifungal[16] and antimicrobial activities,[17] also utilized as hair colour additives[18] and to potentiate the local anaesthetic effect of lidocaine.[19,20] These compounds have been utilized in spectrophotometric determination of metal ions. Many of these reagents give intense colours with transition metal ions, providing sensitive probes and some of them can also coordinate to rare earth ions to form metal complexes with interesting structures.[21]

In this present context we have synthesized Schiff base ligand from 5-chlorosalicylaldehyde and 4-aminoantipyrine and its metal complexes. These have been characterized and analysed by mass, ^{1}H-NMR, FT-IR spectroscopy, P-XRD and studied by anticancer, antifungal and antibacterial assessments.

EXPERIMENTAL

Material and methods

All the chemicals of analytical grade were used. 5-Chlorosalicylaldehyde and 4-aminoantipyrine purchased from Spectrochem Pvt. Ltd. Solvents like ethanol, ethyl acetate, petroleum ether, *n*-hexane were purchased from local provider and purified by standard procedures. Thin layer chromatography (TLC) plate pre-coated with silica gel on aluminium sheet was used to detect the completion of reaction with system of *n*-hexane and ethyl acetate. ^{1}H-NMR spectra of Schiff base ligand (L) recorded on Bruker 500 MHz ^{1}H-NMR instrument in CDCl$_3$ as solvent. EI-MS spectra recorded on a Bruker compass data analysis 4.2. The prepared Schiff base ligand and its metal complexes confirmed by FTIR spectra with KBr disc on Bruker Alpha T FTIR spectrophotometer. The electronic spectra recorded on Perkin Elmer UV-spectrophotometer. Thermal analysis of the complexes performed on TA instruments Trios V4.4.0.41128 TG/DSC thermal system under nitrogen atmosphere. The powder XRD was carried out on Rigaku-Japan Miniflex 600 instrument.

Analytical and spectral data of the synthesized compounds are given in the Supplementary material to this paper.

The biological activity

We have studied synthesized ligand and its metal complexes against the biological activities like anticancer, antibacterial and antifungal activity. From the observation we found that metal complexes shows better results as compared to ligand.

Anticancer activity

Anticancer activity of the Schiff base ligand (L) and metal complexes (M) were tested by using SRB assay on MCF-7 human breast cancer cell line. The growing cell line used medium of L-glutamine and 10 % fetal bovine serum and inoculated in incubator at temperature 37 °C, 5 % CO$_2$ and 95 % air and 100 % relative humidity for 24 h. The L and M dissolved in up to 1 mg/ml of DMSO and diluted in water at up to 100 μg/ml and added into the microtiter wells, incubated for 48 h. the process was finished by adding trichloroacetic acid (TCA) and cell line

fixed, incubated at 4 °C for 1 h. synthesis of sulforhodamine B (SRB) solution 1 % of acetic acid used for removal of unbound dye incubated at room temperature for 20 min. Bounded dye stain was eluted with 10 mM trizma base. Absorbance was measured at a wavelength of 540 nm and reference wavelength of 690 nm against standard 5-fluorouracil.

Antimicrobial activity

Firstly, preparation of Mueller–Hinton agar (MHA) and potato dextrose agar (PDA) medium sterilized by autoclaving for 15 min, then prepared McFarland turbidity standards by utilising 0.5 ml of 1.175 % barium chloride dihydrate ($BaCl_2 \cdot 2H_2O$) solutions were added to 99.5 ml of 0.18 mol/L sulfuric acid with constant stirring. Petri dishes containing Mueller––Hinton agar plus potato dextrose were inoculated by swabbing with standardized bacterial and fungal inoculums. Then application of sample to inoculated agar plate and plates were placed in an incubator already set to 30 °C. After 24 h, each plate was carefully observed, we found that inhibition zone uniformly circular with lawn of growth, the inhibition zone of diameter measured by unaided eye. The zones are measured in millimetre by utilizing sliding callipers on the back of inverted petri dish.

Synthesis of Schiff base ligand (L)

The (*E*)-4-((5-chloro-2-hydroxybenzylidene)amino)-1,5-dimethyl-2-phenyl-1*H*-pyrazol--3(2*H*)-one was prepared by using well known method.[22] 5-chlorosalicylaldehyde (1.56 g, 0.01 mol) and 4-aminoantipyrine (2.03 g, 0.01 mol) were dissolved in in hot ethanol. This mixture was refluxed for 45 min at 70–80 °C after time span temperature was reduced to ambient and yellow precipitation was observed. The mixture was filtered, washed with mild ethanol and dried under vacuum.[23] (Scheme 1)
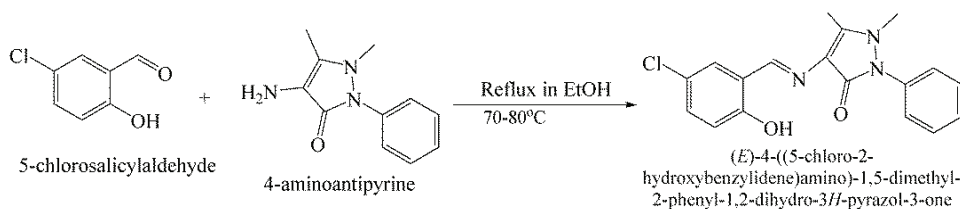
Scheme 1. Synthesis of Schiff base ligand (L).

Synthesis of metal complex (M)

In the preparation of the metal complexes, the ligand and the metals were mixed in 1:1 mole ratio using necessary quantity of ethanol. Hot ethanolic solution of Schiff base ligand (0.01 mol) and hot ethanolic solution of corresponding metal salts (0.01 mol) were mixed together and refluxed for 2–3 h. Coloured solid metal complexes were obtained. The products were filtered, washed with cold ethanol and dried under vacuum. (Scheme 2).

RESULTS AND DISCUSSION

The synthesized Schiff base ligand and its metal complexes were analysed by using sophisticated instruments for the various spectroscopic analytical techniques like FTIR, MS and ^{1}H-NMR, and studied by biological activities like anticancer, antifungal and antibacterial. All complexes have different colours than ligand, are insoluble in ethyl alcohol and methyl alcohol and soluble in

DMSO and DMF. The physical and analytical data of ligand and its transition metal complexes are given in Table S-I of the Supplementary material.

(E)-4-((5-chloro-2-hydroxybenzylidene)amino)-1,5-dimethyl-2-phenyl-1*H*-pyrazol-3(2*H*)-one

M = Mn(II), Co(II) and Cu(II).

(E)-4-((5-chloro-2-hydroxybenzylidene)amino)-1,5-dimethyl-2-phenyl-1*H*-pyrazol-3(2*H*)-one

M = Ni(II) and Zn(II).

(E)-4-((5-chloro-2-hydroxybenzylidene)amino)-1,5-dimethyl-2-phenyl-1*H*-pyrazol-3(2*H*)-one

M = VO(II).
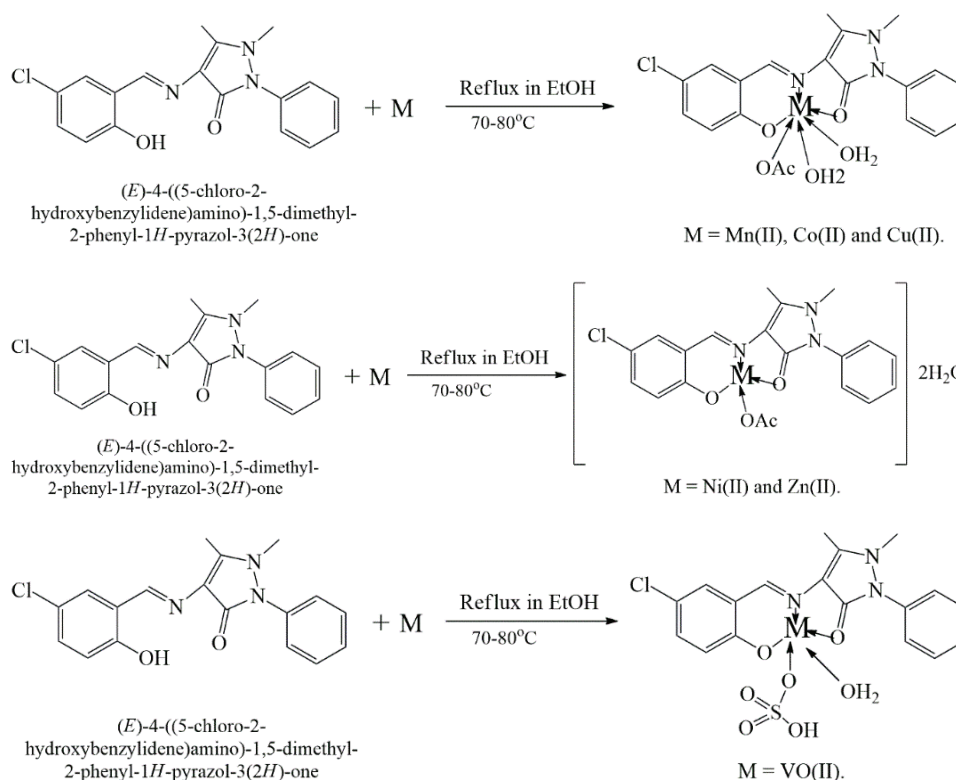
Scheme 2. Synthesis of metal complexes.

^{1}H-NMR spectra of Schiff base ligand(L)

^{1}H-NMR (400 MHz, chloroform-*d*) δ = 13.37 ppm (*s*, 1H) indicates presence of hydrogen bonding between carbonyl group of 4-aminoantipyrine and hydroxy group of salicylaldehyde.[24] δ = 9.78 ppm (*s*, 1H) belongs to azomethine group, δ 7.58–7.49 ppm (*m*, 2H) belongs to hydrogen of benzene ring, δ 7.46––7.35 ppm (*m*, 3H), δ = 7.33 ppm (*d*, *J* = 2.6 Hz, 1H) indicates meta coupling, δ 7.32–7.21 (*m*, 1H), 6.92 (*d*, *J* = 8.8 Hz, 1H), 3.23 ppm (*s*, 3H) are due to N–CH$_3$, whereas δ 2.45 ppm (*s*, 3H) belongs to C–CH$_3$.

Mass spectra of Schiff base ligand (L)

In the mass spectrum of ligand, the molecular ion peak was observed at *m/z* 342 and 343 (M+1) which is in good agreement with the molecular weight of the

proposed structure. There are several other peaks also observed which show fragmentation of ligand.
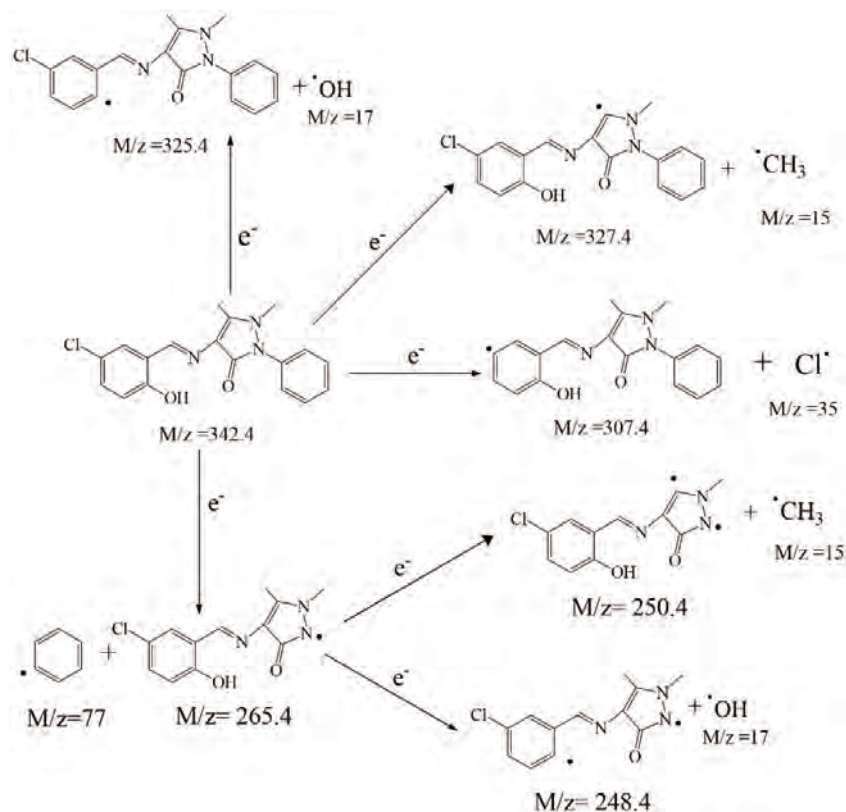
Fig. 1. Fragmentation of Schiff base ligand (L).

FTIR of Schiff base ligand (L) and its metal complexes (M)

The infrared spectra of ligand were recorded on Bruker Alpha T FTIR spectrophotometer and some of the selective bands are shown in Table I. On complexation, the C=N band is shifted to lower frequency corresponding to free ligand, indicating that azomethine group is formed.[25,26] and nitrogen atom of the azomethine group is coordinated to the metal ion.[27,28] Carbonyl group of Schiff base ligand exhibit band at 1639 cm^{−1} and in metal complexes, it is shifted to lower frequency by 30–55 cm^{−1}, indicating that the participating carbonyl oxygen is in coordination with metal.[28,29] In a Schiff base ligand, a band is observed at 3304 cm^{−1} which corresponds to the hydroxy group. In all metal complexes hydroxy group band has disappeared indicating coordination of oxygen atom with central metal ion. A band observed at 1262 cm^{−1} in ligand corresponds to the phenolic C–O group and in all metal complexes this band is shifted to lower

frequency in the range of 1230–1174 cm^{-1} and is further evidence of the formation of metal complexes.[30] From above data it is clear that imine nitrogen, carbonyl oxygen and hydroxy oxygen take part in the coordination with central metal ion. The band at 480–495 cm^{-1} is due to M–N vibration. The band at 669––684 cm^{-1} is due to C–Cl vibration.

TABLE I. FT-IR data of Schiff base ligand and its metal complexes.

No.	Compound	–OH	Azomethine, C=N	4-AAP, C = O	M–O	C–O	M–N	C–Cl
1.	L	3304	1563	1639	–	1262	–	684
2.	Mn(II) complex	–	1556	1616	588	1174	497	669
3.	Co(II) complex	–	1556	1637	588	1230	489	669
4.	Ni(II) complex	–	1562	1627	590	1226	491	673
5.	Cu(II) complex	–	1521	1608	619	1174	495	657
6.	Zn(II) complex	–	1535	1624	588	1178	480	677
7.	VO(II) complex	–	1438	1585	605	1193	443	768

Electronic spectra of Schiff base ligand (L) and its metal complexes (M)

The electronic spectra of Schiff base ligand and its metal complexes were recorded in DMSO at concentration of $\approx 5 \times 10^{-4}$, molar range of 50000 to 16666 cm^{-1}.[23,31,32] Electronic spectral data of ligand and its metal complexes are represented in Table II.

TABLE III Electronic spectral data

No.	Compound	λ_{max} nm	Absorption band cm^{-1}	Proposed transition	Molar conductance S mol^{-1} cm^2
1.	L	350	28571	n → π*	4.6
		300	33333	π → π*	
2.	Mn(II)	365	27397	MLCT	6.7
3.	Co(II)	420	23809	$^4T_{1g} \rightarrow {}^4T_{2g}$	5.2
		375	26666	$^4T_{1g} \rightarrow {}^4T_{1g(P)}$	
		320	31250	$^4T_{1g} \rightarrow {}^4A_{2g}$	
4.	Ni(II)	425	23539	$^3A_{2g} \rightarrow {}^3T_{2g}$	4.3
		360	27777	$^3A_{2g} \rightarrow {}^3T_{1g(f)}$	
		324	30864	$^3A_{2g} \rightarrow {}^3T_{1g(P)}$	
5.	Cu(II)	430	29441	$^2E_g \rightarrow {}^2T_{2g}$	5.1
		400	25000	$^2E_g \rightarrow {}^2T_{2g}$	
		340	23255	LMCT	
6.	Zn(II)	355	28169	MLCT	4.8
		470	21276	$^2B_2 \rightarrow {}^2A_1$	
7.	VO(II)	435	22948	$^2B_2 \rightarrow {}^2B_1$	4.4
		365	27397	$^2B_2 \rightarrow {}^2E$	

Thermogravimetric analysis

The thermal stability of metal complexes, synthesized from Schiff base ligand, were investigated by varying the temperature range from 50 to 800 °C. With the help of thermal gravimetric analysis (TGA), it is found that the metal complexes decompose in two steps. In the first step, the two coordinated water molecules are removed in the temperature range 50 to 205 °C and the ligand molecule is removed in the 250–580 °C range along with acetate ion for Mn(II), Co(II) and Cu(II) complexes, two lattice water molecules are removed in the temperature range 50 to 215 °C then ligand molecule is removed in the 250–605 °C range along with acetate ion for Ni(II) and Zn(II) complexes and one coordinated sulphate and one coordinated water molecule are removed in the temperature range 50 to 205 °C and ligand molecule is removed in the 260–518 °C range for VO(II) complex. In all metal complexes the mass of the final residue corresponds to stable metal oxides.[27] Thermogravimetric data of transition metal complexes are given in Table III.

TABLE III. Thermogravimetric data

No.	Compound	TG range °C	Mass loss % (Calc.)	Cmpd. decomposition	Metallic residue
1.	Mn(II) complex	55–210	7.81(7.34)	$2\,H_2O$	MnO
		260–590	79.05(78.17)	Acetate + L	
2.	Co(II) complex	55–205	7.47(7.28)	$2\,H_2O$	CoO
		255–565	78.05(77.53)	Acetate + L	
3.	Ni(II) complex	50–180	7.418(7.30)	$2H_2O$	NiO
		255–530	85.03(84.02)	Acetate + L	
4.	Cu(II) complex	50–200	7.09 (7.22)	$2\,H_2O$	CuO
		250–580	77.10(76.91)	Acetate + L	
5.	Zn(II) complex	50–215	7.04(7.21)	$2\,H_2O$	ZnO
		250–604	78.95(79.75)	Acetate + L	
6.	VO(II) complex	50–205	20.82(21.64)	$H_2O + SO_4$	VO
		260–518	66.04(65.49)	Ligand	

Powder X-ray diffraction

The P-XRD of metal complexes derived from ligand were scanned in 2θ range 20–80° at wavelength of 1.540 Å for the prediction of cell parameter, crystal system, lattice parameter etc. From the observed data we have found that the metal complexes of Co(II), Ni(II) and VO(II) have monoclinic crystal system, Mn(II) and Zn(II) orthorhombic crystal system and Cu(II) hexagonal crystal system.[26,27] The XRD diffractograms exhibit the crystalline nature of metal complexes.[34] The Powder XRD data of metal complexes are given in Table S-II of the Supplementary material.

Biological studies of Schiff base ligand (L) and its metal complexes (M)

Antimicrobial activities. The Schiff base ligand and metal complexes were investigated against antifungal and antibacterial activities.[35] The observation suggest that the metal complexes are more active than the Schiff base ligand (L).

Antifungal activity. The ligand and its metal complexes were evaluated for their antifungal activity against *Penicillium chrysogenum, Tricoderma viride* and *Aspergillus niger* fungi by using well known disc diffusion method. For the purification culture of fungi, we have used a single-spore isolation technique according to the literature procedure.[15] This antifungal susceptibility testing was performed on the basis of diameter of inhibition zones against albicans and on albicans strains of fungi.[36,37]

The antifungal activity of the imine metal complexes has been assessed for their potential application in the region of medicinal bioinorganic chemistry. All related tests were performed using disc diffusion method, under the same experimental conditions and against the same organisms, the results are given in Table IV. It was found that some metal complexes show better antifungal activity than corresponding ligand.

Antibacterial activity. The antibacterial activity of the synthesized ligand and its metal complexes were screened against gram positive and gram negative bacteria using disc diffusion method. From findings, it is clear that some metal complexes exhibit greater inhibition zone than that of ligand.[38,39] The findings of antimicrobial activities of ligand and its metal complexes are given in Table IV.

TABLE IV. Results of antibacterial and antifungal activities; interpretation key: – resistant, up to 8 mm, intermediate sensitive, 8–12 mm, sensitive, 12–18 mm, highly sensitive, $\geq$ 18 mm

Test organism	Zone of inhibition (diameter in mm)						
	Ligand(L)	Mn(II)	Co(II)	Ni(II)	Cu(II)	Zn(II)	VO(II)
Antibacterial activity							
Staphylococcus aureus	–	10	9.5	–	–	–	–
Bacillus subtilis	–	–	12.5	–	9	–	–
Klebsiella pneumoniae	–	–	13.5	–	10	11	–
Pseudomonas aeruginosa	–	10.5	13	–	–	10	11
Antifungal activity							
P. chrysogenum	–	–	15	–	20	12	–
T. viride	–	–	22.5	–	10	8	–
A. niger	–	–	12	–	15	8	–

Anticancer activity

The anticancer activity of the prepared ligand (L) and metal complexes (M) were determined using technique of the sulpho-rhodamine-B-stain (SRB) assay on MCF-7 human breast cancer cell line in comparison to 5-fluorouracil as a

standard and it was observed that activity of all the tested compounds is less than that of standard but greater than that of Schiff base ligand (L), Table V.[40]

TABLE V. Results of anticancer activity

No.	Test Compound	Concentration, µg/mL	Inhibition, %
1.	5-Fluorouracil (standard)	20	69.66
2.	L_1	100	32.69
3.	Co(II)	100	56.04
4.	Cu(II)	100	57.06
5.	Zn(II)	100	62.72

CONCLUSION

In the course of our research we have synthesized the Schiff base ligand along with its metal complexes. Based on all spectroscopic techniques, ligand shows tridentate character. The metals Co(II), Ni(II) and VO(II) show monoclinic crystal system, Mn(II) and Zn(II) show orthorhombic and Cu(II) shows hexagonal crystal system. From the biological studies of metal complexes, it was found that some metal complexes show better antibacterial and antifungal activities than ligand, and all metal complexes show better anticancer activities than ligand.

SUPPLEMENTARY MATERIAL

Additional data and information are available electronically at the pages of journal website: https://www.shd-pub.org.rs/index.php/JSCS/article/view/12524, or from the corresponding author on request. CCDC 2269543-2269546.

И З В О Д
АНТИТУМОРСКА АКТИВНОСТ ШИФОВЕ БАЗЕ (*E*)-4-((5-ХЛОРО-2-ХИДРОКСИ-БЕНЗИЛИДЕНЕ)АМИНО)-1,5-ДИМЕТИЛ-2-ФЕНИЛ-1*H*-ПИРАЗОЛ-3(2*H*)-ОН КАО ЛИГАНДА И ОДГОВАРАЈУЋИХ КОМПЛЕКСА CO(II), CU(II) И ZN(II)

KULDEEP B. SAKHARE, KIRTI N. SARWADE, YOGESH N. BHARATE и MAHADEO A. SAKHARE

Department of Chemistry, Balbhim Arts, Science & Commerce College, Beed (MS) 431122, India

Синтетисана је серија комплекса јона прелазних метала, Mn(II), Co(II), Ni(II), Cu(II), Zn(II) и VO(II), који као лиганд садрже Шифову базу (L), која представља дериват од 4-аминоантипирина и 5-хлоросалицилалдехида. Структурне карактеристике Шифове базе су одређене применом масене спектрометрије, као и FT-IR, UV–Vis и ^{1}H-NMR спектроскопије. Поред наведених спектроскопских метода, за карактеризацију комплекса употребљени су P-XRD, елементална микроанализа и термогравиметријска мерења. Испитивана је антимикробна и антитуморска активност претходно наведених једињења. На основу резултата аналитичких испитивања закључено је да су у комплексима јон метала и лиганд (L) координовани у 1:1 молском односу. Нађено је да су испи-

тивани комплекси показали бољу антибактеријску, антигљивичну и антитуморску актив-
ност у односу на Шифову базу (L).

REFERENCES

1. M. Cinarli, C. YuksektepeAtaol, E. Cinarli, O. Idil, *J. Mol. Struc.* **1213** (2020) 128 (http://dx.doi.org/10.1016/j.molstruc.2020.128152)
2. F. I. Abouzayed, S. M. Emam, S. A. Abouel-Enein, *J. Mol. Struc.* **1216** (2020) 128 (http://dx.doi.org/10.1016/j.molstruc.2020.128314)
3. I. E. Leon, J. F. Cadavid-Vargas, A. L. Di Virgilio, S. B. Etcheverry, *Curr. Med. Chem.* **24** (2017) 2 (http://dx.doi.org/10.2174/0929867323666160824162546)
4. M. R. Gill, K. A. Vallis, *Chem. Soc. Rev.* **48** (2019) 540 (https://doi.org/10.1039/C8CS00641E)
5. A. Bijelic, M. Aureliano, A. Rompe, *Angew. Chem. Int. Ed.* **58** (2019) 2980(https://doi.org/10.1002/anie.201803868)
6. U. Ndagi, N. Mhlongo, M. E. Soliman, *Drug Des. Dev. Ther.* **11** (2017) 599 (https://doi.org/10.2147/DDDT.S119488)
7. T. Sakaeda, K. Kadoyama, Y. Okuno, *Int. J. Med. Sci.* **8** (2011) 487 (http://doi.org/10.7150/ijms.8.487)
8. N. J. Wheate, S. Walker, G. E. Craig, R. Oun, *Dalton Trans.* **39** (2010) 8113 (https://doi.org/10.1039/C0DT00292E)
9. E. Tisato, C. Marzano, M. Porchia, M. Pellei, C. Santini, *Med. Res. Rev.* **30** (2010) 708 (https://doi.org/10.1002/med.20174)
10. D. Denoyer, S. Masaldan, S. La Fontain, M. A. Cater, *Metallomics* **7** (2015) 1459 (https://doi.org/10.1039/c5mt00149h)
11. I. Mohanram, J. Meshram, *Hindawi Publishing Corporation ISRN Organic Chemistry,* 639392 (2014) (http://dx.doi.org/10.1155/2014/639392)
12. A A. Fadda, K. M. Elattar. *J. Biosci. Med.* **3** (2015) 114 (http://dx.doi.org/10.4236/jbm.2015.311015)
13. G. T. Zitouni, M. Sivaci, F. S. Kilic, K. Erol, *Eur. J. Med. Chem.* **36** (2001) 685 (https://doi.org/10.1016/S0223-5234(01)01252-1)
14. S. M. Sondhi, V. K. Sharma, N. Singhal, R. P. Verma, R. Shukla, R. Raghubir, M. P. Dubey, *Phosphorous, Sulfur, Silicon Relat. Elem.* **156** (2000) 21 (https://doi.org/10.1080/10426500008044991)
15. H. M. Y. Al-Labban, H. M. Sadiq, A. A. J. Aljanaby. *J. Phys.: Conf. Ser.* **1294** (2019) 052007 (https://doi.org/10.1088/1742-6596/1294/5/052007)
16. M. Gowri, B. Saranya, S. Athimoolam, *Ind. J. Chem., B* **60** (2021) 1110 (http://nopr.niscair.res.in/handle/123456789/58188)
17. E. S. H. El ashry, L. F. Awad, E. I. Ibrahim, O. Kh. Bdeewy, *China J. Chem.* **25** (2007) 520 (https://doi.org/10.1002/cjoc.200790107)
18. A. Fadda, K. M. Elatter, *Am. J. Org. Chem.* **2** (2012) 52 (http://dx.doi.org/10.5923/j.ajoc.20120203.03)
19. Y.-X. Zou, X. Feng, Z.-Y. Chu, W.-H. Liu, X.-D. Zhang, J.-B. Ba, *Regulat. Toxicol. Pharmacol.* **103** (2019) 34 (https://doi.org/10.1016/j.yrtph.2019.01.018)
20. M. Verleyeu, I. Heulardand, J. M. Gillardin, *Pharmacol. Res.* **41** (2000) 539 (http://dx.doi.org/10.1006/phrs.1999.0619)
21. R. K. Mishra, B. G. Thakur, *Asian J. Chem.* **27** (2015) 860 (http://dx.doi.org/10.14233/ajchem.2015.17144)

22. Y. N. Bharate, M. A. Sakhare, S. B. Jadhav, S. D. Naikade, *Rasayan J. Chem.* **14** (2021) 479 (http://dx.doi.org/10.31788/RJC.2021.1416097).
23. Y. X. Sun, *Acta Crystallogr., E* **62** (2006) o5858 (http://doi.org/10.1107/S1600536806049348)
24. B. Anupama, M. Padmaja, C. Gyana Kumari, *E-J. Chem.* **9** (2012) 389. (http://dx.doi.org/10.1155/2012/291850)
25. R. Ramesh, S. Maheshwaram, *J. Inorg. Biochem.* **96** (2003) 457 (https://doi.org/10.1016/S0162-0134(03)00237-X)
26. S. A. Ali, A. A. Soliman, M. M. Aboaly, R. M. Ramadan, *J. Coord. Chem.* **55** (2013) 1161 (http://dx.doi.org/10.1080/0095897021000023509)
27. K. Singh, Y. Kumar, P. Puri, C. Sharma, K. R. Aneja, *Arab. J. Chem.* **10** (2017) 978 (https://doi.org/10.1016/j.arabjc.2012.12.038)
28. M. A. Sakhare, S. A. Khillare, M. K. Lande, B. R. Arbad, *Adv. Appl. Sci. Res.* **4** (2013) 94 (https://www.primescholars.com/articles/synthesis-characterisation-and-antimicrobial-studies-on-laiii-ceiii-andpriii-complexes-with-a-tetraaza-macrocyclic-ligand.pdf)
29. T. J. Saritha, P. Metilda, *J. Saudi Chem. Soc.* **25** (2021) 101245 (https://doi.org/10.1016/j.jscs.2021.101245)
30. P. Jayaseelan, E. Akila, M. Usha Rani, R. Rajavel, *J. Saudi Chem. Soc.* **20** (2016) 625(http://dx.doi.org/10.1016/j.jscs.2013.07.001)
31. A. A. S. Al-Hamdani, A. M. Balkhi, A. Falah. S. A. Shaker, *J. Chil. Chem. Soc.* **60** (2015) 2774 (http://dx.doi.org/10.4067/S0717-97072015000100003)
32. Y. N. Bharate, K. B. Sakhare, S. A. Surwase, M. A. Sakhare, *Heterocycl. Lett.* **13** (2023) 45 (https://www.heteroletters.org/issue131/Paper-5.pdf)
33. A. Aghao, D. Janrao, S. Janrao, M. Farooqui, *J. Pharma Res.* **5** (2016) 94 (https://jprinfo.com/storage/live/2020-04-05%2000_02_574.Arvind%20Aghao.pdf)
34. Y. N. Bharate, K. B. Sakhare, S. J. Chavan, M. A. Sakhare, *Int. J. Sci. Res. Sci. Tech.* **9** (2022) 116 (https://ijsrst.com/IJSRST22291617)
35. L. K. Dammu, S. K. Nara, V. Venkata, J. Nimmagadda, S. Kalluru., *J. Adv. Sci. Res.* **14** (2023) 35-39 (https://doi.org/10.55218/JASR.202314105)
36. L. H. Abdel-Rahman, A. M. Abu-Dief, E. F. Newair, S. K. Hamdan, *J. Photochem. Photobiol.* **18** (2016) 160 (http://dx.doi.org/10.1016/j.jphotobiol.2016.03.040)
37. A. M. Abu-Dief, L. A. Nassr, *J. Iran. Chem. Soc.* **12** (2015) 943 (https://doi.org/10.1007/s13738-014-0557-9)
38. P. S. Mane, S. G. Shirodkar, B. R. Arbad, T. K. Chondhekar, *Ind. J. Chem., A* **40** (2001) 648 (http://nopr.niscpr.res.in/handle/123456789/21060)
39. P. V. Rao, A. V. Narasaiah, *Ind. J. Chem., A* **42** (2003) 1896 (http://nopr.niscpr.res.in/handle/123456789/20716)c
40. H. Laila, A. Rahman, A. M. Abu-Dief, R. M. El-Khatib, S. M. Abdel-Fatah, *Photochem. Photobiol.* **69** (2016) 140 (http://doi/10.1016/j.jphptobiol.2016.06.052).

Anticancer acitivity of Schiff base ligand (*E*)-4-((5-chloro-2--hydroxybenzylidene)amino)-1,5-dimethyl-2-phenyl-1*H*-pyrazol--3(2*H*)-one and its Co(II), Cu(II) and Zn(II) metal complexes

KULDEEP B. SAKHARE, KIRTI N. SARWADE, YOGESH N. BHARATE
and MAHADEO A. SAKHARE*

*Department of Chemistry, Balbhim Arts, Science & Commerce College,
Beed (MS) 431122, India*

TABLE I. Physical and analytical data of ligand and its metal complexes; M.P.: melting point

No.	Compound	Colour	Yield (%)	M.P. (°C)	Elemental analysis Found % (Calcd.%)		
					C	H	N
1.	L	Yellow	71	275	62.85(63.25)	4.92(4.72)	11.90(12.29)
2.	Mn(II) complex	Pink	68	>300	48.92(49.86)	4.50(4.98)	8.50(8.31)
3.	Co(II) complex	Brown	75	>300	48.85(49.47)	4.15(4.94)	8.65(8.24)
4.	Ni(II) complex	Light yellow	64	>300	48.75(49.50)	4.30(4.94)	7.95(8.25)
5.	Cu(II) complex	Green	72	>300	49.50(49.03)	4.80(4.90)	7.55(8.17)
6.	Zn(II) complex	Yellow	62	>300	48.03(48.85)	4.75(4.88)	7.58(8.14)
7.	VO(II) complex	Light brown	69	>300	48.10(48.72)	3.95(4.32)	8.96(9.47)

TABLE S-II. XRD spectral data of metal complexes

Compounds	Mn(II)	Co(II)	Ni(II)	Cu(II)	Zn(II)	VO(II)
No. of reflections	12	10	19	25	29	23
Maxima(2θ)	49.56⁰	54.51⁰	32.13⁰	72.00⁰	35.20⁰	60.19⁰
Intensity	82.5 a.u.	100 a.u.	21.4 a.u.	14.2a.u.	59.6 a.u.	100a.u.
d value	9.762 Å	12.106 Å	18.560 Å	7.983Å	15.808 Å	7.470 Å
Lattice constant (Å)	a = 7.8130 b = 8.0580 c = 10.2120	a = 12.4230 b = 4.7220 c = 16.1100	a = 8.4047 b = 25.3897 c = 18.6676	a = 15.9658 b = 15.9658 c = 7.1487	a = 8.9034 b = 10.0168 c = 16.7090	a = 5.9645 b = 12.5730 c = 9.4371
Unit cell volume	590.695	920.888	2952.077	1578.117	1281.614	696.431
Axis and axis angle	a ≠ b ≠ c and α ≠ β ≠ γ	a ≠ b ≠ c and α = γ	a ≠ b≠ c and α = γ =90⁰	a = b ≠ c and α = β =	a ≠ b ≠ c and α ≠ β	a ≠ b ≠ c and α = γ =

---

* Corresponding author. E-mail: kuldeep.org.chem@gmail.com

		$= 90^0 \neq \beta$	$\neq \beta$		$90^0 \neq \gamma$	$\neq \gamma$	$90^0 \neq \beta$
Z Value	1	2	6		1	2	4
Crystal system	Orthorhom.	Monoclinic	Monoclinic		Hexagonal	Orthorhom.	Monoclinic

MASS SPECTRUM OF SCHIFF BASE LIGAND
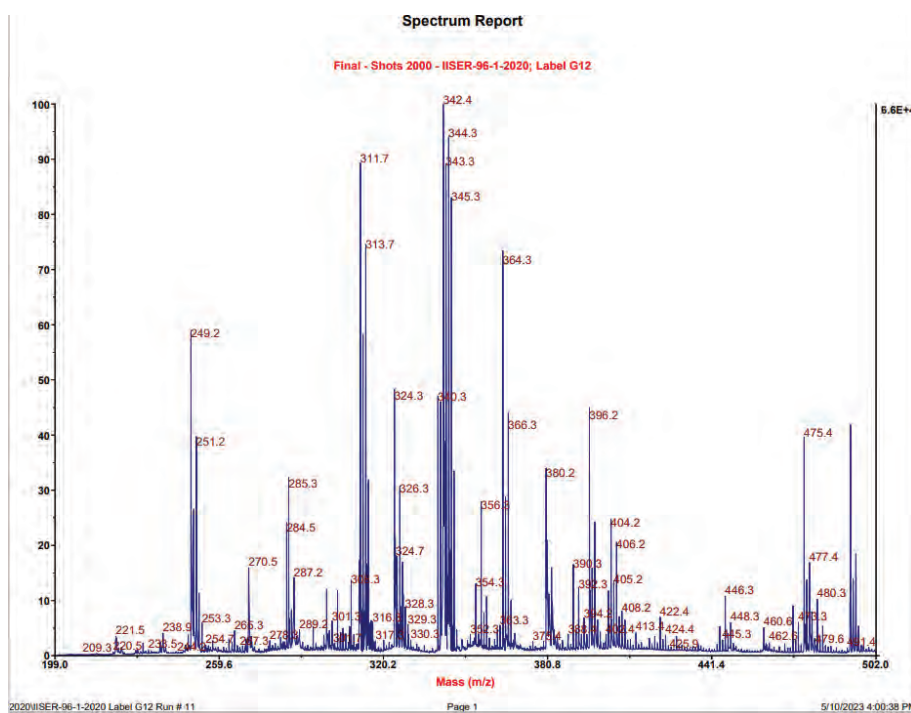
Fig. S-1. The mass spectrum of Schiff base ligand was expected to show the peak at 342 and in spectrum it showed 342 and 343(M+1).

^{1}HNMR SPECTRUM OF SCHIFF BASE LIGAND
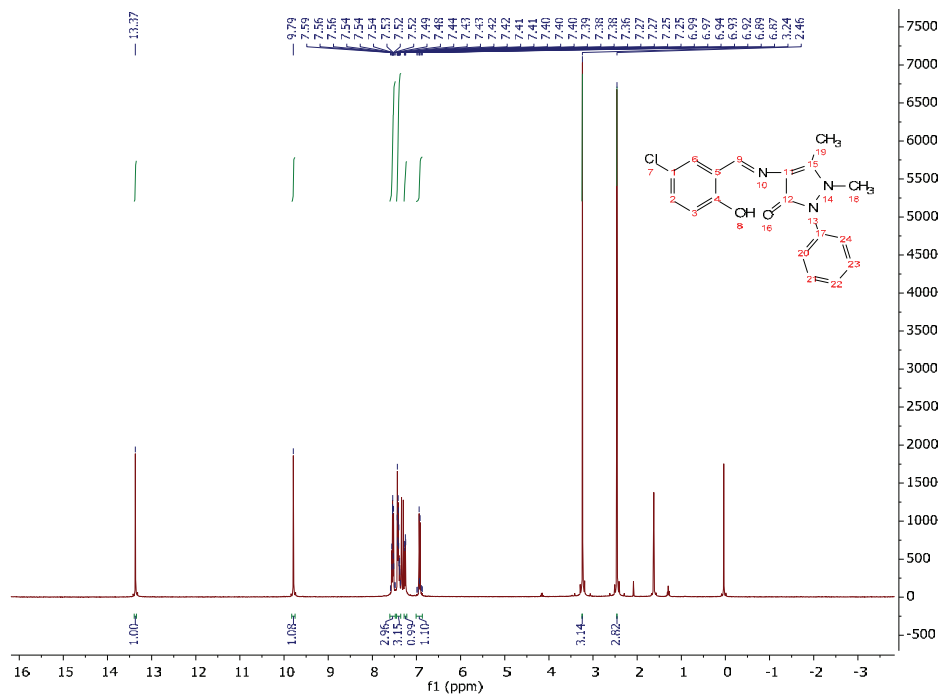
Fig. S-2. In the ^{1}H-NMR the above figure shows peaks at δ 13.36(s, 1H), 9.78(s, 1H), 7.58 – 7.49 (m, 2H), 7.46 – 7.35 (m, 3H), 7.33 (d, *J* = 2.6 Hz, 1H) meta coupling, 7.36 – 7.25 (m, 1H), 6.92 (d, *J* = 8.8 Hz, 1H), 3.24 (s, 3H) it goes to N-CH$_3$, 2.46 (s, 3H) it belongs to C-CH$_3$.

FTIR SPECTRUM OF SCHIFF BASE LIGAND
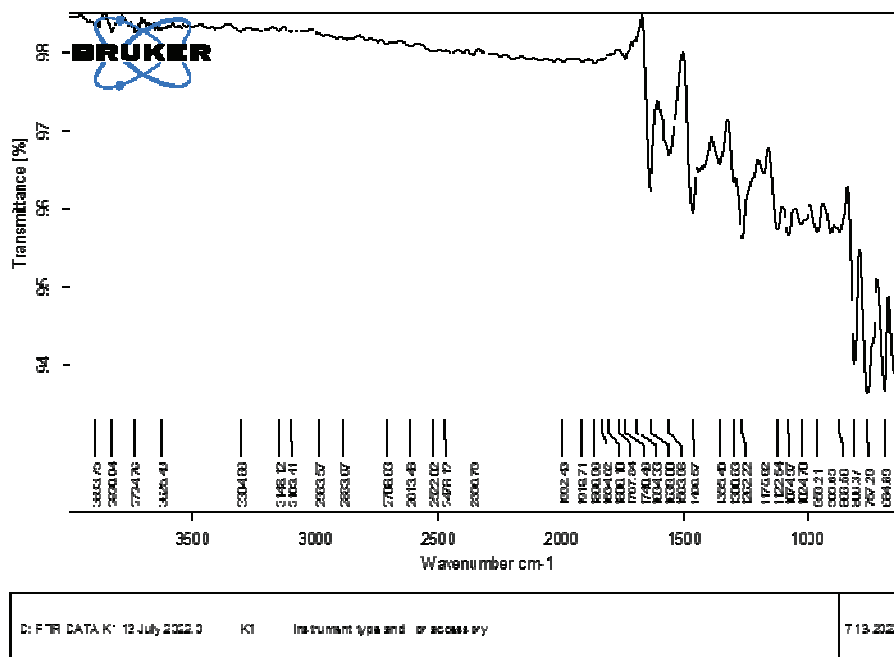
Fig. S-3. FTIR Spectrum of Schiff base ligand shows bands at 1639cm^{-1}.

FTIR SPECTRUM OF METAL COMPLEXES

Wavenumber in cm^{-1}
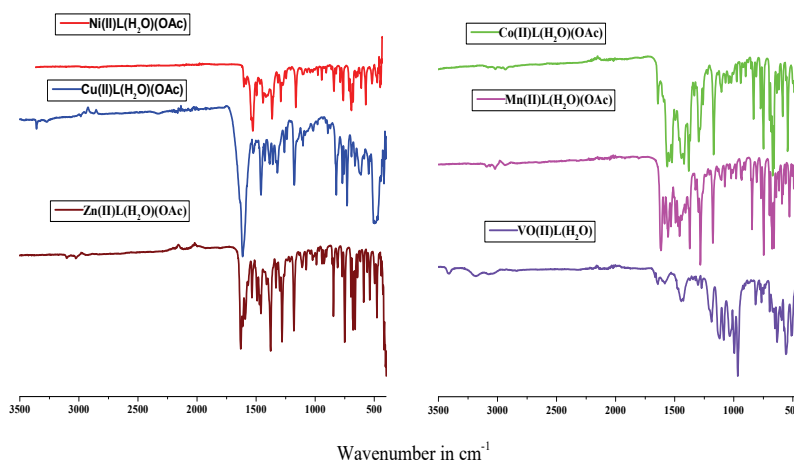
Fig. S-4. The FTIR spectrum of metal complexes decreased by 30-35cm^{-1} it is primary suggestion that metal complexes may be formed.

ELECTRONIC SPECTRA
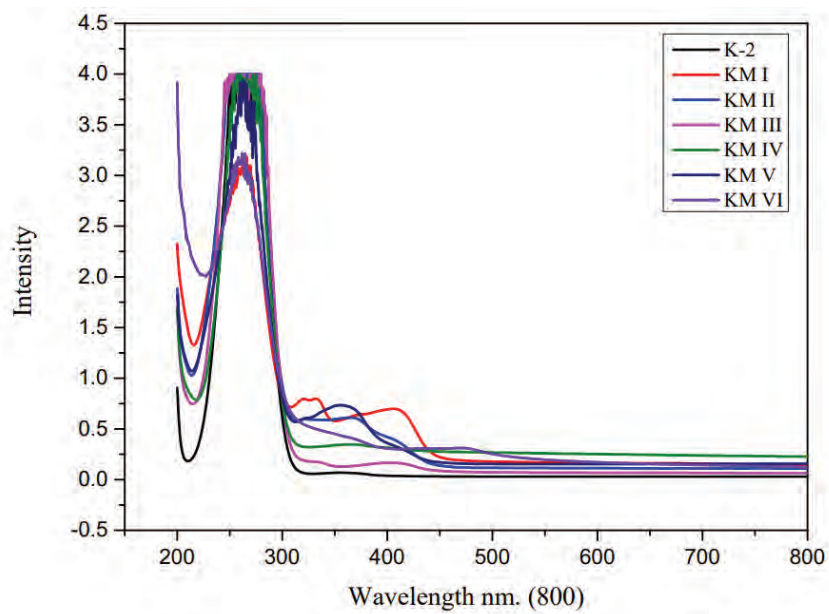
Fig. S-5. The electronic spectra of Schiff base and metal complexes is represented as above.

TGA-DTA OF METAL COMPLEXES
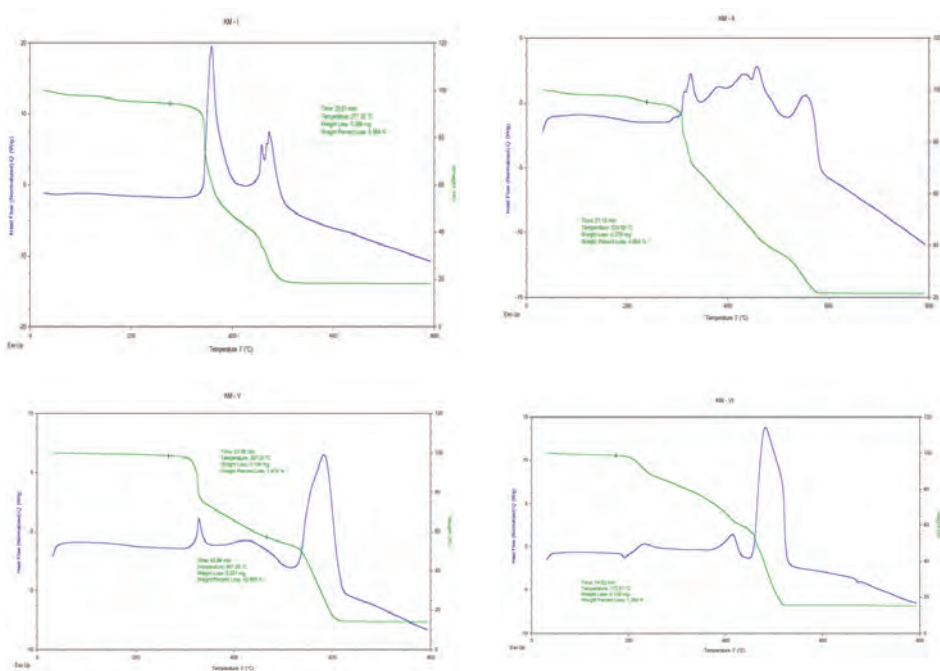
Fig. S-6. The TGA-DTA shows the formation of metal oxide which give the confirmation regarding the formation of metal complexes by loss of coordinated molecules.

POWDER XRD
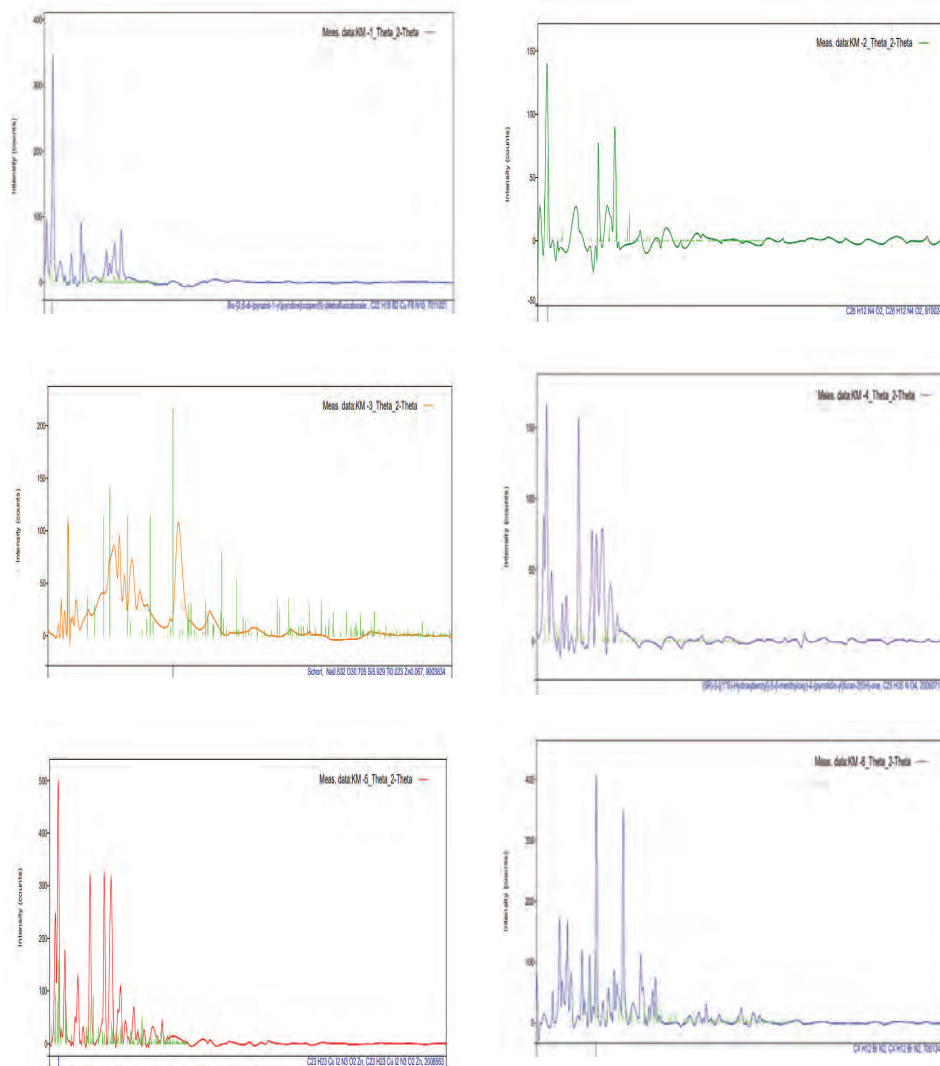
Fig. S-7. The powder XRD gives the information regarding the crystal systems of metal complexes.

ANTIBACTERIAL ACTIVITY
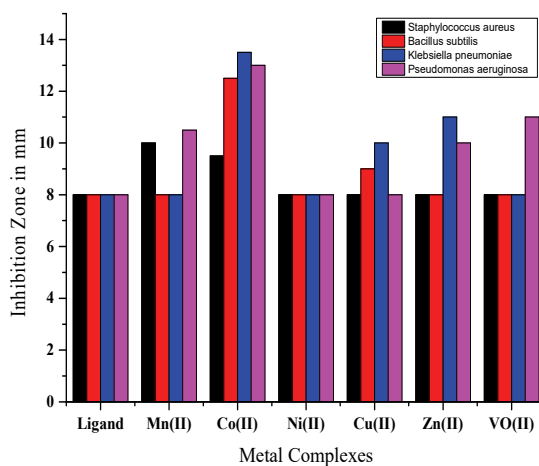
Fig. S-8. The antibacterial activity of Schiff base ligand and metal complexes shows that metal complexes are more active than that of ligand.

ANTIFUNGAL ACTIVITY
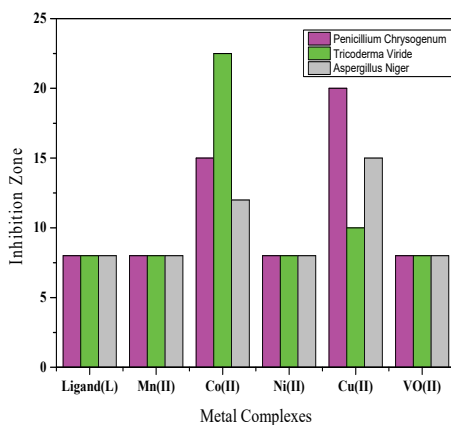
Fig. S-9. The antifungal activity of Schiff base ligand and metal complexes shows that metal complexes are more active than that of ligand.

ANTICANCER ACTIVITY
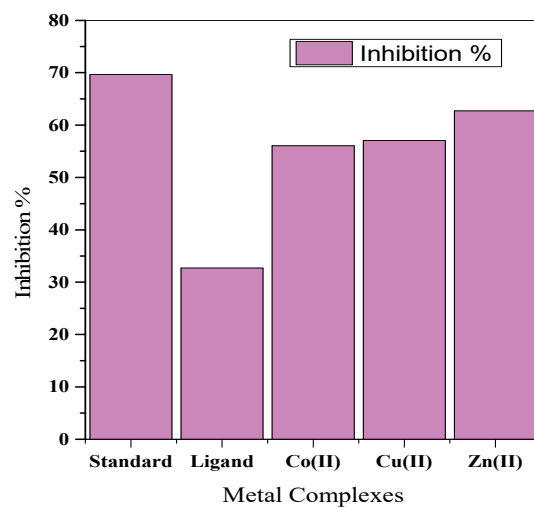
Fig. S-10. The Anticancer Activity of Schiff base ligand and metal complexes shows that metal complexes are more active than that of ligand.

PHOTOGRAPHS OF BIOLOGICAL ACTIVITY
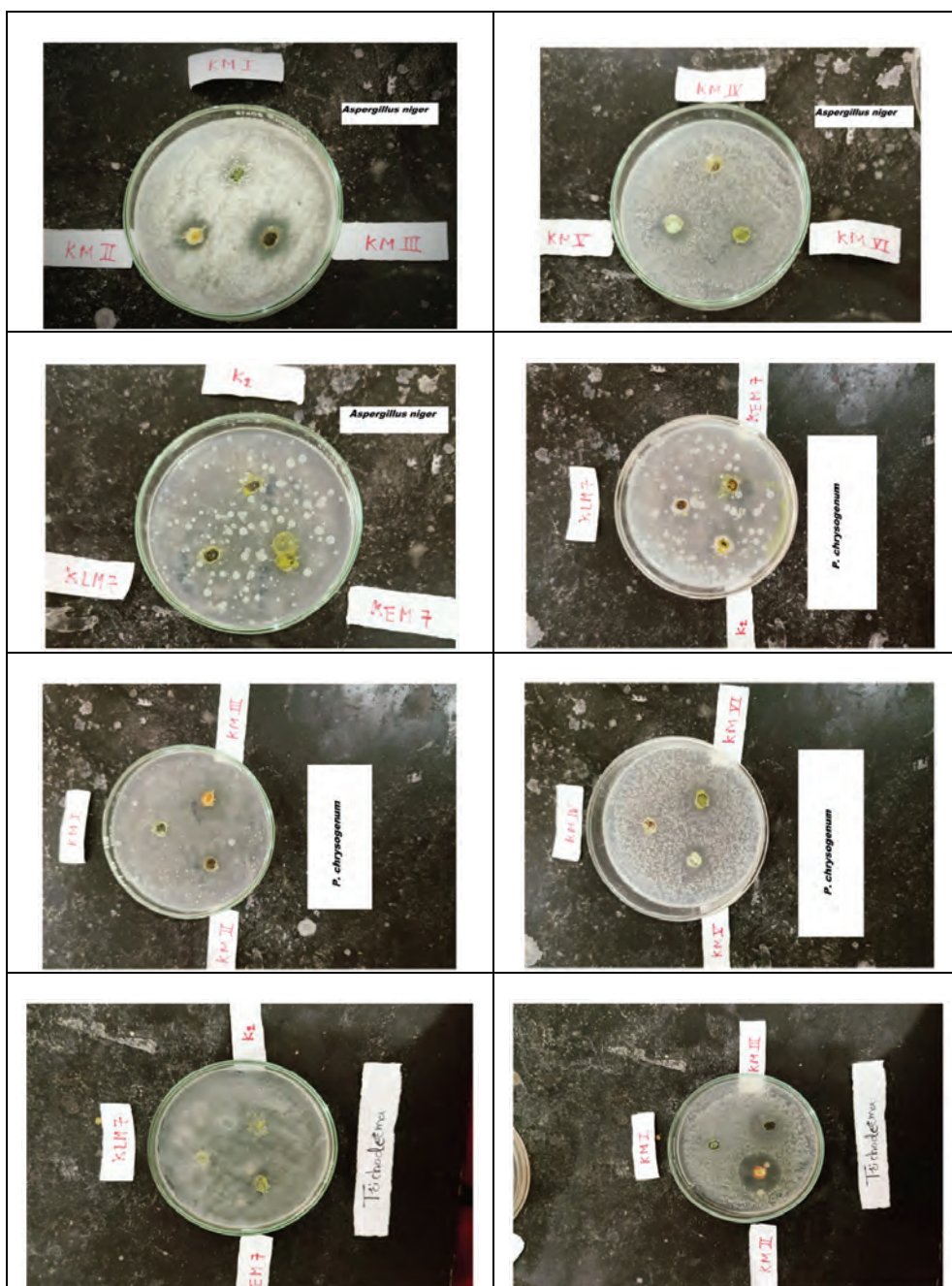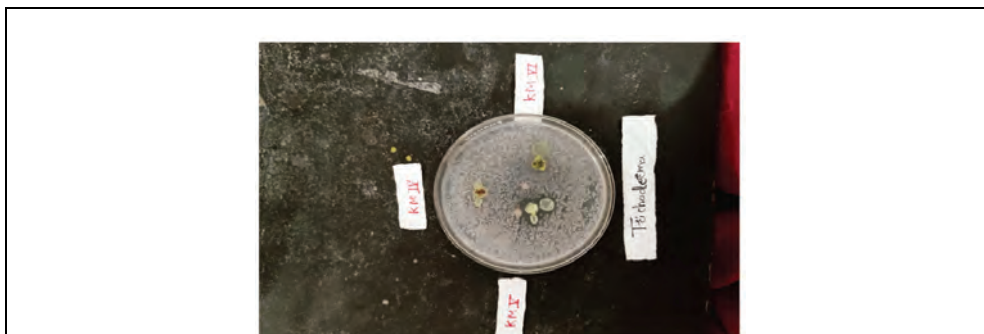
Fig S-11. These photograph shows the biological activities of Schiff base ligand and metal complexes.

This article has been corrected. See *JSCS* 2024:**89**(3), doi: 10.2298/JSC240325036E

Computer-aided approach for the identification of lead molecules as the inhibitors of cholinesterase's and monoamine oxidases: Novel target for the treatment of Alzheimer disease

SYEDA ABIDA EJAZ[1]*, MUBASHIR AZIZ[1], AMMARA FAYYAZ[1],
TANVEER A. WANI[2] and SEEMA ZARGAR[3]

[1]Department of Pharmaceutical Chemistry, Faculty of Pharmacy, The Islamia University of Bahawalpur, Bahawalpur 63100, Pakistan, [2]Department of Pharmaceutical Chemistry, College of Pharmacy, King Saud University, P.O. Box 2457, Riyadh 11451, Saudi Arabia and [3]Department of Biochemistry, College of Science, King Saud University, P.O. Box 22452, Riyadh 11451, Saudi Arabia

Abstract: Molecular docking is a promising and reliable technology for the purpose of discovering lead compounds *via* virtual screening. In addition to allowing for the testing of a large number of compounds, it also allows for the determination of how the selected compounds inhibit the targeted protein/receptor based on the scoring function and ranking. Because selective cholinesterase and monoamine oxidase inhibitors play a critical role in the treatment of Alzheimer disease, this research focuses on elucidating the mechanism of binding interactions of a few quinolone derivatives within the active sites of cholinesterase (acetyl-cholinesterase (AChE) and butyrylcholinesterase (BChE) and monoamine oxidase (MAO, monoamine oxidase A & B). As a result of these discoveries, it is possible that the newly identified inhibitors will be used as lead compounds in the development of novel enzyme inhibitors for the treatment of specific diseases, hence enabling the development of novel therapeutic approaches.

Keywords: molecular docking; acetyl-cholinesterase (AChE); butyrylcholineesterase (BChE); active pocket; monoamine oxidases A & B, Alzheimer disease.

INTRODUCTION

The actions of brain neurons, particularly neurotransmission, are grouped into systems of individually distinct neurons, neurotransmitters, neuromodulators, receptors and hormones. The monoaminergic and cholinergic systems are essential in these systems. A crucial component of the cholinergic system of neurotransmission is the neurotransmitter acetylcholine.[1] Neuromuscular syn-

---

apses, the brain and autonomic ganglia all contain acetylcholine (ACh) which is fast acting. Two enzymes, acetylcholinesterase (AChE; EC 3.1.1.7) and butyryl-cholinesterase are present in tissues that catalyze the breakdown of acetylcholine (BChE; EC 3.1.1.8).[2] The two enzymes are both glycoproteins that can either be membrane-bound or soluble. AChE is a critical enzyme in cholinergic neuro-transmission on both the central and peripheral level. It is mostly membrane--bound and located in the neuromuscular junctions and synapses between neu-rons in the central nervous system, where it inhibits the activity of acetylcholine (Ach) produced during nerve stimulation.[3] The enzyme is also present in soluble forms and linked with the erythrocyte membrane. BChE is found in a broad variety of human tissue types. It is expressed in several different groups of neu-rons in the human brain that are not connected with AChE, as well as glial cells. BChE is significantly more abundant in the serum than AChE is. BChE, like AChE, is a soluble enzyme that may also be membrane-bound.[4] AChE is highly effective at hydrolyzing Ach, but its catalytic site is buried deep inside a deep cavity, which restricts its ability to cleave esters with heavier acyl groups.[5] As compared to AChE, butyrylcholinesterase has a bigger cavity and is a less select-ive esterase capable of cleaving a variety of esters with larger acyl groups.[6]

The network of monoamine neurotransmission systems, each of which is regulated by a unique monoamine neurotransmitter, is known as the monoamine neurotransmission system. These include the dopaminergic, noradrenergic and serotonergic systems, which are each regulated by the neurotransmitters dop-amine, noradrenaline and serotonin, respectively.[7] Two isoforms of the mono-amine oxidase (MAO) enzyme, MAO A and MAO B, are involved in the oxidat-ive deamination of biogenic amines, including neuroamines, vasoactive amines and exogenous amines, and hence regulate the concentration of amine neuro-transmitters and numerous amine medications.[8] Due to their location on the mito-chondrial outer membrane, the MAO flavoproteins metabolize amines inside the cell. Each MAO has a different tissue concentration, with the two versions func-tioning identically in the human liver. MAO B is highly expressed in platelets, glial cells and serotonergic neurons, whereas MAO A is expressed primarily in the stomach, placenta and dopaminergic and noradrenergic neurons.[9] Despite having the identical catalytic center structure, with substrate-orienting tyrosinase leading to covalently bound FAD,[10] the two forms exhibit distinct intrinsic act-ivity (k_{cat} and K_m values) with each substrate. Serotonin is metabolized mostly by MAO A in the human brain, but dopamine is metabolized by both forms.[11]

Alzheimer disease (AD) is the most common neurodegenerative ailment, affecting millions of individuals worldwide, including 5 % of the over-65 popul-ation. The primary clinical manifestation of AD is increasing memory loss and other abnormalities in brain function, such as aberrant behavior and impairments in language, comprehension, and visual-spatial abilities.[12]

It has been postulated that BChE collaborates with AChE in the brain to regulate ACh neurotransmission when ACh levels become excessive, especially given that AChE is inhibited by high concentrations of its substrate.[13] In the average human brain, BChE activity is lower than AChE activity, whereas AD patients have much higher BChE/AChE ratios,[14] indicating that BChE inhibition can get critical as AD advances. This has generated the concept that inhibiting both ChEs may result in enhanced therapeutic advantages or that inhibiting BChE alone may be advantageous.[15]

The first therapy methods for AD were aimed at boosting cholinergic transmission in the brain, in accordance with the "cholinergic hypothesis" of memory loss. Among the several strategies used to raise synaptic ACh levels, inhibiting acetylcholinesterase (AChE) has shown to be the most effective. Inhibiting the enzyme butyrylcholinesterase (BuChE), which is present in trace amounts in normal brains but is elevated in the brains of AD patients with plaques and tangles, may enhance cholinergic transmission.[16] Dopamine, serotonin and noradrenaline, which are all metabolized by MAO or catechol-O-methyltransferase (COMT), are reduced as a consequence of other neurons being gradually eliminated in AD. MAO inhibitors have long been used as antidepressants, and an early study against Parkinson's disease (PD) led in the acceptance of L-deprenyl (selegiline) as a disease-delaying medication for the condition. Thus, MAO inhibitors may promote amine neurotransmission and have beneficial biochemical effects in the therapy of AD.[17] Increased MAO B levels have been found in AD patients' brains as a result of increased astrogliosis,[18] suggesting that combined MAO A/B inhibition may be an effective AD treatment. MAO inhibitors' beneficial features also include a decrease in the generation of reactive oxygen species, which may contribute to greater neuronal damage.[19]

Current novel therapeutic approaches suggest that drugs targeting a single target may be insufficient for treating multifactorial neurodegenerative diseases such as AD, PD, Huntington's disease (HD) and amyotrophic lateral sclerosis (ALS), which are all characterized by the coexistence of multiple etiologies. These include, but are not limited to, the development of oxidative stress (OS) and reactive oxygen species (ROS), protein misfolding and aggregation, mitochondrial dysfunction, inflammation, metal dyshomeostasis and accumulation at neurodegenerative sites.[20] Thus, it is plausible to assume that AD treatment will likely need a combination of drugs to address the disease's many clinical manifestations. Due to the multifactorial character of AD and the variety of brain pathways involved in its control,[21] multi-targeted ligands have been widely investigated as potential therapeutic candidates with favorable benefits in AD treatment.[22]

The current study is focused on the identification of quinolone derivatives as the inhibitors of either class of enzymes, $i.e.$, cholinesterases (AChE and BChE)

and monamine oxidases (MAO-A and MAO-B). Quinolones have been previously identified for their anti-bacterial activity in the treatment of various infections. They are specifically designed to selectively target two bacterial topoisomerase enzymes: DNA gyrase that targets Gram-negative bacteria and topoisomerase IV that effects Gram-positive bacteria.[23] The approved quinolone derivative drug tacrine lowers AChE levels in AD. One study showed that quinolone derivatives were active against AChE with an IC_{50} values ranging from 7.31 to 88.10 μM.[24] The long-term use, however, of quinolones is not recommended as it may be carcinogenic to adults and arthropathogenic in children. However, they can be used for the short-term treatment and symptomatic management of AD. This study will lead a comprehensive knowledge of the structures, activity correlations, and roles of the discovered inhibitors/drug-like compounds which promises well enough for the future development of novel pharmaceuticals. The following compounds were selected for this study.

EXPERIMENTAL

Molecular docking

In the present work, we employed molecular docking using MOE Software[23] to predict the inhibitory mechanism of chosen quinolone and quinoline derivatives. The crystal structure of the chosen target (AChE, PDB id: 4BDT), (BChE, PDB id: 4BDS), (MAO-A, PDB id: 2Z5Y), and (MAO-B, PDB id: 2V5Z) was obtained from the protein data bank and utilized for further research. The force field MMFF94x with an *RMSD* gradient of >0.01 kcal* mol⁻¹ Å⁻¹ was used to minimize the energy of the selected quinoline and quinolone compounds. Additionally, when the ligands and protein were created, charges were assigned and hydrogen atoms were added to all molecules, the MOE site finder tool was used to locate the binding site, as mentioned before. For considering the conformational flexibility parameters, we have employed a simulation approach for docking purposes in which the ligand is allowed to interact with the groove of a targeted protein after a series of moves in its conformational space. These moves include changes in the structures of ligands either internally by rotating the torsional angles or the number of rotatable bonds, or externally by translation and rotation. Each rotation of ligand produced intermolecular interactions with the targeted protein. This approach is preferred for taking into account the conformational flexibility of ligands, and it may take longer time depending upon the performance of computing system. In a current study, two series of ligands were docked. Quinoline derivatives have four rotatable bonds, whereas quinolone derivatives have only two rotatable bonds. By employing a simulation approach, ligands were allowed to interact with targeted protein through torsional angles. The rigid receptor model was employed and total numbers of poses were set to 100. Finally, the MOE software was used to produce 3D and 2D poses for further investigation.[25] The docking of all the compounds was reconfirmed by SeeSAR Analysis.[26]

---
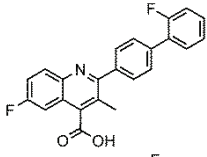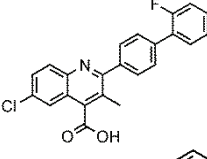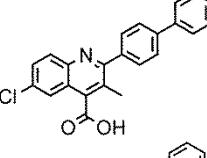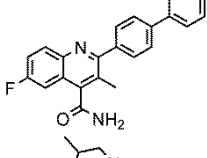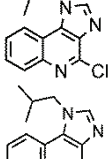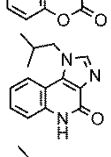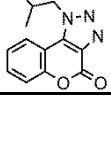
* 1 kcal = 4184 J

RESULTS AND DISCUSSION

AChE Results

As shown in Table I, the derivative **4**, which has the most binding score –26.9 kJ/mol showed binding interactions. The amino acid His447 formed carbon hydrogen bonding with the hydrogen attached with nitrogen in the imidazole. Similarly, Trp86 and Tyr337 formed π–π stacked interaction with imidazole and pyridine ring. The binding energy and bonding and non-bonding interactions of

TABLE I. List of the chosen derivatives

Code	IUPAC Name	Structure
3	6-Fluoro-2-[4-(2-fluorophenyl)phenyl]-3-methylquinoline-4-carboxylic acid	
3-A	6-Chloro-2-[4-(2-fluorophenyl)phenyl]-3-methylquinoline-4-carboxylic acid	
3-B	6-Chloro-3-methyl-2-(4-phenylphenyl)quinoline-4-carboxylic acid	
3-C	6-Fluoro-3-methyl-2-(4-phenylphenyl) quinoline-4-carboxamide	
4	4-Chloro-1-(2-methylpropyl)imidazole[4,5-*c*]quinoline	
4-A	1-(2-Methylpropyl)chromeno[3,4-*d*]imidazol-4-one	
4-B	1-(2-Methylpropyl)-5*H*-imidazo[4,5-*c*]quinolin-4-one	
4-C	1-(2-Methylpropyl)chromeno[3,4-*d*]triazol-4-one	

quinolone derivatives within the active pocket of AChE is given in Supplementary material to this paper.

The alkyl interaction was formed with the amino acid Pro446 which formed interaction with the chlorine attached with the pyridine ring and similarly, the amino acid Trp439 formed π-alkyl interaction with the chlorine attached with the pyridine ring, Fig. 1. The amino acids which formed van der Waals interactions were Ile451, Glu202, Ser203, Tyr133, Gly122, Gly121, Asp74, Tyr341, Thr83, Tyr77. The derivative **4-C** which has the best binding score –26.5 kJ/mol after the derivative **5** formed the following interactions. The amino acids Trp86, Tyr337 which formed π–π stacked interaction with the imidazole ring and with pyridine ring. The derivative **4-A** which has the binding score –26.1 kJ/mol. The amino acids Glu202 and Gly126 which formed carbon hydrogen bond with the oxygen attached with pyran ring and with the hydrogen of imidazole ring. The π-sigma interaction was formed with the amino acid Trp86. Similarly, the binding score of the derivative **4-B** is –25.6 kJ/mol made C–H bond with the amino acid Thr83 involving oxygen attached with pyran ring. The π–π stacked interaction involved with the amino acids Trp86, Tyr337 with the imidazole and pyridine ring. The derivative **3-C** showed binding score –22.3 kJ/mol and formed interactions. The amino acid Trp86 formed conventional hydrogen bonding with the amino group and the amino acid Gly126, Gly121 formed carbon hydrogen bonding with the oxygen attached with pyridine ring and the derivative **3** that has the binding score –21.8 kJ/mol formed alkyl interaction with amino acid His447 with the substitution on pyridine ring. The amino acid Trp86 formed π-sigma bond with the substituted benzene ring. Similarly, the derivative **3-A** has the binding score –20.8 kJ/mol formed conventional hydrogen bonding with the amino acid His447. The amino acids Tyr119, Tyr133 and Leu130 formed π-alkyl interaction with chlorine attached with the benzene ring and the derivative **3-B** which has a binding score of –20.7 kJ/mol formed conventional hydrogen bonding involving amino acid His447 with the hydrogen attached with the oxygen in pyridine ring. The amino acids Tyr119, Tyr133 and Leu130 which formed alkyl and π-alkyl chlorine attached with the benzene ring.

SeeSAR Analysis. The best derivative **4** was subjected to SeeSAR analysis in order to predict the virtual visualization of binding interactions. Green colored coronas were used to indicate the structural components of potent compounds, whereas red colored coronas were used to indicate those parts that had an adverse impact on binding interactions. A colorless corona was used to shade structural elements that made little contribution. Corona size predicts the contribution of a structural component. SeeSAR visualization of potent derivative **4** is given in Fig. 2. Hyde energy of favorable corona (green colored) for **4** was –8.3 kJ/mol while the hyde energy of unfavorable corona (red colored) was 9.0 kJ/mol.
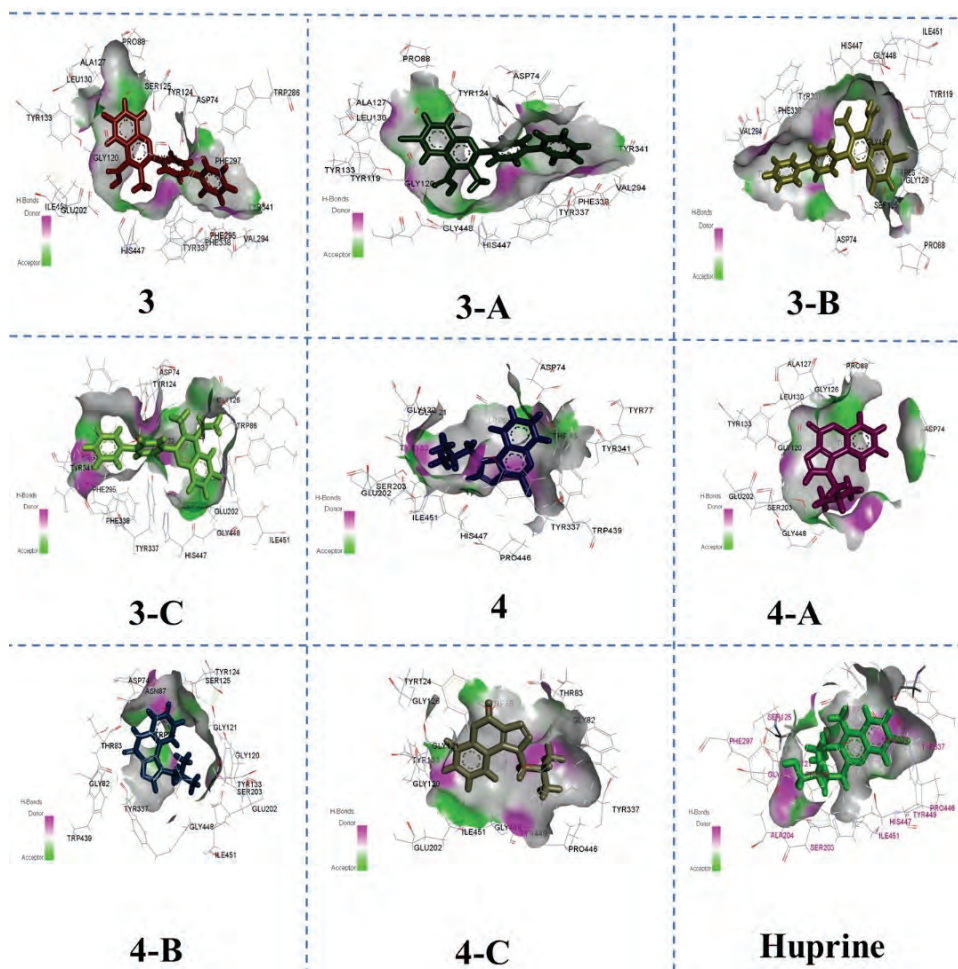
Fig. 1. 3D binding interactions of selected compounds within the active pocket of AChE.

BChE results

As shown in Table I, the derivative **3-C** which has the most binding score –29.3648 kJ/mol showed binding interactions. The amino acids Thr122, Tyr128 and Gly121 which formed conventional hydrogen bonding and carbon hydrogen bonding with the chlorine attached with the benzene ring. Similarly, the amino acids Phe329 and Trp231 made π–π T shaped interaction with the benzene ring. Binding energy and bonding and non-bonding interactions of quinolone derivatives within the active pocket of BChE is provided in Supplementary material.

The π-alkyl interaction was formed with the amino acid His438 and Leu286 which formed interaction with the substitution attached with the pyridine ring and with the benzene ring. Similarly, the amino acid Trp82 formed π-sigma inter-
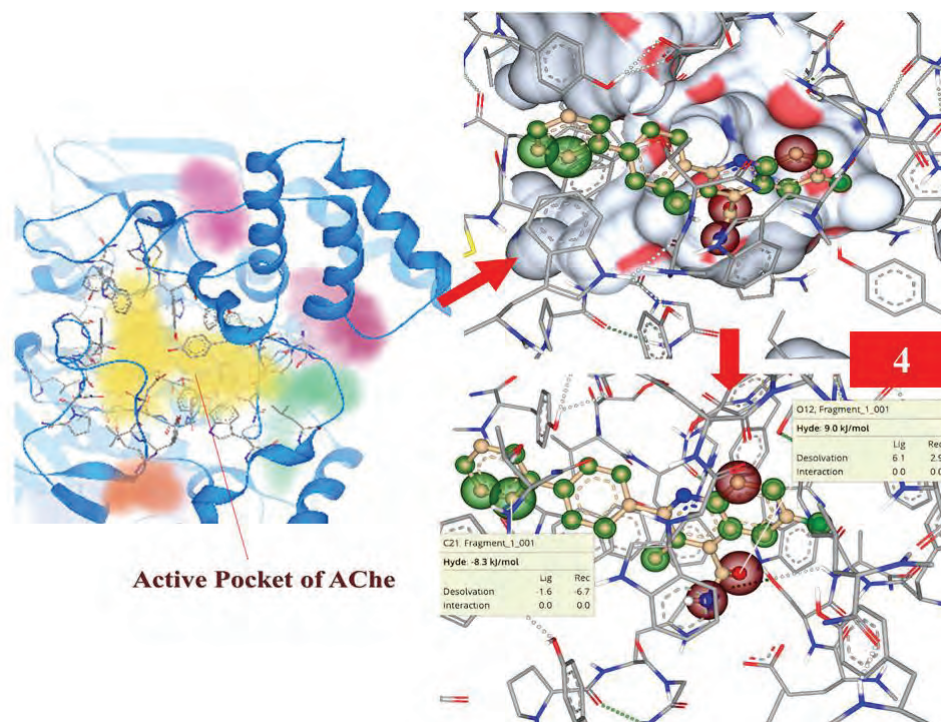
Fig. 2. Left: SeeSAR analysis of the active pocket of AChE. Right: showing docked conformations with coronas. Red colored coronas represent undesirable characteristics, green colored coronas show favorable contributions and colorless coronas represent no structural component contribution.

action with the substituted benzene ring. The amino acid Glu197 formed unfavorable acceptor–acceptor with the oxygen attached with pyridine ring. The amino acids which formed van der Waals interactions were Val288, Pro285, Gly116, Leu125, Gly115, Ile442, Gly439 and Phe398. The derivative **3** which has the best binding score –28.6 kJ/mol after the derivative **1** produced the following interactions. The amino acids Gly116 which formed π–π T shaped interaction with the pyridine ring and with substituted benzene ring. The amide–π stacked interaction was formed with the amino acid Trp82 involving the benzene ring and the amino acid Ala328 formed π-alkyl interaction with the substituted benzene ring. The derivative **3-B**, which has the binding score –26.6 kJ/mol: the amino acids Gly117 and Ser198, which formed conventional hydrogen bond with the oxygen attached with pyridine ring. The amide–π stacked interaction was formed with the amino acid Gly116. Similarly, the binding score of the derivative **3-A** is –26.5 kJ/mol formed conventional hydrogen bond with the amino acid Gly117 and Ser198 involving oxygen attached with pyridine ring. The amide–π stacked interaction involved with the amino acids Gly116 with the pyridine ring and sub-

stituted benzene ring. The amino acid His438 formed π-alkyl interaction with the chlorine. The derivative **4-B** showed binding score –25.3 kJ/mol and formed interactions. The amino acid Tyr128 formed conventional hydrogen bonding with the oxygen attached with the pyridine ring and the amino acid His438 formed alkyl interaction with the dimethylpropane and the derivative **7**, which has the binding score –25.2 kJ/mol formed hydrogen bond and C–H bond with the amino acid Trp82, Tyr128 and Gly121 with the oxygen attached with the pyridine ring. Similarly, the derivative **8** has the binding score –24.9328 kJ/mol formed hydrogen bond with the amino acid Gly121 with the oxygen attached with pyridine ring. The amino acids His438 formed π-alkyl interaction with dimethylpropane and the derivative **5**, which has a binding score of –24.1 kJ/mol formed π-alkyl interaction involving amino acid Tyr128 with chlorine attached with pyridine ring. The amino acid Trp82 formed π-sigma interaction with pyridine ring, Fig. 3.
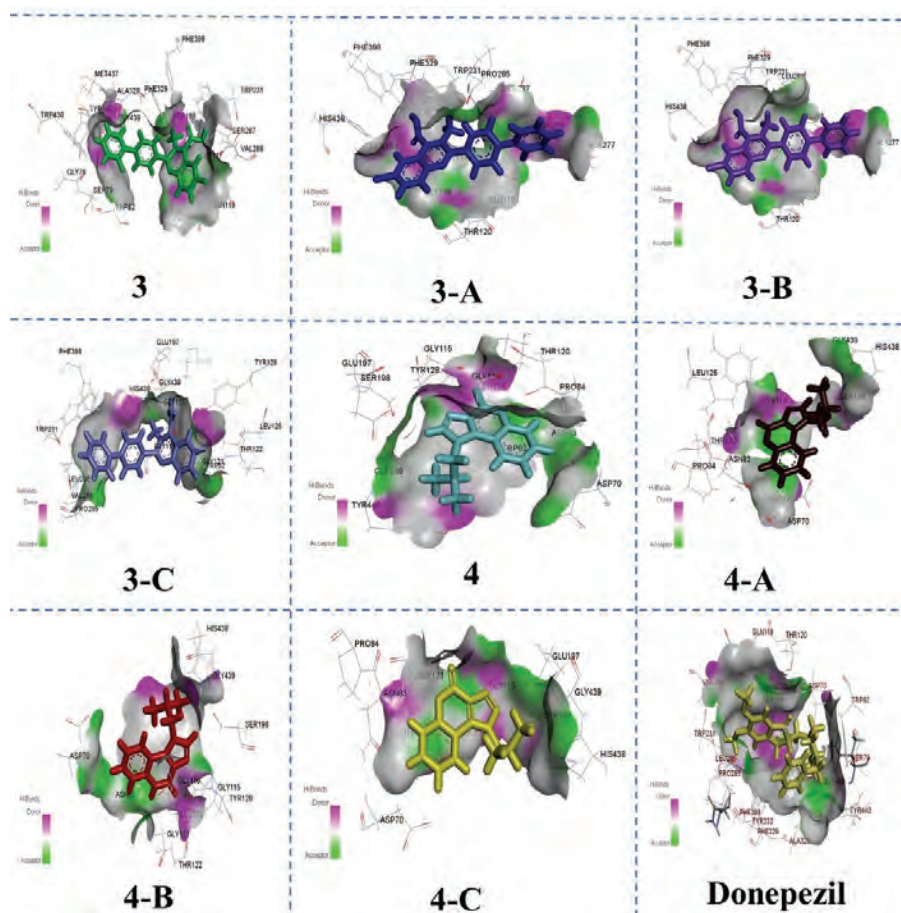
Fig. 3. 3D binding interactions of selected compounds within the active pocket of BChE.

SeeSAR Analysis. SeeSAR analysis of the best derivative **3-C** was executed, which anticipate virtual display of binding interactions. Green colored coronas were used to positively present the structural components of potent compounds, whereas red colored coronas were used to favorably convey the structural members that had a detrimental impact on binding interactions. A colorless corona was used to represent structural elements that made little contribution. Corona size determines the contribution of a structural component. SeeSAR visualization of potent derivative **3-C** is given in Fig. 4. Hyde energies of favorable coronas (green colored) for **3-C** was –4.7 and –4.5 kJ/mol while the hyde energy of unfavorable corona (red colored) was 13.8 kJ/mol.
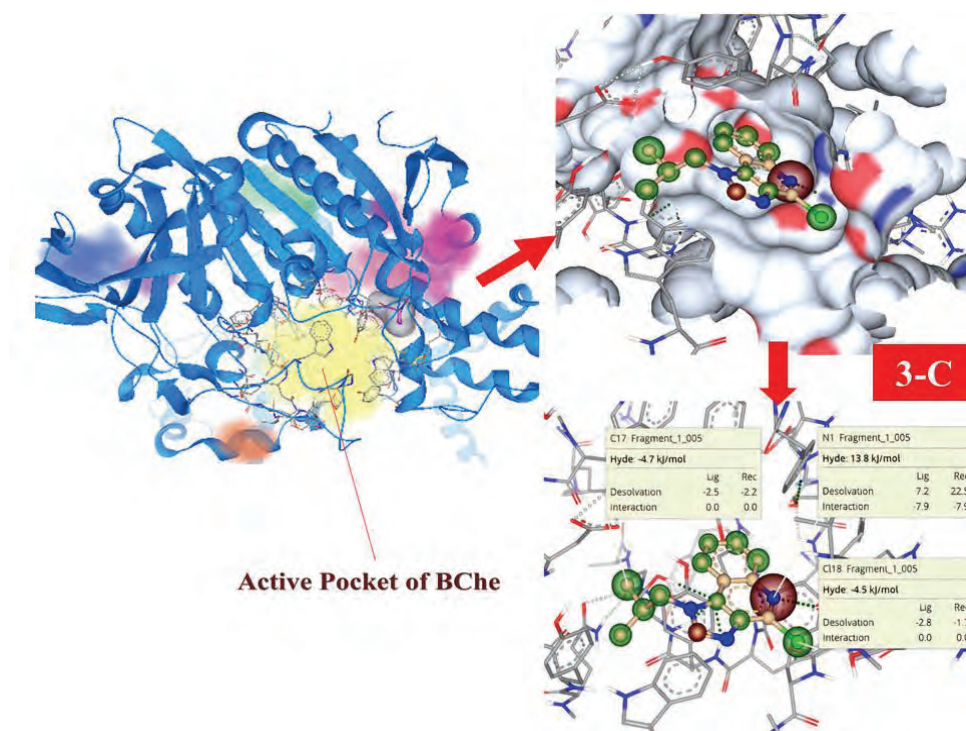
Fig. 4. Left: SeeSAR analysis of the active pocket of BChE. Right: showing docked conformations with coronas. Red colored coronas show unfavorable interactions whereas green coronas are representing favorable contributions and colorless coronas are showing no contribution of components.

MAO-A Results

As shown in Table I, the derivative **3** which has the most binding score –37.5 kJ/mol showed binding interactions, Fig. 5. The amino acids Thr52 and Ile23, which formed conventional hydrogen bond and π-donor hydrogen bond with the fluorine attached with the benzene ring and with the benzene ring.

Similarly, the amino acid Trp397 which formed π–π stacked interaction with the substituted benzene ring. Binding energy and bonding and non-bonding interactions of quinolone derivatives within the active pocket of MAO-A is given in Supplementary material.

Fig. 5. 3D binding interactions of selected compounds within the active pocket of MAO-A

Amide–π stacked interaction was formed involving the amino acid residue Tyr444 with the benzene ring. The amino acids Ala448 and Met445 formed π-alkyl interaction with the substituted benzene ring and with the benzene ring. The amino acids which formed Van der Waals interactions were Ser24, Gly434, Thr435, Gly66, Lys305, Phe352, Ala68 and Gly50. The derivative **3-A** which has the best binding score –37.5 kJ/mol after the derivative **1** formed the following interactions. The substituted benzene ring and the pyridine ring produced con-

ventional hydrogen bonds and carbon hydrogen bonds with the amino acids Arg51, Thr52 and Tyr444. The benzene ring and the amino acid Met444 established π-sulphur interaction. The pyridine ring was involved in the formation of the amide-stacked interaction with the amino acid Tyr407. The derivative **3-B**, which has the binding score –37.1 kJ/mol. The amino acids Tyr444, which formed carbon hydrogen bond with the benzene and pyridine ring. The amino acid Ala448 and Cys406, Met445 formed alkyl and π-alkyl interactions with the benzene and the pyridine ring. The π-cation interaction was formed with the amino acid Arg51. Similarly, the binding score of the derivative **3-C** is –36.9 kJ/mol formed amide–π stacked interaction involving the amino acid Trp397 with the substituted benzene ring. The amino acid Tyr407 formed π–π stacked interaction with the pyridine ring. The amino acids Met445 and Ala448 formed π-alkyl interaction with the benzene and pyridine ring. The derivative **4** showed binding score of –30.3 kJ/mol. The amino acid Tyr407 and Gly443 formed carbon hydrogen bond with the hydrogen attached with the nitrogen in imidazole ring. The amino acid Arg51 and Phe352 formed alkyl and π-alkyl interaction with the imidazole ring and with the chlorine attached with benzene ring and similarly, the derivative **4-C**, which has the binding score -29.5 kJ/mol formed carbon hydrogen bond with the amino acid Tyr407 and Gly443 with the hydrogen of dimethylpropan and the amino acid Arg51 formed alkyl interaction with the imidazole ring. Similarly, the derivative **4-A** has the binding score –29.1 kJ/mol and formed carbon hydrogen bond with the amino acid Tyr407 with the hydrogen of dimethylpropan. The amino acids Met445 formed π-alkyl interaction with benzene ring and the derivative **4-B**, which has a binding score of –28.4 kJ/mol formed carbon hydrogen bond involving the amino acid Gly67 with the hydrogen of dimethylpropan and the amino acid Arg51 and Met445 formed alkyl and π-alkyl interaction imidazole ring.

SeeSAR Analysis. SeeSAR analysis of the best derivative **3** was executed which anticipate virtual display of binding interactions. Green colored coronas were used to favorably identify the structural elements of potent compounds, whereas red colored coronas were used to distinguish those elements that had a negative impact on binding interactions. Colorless coronas were used to shade structural elements that made no contribution. The size of the corona predicts the contribution of structural components. SeeSAR display of potent derivative **3** is given in Fig. 6. Hyde energies of favorable coronas (green colored) for **3** was –8.7 and –4.8 kJ/mol while the hyde energy of unfavorable corona (red colored) was 12.1 kJ/mol.

MAO-B Results

The derivative **3-B**, which has the most binding score –36.9 kJ/mol showed binding interactions. The amino acids Trp388 and Tyr398 established interact ions
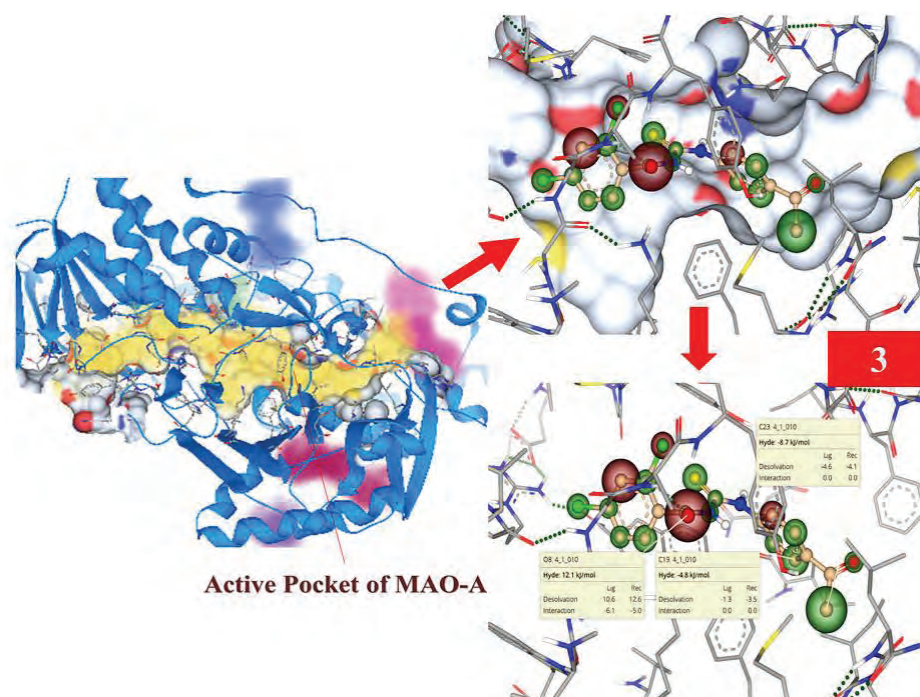
Fig. 6. Left: SeeSAR analysis of the active pocket of MAO-A. Right: showing docked conformations with coronas. Colorless coronas represent no structural component contribution, while green coronas indicate favorable contributions and red coronas indicate undesirable aspects.

with the substituted benzene ring and the pyridine, respectively, that were π–π stacked and a T shape, respectively. The amino acids Ala439 and Lys296 and Val294, Cys397 and Phe343 developed alkyl and π-alkyl interactions with the benzene, substituted benzene ring and with chlorine attached with benzene ring, Fig. 7. Binding energy and bonding and non-bonding interactions of quinolone derivatives within the active pocket of MAO-B is provided in Supplementary material.

The π-cation interaction was also observed involving the amino acid Arg42 with the benzene ring. The amino acids, which formed van der Waals interactions were Ala263, Ile264, Gly13, Ile14, Thr43, Gly57, Leu56, Tyr435, Gly434, Thr426, Gly425 and Ser15. The derivative **3-A**, which has the best binding score –36.7 kJ/mol after the derivative **1** formed the following interactions. The amino acids Gly58 and Arg42, which formed carbon hydrogen bond and conventional hydrogen bond with the oxygen attached with pyridine ring and with fluorine and benzene ring. The amino acid Thr43 formed π-cation interaction with the fluorine attached with benzene ring. The derivative **3-C**, which has the binding score
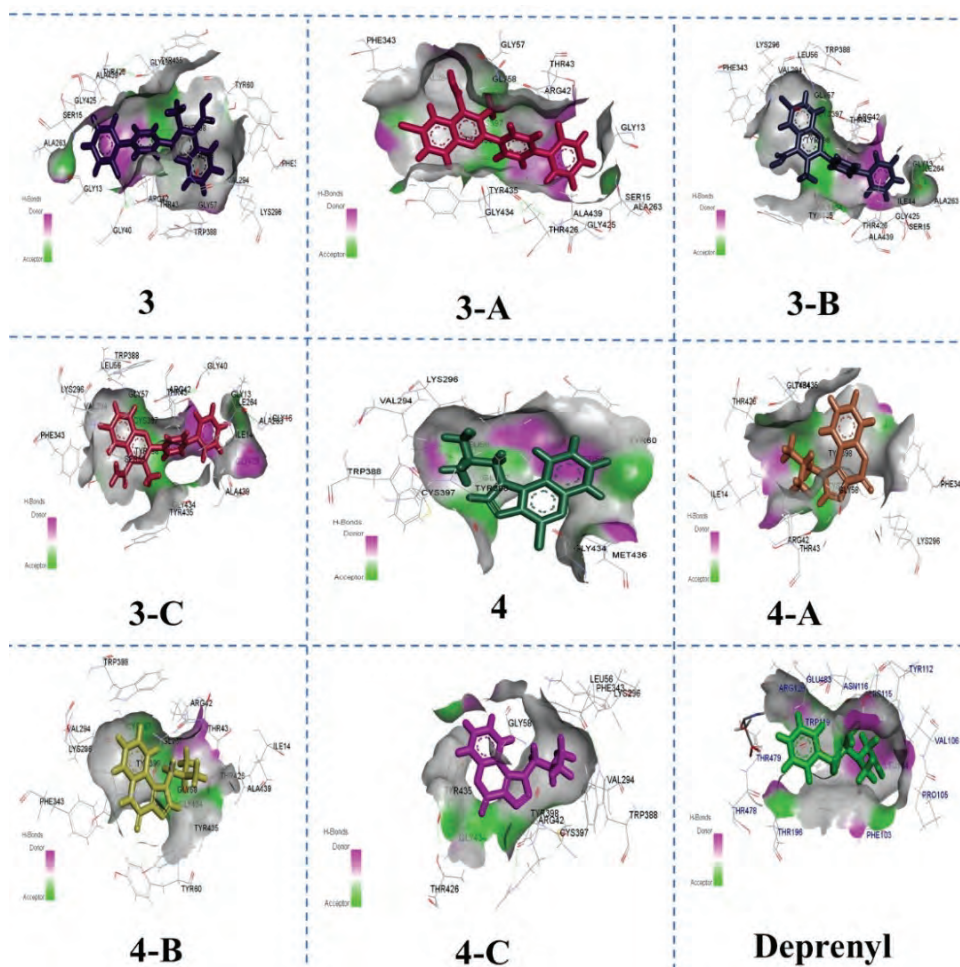
Fig. 7. 3D binding interactions of selected compounds within the active pocket of MAO-B.

–35.9 kJ/mol. The amino acid Ala439 formed alkyl interactions with the benzene ring. The π–π interaction was formed involving the amino acid Arg42 with the benzene ring. Similarly, the binding score of the derivative **3** is –34.9 kJ/mol formed amide–π stacked interaction involving the amino acid Gly57 with the substituted benzene ring. The amino acid Tyr398 formed π–π stacked interaction with the substituted benzene ring. The amino acids Met445 and Ala439 formed π-alkyl interaction with the substituted benzene ring. The π-cation interaction was formed involving the amino acid Arg42 with the benzene ring. The derivative **4-C** showed binding score –28.7 kJ/mol and formed interactions. The amino acid Tyr398 formed carbon hydrogen bond with the dimethylpropan. The amino acid Val294 and Arg42 formed alkyl and π-alkyl interaction with the

dimethylpropan and with the imidazole ring. The π-sulphur interaction was formed involving the amino acid Cys397 with the imidazole ring and similarly, the derivative **4**, which has the binding score –28.6 kJ/mol formed alkyl and π-alkyl interaction involving the amino acid Val294, Tyr398 and Met436 with the substituted benzene ring and with the imidazole ring. The derivative **7** has the binding score –28.5 kJ/mol formed carbon hydrogen bond with the amino acid Tyr398 with the hydrogen of dimethylpropan. The amino acid Gly57 formed amide-π stacked interaction involving the amino acid with the imidazole ring and the derivative **4-A** which has a binding score of –27.7 kJ/mol formed conventional hydrogen bond involving the amino acid Lys296 and the amino acid, which formed carbon hydrogen bond Tyr398, Arg42 with the oxygen of pyridine ring and with the hydrogen of imidazole ring.

SeeSAR Analysis. SeeSAR analysis of the best derivative **3-B** was executed which anticipate virtual display of binding interactions, Fig 8. Green colored coronas were used to favorably present structural elements of active compounds, whereas red colored coronas are used to present elements that had a negative
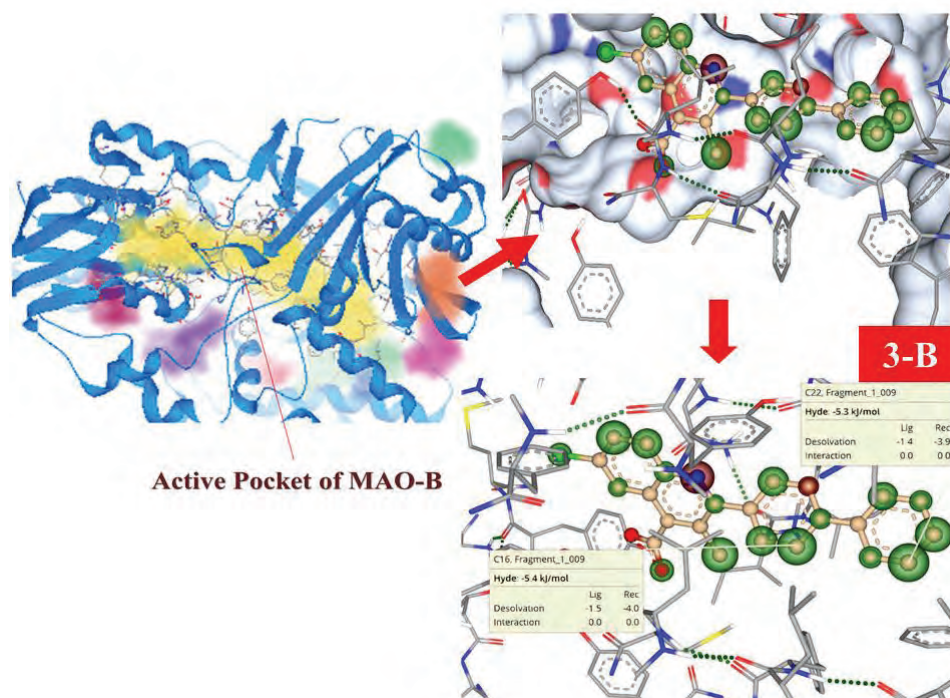
Fig. 8. Left: SeeSAR analysis of the active pocket of MAO-B. Right: showing docked conformations with coronas. Red colored coronas show unfavorable features whereas green colored coronas represent favorable contributions and colorless coronas are showing no contribution of structural components.

effect on binding interactions. A colorless corona was used to shade structural elements that made zero contribution. Corona size reflects the contribution of a structural element. SeeSAR visualizations of potent derivative **3-B** is given in Fig. 8. Hyde energies of favorable coronas (green colored) for **3-B** was –5.4 and –5.3 kJ/mol.

CONCLUSION

To identify new BChE inhibitors, which may serve as a potential lead candidate for the treatment of AD, the structure-based virtual screening method was used to examine the interactions between proteins and ligands. The PubChem database was filtered, and then screened for both AChE and BChE protein. Furthermore, their predicted inhibition constant values and binding energy values were both correlated. The results revealed that these compounds might serve as a foundation for the future development of novel BChE inhibitors.

SUPPLEMENTARY MATERIAL

Additional data and information are available electronically at the pages of journal website: https://www.shd-pub.org.rs/index.php/JSCS/article/view/12309, or from the corresponding author on request.

ИЗВОД

РАЧУНАРСКИ ПОТПОМОГНУТ ПРИСТУП ЗА ИДЕНТИФИКАЦИЈУ НАВОДЕЋИХ (*LEAD*) МОЛЕКУЛА ЗА ИНХИБИТОРЕ ХОЛИНЕСТЕРАЗА И МОНОАМИН ОКСИДАЗА: НОВЕ МЕТЕ ЗА ТРЕТИРАЊЕ АЛЦХАЈМЕРОВЕ БОЛЕСТИ

SYEDA ABIDA EJAZ[1], MUBASHIR AZIZ[1], AMMARA FAYYAZ[1], TANVEER A. WANI[2] и SEEMA ZARGAR[3]

¹Department of Pharmaceutical Chemistry, Faculty of Pharmacy, The Islamia University of Bahawalpur, Bahawalpur 63100, Pakistan, ²Department of Pharmaceutical Chemistry, College of Pharmacy, King Saud Univeristy, P.O.Box 2457, Riyadh 11451, Saudi Arabia и ³Department of Biochemistry, College of Science, King Saud Univeristy, P.O. Box 22452, Riyadh 11451, Saudi Arabia

Молекулски докинг је обећавајућа и поуздана технологија за откривање наводећих једињења путем виртуелног скрининга. Поред тога што дозвољава тестирање великог броја једињења, он такође допушта одређивање како одабрана једињења инхибишу циљани протеин/рецептор на бази оцењивачке функције и рангирања. Пошто селективни инхибитори холинестеразе и моноамин оксидазе играју критичну улогу у третирању Алцхајмерове болести, ово истраживање се фокусира на расветљавање механизма везивних интеракција неколико хинолинских деривата у активним местима холинестеразе (ацетил-холинестеразе (AChE) и бутирилхолинестеразе (BChE) и моноамин оксидазе (MAO) (моноамин оксидазе A & B). Као резултат ових открића, могуће је да се новоидентификовани инхибитори употребе као наводећа једињења у развоју нових инхибитора ензима за третирање специфичних болести, па тако омогуће развој нових терапијских приступа.

(Примљено 7. марта, ревидирано 26. јуна, прихваћено 14. августа 2023)

REFERENCES

1. J. M. Shine, E. J. Müller, B. Munn, J. Cabral, R. J. Moran, M. Breakspear, *Nat. Neurosci.* **24** (2021) 765 (https://doi.org/10.1038/s41593-021-00824-6)
2. I. Gülçin, A. Scozzafava, C. T. Supuran, Z. Koksal, F. Turkan, S. Çetinkaya, S. H. Alwasel, *J. Enzyme Inhib. Med. Chem.* **31 (**2016) 1698 (https://doi.org/10.3109/14756366.2015.1135914)
3. J. Patočka, K. Kuča, D. Jun, *Acta Med. (Hradec Kral.)* **47** (2004) 215 (https://actamedica.lfhk.cuni.cz/media/pdf/18059694.2018.95.pdf)
4. J. R. Atack, E. K. Perry, J. R. Bonham, J. M. Candy, R. H. Perry, *J. Neurochem.* **47** (1986) 263 (https://doi.org/10.1111/j.1471-4159.1986.tb02858.x)
5. B. Li, J. A. Stribley, A. Ticu, W. Xie, L. M. Schopfer, P. Hammond, O. J. Lockridge, *J. Neurochem*. **75** (2000) 1320 (https://doi.org/10.1046/j.1471-4159.2000.751320.x_)
6. C. N. Pope, S. Brimijoin, *Biochem. Pharmacol.* **153** (2018) 205 (https://doi.org/10.1016/j.bcp.2018.01.044
7. R. M. Geha, K. Chen, J. Wouters, F. Ooms, J. C. Shih, *J. Biol. Chem* **277** (2002) 17209 (https://doi.org/10.1074/jbc.M110920200)
8. J. Grimsby, K. Chen, L. J. Wang, N. C. Lan, J. C. Shih, *Proc. Nat. Acad. Sci.* **88** (1991) 3637 (https://doi.org/10.1073/pnas.88.9.3637)
9. R. M. Geha, I. Rebrin, K. Chen, J. C. Shih, *J. Biol. Chem.* **276** (2001) 9877 (https://doi.org/10.1074/jbc.M006972200)
10. J. Grimsby, N. C. Lan, R. Neve, K. Chen, J. C. Shih, *J. Neurochem.* **55** (1990) 1166 (https://doi.org/10.1111/j.1471-4159.1990.tb03121.x)
11. K. N. Westlund, R. M. Denney, L. M. Kochersperger, R. M. Rose, C. W. Abell, *Science* **230** (1985) 181 (https://doi.org/10.1126/science.3875898)
12. R. J. Castellani, R. K. Rolston, M. A. Smith, *Disease-a-Month* **56** (2010) 484 (https://dx.doi.org/10.1016%2Fj.disamonth.2010.06.001)
13. C. Geula, S. Darvesh, *Drugs Today* **40** (2004) 711 (https://doi.org/10.1358/dot.2004.40.8.850473)
14. M. Mesulam, A. Guillozet, P. Shaw, B. Quinn, *Neurobiol. Dis*. **9** (2002) 88 (https://doi.org/10.1006/nbdi.2001.0462)
15. E. Giacobini, *Int. J. Geriatr. Psychiatry* **18** (2003) S1 (https://doi.org/10.1002/gps.935)
16. S. Darvesh, *Curr. Alzheimer Res.* **13** (2016) 1173 (https://doi.org/10.2174/1567205013666160404120542)
17. Z. Cai, *Mol. Med. Rep.* **9** (2014) 1533 (https://doi.org/10.3892/mmr.2014.2040)
18. S. Manzoor, N. Hoda, *Eur. J. Med. Chem.* **206** (2020) 112787 (https://doi.org/10.1016/j.ejmech.2020.112787)
19. P. O. Patil, S. B. Bari, S. D. Firke, P. K. Deshmukh, S. T. Donda, D.A. Patil, *Bioorg. Med. Chem.* **21** (2013) 2434 (https://doi.org/10.1016/j.bmc.2013.02.017)
20. G. Nesi, S. Sestito, M. Digiacomo, S. Rapposelli, *Curr. Top. Med. Chem.* **17** (2017) 3062 (https://doi.org/10.2174/1568026617666170607114232)
21. L. Mucke, *Nature* **461** (2009) 895 (https://doi.org/10.1038/461895a)
22. L. Blaikie, P. Kay, P. K. T. Lin, *MedChemComm* **10** (2019) 2052 (https://doi.org/10.1039/C9MD00337A)
23. T. Tomašić, L. Peterlin Masic, *Curr. Top. Med. Chem.* **14** (2014) 130 (https://doi.org/10.2174/1568026613666131113153251)
24. J. H. Xu, Y. L. Fan, J. Zhou, *J. Heterocycl. Chem.* **55** (2018) 1854 (https://doi.org/10.1002/jhet.3234)

25. Chemical Computing Group, *M. O. E. Molecular Operating Environment*. Chemical Computing Group, Montreal, 2008

26. *BioSolveIT-SeeSAR* (https://www.biosolveit.de/SeeSAR).

SUPPLEMENTARY MATERIAL TO

Computer-aided approach for the identification of lead molecules as the inhibitors of cholinesterase's and monoamine oxidases: Novel target for the treatment of Alzheimer's disease

SYEDA ABIDA EJAZ[1]*, MUBASHIR AZIZ[1], AMMARA FAYYAZ[1], TANVEER A. WANI[2] and SEEMA ZARGAR[3]

[1]*Department of Pharmaceutical Chemistry, Faculty of Pharmacy, The Islamia University of Bahawalpur, Bahawalpur 63100, Pakistan,* [2]*Department of Pharmaceutical Chemistry, College of Pharmacy, King Saud Univeristy, P.O. Box 2457, Riyadh 11451, Saudi Arabia and* [3]*Department of Biochemistry, College of Science, King Saud Univeristy, P.O. Box 22452, Riyadh 11451, Saudi Arabia*

MOLECULAR DOCKING

AChE Results:

Table S-I: Binding Energy and bonding and non-bonding interactions of quinolone derivatives within the active pocket of AChE

Code	Binding Energy (kJ/mol)	Hydrophobic Interactions	H-Bond Interactions	Other Interactions
3	-21.8	His447 (π-alkyl)	-------	Trp86 (π-sigma), Gly120 (Halogen), Tyr123, Tyr337 (π lone pair), Glu202 (unfavorable acceptor-acceptor), Trp286, Asp74, Ser125, Pro88, Leu130, Ala127, Tyr133, Ile451, Gly122, Tyr341, Phe338, Phe297, Val294 (Van der Waals)
3-A	-20.8	Tyr119 (π-alkyl), Tyr133 (π-alkyl), Leu130 (π-alkyl)	His447 (Conventional H-bond)	Tyr123, Tyr337 (π lone pair), Trp86 (π-sigma), Trp286, Asp74, Ser125, Pro88, Leu130, Ala127, Gly448, Glu202, Tyr341, Phe338, Val294, Phe295 (Van der Waals)
3-B	-20.7	Tyr119 (alkyl),	His447	Tyr337 (π lone pair), Trp86 (π-

* Corresponding author. E-mail: abida.ejaz@iub.edu.pk; abidaejaz2010@gmail.com

		Tyr133 (alkyl), Leu130 (π-alkyl)	(Conventional H-bond)	sigma), Phe295, Val294, Tyr341, Asp74, Gly121, Ser125, Pro88, Gly126, Gly448, Ile451, Glu202, Phe338, (Van der Waals)
3-C	-22.3	--------------	Trp86 (Conventional H-bond) Gly126, Gly121 (C-H bond)	Tyr123, Tyr337 (π lone pair), Glu202 (halogen), Arg296, Trp286, Asp74, His447, Gly448, Ser203, Ile451, Leu130, Gly122, Tyr341, Phe338, Phe295 (Van der Waals)
4	-26.9	Trp86, Tyr337 (π-π stacked), Pro446 (alkyl), Trp439 (π-alkyl)	His447 (C-H bond)	Ile451, Glu202, Ser203, Tyr133, Gly122, Gly121, Asp74, Tyr341, Thr83, Tyr77 (Van der Waals)
4-A	-26.1	--------	Glu202, Gly126 (C-H bond)	Trp86 (π -sigma) Ser203, Tyr133, Gly120, Ala127, Leu130, Pro88, Asp74, His447, Gly448 (Van der Waals)
4-B	-25.6	Trp86, Tyr337 (π-π stacked),	Thr83 (C-H bond)	Asp74 (π-anion), Trp439, Gly82, Thr83, Asn87, Tyr124, Ser125, Gly121, Gly120, Ser203, Glu202, Ile451, Gly448, Tyr133, Tyr449 (Van der Waals)
4-C	-26.5	Trp86, Tyr337 (π-π stacked), Trp86 (π-alkyl)	------------	Thr83, Asp74, Tyr124, Gly121, Gly126, Gly120, Tyr133, Glu202 Ile451, Gly448, Pro446, Tyr449, Trp439, Gly82 (Van der Waals)
Huprine	-29.5	Trp86, Tyr337 (π-π stacked), His447 (alkyl), Trp439, Pro446, Tyr449 (π-alkyl)	Ser203 (C-H Bond)	Phe295, Phe297, Ala204, Gly122, Phe338, Gly121, Ser125, Tyr341, Ile451 (Van der Waals)

BChE Results:

Table S-II: Binding Energy and bonding and non-bonding interactions of quinolone derivatives within the active pocket of BChE

Code	Binding Energy (kJ/mol)	Hydrophobic Interactions	Hydrogen Bond Interactions	Other Interactions
3	-28.6	Gly116 (π- π T shaped), Trp82 (Amide π stacked), Ala328 (π-alkyl), Ser287 (Halogen)	-------	Tyr440, Gly439, Thr120, Gln119, Trp231, Val288, Gly117, Ser198, Phe328, Phe398, Ser79, Gly78, Trp430, Met437 (Van der Waals)
3-A	-26.5	Gly116 (Amide π stacked), His438 (π-alkyl)	Gly117, Ser198 (conventional H-bond)	Phe398, Ala199, Trp231, Phe329, Pro285, Ser287, Asn289, Gln119, Thr120 (Van der Waals)
3-B	-26.6	Gly116 (Amide π stacked), Val288 (π-alkyl), Ala277 (alkyl)	Ser198, Gly117 (conventional H-bond)	Asn289, Gln119, Thr120, Phe398, Ala199, Trp231, Leu286, Phe329 Van der Waals)
3-C	-29.3	Phe329, Trp231 (π- π T shaped), His438, Leu286 (π-alkyl)	Thr122, Tyr128 (conventional H-bond), Gly121 (C-H bond)	Trp82 (π-sigma), Glu197 (unfavorable acceptor-acceptor) Val288, Pro285, Gly116, Leu125, Gly115, Ile442, Gly439, Phe398 (Van der Waals)
4	-24.1	Tyr128 (π-alkyl)	--------	Trp82 (π-sigma), Tyr440, Ser198, Gl197, Gly116, Gly115, Thr122, Asn83, Thr120, Asp70 (Van der Waals)
4-A	-25.3	His438 (π-alkyl)	Tyr128(Conventional H-bond)	Ser198, Gly115, Thr122, Tyr114, Leu125, Pro84, Asn83, Thr120, Asp70, Gly439 (Van der Waals)
4-B	-25.2	Trp82 (alkyl),	Trp82, Tyr128	Ser198, Gly115,

Code	Binding Energy (kJ/mol)	Hydrophobic Interactions	Hydrogen Bond Interactions	Other Interactions
		His438 (π-alkyl)	(Conventional H-bond), Gly121 (C-H bond)	Leu125, Thr122, Asn83, Asp70, Gly116, Gly439 (Van der Waals)
4-C	-24.9	His438 (π-alkyl)	Gly121 (C-H bond)	Glu197, Ser198, Gly116, Gly115, Pro84, Asn83, Thr120, Asp70, Gly439 (Van der Waals)
Donepezil	-30.6	Gly121 (π-π stacked), Tyr337, Trp439 (Amide-π stacked)	Tyr83, His447, Glu202, Thr83 (C-H Bond)	Ile451, Asn87, Asp74, Tyr449, Ser125, Tyr124, Gly122(Van der Waals)

MAO-A Results:

Table S-III: Binding Energy and bonding and non-bonding interactions of quinolone derivatives within the active pocket of MAO-A

Code	Binding Energy (kJ/mol)	Hydrophobic Interactions	Hydrogen Bond Interactions	Other Interactions
3	-37.5	Trp397 (π- π stacked), Tyr444 (Amide-π stacked), Tyr407 (π-π stacked), Met445, Ala448 (π-alkyl),	Thr52 (Conventional H-bond) Ile23 (π-donor hydrogen bond)	Ser24, Gly434, Thr435, Gly66, Lys305, Phe352, Ala68, Gly50 (Van der Waals)
3-A	-37.5	Tyr407 (π- π stacked), Tyr407 (Amide-π stacked), Tyr407 (π-π stacked), Phe352, Cys406 (alkyl), Ala448 (π-alkyl Gly49 (halogen)	Arg51, Thr52 (Conventional H-bond) Tyr444 (H-bond donor)	Met445 (π-sulphur), Ala272, Ser24, Gly434, Thr435, Gln215, Val303, Lys305, Gly66, Gly67, Ile23 (Van der Waals)
3-B	-37.1	Gln215 (Halogen) Ala448 (alkyl), Cys406, Met445 (π-alkyl)	Tyr444 (C-H bond)	Arg51 (π-cation), Ala272, Ile273, Ser24, Gly434, Thr435, Ala68, Gly214, Gln74, Phe352, Lys305, Gly67 (Van der Waals)
3-C	-36.9	Trp397 (Amide-π stacked), Tyr407 (π-π stacked), Val303 (alkyl), Met445, Ala448 (π-	------	Arg51 (π-cation), Gly434, Ser24, Ala272, Gly49, Ile23, Thr52, Gly66, Lys305, Phe352, Ala68,

Code	Binding Energy (kJ/mol)	Hydrophobic Interactions	Hydrogen Bond Interactions	Other Interactions
		alkyl)		Gly443 (Van der Waals)
4	-30.3	Gly66 (Amide- π stacked), Arg51 (alkyl), Phe352 (π-alkyl)	Tyr407, Gly443 (C-H bond)	Gly67, Lys305, Gln215, Gly214, Tyr444, Ala448, Thr435, Ile23, Thr52 (Van der Waals)
4-A	-29.1	Gly66 (Amide- π stacked), Met445 (π-alkyl)	Tyr407 (C-H bond)	Cys406 (π-Sulphur), Ala448, Arg51, Ile23, Thr52, Gly67, Lys305, Phe352, Gln215, Gly214, Gln74, Thr435, (Van der Waals)
4-B	-28.4	Trp397 (Amide- π stacked), Gly66 (π-π T shaped), Arg51 (alkyl), Met445 (π-alkyl)	Gly67 (C-H bond)	Ala448, Thr435, Ile23, Thr52, Tyr444, Phe352, Tyr444, Thr52, Ile23, Thr435 (Van der Waals)
4-C	-29.5	Trp397 (Amide- π stacked), Gly66 (π-π T shaped), Arg51 (alkyl)	Tyr407, Gly443 (C-H bond)	Ile23, Lys305, Phe352, Gln215, Thr435, Aal448, Thr52, Ile23 (Van der Waals)
Clorgyline	-29.8	Lys102 (alkyl), Lys357 (π-alkyl)	Glu329, Asp328, Asn179 (C-H bond)	Arg172 (π-cation), Val101, Tyr175, Ile326, Glu185, Leu354, Ala355, Ser334 (Van der Waals)

MAO-B Results:

Table S-IV: Binding Energy and bonding and non-bonding interactions of quinolone derivatives within the active pocket of MAO-B

Code	Binding Energy (kJ/mol)	Hydrophobic Interactions	Hydrogen Bond Interactions	Other Interactions
3	-34.9	Tyr398 (π- π stacked), Trp338 (π- π T shaped), Gly57 (Amide-π stacked), Gly40 (Halogen), Ala439 (π-alkyl)	-------	Arg42 (π-cation) Ser15, Thr426, Gly58, Val294, Lys296, Phe343, Tyr60, Tyr435, Thr43, Gly13, Ala263, Gly425 (Van der Waals)
3-A	-36.7	Tyr398 (π- π stacked), Ala439 (alkyl), Cys397, Phe343 (π-	Gly58 (C-H bond), Arg42 (Conventional H-Bond)	Thr43 (π-cation), Gly13, Ala263, Ser15, Gly425, Thr426, Gly434, Thr435, Gly57, Val294

		alkyl)		(Van der Waals)
3-B	-36.9	Trp388 (π- π stacked), Tyr398 (π- π T shaped), Ala439 (alkyl), Lys296, Val294, Cys397, Phe343 (π-alkyl)	------	Arg42 (π-cation), Ala263, Ile264, Gly13, Ile14, Thr43, Gly57, Leu56, Tyr435, Gly434, Thr426, Gly425, Ser15 (Van der Waals)
3-C	-35.9	Trp388 (π- π stacked), Tyr398 (π- π T shaped), Ala439 (alkyl)	------	Arg42 (π-cation), Ala263, Ile264, Gly13, Ile14, Gly40, Gly57, Leu56, Val294, Lys296, Phe343, Ser59, Tyr435, Gly434, Gly425(Van der Waals)
4	-28.6	Val294, Tyr398 (alkyl), Met436 (π-alkyl)	---------	Cys397 (π-Sulphur) Gly57,Gly434, Ser59, Tyr60, Lys296, Leu56, Trp388 (Van der Waals)
4-A	-27.7	Tyr435 (π-π stacked), Cys397 (π-alkyl)	Lys296 (Conventional H-bond) Tyr398, Arg42 (C-H Bond)	Thr43, Ile14, Gly58, Phe343, Gly434, Thr426 (Van der Waals)
4-B	-28.5	Gly57 (Amide- π stacked), Trp388 (π-π T shaped), Lys296 (alkyl), Cys397 (π-alkyl)	Tyr398 (C-H bond)	Ile14, Tyr435, Gly58, Tyr60, Phe343, Val294, Arg42, Thr426, Ala439, Gly434, Thr43 (Van der Waals)
4-C	-28.7	Val294 (alkyl), Arg42 (π-alkyl)	Tyr435 (C-H bond)	Cys397 (π-sulphur), Thr426, Gly434, Gly58, Phe343, Lys296, Leu56, Trp388 (Van der Waals)
Deprenyl	-22.5	Phe103,Val106, Trp119, His115, Leu164 (alkyl), Tyr112 (π-alkyl)	---------	Glu483 (π-anion), Asn116, Thr196, Thr478, Thr479, Arg120 (Van der Waals)

The non-ideality in binary aqueous systems contributed to the different abilities of solvent entities incorporated in the solvation shell of methylene blue

SOKAINA S. HEMDAN[1]* and RADWAN ALNAJJAR[2,3]

[1]*Department of Chemistry, Faculty of Science and Art El Marj, Benghazi University, El Marj, Libya,* [2]*Department of Chemistry, Faculty of Science, Benghazi University, Benghazi, Libya and* [3]*PharmD, Faculty of Pharmacy, Libyan International Medical University, Benghazi, Libya*

Abstract: The solvatochromic properties of methylene blue (MB) were investigated in neat water, methanol, ethanol, propanol, dioxane and their corresponding aqueous mixtures. The correlation of the empirical solvent polarity scale (E_T) values of MB with solvent composition was analysed using the solvent exchange model of Bosch and Roses to explain the preferential solvation of the probe thiazine dye in the binary mixed solvents. Non-linear solvatochromism of MB was observed in aqueous mixtures of methanol, ethanol, propanol and dioxane. The influence of the composition of the solvating shell in preferential solvation of the solute dye was investigated in terms of both solvent–solvent and solute–solvent interactions, and the local mole fraction of each solvent composition in the cybotactic region of the probe was also calculated. Effective mole fraction variation can provide important physicochemical insights into the microscopic and molecular interactions between MB species and solvent components. The results showed that the MB solvation shell was thoroughly saturated with the solvent complex S_{12} for dioxane more than ethanol and propanol mixtures, and opposite trends for methanol mixtures, whereas the solvent complex S_{12} could not incorporate into the MB solvation shell. Data from the binary systems were analysed with KAT parameters using a dual model of basicity and polarity. The results showed that the polarity was better suited for spectral shift in aqueous methanol and ethanol solutions, while the basicity was better for aqueous propanol and dioxane solutions.

Keywords: thiazine dye; preferential solvation; aqueous-solvent aggregates; KAT scale.

195

HEMDAN and ALNAJJAR

INTRODUCTION

The term solvatochromism is used to explain the pronounced change in position and intensity of the visible absorption peak(s) due to the change of the polarity of the medium when absorption spectra are measured in neat solvents of different polarities.[1] It is found that in addition to the position of the absorption band of the dissolved chromosphere, the intensity and shape are also significantly affected by choice of different solvents, due to the different stabilization of their electronic ground state and excited states.[1] Solvatochromic dyes show significant shifts in absorption wavelength when dissolved in the different solvents.[2,3] The shift is hypsochromic when the shift is to lower wavelengths or bathochromic when the shift is to a longer wavelength. The electronic absorption of organic molecules usually changes when the molecules dissolve in different solvents. This change can also be seen as variations in the absorption spectra' intensity or shape.[4] Solvatochromism is a convenient and straightforward way to study solute–solvent interactions, showing the electrostatic and non-electrostatic solute––solvent interactions.[5,6]

The solution chemistry of binary solvent mixtures is used to understand the effect of the medium on solutes; those solutions can form new solvents with new properties that differ from the neat solvents.[7,8] However, several aqueous protic and aprotic solvent mixtures have similar macroscopic properties(*e.g.*, dielectric constant) but behave very differently from the solvation point.[9] Solute behaviour in binary solvent systems is more complicated than in pure solvents due to the preferential solvation (PS), in which the solute is solvated by one solvent more than the other.[10] Therefore, the solvation shell of the solute is completely saturated with an excess of the more polar solvent compared to the bulk composition, which is related to the preferential solvation. In other words, the preferential solvation occurs when a solute interacts with more molecules of one solvent component in its cybotactic region than the others, compared to the bulk composition. According to the explanation above, the preferential solvation is the key to understanding the solvation in solvent mixing processes. Furthermore, when the preference dominates to the extent that one component is effectively excluded from the solvation shell of the solute, it is called selective solvation.[10] Solvatochromism, which describes the spectral changes of a solute caused by a change in solvent polarity, provides a convenient way to monitor the interactions in the cybotactic region of a solute.[11] In particular, the electronic transition energy of a solute at the absorption maxima, called the polarity scale (E_T), includes all possible interactions between the solute and solvent components, including specific (such as hydrogen bonding and electron donor–acceptor interactions) and non--specific (polarity–polarizability effects) interaction.[12] The changes in absorption maxima follow the changes in solvent composition and E_T values can reveal the nature of the solute–solvent and solvent–solvent interactions in solvent mixing.

Consequently, a solute's E_T parameters can be manipulated to elucidate the preferential solvation phenomena in the mixtures. The $E_{T(30)}$ values for many binary mixtures of molecular and ionic solvents have various models. Both theoretical and experimental methods have been developed for the preferential solvation problem in the literature. Among the theoretical models, models such as the quasi lattice-quasi chemical theory, the Kirkwood–Buff theory, the dielectric enrichment developed by Suppan, the competitive preferential solvation theory of Nagy, and the stepwise solvent exchange model of Covington have been used successfully in a lot of papers.[13–15] The solvent exchange model has been proposed by Bosch and Roses to investigate the preferential solvation experimentally.[16] This model is an extension of Connors's stepwise solvent exchange model, which derives the equations that relate the E_T values of a solute with the solvent composition.[17] In this model, the competition between different solvent––solvent species to solvate the solute is described by some exchange equilibria near the solute.[17] An equilibrium constant, named the preferential solvation parameter, is defined for each exchange reaction, which relates the mole fraction of solvents in the solvation shell to that in the bulk mixture. In addition, the formation of solvating complexes is postulated from solvent-solvent interaction on the microsphere of solvation.

This work describes the solvatochromism of methylene blue in binary aqueous mixtures over the entire composition range, *i.e.*, from neat water to neat cosolvent. The solvents employed include methanol (MeOH), ethanol (EtOH), propanol (PrOH), dioxane and water, the structure of methylene blue, Fig. S-1 of the Supplementary material to this paper. The preferential solvation method was used to interpret the solute–solvent and solvent-solvent interactions. In addition, the spectral shift, λ_{max}, of methylene blue in binary aqueous mixtures was analysed with the linear solvation energy relationship model in two terms KAT parameters for all aqueous mixtures using the SPSS program to obtain more information about the sensitivity of methylene blue to the medium upon change of the mole fraction of cosolvents.

EXPERIMENTAL

Reagents and material

MB was purchased from Merck and applied without purification. The solvents employed, EtOH (96 %), MeOH (99.9 %), PrOH (99.8 %) and dioxane (99.8 %), were all analytical grade and were used without further purification. The used solvents have different polarities mainly related to the refractive index (n) and dielectric constant (ε) of each solvent, which was reported within the literature.[4] The KAT parameter values for all the aqueous organic mixtures used in this work were obtained from the values reported within the literature.[18]

Preparation of solutions and absorption spectra measurements

A 25±0.01 mg quantity of methylene blue was weighed separately and dissolved in some quantity of 96 % ethanol before making up to 25 mL volume in a 25 mL volumetric flask with

the same solvent to give 3.13×10^{-3} mol L^{-1} stock solution of methylene blue. This solution is homogenized and stored in a dark place. Binary mixtures of aqueous methanol, ethanol, propanol and dioxane were prepared by mixing in a volumetric flask the appropriate pure solvents in the volume ratios (water:cosolvent): 0:1.0, 0.2:0.8, 0.3:0.7, 0.4:0.6, 0.5:0.5, 0.6:0.4, 0.7:0.3, 0.8:0.2, and 1.0:0. Adequate equilibrations were allowed before using the solvent mixtures for sample measurements. 0.1 mL of dye stock solute was transferred in a volumetric flask of 10 mL and diluted up to volume by each of the studied binary mixtures in a volumetric flask of 10 mL. The mixtures were homogenized and left to equilibrate before measurement. The visible absorption spectral data were recorded in the appropriate neat solvent and binary mixtures with Cecil-CE 7400 (S.n.146368, England) UV–Vis spectrophotometer model cell, covering the wavelength extending 400–750 nm with a 1.00 cm quartz cell. The distilled water was obtained by using a Gambro distilled water device (AK95 S, Sweden).

Density functional theory (DFT) calculations

Density functional calculations were performed at different levels, including B3LYP[19] levels CAM-B3LYP[20], ωB97XD[21], APFD[22] and M062X[23] combined 6–31+G* basis sets. Further, a full geometry optimization calculation was carried out, followed by frequency calculation, to ensure minimal structures.[24] TD-DFT calculations were carried out in methanol, ethanol, propanol and dioxane. The solvent effects were included using the conductor-like polarizable continuum model (CPCM).[25] All calculations were conducted using Gaussian 16 software.[26]

Data analysis

The spectral characteristics of methylene blue were analysed in numerous binary aqueous organic solvents at a temperature of ~25 °C. The statistical linear regression was performed by using IBM-SPSS (a program of a statistical package of social sciences version 26) to determine coefficients by multiple linear regression techniques.

Preferential solvation (PS) model

Details related to applied model are given in the Supplementary material.

RESULTS AND DISCUSSION

Solvatochromism in binary aqueous systems related to neat solvents

The visible absorption spectra of methylene blue are recorded in several neat solvents with different HBD abilities. Fig. S-2 of the Supplementary material shows the spectra of methylene blue in the neat solvents used in this work. The spectrum in Fig. S-2 exhibits two bands, and the first band is broad and weak. The second band is strong in the wavelength range 650–665 nm, and their λ_{max} values are shifted to higher wavelengths as the dielectric constant of the solutions is increased.[28] The λ_{max} values of MB are red-shifted ($\Delta\lambda = 15$ nm) when proceeding from dioxane into water solvent. This may be described by the formation of ion-pair species, especially in HBA solvent dioxane with a low dielectric constant.[29] The solvation of MB in HBA solvent dioxane possibly occurs from ion––dipole interactions, whereas in HBD solvents, it is a result of the formation of hydrogen bonding interactions.[28]

Structure optimization, DFT calculations and nature of the frontier molecular orbitals

DFT calculations were used to study the behaviour of MB at a molecular level. The structure of the MB was optimized at B3LYP, CAM-B3LYP, WB97XD, APDF and M062x level of theory combined with a 6-31+G* basis set in the gas phase. The optimized structure is presented in Fig. 1, and critical bond lengths and angles are presented in Table I.
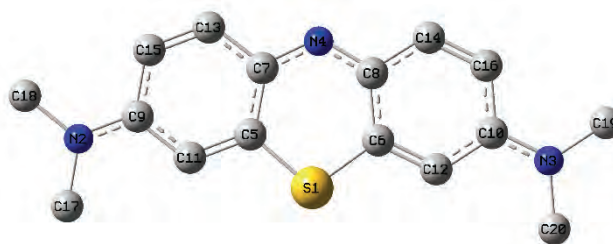
Fig. 1. The optimized structure of MB at B3LYP/6–31+G∗ in the gas phase.

TABLE I. Bond length (Å) and angle (°) at different levels using the 6-31+G* basis set in the gas phase

Bond	B3LYP	CAM-B3LYP	WB97xd	APFD	M062x	Exp[27]
S_1–C_6	1.7509	1.7377	1.7367	1.7372	1.7365	1.729
N_4–C_8	1.3357	1.3287	1.3299	1.3305	1.3302	1.336
N_3–C_{10}	1.3543	1.3458	1.3464	1.3479	1.3441	1.340
N_3–C_{20}	1.4654	1.4590	1.4585	1.4548	1.4592	1.472
C_5–S_1–C_6	103.3057	103.4491	103.4245	103.5806	103.3998	103.80
C_7–N_4–C_8	123.8177	124.0750	123.7826	123.6389	123.6826	123.04
C_{15}–C_9–N_2	120.8189	120.6845	120.6763	120.7437	120.5855	122.03
C_9–N_2–C_{17}	120.5398	120.4203	120.3433	120.5019	120.2480	121.61

As can be seen in Table I, most levels deviated from the experimental bond length of S_1–C_6 by around 0.1 Å, while B3LYP was the most accurate in predicting the C–N bond lengths. Regarding the thiazine ring angles, most levels were able to predict the angle with high accuracy with a deviation of 0.49, 0.35, 0.38, 0.22 and 0.40° observed in the C_5–S_1–C_6 angle for B3LYP, CAM-B3LYP, WB97xd, APFD and M062x, respectively. In the case of the C–N–C angles, most levels predict it with less than 1.00° deviation except for CAM-B3LYP, where a variation of 1.04° was observed.

Using larger bases set (Table II) results in better prediction of the bond lengths, with a deviation in S–C bond of 0.0219, 0.0218 and 0.0206 Å for 6-31+G*, 6-31++G** and 6-311++G**, respectively. In addition, the bond angles in the thiazine ring were predicated more accurately, the C_5–S_1–C_6 angle

predicated to be 103.332° in the case of 6-311++G** which deviates 0.4676° from the experimental finding.

TABLE II. Bond length (Å) and bond angle (°) at B3LYP levels using various basis sets in the gas phase

Bond	6-31+G*	6-31++G**	6-311++G**	Exp[27]
S_1–C_6	1.7509	1.7508	1.7496	1.729
N_4–C_8	1.3357	1.3357	1.3328	1.336
N_3–C_{10}	1.3543	1.3541	1.3515	1.340
N_3–C_{20}	1.4654	1.4655	1.4650	1.472
C_5–S_1–C_6	103.3057	103.3195	103.3324	103.80
C_7–N_4–C_8	123.8177	123.8200	123.9202	123.04
C_{15}–C_9–N_2	120.8189	120.7931	120.7988	122.03
C_9–N_2–C_{17}	120.5398	120.5666	120.6147	121.61

Following the optimization step, time-dependent (TD) DFT was implemented to study the electronic spectra of methylene blue at molecular levels. TD-DFT calculations were carried out at the same levels as the optimization process, and the obtained results are presented in Table III.

TABLE III. The vertical transitions of methylene blue in nm calculated at various DFT levels with 6-31+G* basis set in the gas phase

DFT level	Bond					
	S_0–S_1	S_0–S_2	S_0–S_3	S_0–S_4	S_0–S_5	S_0–S_6
B3LYP	500.61	473.89	382.81	340.49	325.71	289.68
CAM-B3LYP	472.55	412.84	352.62	288.31	286.31	251.90
WB97xd	473.21	412.39	356.17	288.49	282.01	262.01
APFD	492.13	462.05	377.39	331.15	315.38	274.69
M062x	474.13	411.76	369.73	284.84	283.31	262.95
Exp	660					

As can be seen in Table III, the first excited state (S_0–S_1) has the highest oscillator strength, which corresponds to the observed λ_{max}. The deviation in λ_{max} was too high, which indicates that DFT could not reproduce the experimental UV spectra. However, adding the chlorine atom and reoptimizing the structure at B3LYP/6-31+G* in the gas phase incapacitated this deviation, Fig. 2.

The obtained electronic spectra agreed with the experimental finding; the λ_{max} shifted from 500 nm when the chlorine atom was absent to 670 nm in the presence of the chlorine atom, as it can be seen in Fig. 3.

Once a spectrum that is most in agreement with the experimental spectra in the gas phase was obtained, the solvation effect was implemented via the conductor-like polarizable continuum model (CPCM). The obtained electronic spectra are presented in Table IV.
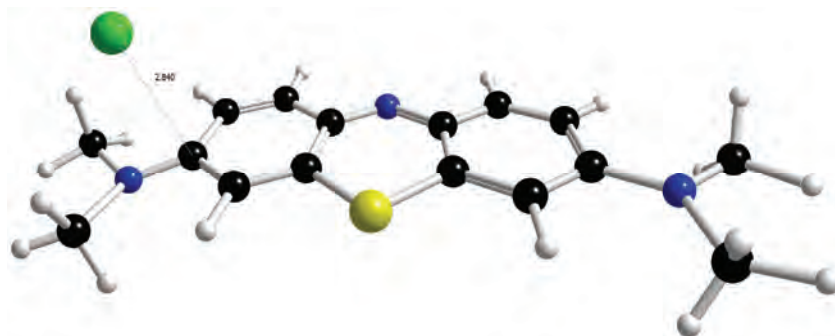
Fig. 2. The optimized structure of MB-Cl at B3LYP/6–31+G* in the gas phase.
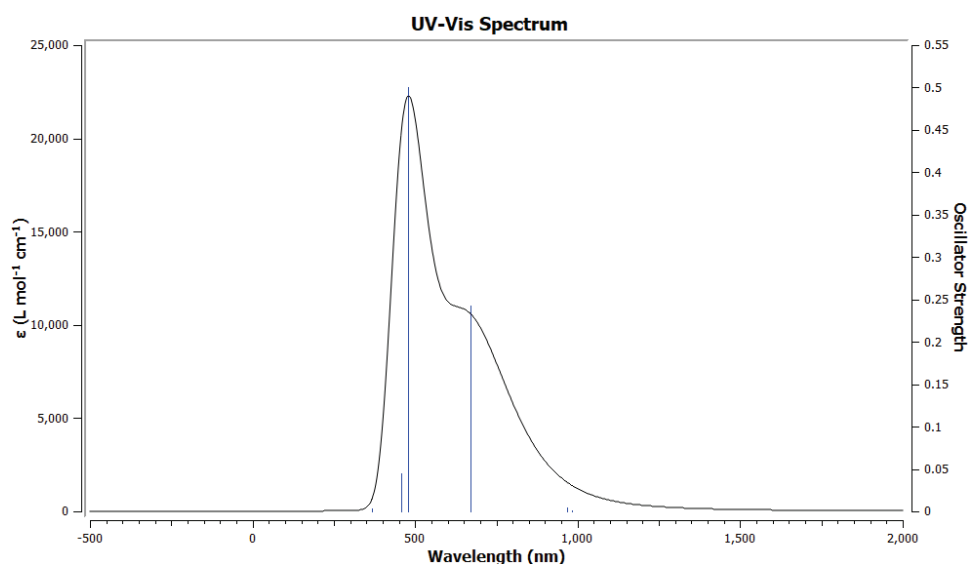
Fig. 3. The electronic spectra of MB-Cl optimized at B3LYP/6-31+G* in the gas phase.

Interestingly, once the solvent effect was implemented, the effect of the chlorine atom disappeared, and the absorption spectra were in the range of 523 to 547 nm. Most electronic spectra come from the first transition S_0–S_1, corresponding to HOMO-1 to LUMO+1, HOMO to LUMO and LUMO to HOMO, Fig 4.

The maximum electronic transition energy values, E_T, of methylene blue are calculated as:

$$E_T = hcN_A/\lambda_{max} = 119626.8/\lambda_{max} \text{ (in nm) kJ/mol} \qquad (1)$$

For investigated solvents and their binary aqueous mixtures, the values are listed in Table V. In fact, the electrostatic and non-electrostatic interactions between the solute and solvent molecules are included in the E_T values. The absorption maxima again shift to shorter wavelengths when the percentages of

the organic solvents increase in their aqueous binary mixtures, Table V. The changes are probably the result of the intermolecular solute–solvent interaction forces when the dielectric constant of the solutions decreases.

TABLE IV. The electronic spectra of methylene blue calculated in selected solvents at B3LYP/ 6-31+G* level

Solvent		Bond					
		$S_0–S_1$	$S_0–S_2$	$S_0–S_3$	$S_0–S_4$	$S_0–S_5$	$S_0–S_6$
Gas	MB	**500.61**	473.89	382.81	340.49	325.71	289.68
	MB–Cl	981.92	968.46	**670.93**	479.83	456.86	367.72
H_2O	MB	**536**.16	490.53	368.96	344.03	326.47	294.27
	MB–Cl	**536.72**	490.70	459.74	458.75	458.62	368.45
MeOH	MB	**535.79**	490.09	368.96	343.39	326.11	285.01
	MB–Cl	**536.75**	491.56	474.54	474.09	473.18	368.57
EtOH	MB	**537.75**	490.37	369.19	343.54	326.14	294.18
	MB–Cl	**538.81**	492.80	482.69	482.35	480.63	368.73
PrOH	MB	**539.12**	490.55	369.39	343.65	326.15	285.03
	MB–Cl	**547.07**	498.76	487.25	486.06	477.61	368.19
Dioxane	MB	**536.88**	485.69	376.43	343.50	326.21	293.51
	MB–Cl	959.77	952.96	918.85	**532.95**	483.07	369.42
Exp				660			
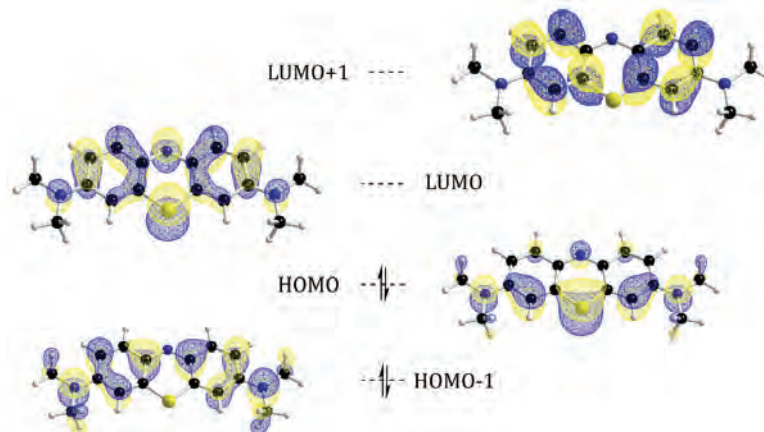
Fig. 4. The frontier orbitals of the MB optimized at B3LYP/6-31+G* in the gas phase.

TABLE V. Preferential solvation parameters of methylene blue in different aqueous binary mixtures at room temperature 25 °C; $E_1 = 179.89$ kJ mol^{-1}

Mixture	E_2 / kJ mol^{-1}	E_{12} / kJ mol^{-1}	$f_{2/1}$	$f_{12/1}$	$f_{12/2}$
H_2O–Dioxane	184.04	180.32	0.621	8.423	13.57
H_2O–PrOH	182.63	179.96	5.846	8.460	1.447
H_2O–EtOH	182.63	177.85	10.89	4.945	0.454
H_2O–MeOH	182.63	180.00	1.944	0.000	0.000

Fig. 5 presents the calculated E_T values of MB as a function of the mole fraction of the organic solvents. The ideal solvation behaviour of the mixtures can also be seen in the figure by the dashed line. Ideally, there is no preferential solvation between the solute and solvent molecules, and the composition of the solvent in the cybotactic region of the probe is the same as in the bulk solution. The apparent deviation from the linearity of E_T as a function of the mole fraction of the organic solvents shown in Fig. 5 can be interpreted as a preferential solvation of the probe by one of the components of the mixtures. Preferential solvation results from differences between the immediate surroundings of the solute and the bulk composition of the mixture. In fact, the non-linear behaviour of the E_T plots is due to the selective enrichment of a specific solvent species in the cybotactic region of the probe. The selective solvation results from the differences in the specific and non-specific interactions between the solute molecules and each of the solvent components.
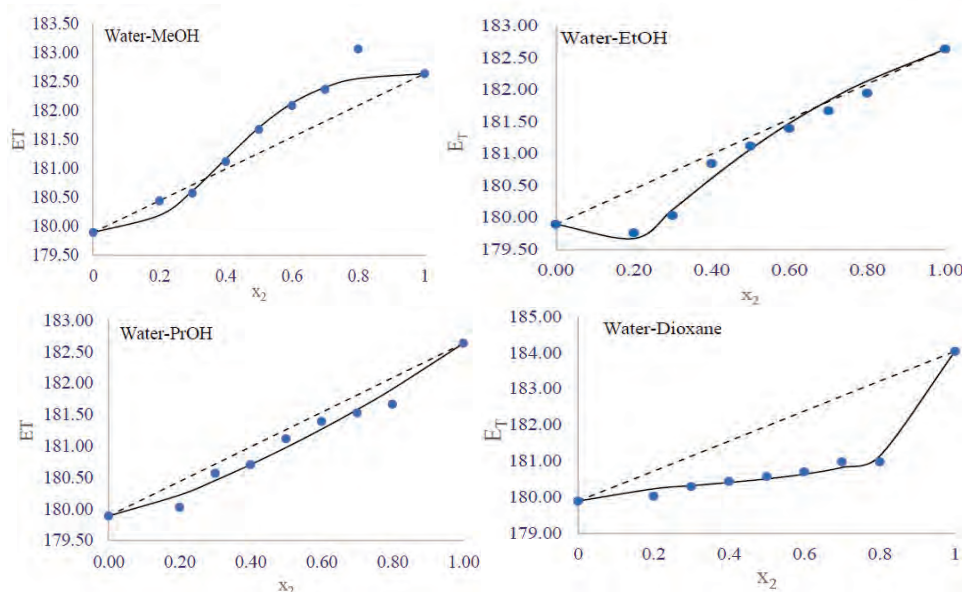
Fig. 5. Plots of the experimental and calculated E_T of MB versus the mole fraction of organic solvent: experimental values (filled circle), calculated values (solid line) and ideal values (dashed line).

The dependence of the E_T values of MB on the mole fraction of organic solvents shown in Fig. 5 are almost the same but with a significant difference from the dioxane values except for aqueous MeOH mixtures. The curves of MB E_T values show two different patterns, one in aqueous solutions of ethanol, propanol and dioxane and the other in water–MeOH mixtures. The E_T values for MB in

water with mixtures of ethanol, propanol and dioxane indicate selective solvation with the organic solvents. A negative deviation indicates that the MB is preferentially solvated in the solvent entities with a lower corresponding E_T. Regarding this account, the MB molecules are preferentially solvated by the organic solvent and the water–organic complexes resulting from solvent–solvent interactions. On the other hand, The E_T values have a sigmoidal dependence on the mole fraction of the organic solvent in water–MeOH mixtures. These observations indicate that in the water-rich region, MB molecules are preferentially solvated by water, while in the methanol-rich region, the MB molecules are selectively solvated with methanol molecules. In Fig. 5 there is a negative deviation from neat water up to $x_2 = 0.3$, Fig. 6, the local mole fractions of methanol in this region are lower than in water, indicating that MB is preferentially solvated by water due to hydrophobic hydration around the aromatic rings and methyl groups contributes to the negative deviation in methanol mixtures, this result is in agreement with results reported by Chen *et al*.[30] In Fig. 6, the compositions $0.3 < x_2 < 1$, the local mole fractions of methanol are greater than the values of water, leading to positive deviation, indicating that MB is preferentially solvated by methanol. The effect of cosolvents in increasing the solubility of the solute can be related to the disruption of the ordered structure of water around the polar moiety of methylene blue.
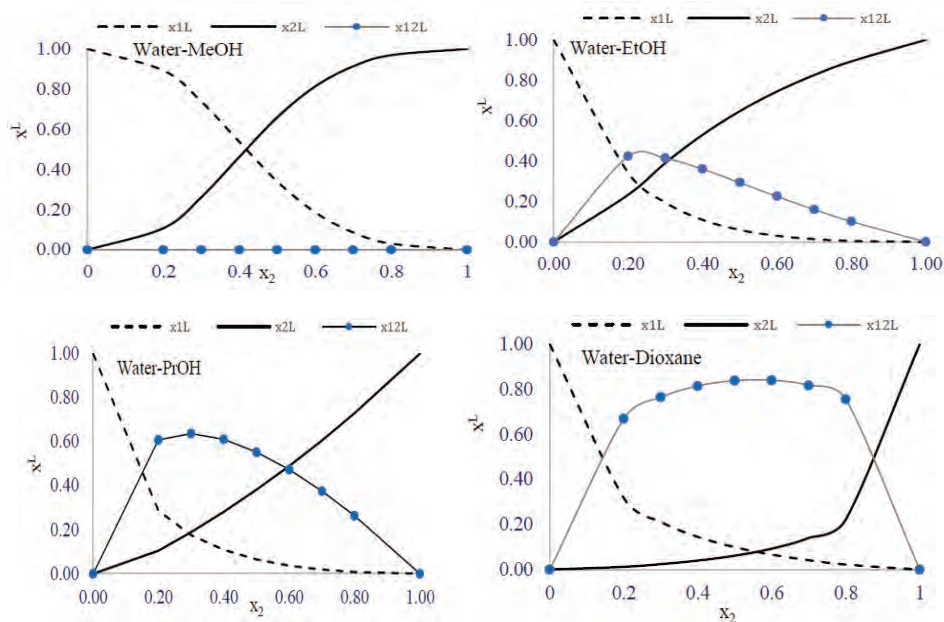
Fig. 6. Local mole fractions in the solvation shell of MB in various aqueous–organic systems at room temperature 25 °C.

Thus, the difference between the methanol, ethanol and propanol in the curve is reflected in the difference in the hydrogen bond donor (α), hydrogen bond acceptor (β) and hydrophobic properties of alcoholic solvents. Methanol is a higher hydrogen bond donor (0.93) and weaker hydrogen bond acceptor (0.62) than ethanol ($\alpha = 0.83$, $\beta = 0.77$) and propanol ($\alpha = 0.84$, $\beta = 0.85$). The hydrophobicity of ethanol and propanol is also higher than that of methanol. Thus, ethanol, in comparison with methanol, has a much greater tendency to solvate acidic and hydrophobic molecules such as MB, which preferentially occurs in water-rich environments. This means that when methanol is replaced by ethanol or propanol, the preferential solvation of the solute increases to more extent by an alcoholic solvent. In other words, in the HBD solvents, the hydrogen bonds between the dimethyl amino group of the dye and, thus, the OH group in the solvents play an important role in the solvation of the dye. The interaction of the hydroxyl solvent with other components of the mixture can lead to the formation of hydrogen-bonded complexes that solvate the less polar part of the dye, *i.e.*, alkyl groups present in the solvents.[31] Based on the strong interaction between the dioxane and water molecules, the behaviour of the mixture is different compared to water–alcohol solutions. The hydrogen bond between dioxane and water molecules is stronger than water–water. The presence of dioxane molecules significantly destroys the net structure of water, and therefore, water-dioxane complexes are the dominant species in the preferential solvation of the solute over the whole range of mole fractions of dioxane, Fig. 6.

Analysis of data in binary aqueous systems by the preferential solvation parameters

To describe the solvation, we need to consider the preferential solvation parameters listed in Table V. The preferential solvation parameters, $f_{12/1}$ and $f_{2/1}$, show the tendency of the solute to be solvated by S_{12} and S_2 in preference of the solvent S_1, respectively, and the $f_{12/2}$ parameter measures the preferential solvation of the solute by S_{12} relative to solvent S_2. If $f_{12/1}$ and $f_{12/2}$ are higher than unity, then this will demonstrate that the solute tends to be solvated by S_{12} (water–organic solvent complex) rather than by the pure solvents.[32]

Observing the results in Table V for the MB in the alcoholic solutions, the results show that the $f_{2/1}$ parameter is higher than unity in the order ethanol > propanol > methanol, suggesting that the MB molecules are preferentially solvated with alcohol molecules and water–alcohol complexes formed by solvent––solvent interactions. The value of $f_{2/1}$ is higher than $f_{12/2}$ in aqueous mixtures of ethanol and propanol, indicating that the order of preferential solvation in these mixtures is $S_2 > S_{12} > S_1$. In addition, the parameter $f_{12/1}$ is greater than $f_{12/2}$, which indicates that the nature of the complex is closer to that in water than in alcohols for ethanol and propanol mixtures. The local mole fraction of the com-

plex solvent reaches a maximum of approximately x_2 in aqueous mixtures of 0.2–
–0.3 ethanol and 0.2–0.5 propanol. As it can clearly be seen in Fig. 6, the solvat-
ion shell of MB is fully saturated with protic solvent and a complex solvent over
the whole composition range. This result is consistent with the molecular struc-
ture of MB, Fig. S-1, because MB has several amino groups in its structure,
which makes the solute able to protonate from the solvent by forming HB with
amino groups. Therefore, the values of $f_{12/1}$ and $f_{12/2}$ in aqueous propanol sol-
utions are higher than in aqueous ethanol solutions, indicating that the water–
–propanol complex plays a significant role in the solvation of the probe.

A different scenario is observed for water–MeOH mixtures with zero values
of $f_{12/1}$ and $f_{12/2}$. These results indicated that the solvated complex species
formed by water–methanol interaction could not be incorporated into the solvat-
ion shell of MB with respect to the methanol and water. As mentioned, the hyd-
rogen bond between the lone pair electrons of nitrogen and the hydrogen bond
donor of the solvent cause its unstable form. In this case, the solvation of MB is
favoured thermodynamically in solvents with lower hydrogen bond donor capac-
ity. Based on this result, the water–MeOH aggregates have better hydrogen don-
ating ability than MeOH, because E_{T12} is close to E_{T1}, indicating that the com-
plex is closer in nature to water than to methanol; thus, the preferential solvation
by MeOH molecules is favoured in MeOH-rich region. Therefore, as indicated
by the preferential solvation parameters, the preferential solvation extent of MB
increases as the solvent becomes less of a hydrogen bond donor.

In the case of dioxane as an aprotic solvent (HBA), $f_{2/1}$ has a small value,
and $f_{12/1}$ and $f_{12/2}$ are higher than unity, Fig. 6. However, the E_T values of the
MB have a negative deviation depending on the dioxane mole fraction, Fig. 5. In
this case, the $f_{12/2}$ has the highest value and is significantly different from the
other preferential solvation parameters. This observation indicates that in the
water-rich region, the MB molecules are preferentially solvated by water mole-
cules, while in the dioxane-rich region, the MB molecules are mainly solvated by
the dioxane–water complex molecules. Also, the higher value of $f_{12/2}$ than $f_{12/1}$
indicates that the nature of the dioxane–water complex molecules is closer to
dioxane than to water molecules. The preferential solvation order of aqueous
dioxane solutions is $S_{12} > S_2 > S_1$. These results, supported by the local mole
fraction of the complex solvent, reach a maximum between the range of 0.2 and
0.8. As shown in Fig. 6, the solvation shell of MB is fully saturated with the sol-
vent complex and dioxane over the whole composition range. Table I shows that
the E_T values of S_{12} (E_{12}) are lower than the E_{T2} and higher than the E_{T1} in
aqueous dioxane mixtures, indicating that the β-basicity of the solvated species
increases in the order $S_{12} > S_2 > S_1$. Therefore, in the competition between S_2
and S_{12}, the MB molecules preferentially interact with S_{12} due to stronger hydro-
gen bonding interactions, resulting in the $f_{12/2} > 1$. This means that in the dioxane

binary mixture, the difference between the basicity of S_2 and S_{12} confirms the increasing order of the $f_{12/2}$ shown in Table V.

Analysis of spectral data in binary aqueous systems with the KAT polarity scale

The changes of the obtained E_T values with the solvents used, Table V, reveal that the solute–solvent interactions between the methylene blue and the solvent molecules depend on specific and non-specific interactions. The method introduced by Kamlet, Abboud and Taft (KAT) is used to quantify these interactions.[33] This approach has been successfully applied in correlation analysis of all kinds of solvent-dependent processes.[4] The multi-parametric KAT equation has been introduced in previous reports:[9,15,18]

$$E_{T(MB)} = E_{T(o)} + a\alpha + b\beta + s\pi* \tag{2}$$

Where $E_{T(o)}$ represents the regression value, the $\pi*$ is the index of the solvent dipolarity/polarizability, which is a measure of the ability of a solvent to stabilize a charge or a dipole by its dielectric effects. The α coefficient represents the solvent hydrogen-bond donor (HBD) acidity. In other words, it describes the ability of a solvent to donate a proton in a solvent to a solute hydrogen bond. The β coefficient is a measure of solvent hydrogen-bond acceptor (HBA) basicity and describes the ability of a solvent to accept a proton from a solute molecule. The regression coefficients *a*, *b* and *s* measure the relative susceptibilities of the solvent dependence of E_T. The E_T values were correlated with solvent properties by means of single, dual and multiple regression analysis by a suitable computer program.[18] Gauss–Newton non-linear least-squares method in the computer program is used to refine the values of E_T by minimizing the error squares sum:

$$U = (E_{T,exp} - E_{T,cal})^2 \tag{3}$$

The number of terms in the KAT equation used to correlate the studied property depends on the significance of the solute–solvent interactions.

In the study, several attempts are made to find the best form of the KAT equation to describe the variation of E_T values in the water–organic solvent mixtures. So, a stepwise procedure and least squares analysis were applied to select the significant solvent properties to be influenced in the model and to obtain the final expression for E_T. Therefore, the KAT equation was used as single, dual and multi-parameter forms for correlation analysis of E_T in various solvent mixtures. The computer program used can also give the values of $E_{T(o)}$, *a*, *b*, *s* and some statistical parameters, including the r^2 coefficient, uncertainty value of each parameter (given in brackets) and residual sum of squares (*rss*). The KAT parameter values for all the aqueous organic mixtures used in this work were obtained from the values reported in the literature[18] and are listed in Table S-I.

The most significant resulting regression equations describing the correlation between E_T and the KAT parameters for MB are shown in Table VI.

TABLE VI. Coefficients of LSER equation for MB in the binary systems and statistical parameters; *b* and *s*: coefficients; *R*: correlation coefficients; *F*: Fisher number; *p*: the probability of variation; *SD*: standard deviation; *rss*: residual sum of squares

System	$E_{T(o)}$	*b*	*s*	*R*	*F*	*SD*	*rss*	*p*
Water–dioxane	189.09±1.49	–9.80±2.28	–3.383±0.77	0.92	17.10	0.55	1.8	3×10^{-3}
Water–PrOH	180.61 ±1.08	3.596±0.89	–2.191±0.55	0.99	157.8	0.14	0.1	6×10^{-6}
Water–EtOH	185.54±0.96	–0.480±1.05	–5.080±0.41	0.99	167.1	0.15	0.1	5×10^{-6}
Water–MeOH	184.27±1.39	3.176±1.54	–5.319±0.72	0.97	42.76	0.32	0.6	3×10^{-4}

The analysis of the absorption bands in neat solvents by KAT parameters was conducted to find the best descriptive model. The multi-parametric analysis, including α, β and π^* terms by using LSER is shown in Eq. (4), with a correlation coefficient, $r = 0.999$) and the highest F-value = 955.002:

$$E_{T(MB)} = 188.251 - 0.552\alpha - 2.40\beta - 6.043\pi^* \qquad (4)$$

From the analysis of the result in Eq. (4), the hydrogen bonding acceptance ability and the dipolarity/polarizability are more evident for the spectral shift. A significant contribution of α to MB solvatochromism is not observed alone or in combination with other terms. The negative sign and the magnitude of β and π^* in Eq. (4) show that both solvent dipolarity/polarizability and hydrogen-bonding basicity affect the spectral shift with different strengths. Based on this result, the dual-parametric KAT-LSER is the best descriptive model with β and π^* parameters in all binary mixtures. Compared to Eq. (4), the regression coefficients are changed, and the correlation coefficient decreased, especially for aqueous dioxane mixtures, due to the complexity of interactions between the solute and the solvent molecules in the mixed solvents. The main contributions to this complexity stem from the non-ideality of the solution due to solvent–solvent interactions and the preferential solvation due to different interactions of the solute with solvents in each mixture. The analysis of the coefficients in Table VI shows that the spectrum shifts becomes more sensitive to the value π^* of the medium in aqueous methanol and ethanol mixtures, while in aqueous propanol and especially in aqueous dioxane mixtures, the effect of β becomes more evident. It should be noted that the magnitude of the coefficients for aqueous methanol, ethanol and propanol differs from that in Eq. (4) for mono-solvents; the correlation coefficient of the KAT-LSER model was found to be greater than 0.96. The spectral change in this mixed solvent turns out to follow a linear relationship with the polarity (explained by β and π^*) similar to that of mono-solvents. These observations indicate that the nonlinearity in the spectral shifts, when plotted as a function of mole fraction, is due to the non-ideality of the polarity of these binary systems,

rather than to the preferential solvation with a single solvent. For more clarification, we use β and π^* of binary mixtures present to calculate E_T as a function of composition using Eq. (2). Non-ideality of mixtures is reflected in the compositional dependence of β and π^* of mixtures; therefore, Eq. (2) gives an estimation of the solute's spectral response to solvent composition change when the polarity of solvation shell and bulk is the same as the result of the absence of preferential solvation. When plotting the observed E_T against the estimated values from Eq. (2) in Fig. 7. Clearly, high linear correlations ($r^2 = 0.93$) with a slope close to unity and intercept close to zero are obtained between two sets of data in methanol, ethanol, and propanol binary systems. This evidence shows that the polarity of the solvation shell experienced by the solute differs just slightly from that of the bulk, which in turn results in insignificant compositional differences between the local and bulk environments.[34] This result is in discordance with the one obtained from solvation model analysis, which reveals the significant contribution of preferential solvation to solvatochromism in water with methanol, ethanol and propanol binary mixtures. The latter is well justified by $f_{2/1} = 1.944$, 10.89 and 5.896, respectively, calculated by the proposed model in this work, which shows very high preferential solvation by cosolvents. Fig. 7 displays a notable departure from the bisector line that is directly indicative of the occurrence of preferential solvation in the case of the dioxane binary system. As the main result, the non-ideality of solvent mixtures has a significant influence on the
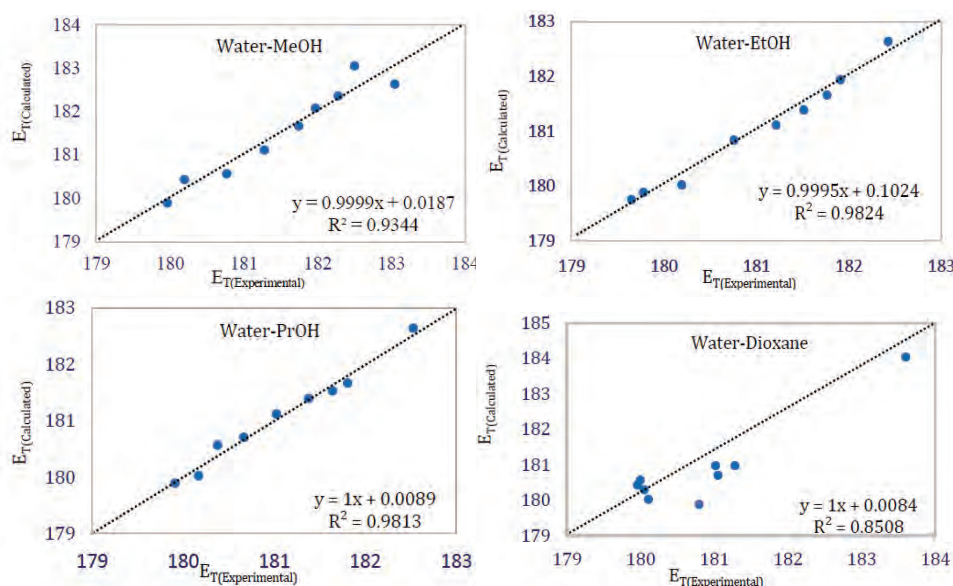
Fig. 7. Plots of correlation of the observed E_T with the estimated E_T using Eq. (2) in the absence of the solute's preferential solvation in aqueous mixtures of methanol, ethanol, propanol and dioxane at 25 °C, dotted lines show the bisector of the first quadrant.

spectral response of the solute related to the local composition and the preferential solvation from the analysis of non-linear solvatochromism. Finally, from Table VI, it is noted that the sign of π^* coefficient is negative in all binary systems, indicating the negative polarity contribution to the spectral shift of MB by a strong contribution of hydrogen bonding interaction of MB with the solvent entities. Interestingly, the β coefficient also has a positive sign in some binary systems, unlike the sign in mono solvents. This unexpected result originates from the different forms of interactions in mixed solvents because the interactions in mixed solvents are more complex than those in pure solvents.

CONCLUSIONS

The spectroscopic behaviour in binary solvent mixtures was analysed using the preferential solvation approach. The obtained results show that the λ_{max} values were blue-shifted to shorter wavelengths as the relative permittivity of the solutions decreases. Although the hydrogen bonding donor acidity of water is highest among the mixture constituents, the downward curvature of the E_{T12} value *versus* the analytical mole fraction of cosolvents indicates that the MB is more solvated by the cosolvent components except in methanol mixtures. It was discussed whether the self-association of water molecules to make network structure is responsible for the reduction of the water affinity to compete with the other solvating species. The solvent exchange model was perfectly fitted to the observed E_T values. The preferential solvation parameters were calculated from the model. The results demonstrate that the solution behaviour of MB in the studied mixtures can be adequately explained by the competition of solvating species to interact with the MB through hydrogen bonding interactions. In a water–methanol mixture, the affinity of S_2 and S_1 to the solvation of MB is $S_2 > S_1$, whereas S_{12} species do not play a role in the solvation of MB, while in the ethanol and propanol mixtures, the solvent species preferentially solvates the solute in order $S_2 > S_{12} > S_1$. In the case of water with dioxane, a different order is observed: $S_{12} > S_2 > S_1$ over the whole range composition.

The molar transition energy of MB in different binary mixtures was analysed in terms of the KAT equation. Dual-parameter correlations showed better results in the HBD solvents and dioxane as HBA solvents, respectively. The correlation of E_{T12} with the KAT parameters showed that the polarity/dipolarity which had more impact in the case of aqueous methanol and ethanol mixtures was responsible for the solvatochromism observed in the absorption spectra of MB, whereas the hydrogen bond accepting ability in the case aqueous of propanol and dioxane mixtures was more responsible for the solvatochromism observed in the absorption spectra of MB. A dramatic deviation from linearity in solvatochromism was observed, which is mainly due to the combined effect of solution non-ideality and preferential solvation.

SUPPLEMENTARY MATERIAL

Additional data and information are available electronically at the pages of journal website: https://www.shd-pub.org.rs/index.php/JSCS/article/view/12388, or from the corresponding author on request.

ИЗВОД

ДОПРИНОС НЕИДЕАЛНОГ ПОНАШАЊА БИНАРНИХ ВОДЕНИХ СИСТЕМА РАЗЛИЧИТИМ СВОЈСТВИМА РАСТВАРАЧА ИНКОРПОРИРАНИХ У СОЛВАТАЦИОНУ ЉУСКУ МЕТИЛЕНСКО ПЛАВОГ

SOKAINA S. HEMDAN[1] и RADWAN ALNAJJAR[2,3]

¹Department of Chemistry, Faculty of Science and Art El Marj, Benghazi University, El Marj, Libya, ²Department of Chemistry, Faculty of Science, Benghazi University, Benghazi, Libya u ³PharmD, Faculty of Pharmacy, Libyan International Medical University, Benghazi, Libya

Солватохромна својства метиленско плавог (MB) испитивана су у чистим растварачима: води, метанолу, етанолу, пропанолу и диоксану, као и њихивом воденим смешама. Испитивана је корелација вредности емпиријске скале поларности растварача (ET) за MB са саставом растварача коришћењем Bosch и Roses модела измене растварача да би се објаснило преференцијално растварање одабране тиазинске боје у бинарним мешаним растварачима. Нелинеарни солватохромизам MB је опажен у воденим смешама метанола, етанола, пропанола и диоксана. Утицај састава на солватациону љуску при преференцијалном растварању MB је испитиван са аспекта растварач–растварач и растворак–растварач интеракција и израчуната је локална молска фракција састава сваког растварача у непосредној околини растворка MB. Варијације ефективне молске фракције могу дати важан физичкохемијски увид у микроскопске и молекулске интеракције између MB и компоненти растварача. Резултати показују да је солватациона љуска MB више засићена комплексом растварача S_{12} у случају диоксана у односу на смеше етанола и пропанола, а супротан тренд је детектован за смеше метанола, с обзиром на то да комплекс растварача S_{12} није могао да се инкорпорира у MB солватациону љуску. Подаци бинарних система су анализирани KAT параметрима коришћењем дуалног модела базности и поларности. Добијени резултати су показали да поларност више одоговара за опис спектралног помераја у воденим растворима метанола и етанола, док је базност прикладнија за водене растворе пропанола и диоксана.

(Примљено 12. маја, ревидирано 18. јуна, прихваћено 1. новембра 2023)

REFERENCES

1. C. Reichardt, T. Welton, *Solvents and Solvent Effects in Organic Chemistry.* Wiley-VCH, Weinheim, 2011 (http://dx.doi.org/10.1002/9783527632220)
2. A. M. Al-Jebaly, S. S. Hemdan, F. K. Ali, *J. Sci. Hum. Studies* **39** (2017) 1 (http://dx.doi.org/10.37376/1571-000-039-003)
3. N. Elmsheeti, S. Hemdan, A. Sammour, R. Alnajjar, *Chem. Data Collect.* **28** (2020) 100465 (https://doi.org/10.1016/j.cdc.2020.100465)
4. M. S. Masoud, R. I. M. Elsamra, S. S. Hemdan, *J. Serb. Chem. Soc.* **82** (2017) 856 (http://dx.doi.org/10.2298/JSC170204032M)

5. A. M. Al-Jebaly, S. S. Hemdan, F. K. Ali, *J. Natur. Sci., Life Appl. Sci.* **1** (2017) 33 (http://dx.doi.org/10.26389/AJSRP.A071217)

6. S. Hemdan, A. Al Jebaly, F. Ali, *Acad. J. Res. Sci. Pub.* **2** (2021) 28 (http://dx.doi.org/10.52132/Ajrsp.e.2021.242)

7. J. Catalán, C. Dıaz, F. Garcıa-Blanco, *J. Org. Chem.* **65** (2000) 9226 (http://dx.doi.org/10.1021/jo001008u)

8. D. C. Da Silva, I. Ricken, M. A. D. R. Silva, V. G. Machado, *J. Phys. Org. Chem.* **15** (2002) 420 (http://dx.doi.org/10.1002/poc.519)

9. S. S. Hemdan, *J. Solution Chem.* (2023) (http://dx.doi.org/10.1007/s10953-023-01301-3)

10. R. I. Stock, L. G. Nandi, C. R. Nicoleti, A. D. S. Schramm, S. L. Meller, R. S. Heying, D. F. Coimbra, K. F. Andriani,G. F. Caramori, A. J. Bortoluzzi, V.G. Machado, *J. Org. Chem.* **80** (2015) 7971 (http://dx.doi.org/10.1021/acs.joc.5b00983)

11. A. Farajtabar, F. Jaberi, F. Gharib, *Spectrochim. Acta A* **83** (2011) 213 (http://dx.doi.org/10.1016/j.saa.2011.08.020)

12. O. A. El Seoud, *Pure Appl. Chem.* **79** (2007) 1135 (http://dx.doi.org/10.1351/pac200779061135)

13. A. Ben-Naim, *J. Phys. Chem.* **93** (1989) 3809 (http://dx.doi.org/10.1021/j100346a086)

14. Y. Marcus, *J. Chem. Soc. Faraday Trans. 1* **84** (1988) 1465 (http://dx.doi.org/10.1039/F19888401465)

15. P. Suppan, *J. Chem. Soc. Faraday Trans. 1* **83** (1987) 495 (http://dx.doi.org/10.1039/F19878300495)

16. F. Gharib, A. Shamel, F. Jaberi, A. Farajtabar, *J Solution Chem.* **42** (2013) 1083 (http://dx.doi.org/10.1007/s10953-013-0007-9)

17. R. D. Skwierczynski, K. A. Connors, *J. Chem. Soc. Perkin Trans. 2* (1994) 467 (http://dx.doi.org/10.1039/P29940000467)

18. S. S. Hemdan, A. M. Algebali, F. K. Ali, *J. Chem. Technol. Metall.* **58** (2023) 125 (https://journal.uctm.edu/node/j2023-1/JCTM_2023_58_15_22-77_pp125-142.pdf)

19. J. P. Perdew, *Phys. Rev., B* **34** (1986) 7406 (https://dx.doi.org/10.1103/PhysRevB.33.8822)

20. T. Yanai, D. P. Tew, N. C. Handy, *Chem. Phys. Lett.* **393** (2004) 51 (https://dx.doi.org/10.1016/j.cplett.2004.06.011)

21. J. Chai, M. Head-Gordon *Phys. Chem. Chem. Phys.* **10** (2008) 6615 (https://dx.doi.org/10.1039/B810189B)

22. A. Austin, G. A. Petersson M. J. Frisch, F. J. Dobek, G. Scalmani, K. Throssell, *J. Chem. Theory Comput.* **8** (2012) 4989 (https://dx.doi.org/10.1021/ct300778e)

23. M. Walker, A. J. A. Harvey, A. Sen, C. E. H. Dessent, *J. Phys. Chem., A* **117** (2013) 12590 (https://dx.doi.org/10.1021/jp408166m)

24. Y. Takano, K. N. Houk, *J. Chem. Theory Comput.* **1** (2005) 70 (https://dx.doi.org/10.1021/ct049977a)

25. N. Elmsheeti, S. Hemdan, A. Sammour, R. Alnajjar, *Chem. Data Collect.* **28** (2020) 100465 (https://dx.doi.org/10.1016/j.cdc.2020.100465)

26. *Gaussian 16, revision C. 01.*, 2016

27. Sabirov V. Kh. Vahobjon CCDC 2223592: Experimental Crystal Structure Determination, 2022 (https://doi.org/10.5517/ccdc.csd.cc2dmtsn)

28. S. S. Hemdan, *J. Fluoresc.* (2023) (http://dx.doi.org/10.1007/s10895-023-03234-y)

29. H. C. Boroujeni, F. Gharib, *J. Solution Chem.* **45** (2016) 95 (https://doi.org/10.1007/s10953-015-0425-y)

30. X. Chen, A. Farajtabar, W. Jia, H.Zhao, *J. Chem. Thermodyn.* **138** (2019) 179 (https://doi.org/10.1016/j.jct.2019.06.019)
31. T. Bevilaqua, T. F. Goncalves, C. G. Venturini, V. G. Machado, *Spectochim. Acta, A* **65** (2006) 535 (http://dx.doi.org/10.1016/j.saa.2005.12.005)
32. M. Rosés, C. Ràfols, J. Ortega, E. Bosch, *J. Chem. Soc. Perkin Trans. 2* (1995) 1607 (http://dx.doi.org/10.1039/P29950001607)
33. R.W. Taft, J.L.M. Abboud, M.J. Kamlet, *J. Org. Chem.* **49** (1984) 2001 (http://dx.doi.org/10.1021/jo00185a034)
34. X. Yao , R. Fang, H. Zhao , A.Farajtabar, A. Jouyban ,W.E. Acree Jr, *J. Mol. Liq.* **349** (2022) 118515 (http://dx.doi.org/10.1016/j.molliq.2022.118515).

The non-ideality in binary aqueous systems contributed to the different abilities of solvent entities incorporated in the solvation shell of methylene blue

SOKAINA S. HEMDAN[1]* and RADWAN ALNAJJAR[2,3]

[1]*Department of Chemistry, Faculty of Science and Art El Marj, Benghazi University, El Marj, Libya,* [2]*Department of Chemistry, Faculty of Science, Benghazi University, Benghazi, Libya and* [3]*PharmD, Faculty of Pharmacy, Libyan International Medical University, Benghazi, Libya*

PREFERENTIAL SOLVATION (PS) MODEL

For binary mixtures consisting of solvents S_1 (water) and S_2 (organic solvent) and a solvatochromic indicator I, the proposed equilibria for the solvent exchange process are expressed as:

$$I(S_1)_2 + 2S_2 \rightleftharpoons I(S_2)_2 + 2S_1 \tag{S-1}$$

In addition, the solvated complex (S_{12}) is formed by the interaction of solvent molecules with each other as follows:[1]

$$I(S_1)_2 + S_2 \rightleftharpoons I(S_{12})_2 + S_1 \tag{S-2}$$

The fully solvated forms of solute I, in Eqs. S-1 and S-2, are shown as $I(S_1)_2$, $I(S_2)_2$, and $I(S_{12})_2$ with the solvents S_1, S_2, and S_{12}, respectively.[2,3] In this model, it is proposed that the solvated complex $I(S_{12})_2$ has new properties distinct from $I(S_1)_2$ and $I(S_2)_2$[11] and that the local composition of the solvation shell of a solute is present in equilibrium with the bulk composition of the solvent mixtures. It noted that the subscript 2 is interpreted as the number of solvent molecules participating in the exchange process in the solvation shell of the solvatochromic indicator and should not be confused with the total number of molecules that solvate the indicator.

It is assumed that in equilibrium, the mole fractions of the solvents involved in the local solvation shell of the indicator I (x^L_1, x^L_2, x^L_{12}) and the mole fractions in the bulk mixtures (x^B_1, x^B_2). Based on the mole fraction scale, the preferential parameters ($f_{2/1}$, $f_{12/1}$, and $f_{12/2}$) are determined from the solvent exchange equilibrium above:

$$f_2 = x^L_2 (x^B_1)^2 / x^L_1 (x^B_2)^2 \tag{S-3}$$

$$f_{12} = x^L_{12}(x^B_1) / x^L_1(x^B_2) \tag{S-4}$$

$$f_{12} = f_{12}/f_2 = x^L_{12}(x^B_2) / x^L_2(x^B_1) \tag{S-5}$$

* Corresponding author. E-mail: Sukains_h@yahoo.com

The preferential solvation parameters fi/j indicate the ability of a solute to solvate with solvent i in the presence of solvent j. In fact, fi/j >1 indicates that the solute is preferably solvated in solvent i relative to solvent j and vice versa.[2]

The electronic transition energy, E_T, of a solvatochromic solute in a binary solvent mixture depends on the local composition of the solvation shell and is a weighted average of the E_T values corresponding to each of the solvation species in the solvation shell:

$$E_T = E_1 x_1^L + E_2 x_2^L + E_{12} x_{12}^L \tag{S-6}$$

The E_T values of the solute are estimated using E_1, E_2, and E_{12} values when the solute is solvated by S_1, S_2, and S_{12}, respectively. Finally, by introducing Eqs. 3 and 4 into Eq. 6 and assuming that the sum of all mole fractions in each region is equal to unity, the general equation to determine the E_T value is derived:

$$E_T = \frac{E_1 x_1 + f_{2/1} E_2 x_2 + f_{12/1} E_{12} x_1 x_2}{x_1 + f_{2/1} x_2 + f_{12/1} x_1 x_2} \tag{S-7}$$

The parameters E_{12}, $f_{2/1}$, and $f_{12/1}$ can be calculated by a non-linear least square fitting of the experimental E_T values and the values from Eq. S-7.

TABLE S-I. The KAT parameters for different mole fraction, x_2, of organic solvents.

% cosolvent /parameters	Water-MeOH			Water-EtOH			Water-PrOH			Water-Dioxane		
	α	β	π*	α	β	π*	α	β	π*	α	β	π*
0	1.17	0.47	1.09	1.17	0.47	1.09	1.17	0.47	1.09	1.17	0.47	1.09
20	1.04	0.56	1.10	1.00	0.63	1.10	1.04	0.56	1.12	0.92	0.54	1.09
30	1.01	0.64	1.04	0.96	0.66	0.99	0.94	0.60	1.09	0.82	0.56	1.05
40	0.98	0.70	0.98	0.96	0.65	0.88	0.87	0.65	1.04	0.77	0.59	0.99
50	0.98	0.73	0.91	0.96	0.65	0.79	0.86	0.70	0.96	0.73	0.61	0.92
60	0.99	0.70	0.85	0.96	0.66	0.73	0.88	0.75	0.88	0.60	0.63	0.55
70	1.00	0.68	0.78	0.94	0.66	0.68	0.89	0.78	0.81	0.52	0.63	0.56
80	1.01	0.65	0.72	0.93	0.68	0.65	0.90	0.79	0.75	0.38	0.61	0.54
100	0.93	0.62	0.60	0.83	0.77	0.54	0.84	0.85	0.52	0.00	0.37	0.55

The values are obtained from Ref. 4
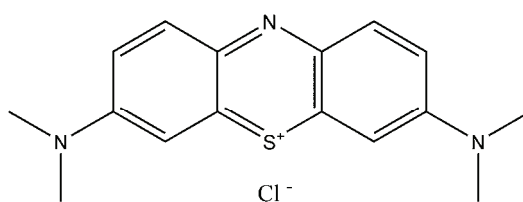
Fig. S-1. Structure of methylene blue (MB).
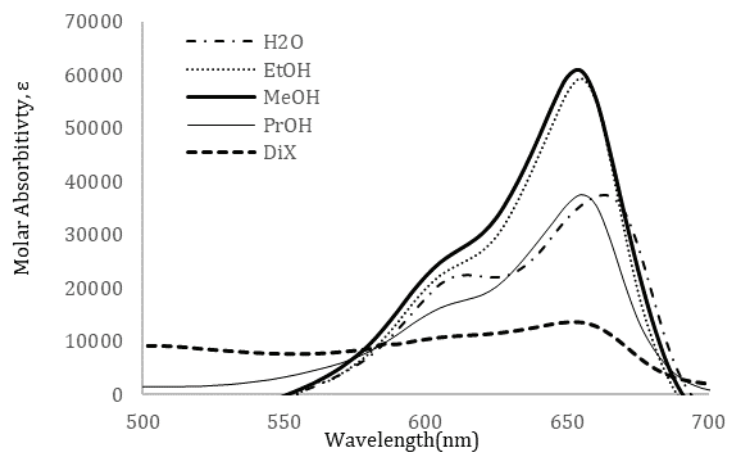
Fig. S-2. The electronic absorption spectrum of 3.13×10^{-5} mol.L^{-1} solution of MB in neat solvents at room temperature 25 °C.

REFERENCES

1. A. Farajtabar, F. Jaberi, F. Gharib, *Spectrochim. Acta A* **83** (2011) 213 (http://dx.doi.org/10.1016/j.saa.2011.08.020)
2. S. S. Hemdan, *J. Solution Chem.* (2023) (http://dx.doi.org/10.1007/s10953-023-01301-3)
3. F. Gharib, A. Shamel, F. Jaberi, A. Farajtabar, *J Solution Chem.* **42** (2013) 1083 (http://dx.doi.org/10.1007/s10953-013-0007-9)
4. S. S. Hemdan, A. M. Algebali, F. K. Ali, *J. Chem. Technol. Metall.* **58** (2023) 125 (https://journal.uctm.edu/node/j2023-1/JCTM_2023_58_15_22-77_pp125-142.pdf).

Physicochemical properties of bioplastic based on hydroxyethylcellulose and polyvinylpyrrolidone blend

BUDIMAN ANWAR*, CITRA NURHASHIVA, WAFA RAIHANAH ARWA
and GALUH YULIANI

Material Chemistry Research Group, Chemistry Programs, Faculty of Mathematics and Natural Sciences Education, Universitas Pendidikan Indonesia, Jl. Dr. Setiabudhi 229, Bandung 40154, Indonesia

Abstract: The aim of this study is to develop a bioplastic based on hydroxyethylcellulose (HEC) and polyvinilpyrrolidone (PVP) which is applied as packaging materials. The effect of incorporation of PVP into HEC on the physicochemical properties of its blend films are investigated. The FTIR and DSC analysis denote that incorporation of PVP induce the intermolecular hydrogen bonds to occur more intensely. The XRD diffractograms indicate that the incorporation of PVP reduces the crystallinity of the film. The mechanical properties of the films become greater as the PVP content increases, and the optimum composition of HEC/PVP is at 5:3 mass ratio with a tensile strength of 34.8±3.4 MPa; elongation at break 104.3±4.9 %; and an elastic modulus of 0.10±0.02 GPa. The SEM and DSC analysis signify an excellent compatibility and miscibility between HEC and PVP. The incorporation of PVP increase the transparency and hydrophilicity of the film. The water vapor transmission rate of the films is relatively unchanged due to the incorporation of PVP. The TGA and DSC analysis reveal that the incorporation of PVP increases the thermal stability and the glass transition temperature of the film. This bioplastic film could be an alternative for biodegradable packaging material.

Keywords: polyblend; biodegradable plastic; cellulose derivative; biopolymers; HEC/PVP blend.

INTRODUCTION

Plastic as petrochemical-based synthetic polymers is one of the most produced, used and versatile materials due to its excellent flexibility, durability and resistance. Nevertheless, exaggerated use of durable plastics, mainly for packaging materials, have made them a big problem because of their build-up in the environment are greater than their degradation rate in landfills.[1,2] Nowadays,

215

there is an augmentative interest in bio-based plastics. The use of biopolymers as a substitute to petrochemical-based synthetic polymers for packaging materials has increased due to their availability, sustainabilty, non-toxicity, relatively low cost, biocompatibility and biodegradability.[3] Several biopolymers have been utilized for plastic packaging films such as carrageenan,[4] pectin,[5] alginate,[6] starch[2] and various cellulose derivatives.[7,8]

Physical blending of polymers is one of the most convinient method to modify polymeric materials to obtain new materials with the desired properties. In order to meet the need for new materials, physical blending could regularly be performed more swiftly and economically than synthesizing materials with novel molecules. Physical blending between biopolymers and synthetic polymers deputize a new class of materials and have gained much attention particularly in bioapplications and as biodegradable packaging materials.[7]

Hydroxyethyl cellulose (HEC) is a nonionic water-soluble cellulose ether and one of the most significant cellulose derivatives (cellulose ether). HEC is obtained by treating cellulose with sodium hydroxide and reacting with ethylene oxide.[9] HEC has very wide applications, including in cosmetics, pharmaceutical, paint industry and battery.[10] This is because HEC has low toxicity, non-immunogenicity and biocompatibility.[11] Moreover, HEC has good film forming and biodegradability properties.[9]

Polyvinilpyrrolidone (PVP) is synthesized by free radical polymerization from *N*-vinylpyrrolidone monomer with AIBN as the initiator.[12] PVP is a high molecular amorphous polymer that dissolve easily in water and several organic solvents, and also has excellent thermal properties. Addtionally, PVP has good biocompatibility, is good complexing agent and non-toxic.[13]

Previous studies have reported on miscibility of HEC with several synthetic polymers, including polyethylenglycol (PEG),[14] polyvinylalcohol (PVA)[15] and PVP.[16] In this study, we have examined the effect of incorporation of PVP into HEC on the physicochemical properties of blend films. The polyblend films were prepared by solution casting method with different composition of HEC and PVP with the addition of a certain amount of glycerol as a plasticizer. The mechanical, morphological, optical, thermal, and moisture barrier properties of the blend films were thoroughly characterized.

<div align="center">EXPERIMENTAL</div>

Materials

HEC technical grade, PVP K30, and glycerol technical grade were purchased from Interco Laboratories, Bandung, Indonesia. All other reagents were of analytical grade and commercially available.

Preparation of blend films

The HEC/PVP blend films were prepared by solution casting method. To obtain an HEC//PVP blend film with a composition of 5:3 mass ratio, 1.25 g of HEC was dissolved in 30 mL

of distilled water and stirred rigorously for 10 min at room temperature. A certain amount of glycerol was added to the HEC solution so that the glycerol composition in film blend was 5 %, and stirring continued for 10 min. Then, 0.75 g of PVP was dissolved in 20 mL of distilled water and stirred rigorously for 10 min at room temperature. Subsequently, both solutions were mixed together and stirred continuosly for 20 min to ensure the homogeneous of the solutions in the blend. The mixture was then degassed ultrasonically for 2 min. Afterwards, casting was undertaken by pouring the mixture into a number of petridishes and then allowed to dry. When dried the films were peeled out of the petridishes and stored in desiccators to prevent moisture. The same procedure was performed for other compositions, *i.e.*, 6:2, 7:1 and 8:0.

Characterization

Mechanical properties including tensile strength, elongation at break, and Young's modulus were characterized using the Textechno Favigraph I-PI-067 instrument at a crosshead speed of 6.0 mm/min under dry conditions at room temperature. All films were cut using the same shaper. The size of the test samples was 3 mm in width and 50 mm in parallel length.

Fourier-transform infrared (FTIR) spectroscopy was carried on FTIR-600 (Jaco Corp, Japan) instrument. The samples analyzed in the frequency range of 4000–400 cm^{-1} with scanning resolution of 2 cm^{-1} to find the information about the changes in chemical composition and crystallinity. Crystallinity ratio (*CrR*) of cellulose and its derivative could be acquired by comparing the absorbance peaks at 1372 (A_{1372}) and 2900 cm^{-1} (A_{2900}):[17,18]

$$CrR = A_{1372} / A_{2900} \qquad (1)$$

The hydrogen bond energy (E_H) for several OH stretching bands is calculated as follows:[17]

$$E_H = \frac{v_0 - v}{kv_0} \qquad (2)$$

where v_0 is the standard frequency corresponding to free OH groups (3650 cm^{-1}), v is the frequency of the bonded OH, and k is a constant ($1/k = 2.625\times10^2$ kJ/mol). Whilst, the hydrogen bond distance (R) is obtained as follows:[17]

$$\Delta v \text{ (cm}^{-1}\text{)} = 4430(2.84 - R) \qquad (3)$$

where $\Delta v = v_0 - v$, v_0 is the frequency of monomeric OH stretching (3600 cm^{-1}), and v is the stretching frequency observed in the infrared spectra of the cellulose samples.

The XRD analysis is conducted to investigate the crystallinity index (*CI*) and crystallite size (*L*) of the film samples. The diffractograms of HEC and HEC/PVP blend films are obtained at room temperature by MiniFlex (Rigaku, Japan) X-ray diffraction instrument using CuKα radiation ($\lambda = 1.54$ Å) in the 2θ range of 3–90°. Potential difference and current used are 40 kV and 15 mA, consecutively. The XRD analysis is conducted to investigate the *CI* and *L*. The crystallinity index of the films can be estimated from the ratio of the crystalline peak area to total and calculated using as follows:

$$CI = 100 \frac{\text{Area of crystalline phase}}{\text{Area under the all peaks}} \qquad (4)$$

The crystallite size is calculated using the Scherrer equation:

$$L = \frac{K\lambda}{H\cos\theta} \qquad (5)$$

where *K* is a constant that Scherrer found to e 0.94; *λ* is the X-ray wavelength (0.154 nm); *H* is the full width at half maximum (FWHM) in rad and *θ* is the Bragg angle.[17]

In order to examine the morphology of films and miscibility of HEC and PVP in blend, the film specimens were coated by gold/palladium using ion sputter coater and observed by EVO MA 10 scanning electron microscope (SEM, Carl Zeiss, Germany) with the operated voltage at 15 kV.

The light transmission and opacity of films were determined using a UVmini-1240 UV––Vis spectrophotometer (Shimadzu, Japan). The light transmission was measured at a wavelength of 200–600 nm with air as a blank.[19] Opacity of the films was calculated as follows:

$$\text{Opacity} = \frac{\text{Absorbance at 600 nm}}{\text{Film thickness (mm)}} \tag{6}$$

A set of laboratory-scale experimental tools were used to measure the water contact angles on film surfaces. Film specimen measuring 10 mm×10 mm was mounted on a platform, onto which distilled water was dropped from a syringe. The water droplet on the surface of film was captured by the camera. The images were then processed using the ImageJ software to acquire the contact angle data, that were used to evaluate the hydrophobicity of films.

The water vapor transmission rate (*WVTR*) was conducted using a method adapted from preceding report with some modifications.[20] The film specimens made into a vial lid which had been filled with 50 g of silica gel until all parts of the vial were covered. Moreover, the vial was put into desiccator which had previously been filled with 120 mL of distilled water instead of silica gel. The silica gel was then weighed after 24 h. *WVTR* was calculated as follows:

$$WVTR = \frac{\Delta W}{At} \tag{7}$$

where Δ*W* is the change in mass of silica gel after 24 h (g), *A* is film surface area (mm), and *t* is time (24 h).

The glass transition temperature (*T*$_g$) and the chang in enthalpy of relaxation (Δ*H*$_{\text{relax}}$) of films were investigated by differential scanning calorimetry (DSC) using DSC-214 Polyma (Netzsch, Germany) under nitrogen atmosphere. Film specimens were sealed hermetically in DSC pans and heated from 25 to 250 °C at a rate of 10 °C/min.

Thermogravimetric analysis (TGA) was performed by TGA701 thermogravimetric analyzer (Leco, USA) to determine the thermal stability of films. The certain mass of each film specimen was sealed hermetically in TGA pans and heated from 25 to 600 °C with heating rate of 5 °C min^{-1} under nitrogen atmosphere. The thermal decomposition temperature (*T*$_d$) and derivative thermogravimetric curve (DTG) were obtained.

RESULTS AND DISCUSSION

Optimization and mechanical properties of blend films

Fig. 1 shows the photographs of blend films with different composition of HEC and PVP. It can be seen that all films are transparent.

Mechanical properties play an important role in packaging area. Considering that fact, in this study the mechanical properties were applied as optimization parameters. Table I represents the mechanical properties of the blend films. The optimum composition of HEC/PVP blend film is at 5:3 mass ratio since it has

mechanical properties comparable to LDPE, *i.e*., tensile strength 8–31 MPa, elongation at break 100–965 %, and Young's modulus 0,2–0,5 Gpa.
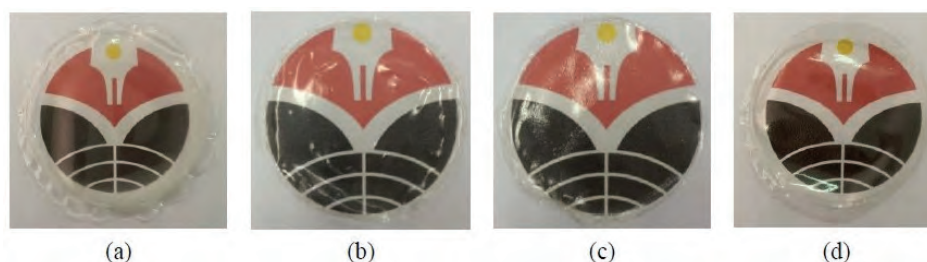
Fig. 1. Photographs of: a) HEC; b) HEC/PVP (7:1); c) HEC/PVP (6:1);
d) HEC/PVP (5:3) films.

TABLE I. Mechanical properties of HEC and HEC/PVP blend films

Sample	Tensile strength, MPa	Elongation at break, %	Young's modulus, GPa
HEC	11.1±3.6	96.9±5.6	0.072±0.01
HEC/PVP (7:1)	10.6±3.0	81.0±9.7	0.067±0.01
HEC/PVP (6:2)	18.5±2.9	82.4±7.7	0.073±0.02
HEC/PVP (5:3)	34.8±3.4	104.3±4.9	0.105±0.03

The mechanical properties of the blend are mostly determined by molecular interactions that occur in the blends. HEC has many hydroxyl groups as proton donors. Whereas, PVP could act as a proton acceptor since it has a carbonyl group on its pyrrolidone ring. As a result, hydrogen bond interactions will ensue between the two polymers.[21] The molecular mass of the polymer, concentration, process of blending, and solvent evaporation may also influence the mechanical properties of the films.[22]

As shown in Table I, the tensile strength, elongation at break, and Young's modulus all become greater as the PVP composition increases. The increase in tensile strength and Young's modulus could be linked to the intermolecular hydrogen bonds and other secondary intermolecular forces that occur more intensely as increasing PVP content.[23,24] This occurrence was evidenced by FTIR and DSC analysis. Whilst, the increase in elongation at break could be attributed to the crystallinity that decrease as increasing PVP content. For semi-crystalline polymers, the amorphous phases can deform more freely.[25] This occurrence also was evidenced by FTIR and XRD analysis.

FTIR analysis

Fig. 2 shows the FTIR spectra of HEC, PVP and blend films with different composition of HEC/PVP. The FTIR spectrum of HEC provides the characteristic absorption bands at 3429, 2924, 1383, 1122 and 1062 cm^{-1}; these bands are assigned to O−H stretching, C−H stretching, CH_3 asymmetric bending, C−O−C

asymmetric stretching and C−O stretching, respectively.[26] Whilst, the character-istic absorption bands at 2955, 1659, 1433 and 1287 cm^{-1} in FTIR spectrum of PVP are attributed to the stretching vibrations of C−H, C=O, C=C and C−N, res-pectively. The broad band at 3427 cm^{-1} indicates that PVP contains absorbed water.[27]
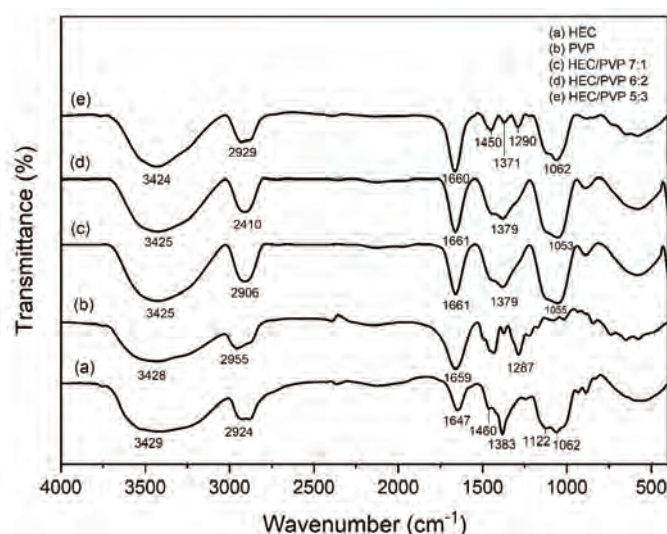
Fig. 2. FTIR spectra for HEC, PVP and HEC/PVP blend films.

The characteristic bands of HEC and PVP appeared in the spectra of HEC/ /PVP blend films. Nevertheless, there is a shift in the absorption band of O−H in HEC to the lower frequency. This is due to the formation of hydrogen bonds between HEC and PVP in the blend films.[28] The values of hydrogen bonds energy (E_H) and hydrogen bond distances (R) for HEC and HEC/PVP blend films were obtained using Eqs. (2) and (3), respectively, and presented in Table II. The value of E_H become greater as the PVP composition increases, and *vice versa* for the R value. Both parameters evidence that intermolecular hydrogen bonds occur more intensely as the PVP content increases.[21] These results con-firm mechanical properties, mainly the tensile strength and Young's modulus of films.

TABLE II. The value of crystallinity ratio (CrR), hydrogen bond energy (E_H), and hydrogen bond distance (R) for the HEC and blend films

Sample	CrR	E_H / kJ mol^{-1}	R / Å
HEC	1.41	15.89	2.8014
HEC/PVP (7:1)	1.19	16.18	2.8005
HEC/PVP (6:2)	1.23	16.18	2.8005
HEC/PVP (5:3)	0.25	16.25	2.8003

The crystallinity ratio (*CrR*) of HEC and HEC/PVP blend films acquired by Eq. (1) are presented in Table II. The decreasing *CrR* value as the PVP content increases indicates that the crystallinity of the blend films decrease as the PVP content increases. This is due to the PVP molecules that prevent HEC molecules to re-organize during film formation. In addition, the absorption peak at about 1650 cm^{-1} in HEC spectrum is related to water which is absorbed in the amorphous region.[26] As seen in Fig. 2, the absorption band intensity at around 1650 cm^{-1} in the HEC/PVP blend films are greater than that of HEC. This also signifies that the HEC/PVP blend films have lower crystallinity than HEC film.

XRD analysis

The X-ray diffraction patterns of HEC and HEC/PVP blend films are displayed in Fig. 3.
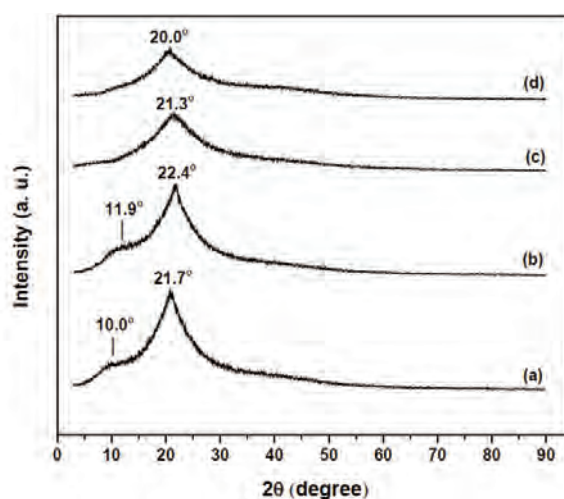
Fig. 3. X-ray diffraction pattern of: a) HEC, b) HEC/PVP (7:1), c) HEC/PVP (6:2) and d) HEC/PVP (5:3) films.

As shown in Fig. 3, the HEC film provide the diffraction peaks at about 2θ 10.0 and 21.7° which are typical to the structure of crystalline HEC.[29] After the incorporation of PVP into HEC (Fig. 3, curves b–d), the broadening of the peaks was observed with lower intensity. Moreover, the diffraction peak at about 2θ 10.0° disappeared in the XRD patterns of HEC/PVP with higher PVP content (Fig 3, curves c and d). The crystallinity index value decreases as the PVP content increases (Table III). This can be related to decrease in crystallinity due to restricted segmental movement by the incorporated PVP in the HEC.[30] Moreover, the incorporation of PVP into HEC would destroy the original semi-crystalline structure of HEC by leading to an amorphous structure.[29] This finding is in

accordance with the FTIR analysis and in turn can clarify the mechanical properties, mainly the elongation at break.

TABLE III. The value of crystallinity index (CI) and crystallite size (*L*) for the HEC and blend films

Sample	2θ / °	*FWHM*[a] / °	*d*-spacing, nm	*CI*[b] / %	*L*[c] / nm
HEC	21.70	5.45	0.41	40.86	9.58
HEC/PVP (7:1)	22.42	5.12	0.40	37.02	10.20
HEC/PVP (6:2)	21.35	9.39	0.42	27.82	5.56
HEC/PVP (5:3)	20.02	6.40	0.44	24.68	8.16

[a]The full width at half maximum of XRD profiles; [b]calculated using Eq. (4); [c]calculated using Eq. (5)

The crystallite size (*L*) values of both HEC film and HEC/PVP blend films are shown in Table III. The crystallite size values show some variation despite of showing constant affect, by the incorporation of the PVP content. However, with higher content of PVP, the crystallite size decrease, which may be associated to variation in cooling rate or annealing process.[30] French and Cintron[31] suggest that there is a nonlinear relationship of crystallinity index to the relative crystallite size for a given structure. Hence, the crystallinity index may not purely relate to the crystallite size.

SEM analysis

Fig. 4 shows the surface morphologies of films detected by SEM. Both the HEC and HEC/PVP films have homogeneous surface. This confirms the compatibility and miscibility of both polymers.[22] Moreover, the HEC/PVP blend film has more delicate surface than HEC film. This can be comprehended since PVP plays a role as a good film-forming agent. The compatibility and miscibility of the two polymers was further evidenced by DSC analysis.
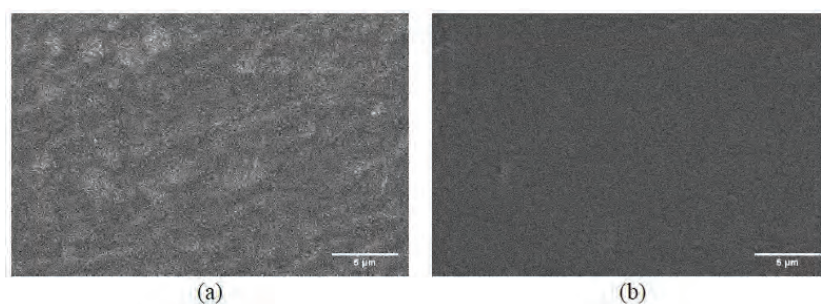
Fig. 4. SEM image for (a) HEC film and (b) HEC/PVP 5:3 blend film.

Optical properties

One of the important factors that should be examined in the manufacture of plastic packaging are optical properties.[32] The most considerably used method to

investigate the optical properties of a film is determining the opacity value of the film. Opacity is defined as the ratio between the absorbance at 600 nm and the film thickness. The opacity values of HEC film (Fig. 1a) and HEC/PVP 5:3 blend film (Fig. 1d) which was obtained using equation (4) are presented in Table IV.

TABLE IV. The opacity value of the HEC and HEC/PVP 5:3 blend films

Sample	Thickness, mm	Absorbance at 600 nm	Opacity, A/mm
HEC	0.144	0.217	1.509
HEC/PVP 5:3	0.228	0.296	1.300

The opacity value is conversely related to the transparency. An increase in the opacity value signifies a decrease in transparency.[33] The opacity value is strongly influenced by the internal structure and surface characteristics. Amorphous polymers have lower opacity values (more transparent) than crystalline one. When molecules with a crystalline arrangement increase, a different refractive index is formed from each part of the crystalline structure, which in turn increases the opacity value (less transparent).[34] The opacity value of films presented in Table IV indicate that the incorporation of PVP into HEC increases the transparency of the film. The results of the optical properties analysis are in accordance with the results of the FTIR and XRD analysis.

Contact angle measurement

Measuring the contact angle of water drop on the surface of a film can be used to determine the hydrophilicity of a film.[35] The value of the contact angle < 90° signifies that the film is hydrophylic. This value also indicates that the film has a high surface energy, so water will wet the surface properly. Contrarily, if the surface energy of the film is low, so water does not wet the surface well. In this case, the value of the contact angle will increase and the film is categorized as hydrophobic.[36]

The contact angle of HEC film and HEC/PVP 5:3 blend film are shown in Fig. 5. It reveals that the contact angle of HEC and HEC/PVP 5:3 blend films are 66.38 and 54.36°, successively. The decline in contact angle is affected by the hydrophilic properties of PVP which contains hydrophilic groups in its molecules.[37] This result deduces that the incorporation of PVP into HEC increases the film hydrophilicity.

Water vapor transmission rate

Water vapor transmission rate (*WVTR*) is one of an important feature in establishing the barrier properties of plastic packaging. The *WVTR* value of the film indicates the quantity of moisture that has passed through the film. Therefore, the value of *WVTR* depicts a film's resistance towards water vapor transmission under particular conditions. The frequently plastic films used as packaging

have relatively slight *WVTR* value (approximately 5–20 g/m^2 h) which refers to good barrier properties.[38,39]
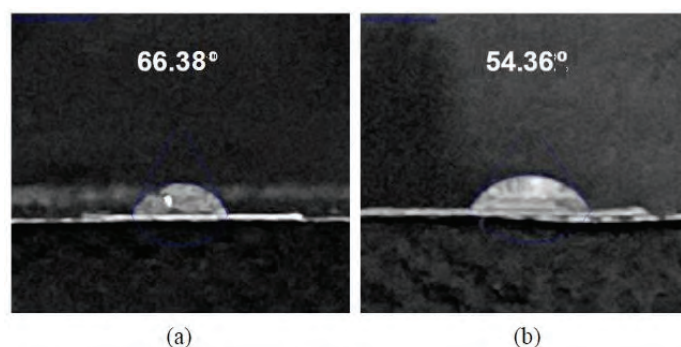
Fig. 5. Contact angle of (a) HEC film and (b) HEC/PVP 5:3 blend film.

The value of *WVTR* is strongly relate to hydrophilicity and porosity of the film-forming materials.[40] The values of *WVTR* for HEC film and HEC/PVP 5:3 blend film acquired, using Eq. (5) successively, are 91.91 and 91.93 g/m^2 h. These values are categorized as medium barrier properties. Hence, the addition of PVP into HEC relatively does not change the barrier properties of the film against water vapor.

DSC analysis

The effect of incorporation of PVP into HEC on T_g and ΔH_{relax} was investigated by DSC technique. There are three types of glass transition temperatures (T_g), *i.e.*, the primary (α) transition, β-transition and γ-transition. The primary transition transpires in the amorphous regions of the polymer. The secondary transition called the β-transition correlates with the mobility of side groups or smaller unit backbone chains. Another secondary transition designated the γ-transition is related to the end-group rotation, crystalline defects, backbone-chain motions of short segments or groups and phase separation of impurities or diluents. The β-transition is higher than the γ-transition.[41] Generally, the primary transition for HEC vary from 90 to 120 °C,[42,43] the β-transition between 0 and 40 °C[41] and the γ-transition among −60 and −120 °C.[41]

The DSC thermograms for HEC and HEC/PVP 5:3 blend films are shown in Fig. 6. The DSC thermograms of HEC and HEC/PVP 5:3 blend films denoted a relatively wide endotherms glass transition temperature (T_g) successively at 90.9 and 92.5 °C. These relatively broadened glass transitions corresponded to a primary transition that occurs in amorphous region of semi-crystalline materials. ΔH_{relax} for HEC and HEC/PVP 5:3 blend films were 255.3 and 310.2 J/g, respectively. These results designate that the intermolecular hydrogen bonds and other secondary intermolecular forces take place more intensely in HEC/PVP 5:3

blend instead in HEC. More vigorous hydrogen bonds and other secondary inter-molecular forces will induce the mobility of side groups or smaller unit backbone chains to be obstructed, leading to high T_g and ΔH_{relax}.[42,44] This finding is in accordance with the FTIR analysis and confirms the mechanical properties, *i.e.*, tensile strength and Young's modulus.
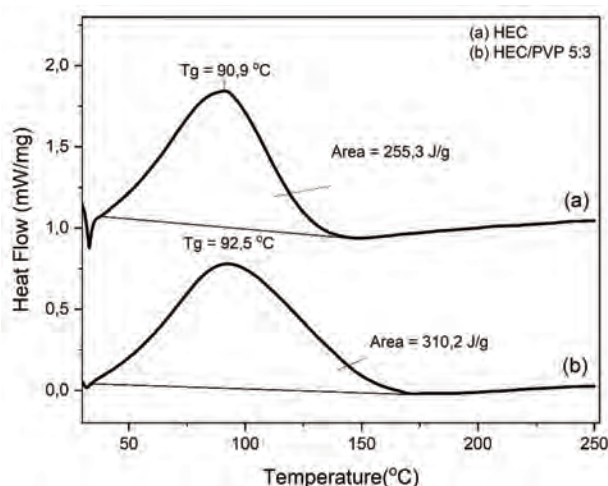
Fig. 6. DSC thermograms of: a) HEC film and b) HEC/PVP 5:3 blend film.

It was observed that in DSC thermogram of HEC/PVP film showed only single broad curve of T_g. This result attribute to the compatibility and miscibility of HEC and PVP.[42] The finding is also in accordance with the SEM analysis.

Thermogravimetric analysis

The other thermal properties of the HEC and HEC/PVP 5:3 blend films were examined by the TGA technique to investigate the thermal stability, composition and thermal degradation kinetics of films. Fig. 7a shows the TGA curves for HEC and HEC/PVP 5:3 blend films which characterized the thermal destruction of all films in nitrogen atmosphere. The derivative thermogravimetric (DTG) curves in Fig. 7b show the temperature of the starting point of decomposition (T_0) and the maximum speed of the thermal degradation (T_{max}) of films.

From the TGA curves, the heating from 27 to 150 °C the weight of HEC film is decreased about 14 %, whilst the HEC/PVP 5:3 blend film is about 16 %. This initial weight loss is due to moisture evaporation or weakly bound water.[26,44] This is also might be due to splitting or volatilization of small molecules from the samples.[42] On following heating runs, the further weight loss was observed both in the HEC and HEC/PVP 5:3 blend films. The starting point (T_0) of the second stage decomposition of the HEC film was observed at about 273 °C with the maximum rate (T_{max}) at about 314 °C, which attribute to the cellulose ethers

degradation including the parallel processes of dehydration and demethoxyl-ation.[45] Whereas, the second stage of the HEC/PVP 5:3 blend film decomposit-ion started (T_0) at about 284 °C with T_{max} at about 334 °C, both of which were higher than those HEC film. This indicates that HEC/ PVP 5:3 blend film has more excellent thermal stability than HEC film. Hereafter, the third stage of the HEC/PVP 5:3 blend film decomposition was observed at about 370 °C (T_0) with T_{max} at about 406 °C which appertain to the degradation of PVP.[46] The thermal degradation properties of the HEC and HEC/PVP 5:3 blend films are summar-ized in Table V.
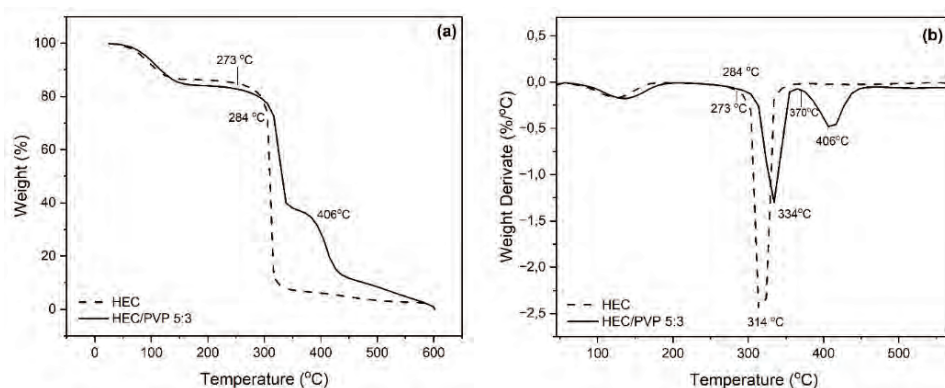
Fig 7. a) TGA and b) DTG curves for the HEC and HEC/PVP 5:3 blend films.

TABLE V. Thermal degradation properties of the HEC and HEC/PVP 5:3 blend films

Sample	Initial stage			Second stage			Third stage			
	T_0 °C	T_{max} °C	WL %	T_0 °C	T_{max} °C	WL %	T_0 °C	T_{max} °C	WL %	Char yield
HEC	50	125	14	273	314	78	–	–	–	8
HEC/PVP 5:3	50	140	16	284	334	48	370	406	24	12

CONCLUSION

The present study is focused on the investigation of physicochemical properties of HEC and HEC/PVP blend films. All films are prepared by solution casting methods with the addition of 5 % of glycerol as a plasticizer. The mechanical properties of blend films increase with increasing PVP content. The optimum composition of HEC/PVP blend is at 5:3 mass ratio with mechanical properties comparable to LDPE (tensile strength of 34.8±3.4 MPa; elongation at break 104.3±4.9 %, and an elastic modulus of 0.105±0.03 GPa). The surface morphology of the HEC/PVP 5:3 blend film more delicate and homogeneous than those of the HEC film, suggesting a good miscibility between HEC and PVP. The incorporation of PVP into HEC reduces the crystallinity of the film,

but on the other hand it causes hydrogen bonds and other secondary forces to occur more intensely. The HEC/PVP 5:3 blend film (opacity = 1.300 A/mm; contact angle = 54.36°) is more transparent and hydrophilic than HEC film (opacity = 1.509 A/mm; contact angle = 56.40°). The barrier properties of HEC (*WVTR* = 91.91 g/m^2 h) and HEC/PVP 5:3 blend (*WVTR* = 91.93 g/m^2 h) films are almost no different, and both have moderate barrier properties. The HEC/ /PVP 5:3 blend film has a good thermal stability up to 284 °C. The excellent polyblend film from low cost and environmentally friendly source could be an alternative for biodegradable packaging material.

ИЗВОД

ФИЗИЧКО–ХЕМИЈСКА СВОЈСТВА БИОПЛАСТИКЕ НА БАЗИ СМЕШЕ ХИДРОКСИЕТИЛЦЕЛУЛОЗЕ И ПОЛИ(ВИНИЛ-ПИРОЛИДОНА)

BUDIMAN ANWAR*, CITRA NURHASHIVA, WAFA RAIHANAH ARWA и GALUH YULIANI

Material Chemistry Research Group, Chemistry Programs, Faculty of Mathematics and Natural Sciences Education, Universitas Pendidikan Indonesia, Jl. Dr. Setiabudhi 229, Bandung 40154, Indonesia

Циљ ове студије је развој биопластике засноване на хидроксиетилцелулози (HEC) и поли(винил-пирилидона) (PVP) који се примењује као материјал за паковање. Истраживан је ефекат уношења PVP u HEC на физичко–хемијска својства филмова бленди. FTIR и DSC показују се да се увођењем PVP интензивније стварају међумолекуларне водоничне везе. XRD дифрактограми указују на то да уградњом PVP смањује кристалиничност филма. Механичка својства филмова постају боља како се PVP масени садржај повећава, а оптимални састав HEC/PVP је на 5:3 са јачином на кидање од 34,8±3,4 MPa; издужење при кидању 104,3±4,9 %; и модул еластичности од 0,10±0,02 GPa. SEM и DSC анализа показују одличну компатибилност и мешљивост између HEC и PVP. Укључивање PVP повећава транспарентност и хидрофилност филма. Брзина преноса водене паре филмова остаје релативно непромењена уградњом PVP. TGA и DSC показују да уношење PVP повећава топлотну стабилност и температуру стакластог прелаза филма. Овај биопластични филм могао би да буде алтернатива за биоразгради материјал за паковање.

(Примљено 23. октобра, ревидирано 7. новембра, прихваћено 25. децембра 2023)

REFERENCES

1. S. Jeremic, J. Milovanovic, M. Mojicevic, S. S. Bogojevic, J. Nikodinovic-Runic, *J. Serb. Chem. Soc.* **85** (2020) 1507 (https://doi.org/10.2298/JSC200720051J)
2. K. E. Rivadeneira-Velasco, C. A. Utreras-Silva, A. Díaz-Barrios, A. E. Sommer-Márquez, J. P. Tafur, R. M. Michell, *Polymers* **13** (2021) 3227 (https://doi.org/10.3390/polym13193227)
3. G. El-Fawal, H. Hong, X. Song, J. Wu, M. Sun, C. He, X. Mo, Y. Jiang, H. Wang, *Food Packag. Shelf Life* **23** (2020) 100462 (https://doi.org/10.1016/j.fpsl.2020.100462)

4. G. El-Fawal, *J. Food Sci. Technol.* **51** (2014) 2234 (https://doi.org/10.1007/s13197-013-1255-9)

5. A. Nesic, J. Ruzic, M. Gordic, S. Ostojic, D. Micic, A. Onjia, *Composites, B* **110** (2017) 56 (http://dx.doi.org/10.1016/j.compositesb.2016.11.016)

6. N. Tabassum, M. A. Khan, *Sci. Hortic.* **259** (2020) 108853 (https://doi.org/10.1016/j.scienta.2019.108853)

7. H. Somashekarappa, Y. Prakash, K. Hemalatha, T. Demappa, R. Somashekar, *Indian J. Mater. Sci.* **2013** (2013) 307514 (http://dx.doi.org/10.1155/2013/307514)

8. X. Zhang, H. Guo, W. Luo, G. Chen, N. Xiao, G. Xiao, C. Liu, *Front. Bioeng. Biotechnol.* **10** (2022) 01 (https://doi.org/10.3389/fbioe.2022.989893)

9. E. Di Giuseppe, in *Reference Module in Earth Systems and Environmental Sciences*, S. A. Elias, Ed., Elsevier, Amsterdam, 2018 (https://doi.org/10.1016/B978-0-12-409548-9.10909-1)

10. Z. Lu, J. Huang, S. E, J. Li, L. Si, C. Yao, F. Jia, M. Zhang, *Carbohydr. Polym.* **250** (2020) 116919 (https://doi.org/10.1016/j.carbpol.2020.116919)

11. N. Aqdas, M. Z. Khalid, T. Shazia, A. Waseem, S. Muhammad, Z. Mohammad, *Int. J. Biol. Macromol.* **15** (2020) 993 (https://doi.org/10.1016/j.ijbiomac.2019.10.254)

12. M. El Achaby, Y. Essamlali, N. El Miri, A. Snik, K. Abdelouahdi, A. Fihri, A. Solhy, *J. Appl. Polym. Sci.* **131** (2014) 41042 (https://doi.org/10.1002/app.41042)

13. X. Sui, Y. Chu, J. Zhang, H. Zhang, H. Wang, T. Liu, C. Han, *Adv. Polym. Technol.* **2020** (2020) 8859658 (https://doi.org/10.1155/2020/8859658)

14. C. S. Reddy, P. K. Babu, K. Sudhakar, M. N. Prabhakar, P. Sudhakar, S. V. Pratap, S. H. R. Prasad, V. N. E. Reddy, M. C. S. Subha, K. C. Rao, *Polym. Res. J.* **7** (2013) 253 (https://www.researchgate.net/profile/Palla-Kumara-Babu/publication/281743945_miscibility_studies_of_hydroxyethyl_cellulose_and_poly_ethylene_glycol_polymer_blends/links/55f7c01a08aeafc8ac0569a1/miscibility-studies-of-hydroxyethyl-cellulose-and-poly-ethylene-glycol-polymer-blends.pdf)

15. G. El Fawal, H. Hong, X. Song, J. Wu, M. Sun, L. Zhang, C. He, X. Mo, H. Wang, *Appl. Biochem. Biotechnol.* **191** (2020) 1624 (https://doi.org/10.1007/s12010-020-03282-1)

16. K. C. Rao, M. C. S. Subha, C. S. Reddy, P. K. Babu, K. Sudhakar, M. N. Prabhakar, Y. Maruthi, U. S. K. Rao, *Int. J. Basic Appl. Chem. Sci.* **3** (2013) 73 (https://www.cibtech.org/J-CHEMICAL-SCIENCES/PUBLICATIONS/2013/Vol%203%20No.%201/10-004...Chowdoji...Miscibility...Blends...73-83.pdf)

17. B. Anwar, B. Bundjali, Y. Sunarya, I. M. Arcana, *Fibers Polym.* **22** (2021) 1228 (https://doi.org/10.1007/s12221-021-0765-8)

18. M. F. Zaltariov, *Cellul. Chem. Technol.* **55** (2021) 981 (https://doi.org/10.35812/CelluloseChemTechnol.2021.55.84)

19. Y. H. Wen, C. H. Tsou, M. R. de Guzman, D. Huang, Y. Q. Yu, C. Gao, Z. H. Wang, *Polym. Bull.* **79** (2022) 3847 (https://doi.org/10.1007/s00289-021-03666-1)

20. D. A. Rusmawati, I. Yuliasih, T. C. Sunarti, *IOP Conference Series: Earth and Environmental Science,* Vol. 443, (2020) International Conference on Food and Bio-Industry 2019, 29-30 July 2019, Bandung, Indonesia (https://doi.org/10.1088/1755-1315/443/1/012054)

21. E. Karavas, E. Georgarakis, D. Bikiaris, *Int. J. Pharm.* **313** (2006) 189 (https://doi.org/10.1016/j.ijpharm.2006.01.015)

22. Y. Prakash, D. Mahadevaiah, H. Somashekarappa, T. Demappa, R. Somashekar, *J. Res. Updates Polym. Sci.* **1** (2012) 24 (http://dx.doi.org/10.6000/1929-5995.2012.01.01.4)
23. R. Kumar, I. Mishra, G. Kumar, *J. Polym. Environ.* **29** (2021) 3770 (https://doi.org/10.1007/s10924-021-02143-0)
24. S. Patil, A. K. Bharimalla, A. Mahapatra, J. Dhakane-Lad, A. Arputharaj, M. Kumar, A. S. M. Raja, N. Kambli, *Food Biosci.* **44** (2021) 101352 (https://doi.org/10.1016/j.fbio.2021.101352)
25. A. Gleadall, in *Modelling Degradation of Bioresorbable Polymeric Medical Devices*, J. Pan, Ed., Elsevier Ltd., Amsterdam, 2015, p. 163 (https://doi.org/10.1533/9781782420255.2.163)
26. C. Ding, M. Zhang, G. Li, *Carbohydr. Polym.* **119** (2015) 194 (http://dx.doi.org/10.1016/j.carbpol.2014.11.057)
27. M. Voronova, N. Rubleva, N. Kochkina, A. Afineevskii, A. Zakharov, O. Surov, *Nanomaterials* **8** (2018) 1011 (https://doi.org/10.3390/nano8121011)
28. S. Wang, J. Ren, W. Li, R. Sun, S. Liu, *Carbohydr. Polym.* **103** (2014) 94 (http://dx.doi.org/10.1016/j.carbpol.2013.12.030)
29. J. F. Mukerabigwi, S. Lei, L. Fan, H. Wang, S. Luo, X. Ma, J. Qin, X. Huang, Y. Cao, *RSC Adv*. **6** (2016) 31607 (https://doi.org/10.1039/C6RA01759B)
30. M. Fiayaz, K. M. Zia, M. A. Javaid, S. Rehman, S. A. S. Chatha, M. Zuber, *Korean J. Chem. Eng*. **37** (2020) 2351 (https://doi.org/10.1007/s11814-020-0664-5)
31. A. D. French, M. S. Cintron, *Cellulose* **20** (2013) 583 (https://doi.org/10.1007/s10570-010-9420-z)
32. A. Emblem, in *Packaging Technology: Fundamentals, Materials and Processes*, A. Emblem, H. Emblem, Eds., Elsevier Ltd., Amsterdam, 2012, p. 287 (https://doi.org/10.1533/9780857095701.2.287)
33. S. Guzman-Puyol, J. J. Benítez, J. A. Heredia-Guerrero, *Food Res. Int.* **161** (2022) 111792 (https://doi.org/10.1016/j.foodres.2022.111792)
34. A. Aydogdu, E. Yildiz, Z. Ayhan, Y. Aydogdu, G. Sumnu, S. Sahin, *Eur. Polym. J.* **112** (2019) 477 (https://doi.org/10.1016/j.eurpolymj.2019.01.006)
35. R. Kumar, B. Rai, G. A. Kumar, *J. Polym. Environ.* **27** (2019) 2963 (https://doi.org/10.1007/s10924-019-01588-8)
36. T. Huhtamäki, X. Tian, J. T. Korhonen, R. H. Ras, *Nat. Protoc.* **13** (2018) 1521 (https://doi.org/10.1038/s41596-018-0003-z)
37. R. Poonguzhali, S. K. Basha, V. S. Kumari, *Polym. Bull.* **74** (2017) 2185 (https://doi.org/10.1007/s00289-016-1831-z)
38. P. Lu, H. Xiao, W. Zhang, G. Gong, *Carbohydr. Polym.* **111** (2014) 524 (https://doi.org/10.1016/j.carbpol.2014.04.071)
39. H. Y. Wu, T. X. Liu, C. H. Hsu, Y. S. Cho, Z. J. Xu, S. C. Liao, S. Y. Lien, *Materials* **10** (2017) 821 (https://doi.org/10.3390/ma10070821)
40. A. Zheng, Y. Xue, D. Wei, S. Li, H. Xiao, Y. Guan, *Soft Mater.* **12** (2014) 179 (https://doi.org/10.1080/1539445X.2013.831357)
41. T. T. Kararli, J. B. Hurlbut, T. E. Needham, *J. Pharm. Sci.* **79** (1990) 845 (https://doi.org/10.1002/jps.2600790922)
42. F. H. Zulkifli, F. S. J. Hussain, W. S. W. Harun, M. M. Yusoff, *Int. J. Biol. Macromol.* **122** (2019) 562 (https://doi.org/10.1016/j.ijbiomac.2018.10.156)

43. K. Beyaz, C. Vaca-Garcia, E. Vedrenne, N. Haddadine, A. Benaboura, S Thiebaud-Roux, *Int. J. Polym. Anal. Charact.* **24** (2019) 245 (https://doi.org/10.1080/1023666X.2019.1567085)

44. T. M. M. Swamy, B. Ramaraj, Siddaramaiah, *J. Appl. Polym. Sci.* **112** (2009) 2235 (https://doi.org/10.1002/app.29738)

45. J. B. Yin, K. Luo, X. S. Chen, V. V. Khutoryanskiy, *Carbohydr. Polym.* **63** (2006) 238 (https://doi.org/10.1016/j.carbpol.2005.08.041)

46. V. Mutalik, L. S. Manjeshwar, A. Wali, M. Sairam, B. Sreedhar, K. V. S. N. Raju, T. M. Aminabhavi, *J. Appl. Polym. Sci.* **106** (2007) 765 (https://doi.org/10.1002/app.25427).

Removal of lead and cadmium from aqueous solution using octacalcium phosphate as an adsorbent

MILJANA M. MIRKOVIĆ[1]*, IVAN D. BRACANOVIĆ[1#], ALEKSANDAR D. KRSTIĆ[2#], DUNJA D. ĐUKIĆ[3], VLADIMIR M. DODEVSKI[1] and ANA M. KALIJADIS[1]

[1]Department of Materials, Vinča Institute of Nuclear Sciences – National Institute of the Republic of Serbia, University of Belgrade, Mike Petrovića Alasa 12–14, 11000 Belgrade, Serbia, [2]Department of Physical Chemistry, Vinča Institute of Nuclear Sciences – National Institute of the Republic of Serbia, University of Belgrade, Mike Petrovića Alasa 12–14, 11000 Belgrade, Serbia and [3]University of Belgrade, Faculty of Biology, Studentski Trg 16, 11000 Belgrade, Serbia

Abstract: Octacalcium phosphate (OCP) is a material from the calcium phosphate group with a crystal structure similar to hydroxyapatite. The removal process of lead and cadmium in aqueous solution using octacalcium phosphate material was investigated. OCP material was synthesized by the solution precipitation method. The structural and phase properties of OCP before and after the removal process were determined by the X-ray diffraction (XRD) method. Microstructural and semi-quantitative analysis of the material was investigated by scanning electron microscopy and energy dispersive X-ray spectroscopy (SEM-EDS). Characteristic bands and functional group determination were revealed using the Fourier-transform infrared spectroscopy with attenuated total reflection (FTIR-ATR). As target pollutants, Cd(II) and Pb(II) were chosen in adsorption experiments. Results show that OCP in the first 10 min has a very fast removal rate for Pb(II); the equilibrium state was reached after 10 min with more than 98 % adsorption efficiency. Results for Cd(II), results showed the same removal rate but somewhat lower adsorption efficiency, amounted to approximately 63 %.

Keywords: calcium phosphate material; adsorption; water purification; heavy metals.

INTRODUCTION

Due to their exceptional crystallographic, ecologically acceptable, non-toxic, and biocompatible properties, materials from the calcium phosphate group have a

231

significantly wide range of uses. One of the interesting ones from this group is octacalcium phosphate (OCP), with particularly unique properties,[1] next to hydroxyapatite (HA), which presents the most common calcium phosphate materials with a wide range of uses.[2,3] Octacalcium phosphate stimulates bone regeneration due to the chemical characteristics of this material, in which Ca^{2+} or PO_4^{3-} are released from the structure, and bone growth occurs in a certain direction; this activity helps the process of bone regeneration and conversion of OCP to HA.[4] Taking into account that certain good structural and, therefore, chemical properties of octacalcium phosphate can be designed by various synthesis methods, this material also can be used as an adsorbent for the removal of organic pollutants from aqueous solutions or a cation exchanger for water defluoridation.[5,6]

The possibility of using octacalcium phosphate material as a potential remover for the immobilization of organic molecules but also heavy metals, regarding its non-stoichiometric composition and structural defects at calcium ion sites and phosphate ion lattice positions, which can be replaced with cationic and anionic ions in structure.[2,7] This material has an interesting layered structure, where the HPO_4^{2-} in a hydrated layer of OCP can be replaced and stacked in an apatite layer.[1,8] In the previous studies, it's been reported that interlayers in OCP structure recognize the chirality of some organic compounds during the incorporation process.[8] Various syntheses of this material exist and have been used so far. However, precipitation is one of the simplest and most commonly used methods for obtaining materials with precisely defined characteristics.[10–13]

The main idea of this work is the synthesis of pure octacalcium phosphate material using acetate solutions as a source of calcium and hydrogen phosphate as a source of phosphorus group for its synthesis relying on ecological and cheaper synthesis methods using precursors other than nitrates or phosphoric acid. The study's main goal was to define the morphological and crystallographic parameters of the material obtained, which was used to remove heavy metal ions such as Cd(II) and Pb(II). The results of this study show the benefit of using octacalcium phosphate, which is non-toxic to the environment, where its disposal in the ecosystem represents a biofertilizer because it becomes a source of phosphorus and calcium for plants.[13]

EXPERIMENTAL

Octacalcium phosphate powder (OCP) was synthesized by a slightly modified solution-precipitation method, than the previously published,[11] by titration of 250 mL $Ca(CH_3COO)_2$ (Sigma Aldrich, *p.a.*) solution with a molar concentration of 0.04 M with 750 mL $NaH_2PO_4 \cdot H_2O$ (Kemika, Zagreb, *p.a.*) solution with molar concentration 0.013 M. The temperature during titration synthesis was adjusted to 60 °C, and the pH value of approximately 5 pH units was maintained throughout the titration process, checked by pH meter (LLG Labware, Meckenheim, Germany). The solution in the beaker was stirred at 100 rpm, and the solution in the burette was set to drip one drop per second. After synthesis, the precipitate was transferred to a fine-grade filter paper and washed three times in distilled water and once in

alcohol, after which it was dried at 40 °C for 12 h. As a final result, fine white powder was obtained.

Structural and phase characteristics of the synthesized material were examined by the X-ray diffraction method (XRD) on a polycrystalline sample using a Siemens D500 X-ray diffractometer with CuKα radiation and Ni filter, in the 2θ range from 10 to 60°, with a scanning step size of 0.02, and scanning time of 0.5 s per step. Find It Inorganic Crystal Structure Database was used for structural data calculation and phase identification of octacalcium phosphate, using card number: ICSD #65347, and PDF2 Release 2023, using card numbers: 01-071-5049 for hydroxyapatite and 01-087-2477 for decalead hexakis(phosphate(V)) dihydroxide. Crystallite sample sizes were calculated using the Scherrer equation,[15] and structural parameters were obtained by the Powder Cell crystallographic program.[16]

The sample's morphology and surface properties were investigated using a JEOL JSM-6610LV scanning electron microscope. Before semi-quantitative EDS analysis, the unpolished sample was coated with Au – thickness 18.0 nm.

Fourier transform infrared spectroscopy with attenuated total reflection (FTIR-ATR) was used to analyze surface functional groups and the chemical nature of the OCP sample. FTIR-ATR spectra were recorded on a Thermo Fisher Scientific spectrometer, model Nicolet IS 5. For spectra processing, the Omnic program (Thermo Fisher Scientific) was used.

For adsorption kinetics experiments, Cd(II) and Pb(II) were chosen as target pollutants. The adsorbate solution was prepared from the mixture of nitrate salts, $Cd(NO_3)_2$ and $Pb(NO_3)_2$. The 20 mg of OCP sample was measured and added to the plastic tube containing 50 cm^3 of Cd(II) and Pb(II) mixture solution concentration of 40 mg/dm^3 of each pollutant. Then, the prepared mixture was shaken at 180 rpm for 24 h, and 1 cm^3 of aliquot was taken at intervals, 10, 20, 30, 60, 120, 180, 300 min and 24 h. The pH value of 40 ppm adsorbate solution was 5.5, and that value was chosen for experiments. The reason for that lies in the fact that higher pH values (pH > 6) lead to the formation of insoluble metal hydroxides, while lower pH values (pH < 4) lead to the competitive adsorption between positive Cd(II), Pb(II) ions and protons. After adsorption, the aliquot was properly diluted, acidified with HNO_3, passed through a 0.45 µm PTFE filter, and analyzed by ICP-OES spectrometer (ThermoFisher Scientific ICAP duo 7400). All adsorption experiments were performed at 25 °C in duplicate. The blank probe was also prepared. The removal efficiency of OCP for each contaminant at time τ was calculated by the following equation:[17]

$$\text{Removal} = 100\frac{C_0 + C_t}{C_0} \tag{1}$$

where C_0 and C_t (mg/dm^3) are the initial and concentration at time t (min) of pollutants, respectively.

For analysis of the adsorption kinetics study, pseudo-first-order and pseudo-second-order were used as theoretical models. The equation of pseudo-first-order is given as:[17]

$$Q_t = Q_e(1 - e^{-k_1 t}) \tag{2}$$

Where Q_t (mg/g) is the amount of adsorbed pollutant at time t (min), Q_e (mg/g) is the initial pollutant concentration in equilibrium, and k_1 (1/min) is the pseudo-first-order rate constant.

The equation of pseudo-second-order is given as:[17]

$$Q_t = Q_e(\frac{1}{Q_e} + k_2 + t)^{-1} \tag{3}$$

where k_2 (g/mg min) was the pseudo-second-order rate constant.

The parameters k_1, k_2 and Q_e were obtained from the intercept and slope of the Q_t *versus t.*

The adsorption isotherms were investigated to clarify the interaction between pollutants and OCP in solution at equilibrium and determine maximum adsorption capacity.[18] The mixture was prepared by the same procedure that was mentioned above in the concentration range 40–500 mg/dm^{3} per pollutant. The prepared mixture was shaken at 200 rpm, the pH value of the adsorbate solution was 5.5, and the equilibration time was 3 h. After equilibration, 1 cm[3] of mixture was taken, properly diluted, and analyzed by ICP-OES. All adsorption experiments were performed at 25 °C in duplicate. The blank probe was also prepared. The following equation calculated the adsorption capacity:[17]

$$Q_e = \frac{V(C_0 - C_e)}{W} \tag{4}$$

where Q_e is the adsorbed amount of pollutant (mg/g), W is the mass of OCP (g), V is the volume of sample aliquot (cm[3]), and C_0 and C_e are the initial and equilibrium concentrations of adsorbed pollutant.

Langmuir and Freundlich's isotherms were used as theoretical models to analyze adsorption isotherms. The general Langmuir equation was presented as follows:[17]

$$Q_e = \frac{Q_{max}bC_e}{1 + bC_e} \tag{5}$$

where Q_{max} is the theoretical maximum adsorption capacity of the adsorbent (mg of pollutant per gram of adsorbent, mg/g), b is the constant related to the heat of adsorption (dm[3]/g).

The Freundlich isotherm can be represented as follows:[17]

$$Q_e = K_f C_e^{1/n_F} \tag{6}$$

Where K_f is the Freundlich empirical constant related to the adsorption capacity, (mg/g) (dm[3]/mg))[1/n]; $1/n_F$ is the heterogeneity factor.

RESULTS AND DISCUSSION

SEM micrographs with EDS analysis of obtained OCP material are presented in Fig. 1. Fig. 1a represents agglomerates with sizes in diameters of approximately 35 μm. The morphology of agglomerates is in spherical forms. Fig. 1b shows the detailed morphology of synthesized OCP powder. Proper crystal grains of OCP have plate-like morphology, which agrees with the precipitation method of synthesis.[19] Also, this kind of crystal formation is known in the literature as a petal-like structure.[20] Prismatic plate-like grains are stacked together in such a way that they form the appearance of a blooming flower.

Based on obtained and calculated EDS spectra, the Ca/P ratio is 1.33, typical for octacalcium phosphate materials.[21]

Fig. 2a shows the XRD pattern corresponding to synthesized OCP material. Based on the presented results, slightly wider peaks with a slightly higher baseline indicate a small crystallite size in the material, obtained by the precipitation

method of synthesis.[11–13,15,16,22] Based on the results presented, the material reveals sharp and well-defined peaks indicating proper structural arrangement. Peaks in the 2θ region from about 35 to 55° have higher intensities, which we can assume is a preferential orientation created during the sample preparation. This occurs when plate-like crystals are stacking during the application of the sample to the carrier. This phenomenon often leads to the increment of peak intensities of specific monolayer reflections.[23]
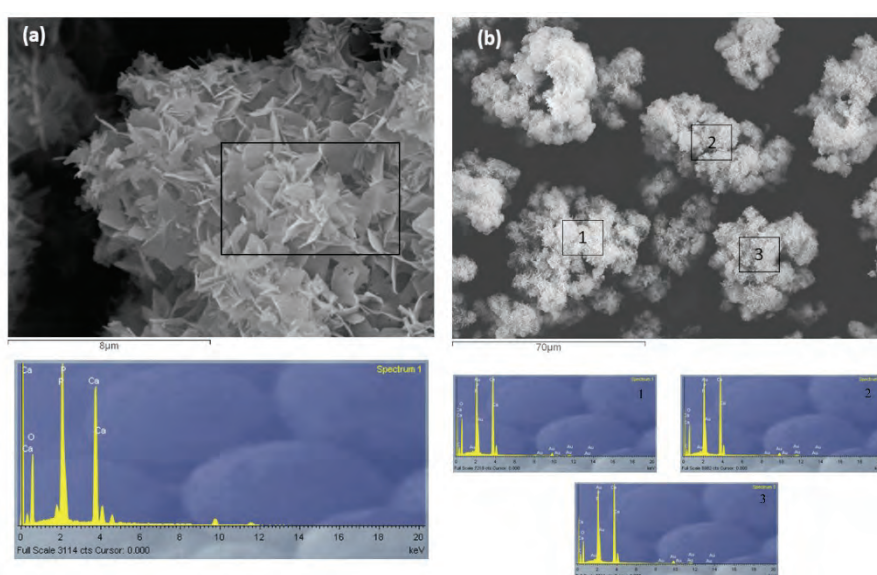
Fig. 1. Micrographs of OCP: a) Lower magnification presentation with EDS spectra, b) enlarged detail with EDS spectrum.

Refinement of structural parameters of the OCP sample is done using the Powder Cell program and ICSD file number 65347, space group $P\bar{1}$. The results of refinement are presented in Table I.

Structural results for OCP shown in Table I indicate that the unit cell parameters have smaller parameters compared to the literature data. Lower lattice parameters are size-related changes of lattice parameters and present a deficit of the intercrystalline pressure in a small particle. The calculated crystallite size of about 200 nm confirms that as the particle size decreases, the lattice parameter of the nanoparticle decreases.[24] Results of OCP confirm that crystal sizes determine the size-related change of the length of each lattice edge in a perpendicular direction or the above mentioned preferred orientation, as explained in Fig. 1a.[25] Also obtained structural strain of 0.000176 ‰, which indicates the existence of low structural deformations, may be related to the dislocations between small

crystallites. The results of the refined parameters indicate that nanocrystalline octacalcium phosphate with good structural order was obtained by this method.
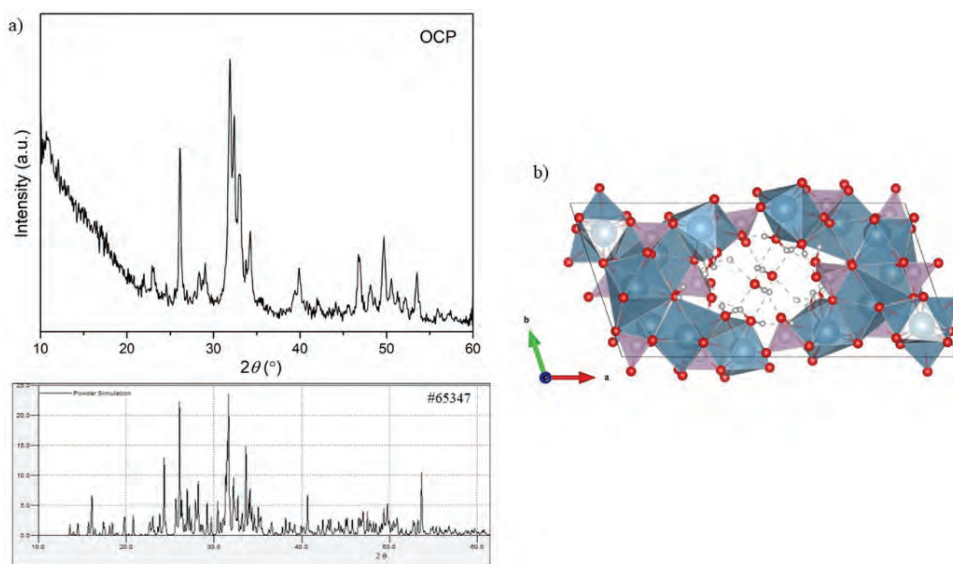
Fig. 2. a) XRD results of OCP with matching card #65347 and b) crystal structure of OCP in the direction of the *c* axis (red spheres are oxygen atoms, grey spheres are hydrogen atoms, hydrogen bonds are shown in dashed lines, PO_4 tetrahedral are presented in purple and CaO_8 octahedral are presented in blue color).

TABLE I. Refinement results; unit cell parameters of synthesized OCP sample

Sample	a / Å	b / Å	c / Å	α / °	β / °	γ / °
ICSD #65347	19.7920(3)	9.6230(3)	6.9350(3)	91.150(3)	93.540(3)	109.650(3)
OCP	19.666(5)	9.519(2)	6.8260(3)	90.120(6)	92.498(4)	108.660(1)

The FTIR-ATR spectra of OCP samples and OCP samples after Pb(II) and Cd(II) removal (OCP_{PC}) are shown in Fig. 3a and b. For both samples, the most dominant peaks are near 1018 and 558 cm^{-1}, which originate from stretching vibrations of P–O bands and bending vibrations of O–P–O, respectively, and can be assigned to the PO_4^{3-} group.[26–29] Additionally, stretching vibration at 865 cm^{-1} can be attributed to the HPO_4^{2-} in the hydrated layers of OCP crystals.[27,29] Crystalline water in samples is represented by a broad peak at 3500 cm^{-1}.[26] Two shoulder straps which can be observed only for pristine OCP sample at 1071 and 1190 cm^{-1} could originate from stretching and bending vibration attributed to the HPO_4^{2-} group in OCP crystal structure (Fig. 3b) and these vibration peaks of PO_4^{3-} and HPO_4^{2-} groups are typical for OCP crystal formation.[27]

From the OCP_{PC} spectrum it can be seen that the main differences, compared to pristine OCP, are the absence of peaks attributed to the HPO_4^{2-} group at

1071 and 1190 cm^{-1} as well as an increase of O–P–O bending vibrations intensity at 600 and 558 cm^{-1} and intensity of stretching vibration at 865 cm^{-1} of HPO$_4^{2-}$ group in the hydrated layers (Fig. 3b).[27,29] These are structural changes of OCP after the adsorption processes of lead and cadmium and the presence of more hydrated layers.
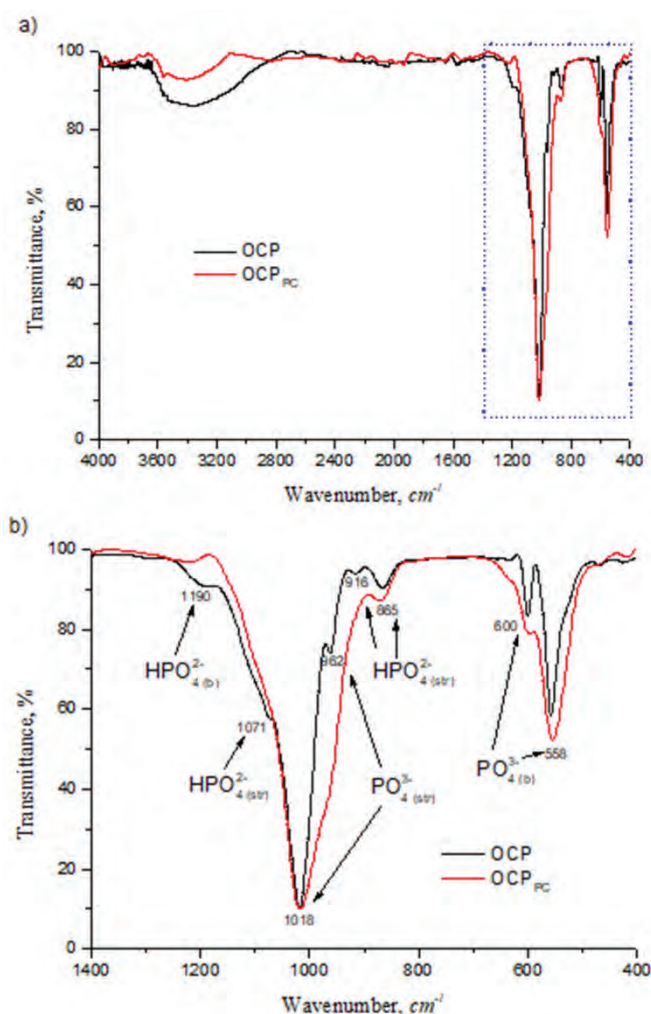
Fig. 3. a) FTIR spectra of OCP and OCP$_{PC}$; b) amplified image of the square marked area in a.

The summarized results of the adsorption kinetic study and the fitting plots are presented in Table II and Fig. 4, respectively. For Pb(II), in the first 10 min, a very fast removal rate with a rapid increase in adsorption capacity was observed. The equilibrium state was reached after 10 min when it adsorbed more than 98 %

Pb(II). In the case of Cd(II), a fast removal rate, also after 10 min, was observed with a lower adsorption capacity of about 63 %. After 10 min, adsorption was slower, and the equilibrium was reached after 2h of adsorption.

TABLE II. The fitting parameters of adsorption kinetics using the pseudo-first-order

Pollutant	Pseudo-first-order parameters		
	R^2	k_1 / min^{-1}	Q_e calcd. / mg g^{-1}
Cd (II)	0.8755	0.0763	74.84
Pb (II)	0.8359	0.2480	125.87
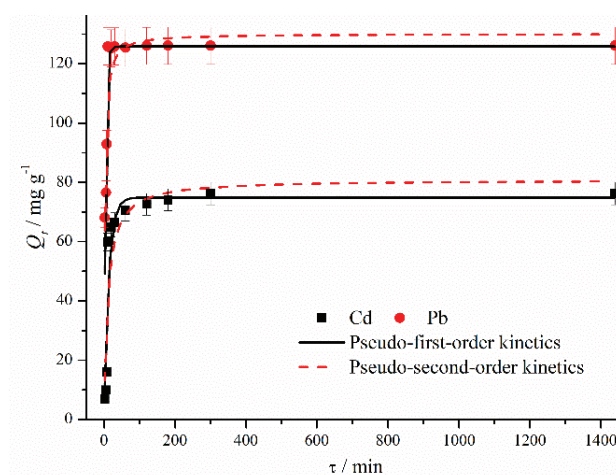
Fig. 4. Adsorption kinetic data for Cd(II) and Pb(II) and nonlinear fit with pseudo-first and pseudo-second-order kinetic models.

Comparing the removal rate after 10 min, it can be concluded that the removal rate of Pb(II) is two times higher than the removal rate of Cd(II) (Fig. 5). The fitting parameters of the adsorption kinetic model are present in Tables II and III. It can be observed that the correlation coefficient (R^2) is very similar for the both theoretical models and the both pollutants (ranged 0.8359–0.8827), but it is slightly higher for pseudo-second-order, and according to this fact, the adsorption of Cd(II) and Pb(II) can be described by the both models which confirm the good agreement, between Q_e experimental and Q_e calculated. According to the recent literature data, the pseudo-second-order model shows better agreement with most adsorption systems in this field. Since there is no adsorbate dissociation in our system, the pseudo-first-order model is the only logical choice to describe the kinetics of Cd(II) and Pb(II) adsorption on the OCP sample.[30] The lower rate constant value for Cd(II) shows that the OCP first adsorb the Cd(II). This observation indicates that the OCP sample has much better adsorption performance for Pb(II) removal in a mixture with Cd(II).
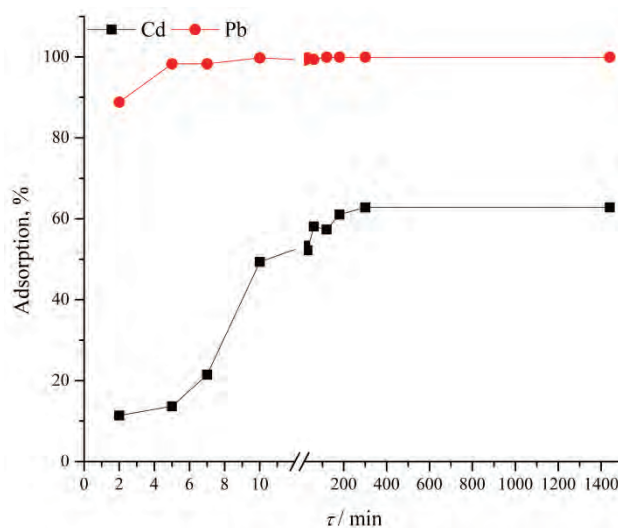
Fig. 5. Adsorption kinetic curves for Cd(II) and Pb(II) adsorption on OCP.

TABLE III. The fitting parameters of adsorption kinetics using the pseudo-second-order models

Pollutant	Pseudo-second-order parameters			Q_e exp. / mg g^{-1}
	R^2	k_2 / g mg min^{-1}	Q_e calcd. / mg g^{-1}	
Cd (II)	0.8827	0.0973	80.90	77.52
Pb (II)	0.8472	0.4805	130.11	128.54

The results of the adsorption isotherms study are presented in Fig. 6 and Tables IV and V. Based on the R^2 value, adsorption data of Cd(II) and Pb(II) could be well described by the Langmuir isotherm model. Theoretical maximum
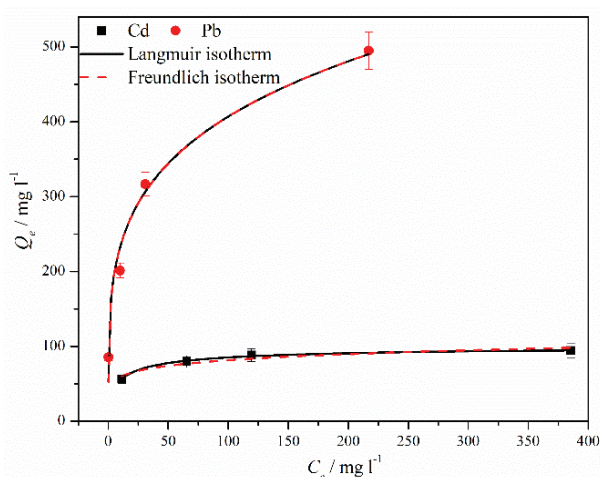
Fig. 6. Adsorption isotherms fitted by Langmuir and Freundlich model.

adsorption capacity (Q_{max}) obtained from Langmuir isotherm is much higher for Pb(II) (1951 mg/g) than Cd(II) (104 mg/g), which confirms excellent adsorption performance of the OCP sample for Pb(II) removal. The shape of the isotherm curve for Pb(II) shows that the plateau stage is not reached, which means that removal of Pb(II) at a higher concentration is possible. Also, the affinity for Pb(II) removal is much higher than the affinity for Cd(II) removal.

TABLE IV. The fitting parameters of Langmuir adsorption isotherm

Pollutant	Parameter		
	R^2	Q_{max} / mg g^{-1}	b / dm^3 mg^{-1}
Cd (II)	0.9863	104	0.2657
Pb (II)	0.9693	1951	6.99×10^{-4}

TABLE V. The fitting parameters of adsorption isotherm using the Freundlich model

Pollutant	Parameter		
	R^2	K_F / mg g^{-1} (dm^3 mg^{-1})$^{1/n}$	$1/n_F$
Cd (II)	0.8920	43.33	0.1373
Pb (II)	0.9248	134.63	0.2403

In order to check the goodness of fit for the Freundlich models in a different range of points, a fitting was done in the middle range of points, with no points at low concentrations and high concentration - near saturation limits. The results are shown in Table VI and Fig. 7. A difference was observed in the case of Pb adsorption. A better agreement of the Freundlich model was established in the middle range of points, which was confirmed by a higher value of the coefficient R^2.

TABLE VI. The fitting parameters of adsorption isotherm for Pb fitted in the middle range of points using the Freundlich model

Pollutant	Parameter		
	R^2	K_F / mg g^{-1} (dm^3 mg^{-1})$^{1/n}$	$1/n_F$
Pb (II)	0.9682	119.50	0.2658

With the aim of better understanding the entire process of removing targeted heavy metal ions from aqueous solutions, XRD analysis of OCP was performed after adsorption experiments. In Fig. 8, the XRD diffractogram of the dried OCP$_{PC}$ sample is presented. On the basis of the presented results, two phases are identified. The peaks primarily belong to the phase declared hexakis(phosphate(V)) dihydroxide – $Pb_{10}(PO_4)_6(OH)_2$, with hexagonal symmetry, *e.g.*, $P6_3/m$. The other identified phase belongs to hydroxyapatite $Ca_5(PO_4)_3OH$ with the same structural property. The identified hydroxyapatite phases are characterized by clear, sharp and well-defined peaks that indicate a good structural arrangement of these phases. A slightly higher background indicates a certain content of
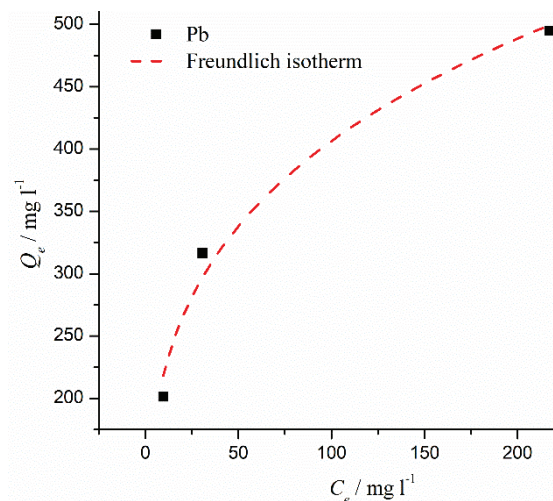
Fig. 7. Adsorption isotherm for Pb fitted in the middle range of points by Freundlich model.
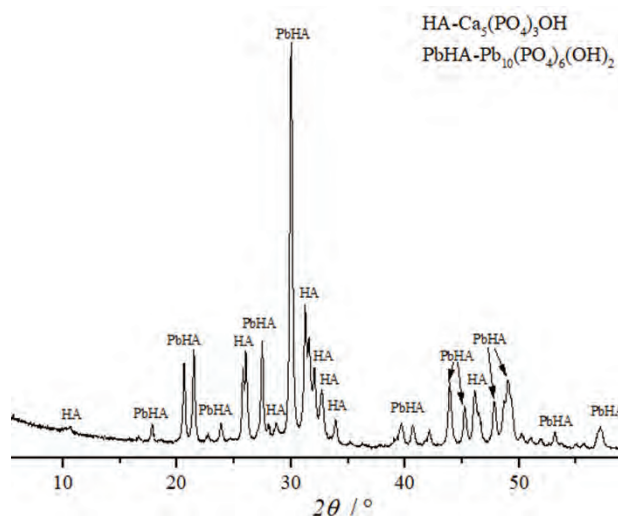
Fig. 8. X-ray powder diffractogram of dried OCP_{PC} sample.

the amorphous phase after adsorption experiments. Based on these analyses, it can be said that phase and structural transformations of octacalcium phosphate occurred in the presence of lead. In the positions where calcium was found, the incorporation of lead and the formation of a hexagonal structure occurred first, along with the formation of hydroxyapatite, which represents a more stable structural hexagonal form into which triclinic octacalcium phosphate tends to convert most often by the dehydration process. This was also confirmed by FTIR-ATR analysis (Fig. 3b). In the OCP structure, the HPO_4–OH layer is unstable in tri-

clinic structure; because of this, it is easily transformed to hydroxyapatite (HAp) *via* dehydration upon further immersion.[31] The same process happened with Pb(II) ions, which made a stable further insoluble salt.

CONCLUSION

The targeted octacalcium phosphate material was successfully obtained by solution precipitation method using acetate and sodium phosphate solutions. The parameters calculated using XRD data show that monocrystalline material was obtained with some lower unit cell parameters compared to data from the literature. FTIR spectra revealed characteristic vibration peaks of PO_4^{3-} and HPO_4^{2-} groups, which are typical for OCP crystal formation. The prismatic and petal-like microstructure of OCP crystal grains is confirmed by SEM analysis, with a 1.33 Ca/P ratio. For Cd(II), the theoretical maximum adsorption capacity was 104 mg/g, and with lower adsorption capacity by about 63 %, while after 10 min adsorption was much slower, and equilibrium was reached after 2h. Excellent adsorption performance of the OCP for Pb(II) removal, which is obtained from Langmuir isotherm, was 1951 mg/g of theoretical maximum adsorption capacity, with up to 98 % of adsorption capacity in the first 10 min. After adsorption experiments, XRD analysis showed the structural transformation of octacalcium phosphate into a hexagonal symmetry structure corresponding to the hydroxyapatite phase. This mechanism of interlocking of lead in the structure of OCP and its translation into a stable, further insoluble lead salt, on the basis of which the use of this material can be recommended for the remediation of soils polluted with high concentrations of lead.

ИЗВОД

УКЛАЊАЊЕ ОЛОВА И КАДМИЈУМА ИЗ ВОДЕНОГ РАСТВОРА КОРИСТЕЋИ ОКТАКАЛЦИЈУМ-ФОСФАТ КАО АДСОРБЕНТ

МИЉАНА М. МИРКОВИЋ[1], ИВАН Д. БРАЦАНОВИЋ[1], АЛЕКСАНДАР Д. КРСТИЋ[2], ДУЊА Д. ЂУКИЋ[3], ВЛАДИМИР М. ДОДЕВСКИ[1] И АНА М. КАЛИЈАДИС[1]

[1]Одсек за материјале, Институт за нуклеарне науке Винча – Национални институт Републике Србије, Универзитет у Београду, Мике Петровића Аласа 12–14, 11000 Београд, [2]Одсек за физичку хемију, Институт за нуклеарне науке Винча – Национални институт Републике Србије, Универзитет у Београду, Мике Петровића Аласа 12–14, 11000 Београд и [3]Универзитет у Београду, Биолошки факултет, Студентски трг 16, 11000 Београд

Октакалцијум-фосфат (OCP) је материјал из групе калцијум-фосфата са кристалном структуром сличном хидроксиапатитској. Испитиван је процес уклањања олова и кадмијума у воденом раствору коришћењем синтетисаног октакалцијум-фосфата. Октакалцијум-фосфатни материјал је синтетисан методом преципитације из раствора. Структурна и фазна својства OCP одређена су методом рендгенске дифракције на поли-

кристалном узорку пре и након процеса уклањања полутаната из раствора. Методе ске-
нирајуће електронске микроскопије са енергетско дисперзивном рендгенском спектро-
скопијом коришћене су за одређивање микроструктурне и семи-квантитативне анализе
синтетисаног материјала (SEM-EDS). Карактеристичне траке и одређивање функцио-
налних група одређиване су коришћењем инфрацрвене спектроскопије са Фоуриеровом
трансформацијом са ослабљеном тоталном рефлексијом (FTIR-ATR). За циљне загађи-
ваче изабрани су кадмијум и олово у експериментима адсорпције. Резултати показују да
OCP у првих 10 min има изузетну брзину уклањања олова; равнотежно стање је постиг-
нуто након 10 min са више од 98 % ефикасности адсорпције. За кадмијум резултати
показују исту брзину уклањања али нешто нижу ефикасност адсорпције која износи око
63 %.

REFERENCES

1. T. Yokoi, M. Kamitakahara, C. Ohtsuki, *Dalton Trans.* **44** (2015) 7943
   (https://doi.org/10.1039/C4DT03943B)
2. R. Hamai, S. Sakai, Y. Shiwaku, T. Anada, K. Tsuchiya, T. Ishimoto, T. Nakano, O.
   Suzuki, *Appl. Mater. Today* **26** (2022) 101279
   (https://doi.org/10.1016/j.apmt.2021.101279)
3. O. Suzuki, R. Hamai, S. Sakai, *Acta Biomater.* **158** (2023) 1
   (https://doi.org/10.1016/j.actbio.2022.12.046)
4. S.V. Dorozhkin, M. Epple, *Angew. Chem. Int. Ed.* **41** (2002), 3130
   (https://doi.org/10.1002/1521-3773(20020902)41:17<3130::AID-ANIE3130>3.0.CO;2-1)
5. A. Idini, E. Dore, D. Fancello, F. Frau, *Heliyon* **5** (2019) e02288
   (https://doi.org/10.1016/j.heliyon.2019.e02288)
6. I. Yamada, M. Tagaya, *Colloid Interface Sci. Commun.* **30** (2019) 100182
   (https://doi.org/10.1016/j.colcom.2019.100182)
7. Z. Jianhu, S. Jiacai, Y. Xiaojun, S. Yiping, *J. Mater.* **55** (2020) 7502
   (https://doi.org/10.1007/s10853-020-04539-0)
8. W.E. Brown, M. Mathew, M.S. Tung, *Prog. Cryst. Growth Charact.* **4** (1981) 59
   (https://doi.org/10.1016/0146-3535(81)90048-4)
9. T. Yokoi, S. Machida, Y. Sugahara, M. Hashimoto, S. Kitaoka, *Chem. Commun.* **53**
   (2017), 6524 (https://doi.org/10.1039/C7CC01169E)
10. R. O'Sullivan, D. Kelly, in *Octacalcium Phosphate Biomaterials*, O. Suzuki, G. Insley,
    Eds., Woodhead Publishing, Sawston, 2020, pp. 147–176 (https://doi.org/10.1016/B978-
    0-08-102511-6.00007-8)
11. M.J. Arellano-Jiménez, R. García-García, J. Reyes-Gasga, *J. Phys. Chem. Solids* **70**
    (2009) 390 (https://doi.org/10.1016/j.jpcs.2008.11.001)
12. S. Mandel, A.C. Tas, *Mater. Sci. Eng., C* **30** (2010) 245
    (https://doi.org/10.1016/j.msec.2009.10.009)
13. O. Suzuki, *Acta Biomater.* **6** (2010) 3379 (https://doi.org/10.1016/j.msec.2009.10.009)
14. P. Sharma, S. Sangwan, S. Mehta, in *Engineered Nanomaterials for Sustainable
    Agricultural Production, Soil Improvement and Stress Management*, A. Husen, Ed.,
    Academic Press, Cambridge, MA, 2023, pp. 71–97 (https://doi.org/10.1016/B978-0-323-
    91933-3.00008-8)
15. A.L. Patterson, *Phys. Rev.* **56** (1939) 978 (https://doi.org/10.1103/PhysRev.56.978)

16. W.K. Nolze, *J. Appl. Cryst.* **29** (1996) 301 (https://doi.org/10.1107/S0021889895014920)
17. A. Krstić, A. Lolić, M. Mirković, J. Kovač, T. M. Arsić, B. Babić, A. Kalijadis, *J. Environ. Chem. Eng.* **10** (2022) 108998 (https://doi.org/10.1016/j.jece.2022.108998)
18. J. Zhu, J. Shu, X. Yue, Y. Su, *J. Mater. Sci.* **55** (2020) 7502 (https://doi.org/10.1007/s10853-020-04539-0)
19. T. Miyazaki, Y. *Mater. Lett.X* **15** (2022) 100151 (https://doi.org/10.1016/j.mlblux.2022.100151)
20. X. Zhao, S. Jiang, J. Rao, J. Zhou, Z. Li, J. Yang, K. Yan, H. Shi, *Mater. Lett.* **328** (2022) 133137 (https://doi.org/10.1016/j.matlet.2022.133137)
21. M. Asadi-Eydivand, M. Solati-Hashjin, A. Farzadi, N.A.A. Osman, *Ceram. Int.* **40** (2014) 12439 (https://doi.org/10.1016/j.ceramint.2014.04.095)
22. K. Onuma, M.M. Saito, Y. Yamakoshi, M. Iijima, Y. Sogo, K. Momma, *Acta Biomater.* **125** (2021) 333 (https://doi.org/10.1016/j.actbio.2021.02.024)
23. H.B. Lu, C.L. Ma, H. Cui, L.F. Zhou, R.Z. Wang, F.Z. Cui, *J. Cryst. Growth* **155** (1995) 120 (https://doi.org/10.1016/0022-0248(95)00229-4)
24. W.H. Qi, M.P. Wang, Y.C. Su, *J. Mater. Sci. Lett.* **21** (2002) 877 (https://doi.org/10.1023/A:1015778729898)
25. M. Ya Gamarnik, *Phys. Status Solidi, B* **178** (1993) 59 (https://doi.org/10.1002/pssb.2221780105)
26. X. Zhao, S. Jiang, J. Rao, J. Zhou, Z. Li, J. Yang, K. Yan, H. Shi, *Mater. Lett.* **328** (2022) 133137 (https://doi.org/10.1016/j.matlet.2022.133137)
27. J. Liu, F.Qiu, Y. Zou, Z. Zhang, A. Wang, Y. Zhang, *Ceram. Int.* **49** (2023) 20315 (https://doi.org/10.1016/j.ceramint.2023.03.155)
28. A. Ressler, T. Ivanković, I. Ivanišević, M. Cvetnić, M. Antunović, I. Urlić, H. Ivanković, M. Ivanković, *Ceram. Int.* **49** (2023) 11005 (https://doi.org/10.1016/j.ceramint.2022.11.295)
29. H. Shi, X. Ye, J. Zhang, T. Wu, T. Yu, C. Zhou, J. Ye, *Bioact. Mater.* **6** (2021), 1267 (https://doi.org/10.1016/j.bioactmat.2020.10.025)
30. Y.S. Ho, G. McKay, *Process Biochem.* **34** (1999) 451 (https://doi.org/10.1016/S0032-9592(98)00112-5)
31. Y. Sugiura, Y. Makita, *J. Cryst. Growth* **583** (2022) 126545 (https://doi.org/10.1016/j.jcrysgro.2022.126545).

Inhibition study of curcumin extract's effect on dissimilar aluminium joint

KAMATCHI PRAVINKUMAR*, VADDI SESHAGIRI RAO
and RENGARAJAN SATHISH

Department of Mechanical Engineering, St. Joseph's College of Engineering, OMR, Chennai-119, India

Abstract: Aluminium welded joints are offering greater interest to researchers owing to the replacement of heavy steel structures and reduction in the weight of the components used in the automobile and marine environments. In this study AA6061 and AA8011 have been welded by using the bobbin tool friction stir welding method and by varying the process parameters with the samples being subjected to corrosion environments. The corrosive nature of the welded alloys in the absence and presence of inhibitors (curcumin) has been examined by electrochemical methods and compared with raw samples. The ratio has been observed between 0.075 and 5.42 A cm^{-2}. The results reveal that corrosion control tendency has been improved by the AA6061 and AA8011 aluminium alloy joint in the presence of curcumin extract.

Keywords: Bobbin tool; aluminium alloys; Tafel plot; scanning electron microscopy.

INTRODUCTION

Researchers are facing many issues between economic growth and natural resource conservation while designing materials for constructive applications. In the 20th century, the climate change was considered to be a serious problem due to industrialization and globalization. Several studies were undertaken to improve the system's performance and the lifetime of the equipment. The efficiency or lifetime can be increased by altering the source metals by adding the minimum weight of low-density components such as aluminium, magnesium alloys and thin-walled components. Apart from various metals, aluminium alloys are used in the aeronautical field such as the construction of rocket fuel tanks owing to their superior strength, extraordinary fracture toughness, and stress corrosion cracking and durability.[1] Though aluminium alloys are exhibiting significant, desirable

---

properties, they are not without limitations such as surface degradation under working conditions, lower durability at high temperatures and lower wear resistance.[2] The modifications of the Al alloys are receiving good attention of the researchers for mechanical applications.[3] Aluminium alloys (ALA) such as 2XXX series (copper-based), 6XXX series, heat treatable and weldable and 8XXX series (iron-based), are used in most of the mechanical designs in manufacturing industries.[4] This component's structure lets modern technologies link comparable or dissimilar materials using solid-state joining methods, which are better than fusion welding.[5] Recently, various processes such as friction stir welding (FSW), friction surfacing, linear friction welding, and rotary friction welding have been used for joining or coating the surface.[6] Due to its solid-state nature, friction stir welding may combine magnesium and aluminium alloys without flaws.[7] FSW of aluminium alloys has been extensively studied for microstructure evolution and mechanical characteristics.[8] Though it possesses the quality of the joint, there are a few limitations such as the need for a backing plate that influences the flow of grain in the nugget zone, multi passes required to join thick plates, the occurrence of root flaws, and weaker heat generation due to a single shoulder. Bobbin tool friction stir welding (BOBTFSW) is a unique take on the commonplace method of friction stir welding. BOBTFSW has many advantages to conventional friction stir welding (CFSW).[9] Bobbin tool friction stir welding (BOBTFSW) is FSW with different tool morphology.[10] The BOBTFSW tool has two shoulders (upper and lower) and a probe, while the FSW standard tool has a shoulder and a probe. These shoulders touch the work piece's top and bottom. The lower shoulder replaces the FSW backing anvil. BOBTFSW's unique force system makes it more sophisticated than FSW.

Generally, aluminium alloys are resistant to corrosion due to the high reactiveness of oxygen and form a thin layer of oxides, but the material is subjected to service temperature which deteriorates its tensile strength and corrosion resistance property. The novelty of this work is to analyse the behaviour of weld joints which are made by a specially designed bobbin tool on AA6061-T6 and AA8011-H14 aluminium alloys in 1M sodium chloride solution at 25 °C. As stated in the earlier reports, only the electrochemical study was used on samples to explain the potentiodynamic polarization curve.[11] Curcumin with zinc sulphate as an inhibitor on dissimilar aluminium weld joints has not been documented in the literature. The welded sample's Tafel graphs are plotted using potentiodynamic data and the parameters will be compared between the raw sample in salt water and the sample with inhibition with salt water.

<div align="center">EXPERIMENTAL</div>

Materials and methods

The dissimilar grade of aluminium alloys of AA6061-T6 and AA8011-H14 grade was ordered and received in the form of plates with a size of 300 mm×300 mm×5 mm thickness.

AA6061 Aluminium forms a quasi-binary combination $AlMg_2Si$ with "balanced" Mg and Si.[12] Aluminium AA8011 is a high-grade alloy that can be used for bobbin tool welding. It was used to prepare the corrosion resistance test specimens from matrix material with iron and silicon alloying elements (Al6 (Fe,Mn)).[13]

The surface to be welded was polished and cleaned with silicon carbide paper and acetone. The BOBTFSW welding process set-up is shown in Fig. 1a. The tool's upper and lower shoulders have a diameter of 24 mm and a thickness of 5 mm. The pin having a diameter of 9 mm and a length of 5mm shown in Fig. 1b and a hardened cylindrical tool shown in Fig. 1c with a hardness of 59 HRC was selected. The alloys, AA6061 and AA8011 specimen plates were wire cut to a precise size of 100 mm×50 mm×5 mm is shown in Fig. 1d. The welding speed at the start was low and it grew to the desired speed. After welding, the metallographic samples were cut perpendicularly, polished and etched with Keller's reagent (2 ml HF, 3 ml HCl, 5 ml HNO_3, 190 ml H_2O) for 13 s. The welded specimens were subjected to the potentiodynamic polarization study. BOBTFSW welded test specimens with an area of 1 cm^2 were used as the working electrode.[14]
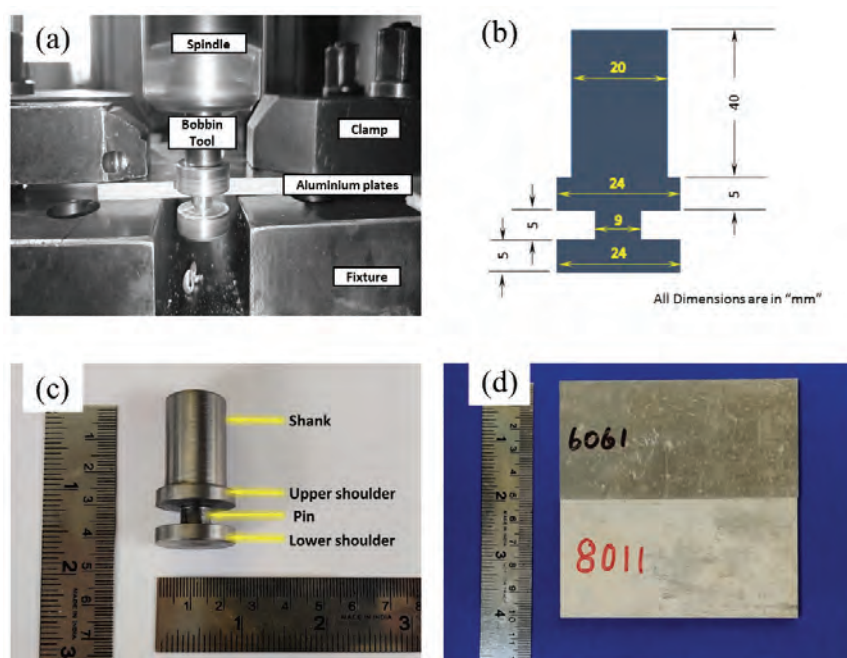
Fig. 1. a) BOBTFSW process; b) nomenclature of BOBTFSW; c) Bobbin tool; d) materials used for welding.

Bobbin tool welding and test specimen preparation

Fig. 2a illustrates the overview of the BOBTFS welding process using AA6061 and AA8011 alloys. The BOBTFSW alloys were nicely welded on both sides, with minor overlaps on the retreating side (RS) and a smooth interface on the advancing side (AS). Consistent arc patterns were observed on both sides, and the distance between arcs rose with a constant traverse speed of 40 mm min^{-1}. The samples were welded by varying the rotational speed from

600 to 1050 rpm. The surface of the tool increased plasticized metal to flow around the stirring pin, which reduced metal fill at the joint nearby area.[23] Because the greater welding rate provided less frictional heat, the specimen welded at a constant 40 mm/min had narrower heat-affected zone widths on both the AS and RS. Hence, this research selected seven samples out of ten for the corrosion-related potentiodynamic study.
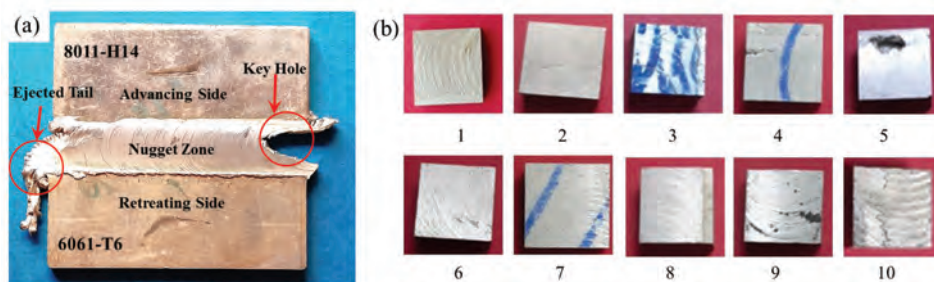
Fig. 2. a) Various zones in BOBTFS welded AA6061 and AA8011 aluminium alloys specimen; b) BOBTFS welded test specimens at various rpm and constant traverse speeds.

After the welding, the samples were sized as 1 cm×1 cm×0.5 cm as dimensions shown in Fig. 2b and subjected to the corrosion investigations. From the ten welded samples, S2, S3, S5, S6, S7, S9 and S10 were selected in the increasing order of their speed of rotation at constant traverse speeds for the corrosion investigation to find the effective rotational speed shown in Table I. The samples' potentiodynamic study in the presence and absence of inhibitors was carried out for stable mechanical design. In order to observe the welded samples' surface morphology, three different rotational speeds of 600, 850 and 1050 rpm of test specimens were used in Quanta 200 FEG-SEM.

TABLE I. Various BOBTFSW samples at constant traverse speed of 40 mm min^{-1} and different rpm

Ser. no.	rpm
1	600
2	650
3	700
4	750
5	800
6	850
7	900
8	950
9	1000
10	1050

Preparation of zinc sulphate solution and inhibitor solution

1.1 g of $ZnSO_4 \cdot 7H_2O$ was dissolved in 250 ml of distilled water and diluted for the corrosion inhibition investigation. 5 ml of this solution diluted to 100 ml gives 50 ppm of Zn^{2+}. 50 g of turmeric powder was boiled with distilled water and the suspending particles

were removed by filtration. The filtrate was used as an inhibitor solution and carried out for a potentiodynamic polarization study with the welded samples. The major chemical component of turmeric is curcumin and its tautomerism is shown in Fig. 3.
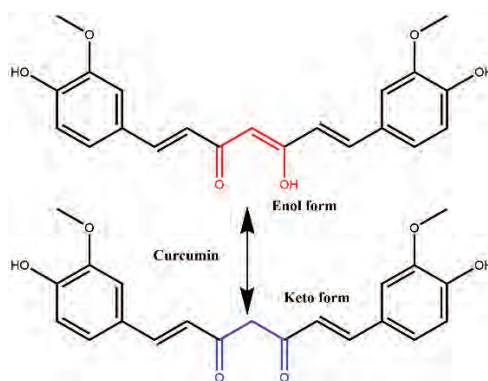
Fig. 3. Structure and keto-enol tautomerism of curcumin.

Potentiodynamic polarization and Tafel study

Electrochemical impedance spectroscopy (EIS) testing employed CH instruments electrochemical workstation system. The working area and metal specimens were immersed in 1 M saltwater electrolyte for 30 min and 1 h, respectively, before measurement. EIS studies at a constant potential used 10 mV excitation signals from 1 kHz to 100 MHz. Based on the charge transfer resistance, the impedance measurements were used to calculate the inhibition percentage. Welded samples were made using commercially pure rods and welded. The specimen for corrosion was prepared for 1 cm^2 active surfaces. Welded samples were impregnated with epoxy resin for electrochemical analysis. Then they were ground on water-resistant SiC abrasive paper to achieve an adequate surface finish. After grinding, the samples were rinsed, degreased and dried. Electrochemical tests were conducted in 1 M sodium chloride solution and the potentials are referred to saturated calomel reference electrode. Analytical purity reagents with 15 µS cm^{-1} demineralized water were used as electrolytes. A similar study was conducted in the presence of a curcumin and zinc salt mixture.[16] The obtained Tafel graphs were interpreted for the corrosion protective sample identification.

To determine the microcell corrosion rates, the reported polarization technique was conducted using the welded test specimens.[17,18] At room temperature, mirror-finished surfaces of BOBTF cuboid specimens and base metals were permitted to come into contact with varied quantities of selected 1 M sodium chloride electrolyte. In order to obtain a stable open circuit potential (OCP), the specimens were exposed to their respective electrolyte solutions for a period of 400 s. For the purpose of recording polarization curves, the specimens were polarized to a potential of 250 mV cathodically and 250 mV anodically with respect to OCP at a scan rate of 1 mV s^{-1}.

RESULTS AND DISCUSSION

This work has successfully welded the two dissimilar aluminium metals AA6061 and AA8011 for mechanical applications. By using this BOBTFS technique, this work has prepared the samples with symmetric thickness and low

distortion without the high force for fastening the selected aluminium plates. It is possible to make efficient use of the heat that is created since the backing plate does not cause any convection loss. Through this welding, the presence of dual rotational shoulders makes the specimens possible to weld alloys with a high melting temperature.[19,20]

The surface morphology of BOBTFS welded samples like low (600 rpm), medium (850 rpm) and higher (1050 rpm) was analysed using SEM.[21] Field emission scanning electron microscope (FESEM) images of selected welded samples are given in Figs. 4a–c. The SEM images have exposed fracture surfaces in different grain sizes due to the heat variation with respect to the rotation of 600 rpm. In Fig. 4a the sample exhibits that dynamic recrystallization in the stir zone area is low and grain size is big owing to minimum heat input. The weak area between the stir zone and mechanically affected zone fractures because the tool's relative displacement is highest in each spinning circle and its extrusion force on the metal conveyed by stirring decreases. Fig. 4b and c have demonstrated that the ductile fracture has several small, shallow dimples with the layered distribution. Likewise, 800 rpm and the highest 1050 rpm have shown dynamic recrystallization which formed fine grains that strengthen the welded zone. Heat input dissolves the stronger phase, increasing the heat-affected zone particle size.[22,23]
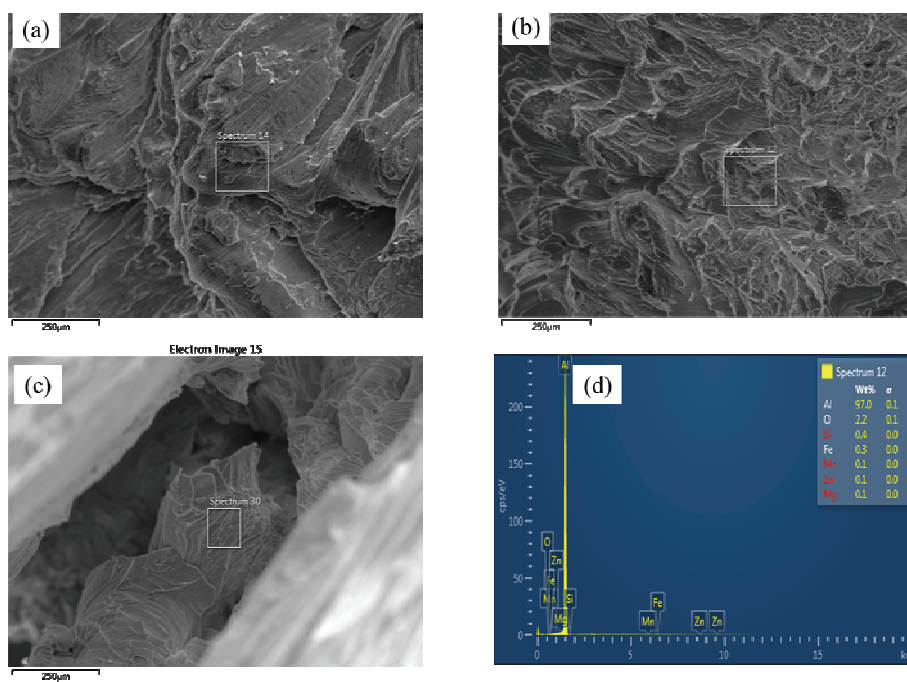
Fig. 4. Surface morphology of 250µm expanded SEM images of: a) 600, b) 850 and c) 1050 rpm welded samples; d) EDX of 850 rpm welded sample.

The samples revealed full penetration through the joint line, which gets rid of root difficulties as well as kissing bond mistakes, both of which are often seen in BOBTFW joints. Moreover, full penetration through the joint line removes any gaps between the joints. It is possible to readily weld thick parts due to the enhanced and balanced heat input at either side (both sides of the plate). This eliminates the need for numerous passes, which enables the complete weld penetration to be achieved in a single pass. In addition to this, the corrosion study was conducted to measure the sample life in NaCl solution and an electrochemical measuring instrument was used for the welded samples to optimize. The measurements of electrochemical polarization yielded corrosion potentials and current data which are used to construct the Tafel plot. According to the reported methods and results, the Tafel outcomes were interpreted.[24,25] The plotting was done for potential *vs.* log I values for the prepared welded samples in 1 M sodium chloride solution along with base metals such as AA8011 and AA6061. The graph potential exists (*x*-axis) between –1.5 and –0.5 V. Similarly, the log of current is observed between –1 and –10 A cm^{-2}. From the plotted graph, this work observed the potential of $E_{cor} = -1.12$ V and $E_{cor} = -1.14$ V for base metals such as AA8011 and AA6011. Similarly, the welded samples have exposed the same anodic (right) curve and different in the cathodic curve (left). In the absence of an inhibitor, the seven test specimens have shown a corrosion potential between –0.949 (sample 2) and –1.071 V (sample 7), which are less than the base metals. The Tafel outcomes of the specimens are shown in Table II. From the Tafel data, the sample 3 has higher corrosion current (I_{corr}) than the sample 6 in the absence of an inhibitor. Also, the welding process modified the samples towards the cathodic region when compared to the aluminium e.m.f. of –1.66 V. The recorded Tafel plots are presented in Fig. 5a–i. All plots show a slight difference in corrosion potential and corrosion current except the samples 2, 3 and 7. This result has revealed the rotating rpm impact on the corrosion resistance character. According to the electrochemical principle, when there is a rise in corrosion potential, it may be ascribed to either a decrease in the anodic reaction with the growth of a passive layer, or an increase in the cathodic reaction with an increase in dissolved oxygen; when there is a drop in corrosion potential, it can be attributed to the opposite of these two factors.[26,27] In addition, the Tafel plots are showing a positive side shift which is called anodic polarization. Anodic polarization causes higher corrosion initially and passive at last. But the corrosion potential is not significantly related to the corrosion rate. The corrosion current is directly related to the corrosion rate and converted to mm per year (mpy):

$$\text{Corr. rate (mpy)} =$$
$$= 0.13 I_{corr} \, (\mu\text{A cm}^{-2}) \times ((\text{eq. wt. of Al} = 9/(\text{density of Al} = 2.7)) \tag{1}$$

TABLE II. Potentiodynamic Tafel outcomes of the samples in the absence of an inhibitor; E_{corr} – corrosion potential; b_c – Tafel slope cathodic; b_a – Tafel slope anodic; I_{corr} – corrosion current density; Corr. rate – corrosion rate

Sample ID	E_{corr} / mV	b_c / mV dec⁻¹	b_a / mV dec⁻¹	I_{corr} / µA cm⁻²	Corr. rate, mpy
6061	−1132	141.4	233.7	1.006	4.359
8011	−1110	207.3	158.5	1.010	4.377
2	−949	227.8	168.0	1.1	4.767
3	−1013	302.8	164.4	3.687	15.977
5	−1041	184.4	154.3	0.5541	2.401
6	−1008	196.6	191.3	0.5033	2.181
7	−1071	209.0	153.8	0.9134	3.958
9	−963	197.8	164.0	0.6642	2.878
10	−1044	193.0	157.0	0.5750	2.492

Fig. 5. Tafel plots of samples in sea water: a) base metal Al8011, b) base metal Al6061 and samples: c) 2, d) 3, e) 5, f) 6, g) 7, h) 9 and i) 10.

From Table II, this research finds a higher corrosion rate for sample 3 (15.977 mpy) and a lower one for sample 6 (2.181 mpy). Also, it has been found that the order of corrosion rate is sample 3 > sample 2 > sample 7 > sample 9 > sample 10 > sample 5 > sample 6. The last four samples have exposed the reduced corrosion rate when compared with the base metal rate. The samples at low rpm between 600 and 700 have shown good corrosion control. Similarly, higher rpm between 1000 and 1050 has exposed corrosion resistance when compared to the base metals. This work tried to enhance the corrosion resistance of the

samples using natural turmeric organic extract and $ZnSO_4$ salt to control the corrosion.[28–30]

Similarly, the potentiodynamic study conducted for the prepared test samples used curcumin as an organic inhibitor with zinc sulphate as a complexing agent for the electron transformation reaction. The results of the potentiodynamic study, along with the inhibitor mixture, are shown in Table III.[31–33] The changes in corrosion potentials are observed when compared to the cases with the absence of inhibitors. The potential is observed between –1.116 and –0.989 V. These values are somehow less than AA6061 potential and close to AA8011. From the corrosion current values, the corrosion rate was calculated in this work and it is shown in Table III.

TABLE III. Potentiodynamic Tafel outcomes of the samples in the presence of inhibitor; E_{corr} – corrosion potential; b_c – Tafel slope cathodic; b_a – Tafel slope anodic; I_{corr} – corrosion current density; Corr. rate – corrosion rate

Sample ID	E_{corr} / mV	b_c / mV dec⁻¹	b_a / mV dec⁻¹	I_{corr} / μA cm⁻²	Corr. rate, mpy
6061	–1160	136.46	273.15	0.9971	4.321
8011	–1013	180.15	181.55	0.3820	1.655
2	–1095	158.03	382.26	1.831	7.934
3	–1116	258.26	196.93	7.652	33.159
5	–1006	127.94	213.17	0.1411	0.611
6	–1015	148.68	192.94	0.1543	0.669
7	–1115	229.36	188.22	4.950	21.450
9	–989	189.18	165.1	0.5509	2.387
10	–1011	157.98	202.51	0.1994	0.864

The calculated values show corrosion rates between 33.159 and 0.611 mpy. Based on the outcomes, the samples are arranged in the increasing order of their corrosion rate as sample 3 > sample 7 > sample 2> sample 9 > sample 10 > sample 6 > sample 5. Out of the seven samples, the samples 5, 6 and 10 have shown reduced corrosion rate when compared to all samples which include base metals represented in Fig. 6. Low rpm and high rpm samples show good control against corrosion and moderate speed affects the corrosion rate. The sample with a medium rotational speed and less penetration exhibits higher corrosion rates.

After the corrosion rate calculation in the presence of inhibition, linear polarization resistance (*LPR*) test was conducted in both the absence and the presence of inhibitors.[34–37] An *LPR* test, also known as a linear polarization resistance test, is a method for measuring the rate of corrosion, and it can provide an indicator of how resistant various materials are to corrosion in an aqueous environment.[38] Tests of *LPR* were carried out while the system was in a static state and also while it was moving back and forth. The corrosion potential and the corresponding current were measured in the potential between 10 and 20 mV. The resultant potential difference between the applied potential and the corrosion

potential *versus* the applied current, $(E_{app} - E_{corr})$ *vs.* I_{app} (positive anodic and negative cathodic) was used to plot the graph. The polarization resistance (Rp) was calculated using the slope value between the potential and the current density plot near E_{corr}. The relation between resistant potential and the current difference is:

$$Rp = \text{potential dif. } (\Delta E)/\text{current dif. } \Delta i \ (\Delta E \rightarrow 0) \tag{2}$$

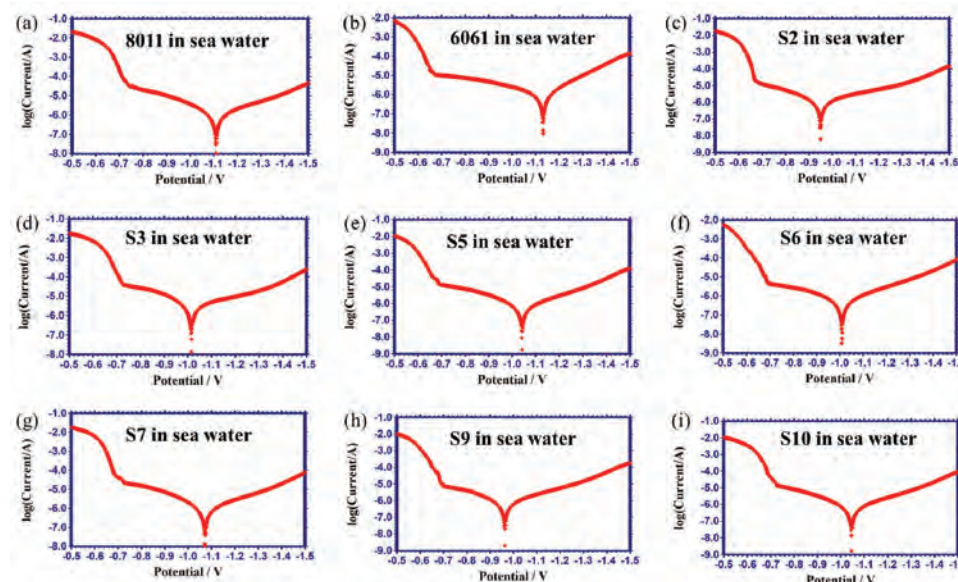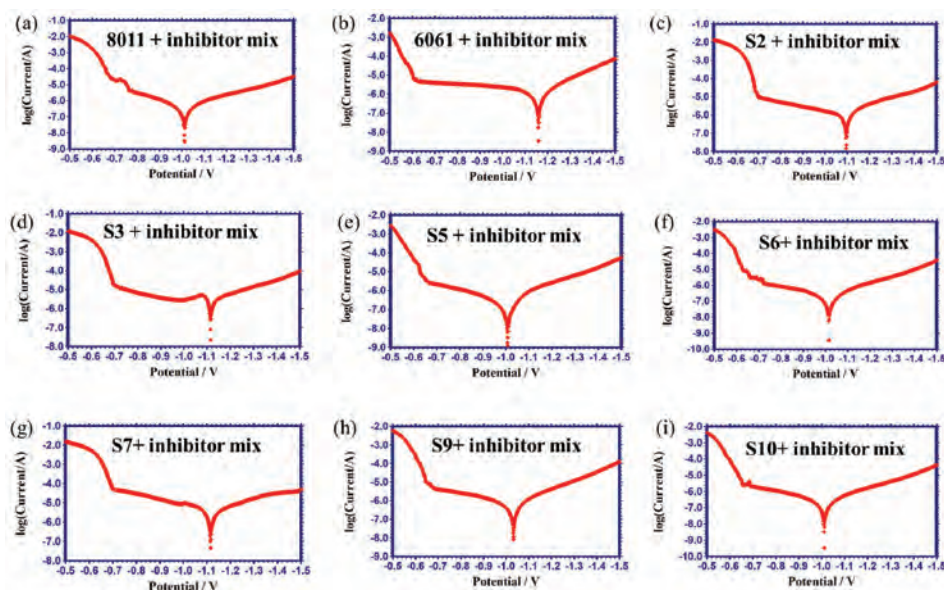Fig. 6. Tafel plots of samples with inhibitor: a) base metal Al8011, b) base metal Al6061 and samples: c) 2, d) 3, e) 5, f) 6, g) 7, h) 9 and i) 10.

The outcomes exposed the inverse proportion of *LPR* with respect to the corrosion rate. When compared to the absence of inhibition, the corrosion rate is decreased in the presence of inhibition. The samples of *LPR* outcomes at both conditions are shown in Table IV. The graphical representation has shown the rotational speed impact on the corrosion current and lower than the base metal. The samples 5, 6 and 10 have shown higher corrosion resistance. The results have revealed that the rotational speed had an impact on the corrosion resistance. Lower rpm results in a big grain size and higher rpm shows small grains with high penetration being the reasons for the higher corrosion resistance. The successful optimization of BOBTFS welded samples shows the difference in the corrosion resistance in the presence and the absence of natural inhibitors. Organic curcumin binds with zinc sulphate and becomes a complex. Due to this nature, the molecule may be a good electron donor which donates an electron to the

welded samples in the salt solution and modifies the atmospheric salt solution. In addition to this Zn acts as an active anode when compared to aluminium.[39]

TABLE IV. Samples of *LPR* outcomes (Ω cm^2)

Sample ID	Condition	
	Absence of inhibitor	Presence of inhibitor
6061	38107	39682
8011	38683	102924
2	38222	26544
3	12563	6349
5	65934	246378
6	83759	236675
7	42178	9080
9	58686	69578
10	65461	193500

CONCLUSIONS

In this study, the effect of the bobbin tool welding process of aluminium on the corrosion behaviour of welded AA6061 aluminium with AA8011 alloy was investigated, and the following conclusions were drawn:

− In comparison with the base metal region, the welded area exhibited a more cathodic behaviour and a higher level of resistance to corrosion in the salt medium.

− The heat treatment technique boosted the corrosion potential of the source metal to more positive values, which is a desired outcome.

− The cathodic sites were provided by coarse metallic particles that were rich in aluminium and acted in relation to the matrix.

− Al 8011 had a greater resistance to corrosion in salt water than aluminium AA6061.

− Even in the presence of an inhibitor system, aluminium 8011 had a higher resistance to corrosion than aluminium 6061.

− In the presence of an inhibitor system, the corrosion resistance of the aluminium metals was improved.

− In the presence of an inhibitor system, the corrosion resistance of the following system decreased: sample 2, sample 3, sample 4 and the sample 7.

− In the presence of an Inhibitor system, the sample 5 system was the best one and the sample 6 was the next best.

− Also, this work observed optimized conditions such as lower rpm and higher rpm at a constant 40 mm/min.

− The inhibition of curcumin was enhanced by adding ZnSO$_4$ solution and achieved in the test aluminium samples.

– Keto-enol tautomerism and the hydroxyl group of the compounds could be the reasons for the improved corrosion resistance in BOBTFSW aluminium samples.

И З В О Д

ПРОУЧАВАЊЕ ИНХИБИТОРНИХ ЕФЕКАТА ЕКСТРАКТА КУРКУМИНА НА
РАЗЛИЧИТЕ АЛУМИНИЈУМСКЕ СПОЈЕВЕ

KAMATCHI PRAVINKUMAR, VADDI SESHAGIRI RAO и SATHISH RENGARAJAN

Department of Mechanical Engineering, St. Joseph's College of Engineering, OMR, Chennai-119, India

Алуминијумски заварени спојеви су све занимљивији за истраживаче због замене тешких челичних конструкција и смањења тежине компоненти које се користе у аутомобилском и поморском окружењу. У овој студији AA6061 и AA8011 су заварени коришћењем методе заваривања трењем и мешањем, помоћу алата са калемом, уз варирање параметара процеса са узорцима изложеним корозивном окружењу. Корозивна природа заварених легура у одсуству и присуству инхибитора (куркумин) је испитана електрохемијским методама и упоређена са сировим узорцима. Уочен је однос између 0,075 и 5,42 A cm^{-2}. Резултати показују да се контрола корозије побољшава спојем од легуре алуминијума AA6061 и AA8011 у присуству екстракта куркумина.

(Примљено 24. априла, ревидирано 1. јуна, прихваћено 8. октобра 2023)

REFERENCES

1. A. Heinz, A. Haszler, C. Keidel, S. Moldenhauer, R. Benedictus, W.S. Miller, *Mater. Sci. Eng., A* **280** (2000) 102 (https://doi.org/10.1016/s0921-5093(99)00674-7)
2. T. Dursun, C. Soutis, *Mater. Des.* **56** (2014) 862 (https://doi.org/10.1016/j.matdes.2013.12.002)
3. J. Hirsch, *Trans. Nonferrous Met. Soc. China* **24** (2014) 1995 (https://doi.org/10.1016/S1003-6326(14)63305-7)
4. C.H. Ng, S. N. M. Yahaya, A. A. A. Majid, *Acad. J. Sci. Res*. **5** (2017) 708 (https://academiapublishing.org/journals/ajsr/pdf/2017/Dec/Ng%20et%20al.pdf)
5. T. Trzepiecinski, *Metals* **10** (2020) 779 (https://doi.org/10.3390/met10060779)
6. D. Feron, *Corrosion Behaviour and Protection of Copper and Aluminium Alloys in Seawater,* Europ. Fed. Corros. Ser., 2007, pp. 145–155 (eBook ISBN: 9781845693084)
7. T. Watanabe, H. Takayama, A. Yanagisawa, *J. Mater. Process. Technol.* **178** (2006) 342 (https://doi.org/10.1016/j.jmatprotec.2006.04.117)
8. M. Khafri, *J. Mater. Sci.* **39** (2004) 6467 (https://doi.org/10.1023/B:JMSC.0000044884.25589.9b)
9. M. Esmaily, N. Mortazavi, W. Osikowicz, *Mater. Des.* **108** (2016) 114 (https://doi.org/10.1016/j.matdes.2016.06.089)
10. W. Y. Li, T. Fu, L. Hutsch, J. Hilgert, F. F. Wang, J. F. Dos Santos, N. Huber, *Mater. Des.* **64** (2014) 714 (https://doi.org/10.1016/j.matdes.2014.07.023)
11. K. Xhanari, M. Finsgar, *Int. J. Electrochem. Sci.* **12** (2017) 5845 (https://doi.org/10.20964/2017.07.71)

12. J.C. Swearengen, *Mater. Sci. Eng.* **10** (1972) 103 (https://doi.org/10.1016/0025-5416(72)90074-2)
13. J. Fayomi, A.P.I. Popoola, O.M. Popoola, O.S.I. Fayomi, *J. Alloys Compd.* **850** (2021) 1 (https://doi.org/10.1016/j.jallcom.2020.156679)
14. C. Shujin, Li. Hao, Lu. Sheng, Ni. Ruiyang, D. Jianghui, *Int. J. Adv. Manuf. Technol.* **86** (2016) 337 (https://doi.org/10.1007/s00170-015-8116-9)
15. D. Ji-Hong, G. Chong, L. Yao, H. Jain, J. Xiang-Dong, Z. Zhi-Xiong, *Int. J. Min. Met. Mater.* **24** (2017) 171 (https://doi.org/10.1007/s12613-017-1392-7)
16. R. Rosliza, W.B. Wan Nik, H.B. Senin, *Mater. Chem. Phys.* **107** (2008) 281 (https://doi.org/10.1016/j.matchemphys.2007.07.013)
17. M. K. Abbass, K. S. Hassan, A. S. Alwan, *Int. J. Manuf. Mater. Mech. Eng.* **3** (2015) 31 (https://doi.org/10.7763/IJMMM.2015.V3.161)
18. N. Sunitha, K.G. Manjunatha, S. Khan, M. Sravanthi, *SN Appl. Sci.* **1** (2019) 1024 (https://doi.org/10.1007/s42452-019-1063-6)
19. M. Mardalizadeh, M. Khandaei, M. Safarkhanian, *J. Adhes. Sci. Technol.* **35** (2020) 1 (https://doi.org/10.1080/01694243.2020.1792156)
20. M. K. Sued, D. Pons, J. Lavroff, E. H. Wong, *Mater. Des.* **54** (2014) 632 (https://doi.org/10.1016/j.matdes.2013.08.057)
21. M. M. Z. Ahmed, M. I. A. Habba, M. M. El-Sayed Seleman, K. Hajlaoui, S. Ataya, F. H. Latief, A. E. El-Nikhaily, *Materials* **14** (2021) 4585 (https://doi.org/10.3390/ma14164585)
22. W. Y. Li, T. Fu, L. Hutsch, J. Hilgert, F. F. Wang, J. F. Dos Santos, N. Huber, *Mater. Des.* **64** (2014) 714 (https://doi.org/10.1016/j.matdes.2014.07.023)
23. Y. Li, D. Sun, W. Gong, *Metals* **9** (2019) 894 (https://doi.org/10.3390/met9080894)
24. S. Sinhmar, D. K. Dwivedi, *Corros. Sci.* **133** (2018) 25 (https://doi.org/10.1016/j.corsci.2018.01.012)
25. F. Gharavi, K. A. Matori, R. Yunus, N. K. Othman, *Mater. Res.* **17** (2014) 672 (https://doi.org/10.1590/S1516-14392014005000053)
26. X. G. Zhang, *Corrosion and Electrochemistry of Zinc*, 1st ed., Springer, New York, 1996, pp. 125–156 (https://doi.org/10.1007/978-1-4757-9877-7_5)
27. S. B. Strbac, R. R. Adzic, in *Encyclopedia of Applied Electrochemistry*, G. Kreysa, K. Ota, R. F. Savinell, Eds., Springer, Berlin, 2014, p. 417 (https://doi.org/10.1007/978-1-4419-6996-5_485)
28. H. Elmsellem, M. H. Youssouf, A. Aouniti, T. Ben Hadda, A. Chetouani, B. Hammouti, *Russ. J. Appl. Chem.* **87** (2014) 744 (https://doi.org/10.1134/s1070427214060147)
29. L. Juhaiman, *Green Sustain. Chem.* **6** (2016) 57 (https://doi.org/10.4236/gsc.2016.62005)
30. E. A. Flores-Frias, V. Barba, R. Lopez-Sesenes, L. L. Landeros-Martinez, J. P. Flores-De Los Rios, M. Casales, J. G. Gonzalez-Rodriguez, *Int. J. Electrochem. Sci.* **14** (2019) 5026 (https://doi.org/10.20964/2019.06.53)
31. Y. Yan, *Metal. Biomed. Devices.* **1** (2010) 178 (https://doi.org/10.1533/9781845699246.2.178)
32. Y. Yan, A. Neville, and D. Dowson, *J. Phys., D* **39** (2006) 3200 (https://doi.org/10.1088/0022-3727/39/15/S10)
33. J. G. Speight, P. J. Subsea, *Deepwater Oil and Gas Science and Technology*, 1st ed., Gulf Professional, Oxford, 2012, p. 213 (https://doi.org/10.1016/B978-1-85617-558-6.00008-8)

34. F. Gharavi, K. Matori, R. Yunus, N. Othman, F. Fadaeifard, *J. Mater. Res. Technol.* **4** (2015) 314 (https://doi.org/10.1016/j.jmrt.2015.01.007)
35. R. Rosliza, W. B. Wan Nik, *Curr. Appl. Phys.* **10** (2010) 221 (https://doi.org/10.1016/j.cap.2009.05.027)
36. J. M. G. De Salazar, A. Urena, S. Manzanedo, M. I. Barrena, *Corr. Sci.* **41** (1998) 529 (https://doi.org/10.1016/s0010-938x(98)00135-8)
37. S. T. Selvamani, *J. Mater. Res. Technol.* **15** (2021) 315 (https://doi.org/10.1016/j.jmrt.2021.08.005)
38. K. Hornbostel, C. K. Larsen, M. R. Geiker, *Cement Concrete Composites* **39** (2013) 60 (https://doi.org/10.1016/j.cemconcomp.2013.03.019)
39. B. T. Ogunsemi, T. E. Abioye, T. I. Ogedengbe, H. Zuhailawati, *J. Mater. Res. Technol.* **11** (2021) 1061 (https://doi.org/10.1016/j.jmrt.2021.01.070).

Stability and computational analyses of selected pesticides in use in the Republic of Serbia

BILJANA ARSIĆ[1]*, STEFAN PETROVIĆ[1], JELENA MRMOŠANIN[1], IVANA DIMITRIJEVIĆ[1], SNEŽANA TOŠIĆ[1], GORDANA STOJANOVIĆ[1#], SANJA GLIŠIĆ[2] and JELENA MILIĆEVIĆ[2#**]

[1]Department of Chemistry, Faculty of Sciences and Mathematics, University of Niš, Višegradska 33, 18106 Niš, Serbia and [2]Laboratory for Bioinformatics and Computational Chemistry, Vinča Institute of Nuclear Sciences, University of Belgrade, Mike Petrovića Alasa 12–14, 11351 Vinča, Belgrade, Serbia

Abstract: Pesticides commonly used in the Republic of Serbia (tebuconazole, pendimethalin, pyraclostrobin, propiconazole and famoxadone) have high stability, so their potential toxicity to humans needs to be investigated. These pesticides are in use in the Republic of Serbia in various formulations. Their toxicity and interactions with acetylcholinesterase were thoroughly investigated in this study using computational tools. The ADMET (adsorption, distribution, metabolism, excretion, toxicity) study showed that all of them are efficient oral compounds, and that pendimethalin was a mutagenic compound. Glide scores ranged from –18.41 (pendimethalin) to –27.61 kJ mol^{-1} (famoxadone) in *Mus musculus*, and from –19.58 (pendimethalin) to –24.31 kJ mol^{-1} (propiconazole) in *Homo sapiens*. In addition, the experimental stability of the pesticides solutions in methanol was studied using the fast gas chromatography–mass spectrometry (GC–MS, retention times of the studied pesticides ranged from 14.47 (pendimethalin) to 22 min (famoxadone)). They showed good stability over time, apart from pyraclostrobin which decomposed mainly into its desmethoxy derivative after 20 months. Based on the promising modelling results, pyraclostrobin and famoxadone emerge as potential candidates for further investigation in the treatment of Alzheimer's disease, taking care to increase their stability.

Keywords: GC–MS; Alzheimer's disease; ADMET.

---

*,** Corresponding authors. E-mail: (*)biljana.arsic@pmf.edu.rs;
(**)jdjordjevic@vin.bg.ac.rs
Serbian Chemical Society member.

259

INTRODUCTION

Five pesticides (propiconazole, famoxadone, pendimethalin, pyraclostrobin and tebuconazole) that are widely used in the Republic of Serbia were selected for this study.[1] There are numerous studies on the toxicological effects of pesticides but there is no such proposed aspect as described here, especially on humans.

The intensive use of pesticides negatively affects the health of the population and also insect pollinators worldwide, as shown in numerous studies. French researchers studied the level of uptake of selected *β*-blockers, anxiolytics, antibiotics, antiepileptics, antidepressants and fungicides (including propiconazole and tebuconazole) by the European eel (*Anguilla anguilla*). Interestingly, the eel consumed the least amount of all substances studied.[2] Dereumeaux *et al.* (2022)[3] determined the levels of five pesticides, including tebuconazole, in urine and hair samples from adults and children living near and around vineyards. The results showed that the levels of the above pesticides and their metabolites are higher in those living near vineyards and also have a stronger effect on children, so their monitoring (degradation time) is crucial. Cang *et al.* (2022)[4] studied the individual and combined effects of tetrachloranatraniliprole and tebuconazole on honey bees (*Apis mellifera* L.). According to their results, tetrachlorantraniliprole shows a higher toxic effect (96-h LC_{50} value of 298.2 mg a.i. dm^{-3}) compared to tebuconazole (96-h LC_{50} value of 1,841 mg a.i. dm^{-3}), while the combined exposure of honeybees to both pesticides leads to an enhanced toxic effect (synergism). Janoš *et al.* (2023)[5] concluded, based on their experimental results, that tebuconazole inhibits DNA glycosylase and thus reduces the DNA methylation process. Kolesárová *et al.* (2013)[6] studied the influence of fungicide formulations (with tebuconazole as one of the active components) on the activity of acetylcholinesterase and butyrylcholinesterase in domestic animals, and their results show the inhibitory properties of these formulations on both enzymes. Rico *et al.* (2016)[7] studied the lethal and sublethal capabilitiles of the common earthworm in soils used for rice cultivation treated with various pesticides, including tebuconazole, and the decrease in enzymatic activity of the following enzymes in the common earthworm: cholinesterase, lactate dehydrogenase, and alkaline phosphatase.

Pendimethalin, an herbicide used for weed control, inhibits plant cell division and mitosis. Results showed that pendimethalin interferes with mitochondrial complexes I and V, which inhibit embryo energy metabolism, leading to developmental defects in the organisms studied.[8,9]

Pyraclostrobin has been found to affect the mitochondrial function in aquatic organisms.[10] The design and synthesis of new pyraclostrobin derivatives with antifungal activities have been reported.[11]

From the available literature, there is no evidence that famoxadone inhibits acetylcholinesterase. Famoxadone and its derivatives have been shown to be

cytochrome bc_1 complex inhibitors.[12,13] How famoxadone interacts with acetylcholinesterase is described in detail here.

Recently, several pesticides different from our studied here were investigated experimentally and *in silico*.[14,15] Average quasi-valence number (*AQVN*)/electron–ion interaction potential (*EIIP*) proved to be a good predictive tool for the behaviour of selected pesticides against acetylcholinesterase. These selected pesticides against acetylcholinesterase show *in silico* the same region for binding in both *Mus musculus* and *Homo sapiens* with some differences. Global minima or free energy of formation values may also give an indication of the degree of acute toxicity.

Therefore, the aim of this study was to investigate the stability of methanolic solutions of different pesticides (tebuconazole, pendimethalin, pyraclostrobin, propiconazole and famoxadone) using gas chromatography–mass spectrometry (GC–MS) over 9 and 20 months to obtain the necessary information for the efficient laboratory work. In addition, the previous computational studies on pesticides were extended to the above selected pesticides to gain insight into the interactions with acetylcholinesterase (AChE) and predict toxicity using two different tools based on different principles.

The stability of the non-aqueous solutions has not been reported before, which is of great importance for laboratory work and therefore represents a novelty. For the first time, molecular docking analysis was performed for five selected pesticides and a detailed study of toxicity. Based on all computational studies performed, the potential candidates for the treatment of Alzheimer's disease were proposed.

EXPERIMENTAL

Preparation of samples

Certified standards of pesticides (propiconazole, famoxadone, pendimethalin, pyraclostrobin and tebuconazole) were purchased from Dr. Ehrenstorfer (Augsburg, Germany). HPLC-grade methanol was purchased from J. T. Baker (Landsmeer, The Netherlands).

Stock solutions of the pesticides: propiconazole (0.25318 mg cm^{-3}), famoxadone (0.24058 mg cm^{-3}), pendimethalin (0.30215 mg cm^{-3}), pyraclostrobin (1.0673 mg cm^{-3}) and tebuconazole (0.23668 mg cm^{-3}) were prepared in methanol and stored at 4 °C. The methanol solutions of tebuconazole, pendimethalin, propiconazole and famoxadone were stored tightly sealed in the refrigerator for 9 months, and the methanol solution of pyraclostrobin was stored for 20 months.

GC–MS analysis

Gas chromatographic analysis of pesticides was performed on a 7890/7000B GC/MS/MS triple quadrupole system (Agilent Technologies, USA, equipped with a Combi PAL auto sampler). The fused silica capillary column HP-5MS (5 % phenylmethylsiloxane, 30 m×0.25 mm, film thickness 0.25 μm) was used with helium as carrier gas (1 cm^3 min^{-1}). The operating conditions were consistent with the previously published work.[16]

Compounds were identified by comparison of their MS with those from Wiley 6, NIST02, Mass Finder 2.3, by the application of the AMDIS software (the Automated Mass Spectral Deconvolution and Identification System, Ver. 2.1, DTRA/NIST, 2011).

*Electron–ion interaction potential (*EIIP*)/average quasi-valence number (*AQVN*)*

The specific recognition and targeting between interacting biological molecules at a distance of > 5 Å are determined by the *AQVN* and the *EIIP* derived from the general model pseudopotential:[17]

$$EIIP = 0.25(Z^*/(2\pi))\sin(1.04\pi Z^*) \tag{1}$$

where Z^* is the *AQVN* determined by:

$$Z^* = \frac{1}{N}\sum_{i=1}^{m} n_i Z_i \tag{2}$$

where Z_i is the valence number of the *i*-th atomic component, n_i is the number of atoms of the *i*-th component, *m* is the number of atomic components in the molecule, and *N* is the total number of atoms. The Z^* and *EIIP* values are expressed in Rydberg units (Ry). *AQVN* and *EIIP* are unique physical properties that characterize, among molecular descriptors, the long-range interactions between biological molecules.[15] *EIIP* and *AQVN* of organic molecules have been shown to correlate strongly with their biological activity (mutagenicity, carcinogenicity, antibiotic activity, *etc.*).[18,19]

Unconstrained conformational search

The conformational analysis of selected pesticides (tebuconazole, pendimethalin, pyraclostrobin, propiconazole and famoxadone, Fig. 1) was performed using MacroModel under Schrodinger Suite 2022-3 and Maestro, v. 13.3, as interface. Chloroform was used as the solvent. The conditions for the simulations were taken from the previously published work.[15]

(a)　　　　(b)　　　　(c)

(d)　　　　(e)
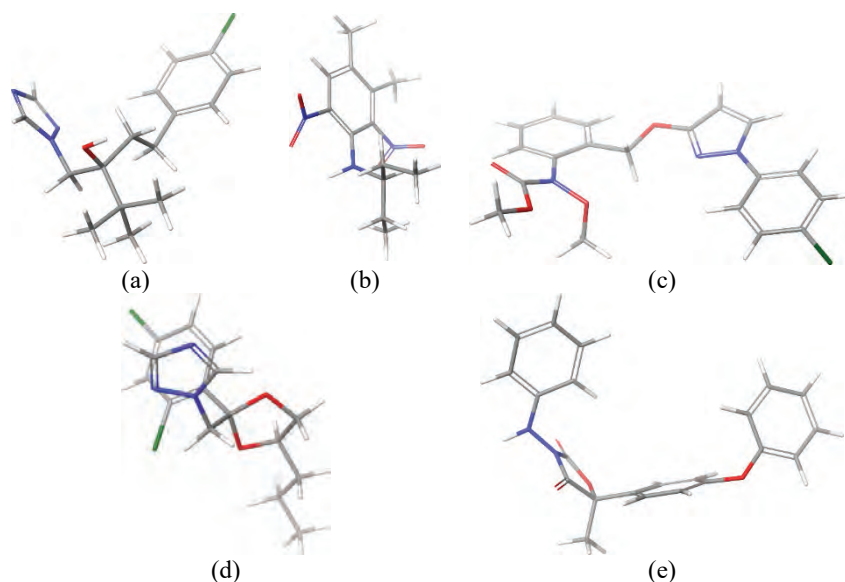
Fig. 1. 3D Structures of conformers with the lowest energies of investigated pesticides: a) tebuconazole, b) pendimethalin, c) pyraclostrobin, d) propiconazole and e) famoxadone.

Molecular docking studies

The molecular docking studies with selected pesticides (tebuconazole, pendimethalin, pyraclostrobin, propiconazole and famoxadone) were performed using acetylcholinesterase as a target from *Mus musculus* and *Homo sapiens*. In addition, molecular docking of selected pesticides was performed at the binding site of donepezil in acetylcholinesterase from *H. sapiens*.[20] In all cases, crystal structures were obtained from the Protein Data Bank (entry ID for *M. musculus* 5DTI[21] and *H. sapiens* 4EY7[20]). Acetylcholinesterase alone was prepared for docking using the Protein Preparation and Refinement tool of Schrodinger Suite 2022-3. The previously optimized structures of selected pesticides in MacroModel were ligands in the molecular docking studies. Molecular docking was performed with Glide under Schrodinger Suite 2022-3.

ADMET in silico *studies*

ADMET parameters of selected pesticides (tebuconazole, pendimethalin, pyraclostrobin, propiconazole and famoxadone) were calculated in normal mode using QikProp v7.0 software (Schrödinger, Inc., New York, NY, USA).

ACD/Percepta 14.53.0 (Build 3577) (Advanced Chemistry Development, Inc., Toronto, Canada) was also used to generate ADMET profiles of selected pesticides based on SMILES strings of the compounds.

RESULTS AND DISCUSSION

Stability analysis of selected pesticides using GC–MS

GC–MS analysis can be used to efficiently determine the stability of methanolic solutions of the selected pesticides (tebuconazole, pendimethalin, pyraclostrobin, propiconazole and famoxadone). The stability in aqueous solutions has been well studied.[22] After nine months, the methanolic solutions of tebuconazole, pendimethalin, propiconazole and famoxadone were not degraded. Their retention times were 16.75 (tebuconazole), 14.47 (pendimethalin), 16.31–16.63 (propiconazole) and 22 min (famoxadone) (Fig. S-1–S-4 of the Supplementary material to this paper). Pyraclostrobin does not show stability in methanol solution like the others (Fig. 2). Besides pyraclostrobin (20.45 min), the solution mainly contains the des-methoxy derivative of pyraclostrobin (18.32–18.51 min, Fig. 2).

*Computational studies (*EIIP *calculation, conformational search, molecular docking and ADMET) of selected pesticides and acetylcholine esterase from* M. musculus *and* H. sapiens

The selected pesticides had AQVN values that were in the intervals of 2.5116–3.0434 (Table I). The absolute values of EIIP ranged from 0.0233 for pendimethalin to 0.0938 for tebuconazole. The previous studies have shown that tebuconazole[23] and propiconazole[24] exhibit AChE inhibitory activity. The specificity of inhibitors between insect and mammalian AChE contributes to selective toxicity.[25] In general, it is safer for insecticides to have a higher affinity for insect AChE than for human AChE.
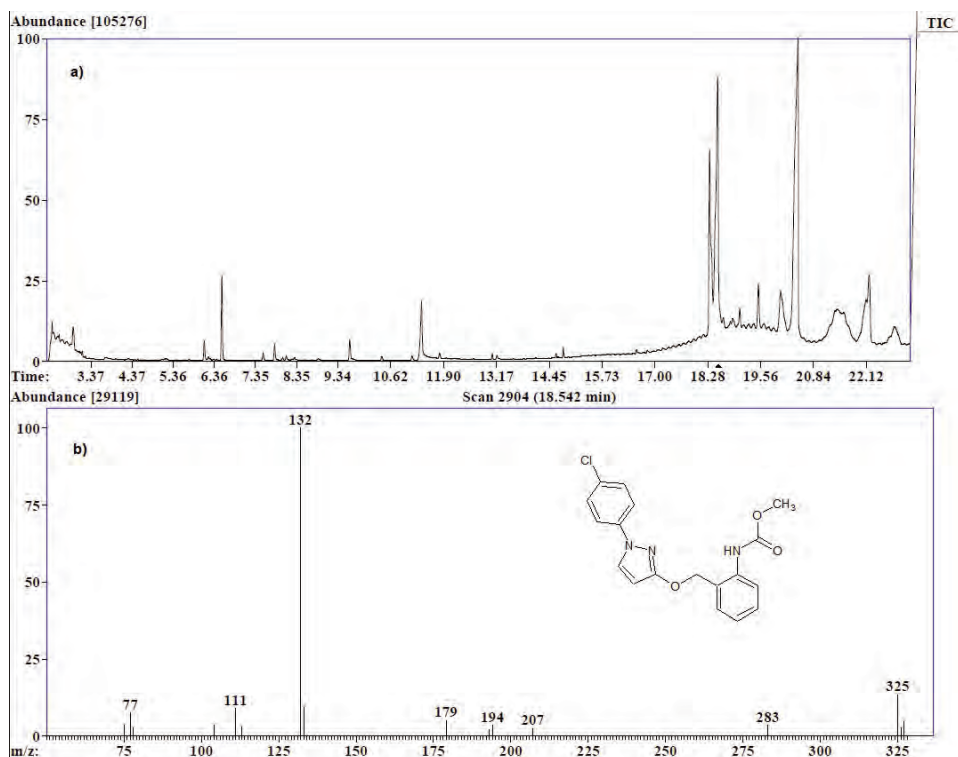
Fig. 2. a) Total-ion chromatogram (TIC) of pyraclostrobin solution, b) mass spectrum of the main degradation product (des-methoxy pyraclostrobin).

TABLE I. Investigated pesticides, their classes, molecular formulae, Z^*, and absolute *EIIP*

Pesticide	Class	Molecular formula	Z^* / Ry	*EIIP* / Ry
Tebuconazole	Triazole fungicide; conazole fungicide	$C_{16}H_{22}ClN_3O$	2.5116	0.0938
Pendimethalin	Dinitroaniline herbicide	$C_{13}H_{19}N_3O_4$	2.8205	0.0233
Pyraclostrobin	Strobilurin fungicide; carbanilate fungicide; phenylpyrazole fungicide	$C_{19}H_{18}ClN_3O_4$	2.9777	0.0355
Propiconazole	Triazole fungicide; conazole fungicide	$C_{15}H_{17}Cl_2N_3O_2$	2.7180	0.0560
Famoxadone	Oxazole fungicide; dicarboximide fungicide	$C_{22}H_{18}N_2O_4$	3.0434	0.0600

Prior to molecular docking, all selected pesticides were prepared in Macro-Model. The global minimum of each pesticide was used for molecular docking. The global minimum energies and replicates of the studied structures are listed in Table II.

After optimization, the selected pesticides were subjected to molecular docking against acetylcholinesterase from *M. musculus* and *H. sapiens*, whose sequences are 89.80 % identical using BLASTP (protein BLAST: search protein databases using a protein query (nih.gov)), and the values of Glide scores[26,27] from molecular docking are listed in Table II. Acetylcholinesterase (AChE) was selected due to its involvement in numerous cholinergic signalling pathways in the central and peripheral nervous system.[28] According to the molecular docking studies performed, famoxadone is the best binder for acetylcholinesterase from the studied pesticides on *M. musculus* AChE, and the weakest is pendimethalin. In the case of *H. sapiens*, the best AChE inhibitor is propiconazole and the worst is pendimethalin.

TABLE II. Global minima energies and repeats of the investigated pesticides, and Glide scores of selected pesticides against AChE from *M. musculus* and *H. sapiens*

Pesticide	Global minimum energy, kJ mol^{-1}	Number of replicates	Glide score, kJ mol^{-1}	
			Mus musculus	*Homo sapiens*
Tebuconazole	215.6	20	–23.81	–22.51
Pendimethalin	479.3	18	–18.41	–19.58
Pyraclostrobin	201.1	17	–26.32	–20.17
Propiconazole	102.6	3	–21.59	–24.31
Famoxadone	409.8	27	–27.61	–23.93

Two interactions are common to all investigated pesticides against AChE in *M. musculus*: His 381 and Phe 531. A different situation was observed in *H. sapiens*. They have no common contact with AChE, and generally fewer interactions with AChE were observed compared to *M. musculus* (Fig. 3).

In general, pesticides are more toxic to lower organisms.[29] More interactions here are observed in *M. musculus* than in *H. sapiens*. Some pesticides have been already studied as potential candidates for drugs against Alzheimer's disease,[15] so it was reasonable to investigate *in silico* selected pesticides here with the same aim.

Molecular docking studies of approved Alzheimer's medicines and selected pesticides against acetylcholine esterase from H. sapiens

Drugs for the treatment of Alzheimer's disease (donepezil, rivastigmine and galantamine) that target AChE[30] fall within the AQVN range of 2.5 and 2.667. The pesticides and drugs for Alzheimer's disease studied have a common target – acetylcholinesterase. The crystal structure of donepezil with acetylcholinesterase from *H. sapiens* was used for our docking studies, taking into account the binding site from chain B including interactions with Ser 293, Trp 286 and Trp 86.[20] The redocking of donepezil resulted in a Glide score of –16.32 kJ mol^{-1}. Two other approved drugs for the treatment of Alzheimer's disease (rivastigmine and gal-

A)

a)

b)
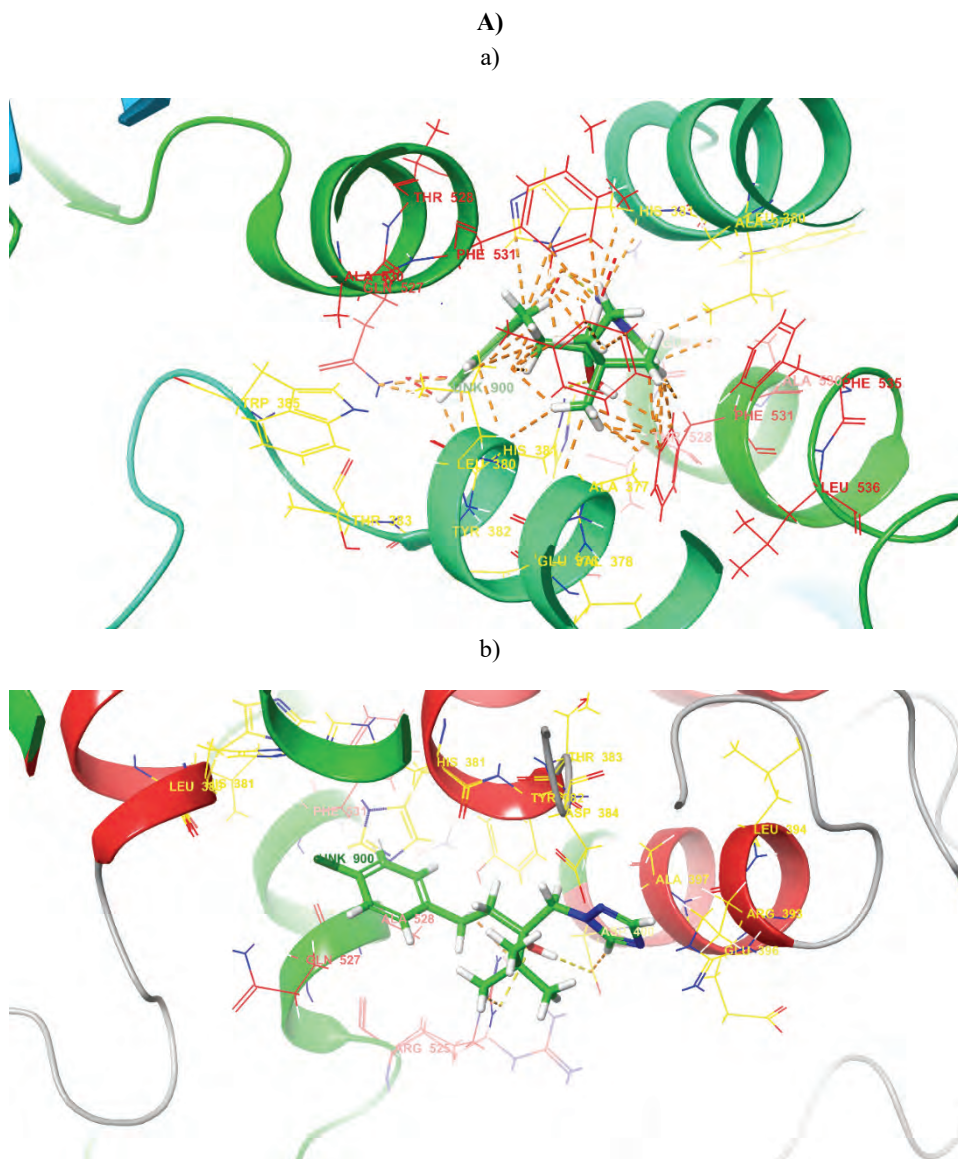
Fig 3. **A)** Graphic representation of molecular docking of tebuconazole into the acetylcholine esterase from a) *Mus musculus*, b) *Homo sapiens*.

antamine) provided better results for galantamine (–22.51 kJ mol^{-1}) and weaker results for rivastigmine (–12.30 kJ mol^{-1}). The acute oral toxicity of pendimethalin, pyraclostrobin and famoxadone in mice/rats is > 4500 mg kg^{-1},[31] therefore their *in silico* inhibitory effects on AChE in *H. sapiens* were compared with those of approved Alzheimer's drugs (donepezil, rivastigmine and galantamine). Values

B)

a)

b)
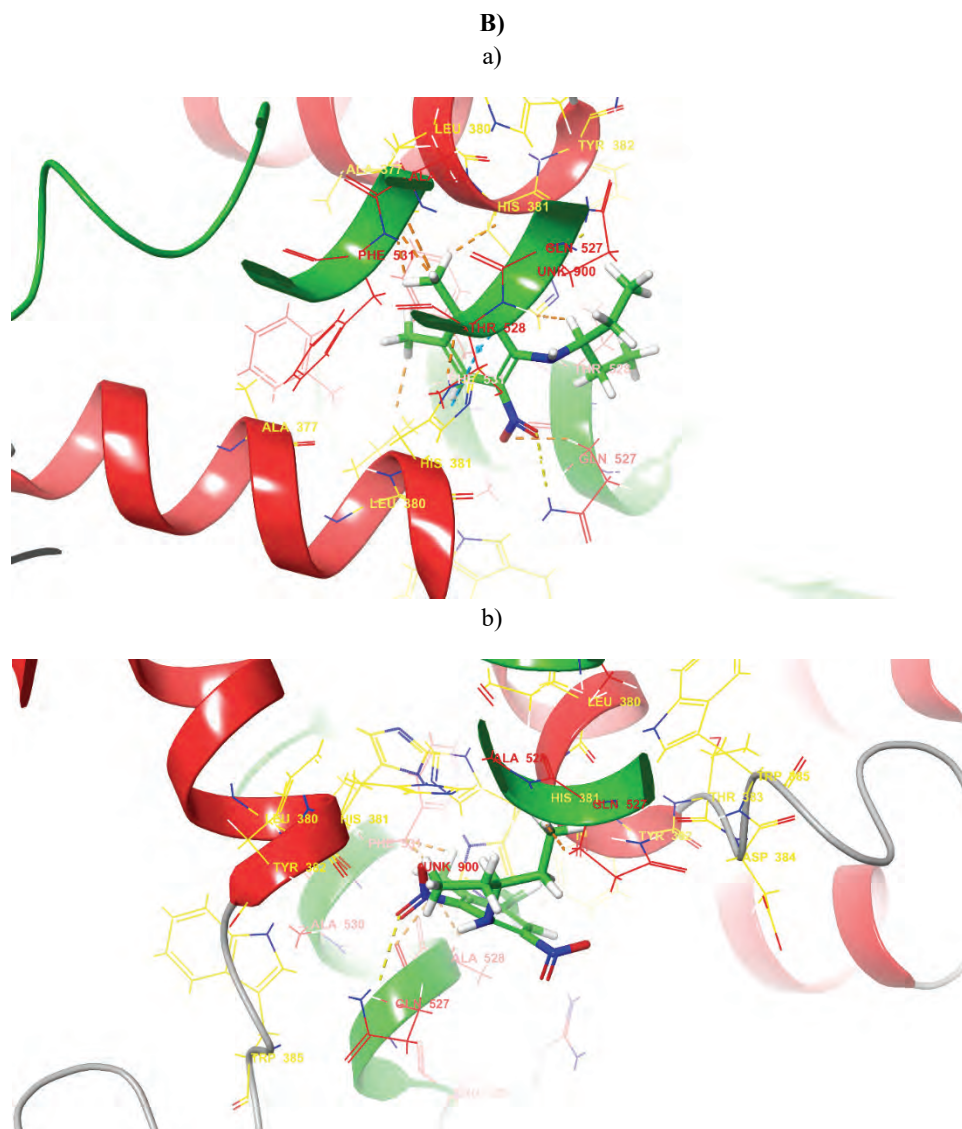
Fig 3 (continued). **B)** Graphic representation of molecular docking of pendimethalin into the acetylcholine esterase from a) *M. musculus*, b) *H. sapiens*.

(in kJ mol^{-1}) of –19.75 (pendimethalin), –18.32 (pyraclostrobin) and –20.08 (famoxadone) were obtained for the selected pesticides. The glide scores for these pesticides were better than those for donepezil and rivastigmine, so they can be further investigated as the replacements for these drugs.

C)

a)

b)
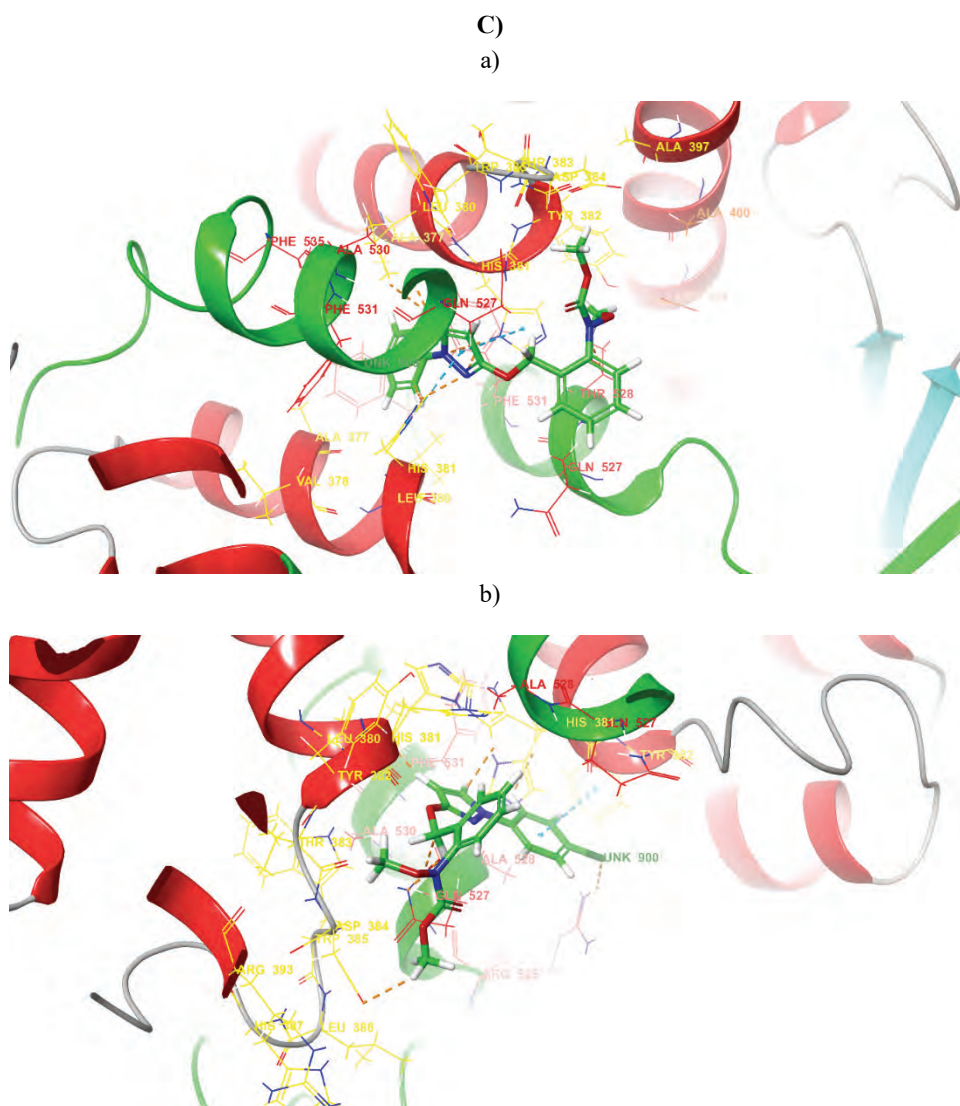
Fig 3 (continued). **C)** Graphic representation of molecular docking of pyraclostrobin into the acetylcholine esterase from a) *M. musculus*, b) *H. sapiens*.

In silico *ADMET studies of selected pesticides*

The toxicity of the compounds was assessed using Lipinski's Rule of Five,[32] which includes molecular weight (<500 Da), number of hydrogen-bond acceptors (≤10) and donors (≤5), octanol/water partition coefficient (≤5), and Jorgensen's rule of three,[33] which includes log S (>–5.7), $PCaco$ (>22 nm s^{-1}), and primary

metabolites (*PM*) (<7). The violations of these rules are essential for the optimization of biologically active compounds and should not exceed 1.

D)

a)

b)

Fig 3 (continued). **D)** Graphic representation of molecular docking of propiconazole into the acetylcholine esterase from a) *M. musculus*, b) *H. sapiens*.

Table S-I of the Supplementary material shows the ADMET properties of the selected compounds (tebuconazole, pendimethalin, pyraclostrobin, propicon-

E)

a)

b)

Fig 3 (continued). **E)** Graphic representation of molecular docking of famoxadone into the acetylcholine esterase from a) *M. musculus*, b) *H. sapiens*.

azole and famoxadone) predicted by QikProp and includes the following para-meters: molecular weight (*MW*), number of rotatable bonds (*RB*), dipole moment (*DM*), molecular volume (*MV*), number of hydrogen donors (*DHB*), number of hydrogen acceptors (*AHB*), polar surface area (*PSA*), octanol/water partition coefficient (log *P*), water solubility (log *S*), apparent Caco-2 cell permeability (*PCaco*), number of probable primary metabolic reactions (*PM*), percentage of oral absorption by humans (*%HOA*), and violations of the rule of three (*VRT*) and

rule of five (*VRF*). The theoretical calculations of ADME parameters are presented in Table S-I along with Lipinski and Jorgensen rule violations. Thus, it can be assumed that according to the predictions of the ADMET properties, all compounds are orally active.

The ADME and drug safety profiles of selected pesticides were predicted using Percepta. The results are presented in Table S-II of the Supplementary material. Based on the Caco-2 values, it can be said that all compounds have high permeability to Caco-2 cells (79×10^{-6}–196×10^{-6} cm s^{-1}). They are all also highly bound to plasma proteins (PPB) based on the values obtained (91–98 %). Based on the calculated scores (ranging from –2.80 to –2.20), they are all permeable to the CNS, implying that those with low toxicity are candidates for Alzheimer's disease because they share the same target – AChE. Percepta predicted only propiconazole not to be an inhibitor of gp-substrates, and only tebuconazole and propiconazole were found to be inhibitors of CYP3A4. Famoxadone was found to be a non-inhibitor for CYP1A2. Based on the Ames test, tebuconazole and propiconazole were found to be non-mutagenic, whereas pendimethalin was a mutagenic compound. The mutagenic effect of pendimethalin was consistent with the experimental data – high concentrations (500 and 1000 μM) which caused mutagenic effects on human umbilical vein endothelial cells.[34] This fact allows us to exclude pendimethalin as a mutagenic compound, and further studies can be proposed for famoxadone and pyraclostrobin.

CONCLUSION

Based on the obtained results from the analyses of five commonly used pesticides in the Republic of Serbia, it is obvious that computer-assisted tools such as ADMET (especially Lipinski's and Jorgensen's rules and mutagenic properties) profiling and molecular docking (Glide scores between –17 and –29 kJ mol^{-1}), with molecular descriptors, such as AQVN (2.5116–3.0434 Ry) showed that compounds, currently used as pesticides, such as pyraclostrobin and famoxadone, may be candidates for the development of effective treatments against Alzheimer's disease. Special attention should be paid to pyraclostrobin which decomposed mainly into its des-methoxy derivative after 20 months in methanol solution, and its newly developed derivative should have higher stability. GC––MS method can be easily used for studying the content and stability of various pesticides in formulations and for their determination in real samples, such as agricultural products.

SUPPLEMENTARY MATERIAL

Additional data and information are available electronically at the pages of journal website: https://www.shd-pub.org.rs/index.php/JSCS/article/view/12490, or from the corresponding author on request.

ИЗВОД

КОМПЈУТЕРСКА АНАЛИЗА И АНАЛИЗА СТАБИЛНОСТИ ОДАБРАНИХ ПЕСТИЦИДА КОЈИ СЕ КОРИСТЕ У РЕПУБЛИЦИ СРБИЈИ

БИЉАНА АРСИЋ[1], СТЕФАН ПЕТРОВИЋ[1], ЈЕЛЕНА МРМОШАНИН[1], ИВАНА ДИМИТРИЈЕВИЋ[1], СНЕЖАНА ТОШИЋ[1], ГОРДАНА СТОЈАНОВИЋ[1], САЊА ГЛИШИЋ[2] и ЈЕЛЕНА МИЛИЋЕВИЋ[2]

[1]Дейаршман за хемију, Природно–машемашички факулшеш, Универзишеш у Нишу, Вишеградска 33, 18106 Ниш и [2]Лаборашорија за биоинформашику и рачунарску хемију, Инсшишуш за нуклеарне науке „Винча", Универзишеш у Беоīраду, Мике Пешровића Аласа 12–14, 11351 Винча, Беоīрад

Пестициди који се често користе у Републици Србији (тебуконазол, пендиметалин, пираклостробин, пропиконазол и фамоксадон) имају високу стабилност, тако да њихова потенцијална токсичност се мора проучити. Ови пестициди се користе у Републици Србији у различитим формулацијама. Њихова токсичност и интеракције са ацетихолинестеразом су детаљно изучене у овом истраживању коришћењем компјутерских алата. ADMET (адсорпција, дистрибуција, метаболизам, екскреција, токсичност) изучавање је показало да су сви они ефикасна орална једињења, и да је пендиметалин мутагено једињење. Glide скорови су били у опсегу од −18,41 (пендиметалин) до −27,61 kJ mol^{-1} (фамоксадон) код миша, и од −19,58 (пендиметалин) до −24,31 kJ mol^{-1} (пропиконазол) код човека. Осим тога, експериментална стабилност раствора пестицида у метанолу је проучавана коришћењем GC–MS (ретенциона времена проучаваних пестицида се кретала од 14,47 (пендиметалин) до 22 min (фамоксадон)). Они показују добру стабилност током времена, осим пираклостробина који се углавном распада на свој дез-метокси дериват после 20 месеци. На основу обећавајућих резултата моделовања, пираклостробин и фамоксадон се појављују као потенцијални кандидати који се могу даље изучавати као третман за Алцхајмерову болест, водећи рачина да се повећа њихова стабилност.

(Примљено 17. јула, ревидирано 20. новембра, прихваћено 24. децембра 2023)

REFERENCES

1. Ministarstvo poljoprivrede, sumarstva i vodoprivrede, Uprava za zastitu bilja (2023) Lista-odobrenih-supstanci-mart2023.pdf (minpolj.gov.rs), (accessed 12/07/2023) (in Serbian)
2. I. Alvarez-Mora, V. Bolliet, N. Lopez-Herguedas, L. Castro, E. Anakabe, M. Monperrus, N. Etxebarria, *Environ. Pollut.* **311** (2022) 120016 (https://doi.org/10.1016/j.envpol.2022.120016)
3. C. Dereumeaux, F. Mercier, P. Soulard, M. Hulin, A. Oleko, M. Pecheux, C. Fillol, S. Denys, P. Quenel, *Environ. Int.* **159** (2022) 107013 (https://doi.org/10.1016/j.envint.2021.107013)
4. T. Cang, Y. Lou, Y.-C. Zhu, W. Li, H. Weng, L. Lv, Y. Wang, *Environ. Int.* **172** (2023) 107764 (https://doi.org/10.1016/j.envint.2023.107764)

5. T. Janoš, I. Ottenbros, L. Blahova, P. Šenk, L. Šulc, N. Palešova, J. Sheardova, J. Vlaanderen, P. Čupr, *Environ. Res.* **222** (2023) 115368 (https://doi.org/10.1016/j.envres.2023.115368)
6. V. Kolesárová, G. Šinko, K. Šiviková, J. Dianovský, *Caryologia* **66** (2013) 346 (https://doi.org/10.1080/00087114.2013.855390)
7. A. Rico, C. Sabater, M. Á. Castillo, *Ecotoxicol. Environ. Saf.* **127** (2016) 222 (https://doi.org/10.1016/j.ecoenv.2016.02.004)
8. H. Park, J.-Y. Lee, W. Lim, G. Song, *J. Hazard. Mater.* **411** (2021) 125153 (https://doi.org/10.1016/j.jhazmat.2021.125153)
9. J. Ham, W. Lim, G. Song, *Environ. Pollut. (Oxford, United Kingdom)* **278** (2021) 116835 (https://doi.org/10.1016/j.envpol.2021.116835)
10. X. Y. Li, Y. J. Qin, Y. Wang, T. Huang, Y. H. Zhao, X. H. Wang, C. J. Martyniuk, B. Yan, *Toxicology* **452** (2021) 152706 (https://doi.org/10.1016/j.tox.2021.152706)
11. L. Wang, S. Zhao, X. Kong, L. Cao, S. Tian, Y. Ye, C. Qiao, *Bioorg. Med. Chem.* **26** (2018) 875 (https://doi.org/10.1016/j.bmc.2018.01.004)
12. F. Wang, H. Li, L. Wang, W.-C. Yang, J.-W. Wu, G.-F. Yang, *Bioorg. Med. Chem.* **19** (2011) 4608 (https://doi.org/10.1016/j.bmc.2011.06.008)
13. Y.-J. Zheng, R. Shapiro, W. J. Marshall, D. B. Jordan, *Bioorg. Med. Chem. Lett.* **10** (2000) 1059 (https://doi.org/10.1016/S0960-894X(00)00164-5)
14. M. Mladenović, B. B. Arsić, N. Stanković, N. Mihović, R. Ragno, A. Regan, J. S. Milićević, T. M. Trtić-Petrović, R. Micić, *Molecules* **23** (2018) 2192 (https://doi.org/10.3390/molecules23092192)
15. S. Petrović, B. Arsić, I. Zlatanović, J. Milićević, S. Glišić, M. Mitić, R. Đurović-Pejčev, G. Stojanović, *Int. J. Mol. Sci.* **24** (2023) 8003 (https://doi.org/10.3390/ijms24098003)
16. Agilent Technologies, *Food_Compendium 2011* – Pesticides, Mycotoxins and Other Contaminants.pdf (agilent.com), application note: Analysis of Pesticide Residues in Spinach Using Agilent SampliQ QuEChERS AOAC Kits by GC/MS (accessed 12/07/2023)
17. V. Veljkovic, I. Slavic, *Phys. Rev. Lett.* **29** (1972) 105 (https://doi.org/10.1103/PhysRevLett.29.105)
18. V. Veljkovic, N. Veljkovic, J. A. Esté, A. Hüther, U. Dietrich, *Curr. Med. Chem.* **14** (2007) 441 (http://dx.doi.org/10.2174/092986707779941014)
19. B. Arsic, J. Barber, A. Cikos, M. Kadirvel, E. Kostic, A. J. McBain, J. Milicevic, A. Oates, A. Regan, *Molecules* **27** (2022) 7280 (https://doi.org/10.3390/molecules27217280)
20. J. Cheung, M. J. Rudolph, F. Burshteyn, M. S. Cassidy, E. N. Gary, J. Love, M. C. Franklin, J. J. Height, *J. Med. Chem.* **55** (2012) 10282 (https://doi.org/10.1021/jm300871x)
21. F. S. Katz, S. Pecic, T. H. Tran, I. Trakht, L. Schneider, Z. Zhu, L. Ton-That, M. Luzac, V. Zlatanic, S. Damera, J. Macdonald, D. W. Landry, L. Tong, M. N. Stojanović, *ChemBioChem* **16** (2015) 2205 (https://doi.org/10.1002/cbic.201500348)
22. L. R. Zeng, L. H. Shi, X. G. Meng, J. Xu, G. F. Jia, T. Gui, Y. P. Zhang, D. Y. Hu, *J. Environ. Sci. Health, B* **54** (2019) 317 (https://doi.org/10.1080/03601234.2019.1571360)
23. S. Altenhofen, D. D. Nabinger, M. T. Wiprich, T. C. Brandao Pereira, M. R. Bogo, C. D. Bonan, *Chemosphere* **180** (2017) 483 (https://doi.org/10.1016/j.chemosphere.2017.04.029)
24. D. K. Hackenberger, G. Palijan, Ž. Lončarić, O. Jovanović Glavaš, B. K. Hackenberger, *Ecotoxicol. Environ. Saf.* **148** (2018) 480 (https://doi.org/10.1016/j.ecoenv.2017.10.072)

25. J. E. Casida, K. A. Durkin, *Annu. Rev. Entomol.* **58** (2013) 99 (https://doi.org/10.1146/annurev-ento-120811-153645)

26. R. A. Friesner, J. L. Banks, R. B. Murphy, T. A. Halgren, J. J. Klicic, D. T. Mainz, M. P. Repasky, E. H. Knoll, D. E. Shaw, M. Shelley, J. K. Perry, P. Francis, P. S. Shenkin, *J. Med. Chem.* **47** (2004) 1739 (https://doi.org/10.1021/jm0306430)

27. R. A.Friesner, R. B. Murphy, M. P. Repasky, L. L. Frye, J. R. Greenwood, T. A. Halgren, P. C. Sanschagrin, D. T. Mainz, *J. Med. Chem.* **49** (2006) 6177 (https://doi.org/10.1021/jm051256o)

28. M. B. Čolović, D. Z. Krstić, T. D. Lazarević-Pašti, A. M. Bondžić, V. M. Vasić, *Curr. Neuropharmacol.* **11** (2013) 315 (http://dx.doi.org/10.2174/1570159X11311030006)

29. D. Spurgeon, E. Lahive, A. Robinson, S. Short, P. Kille, *Front. Environ. Sci.* **8** (2020) 588380 (https://doi.org/10.3389/fenvs.2020.588380)

30. G. Marucci, M. Buccioni, D. D. Ben, C. Lambertucci, R. Volpini, F. Amenta, *Neuropharmacology* **190** (2021) 108352 (https://doi.org/10.1016/j.neuropharm.2020.108352)

31. K. A. Lewis, J. Tzilivakis, D. Warner, A. Green, *Hum. Ecol. Risk Assess.* **22** (2016) 1050 (https://doi.org/10.1080/10807039.2015.1133242)

32. C. A. Lipinski, F. Lombardo, B. W. Dominy, P. J. Feeney, *Adv. Drug Deliv. Rev.* **46** (2001) 3 (https://doi.org/10.1016/S0169-409X(00)00129-0)

33. W. L. Jorgensen, E. M. Duffy, *Adv. Drug Deliv. Rev.* **54** (2002) 355 (https://doi.org/10.1016/S0169-409X(02)00008-X)

34. Q. Saquib, M. A. Siddiqui, S. M.Ansari, H. A. Alwathnani, J. Musarrat, A. A. Al-Khedhairy, *J. Appl. Toxicol.* **41** (2021) 832 (https://doi.org/10.1002/jat.4139).

SUPPLEMENTARY MATERIAL TO
Stability and computational analyses of selected pesticides in use in the Republic of Serbia

BILJANA ARSIĆ[1]*, STEFAN PETROVIĆ[1], JELENA MRMOŠANIN[1], IVANA DIMITRIJEVIĆ[1], SNEŽANA TOŠIĆ[1], GORDANA STOJANOVIĆ[1#], SANJA GLIŠIĆ[2] and JELENA MILIĆEVIĆ[2#]**

[1]Department of Chemistry, Faculty of Sciences and Mathematics, University of Niš, Višegradska 33, 18106 Niš, Serbia and [2]Laboratory for Bioinformatics and Computational Chemistry, Vinča Institute of Nuclear Sciences, University of Belgrade, Mike Petrovića Alasa 12–14, 11351 Vinča, Belgrade, Serbia

*,** Corresponding authors. E-mail: (*)biljana.arsic@pmf.edu.rs;
(**)jdjordjevic@vin.bg.ac.rs

Fig S-1. a) Total-Ion Chromatogram (TIC) of tebuconazole solution, b) Mass spectrum of tebuconazole.
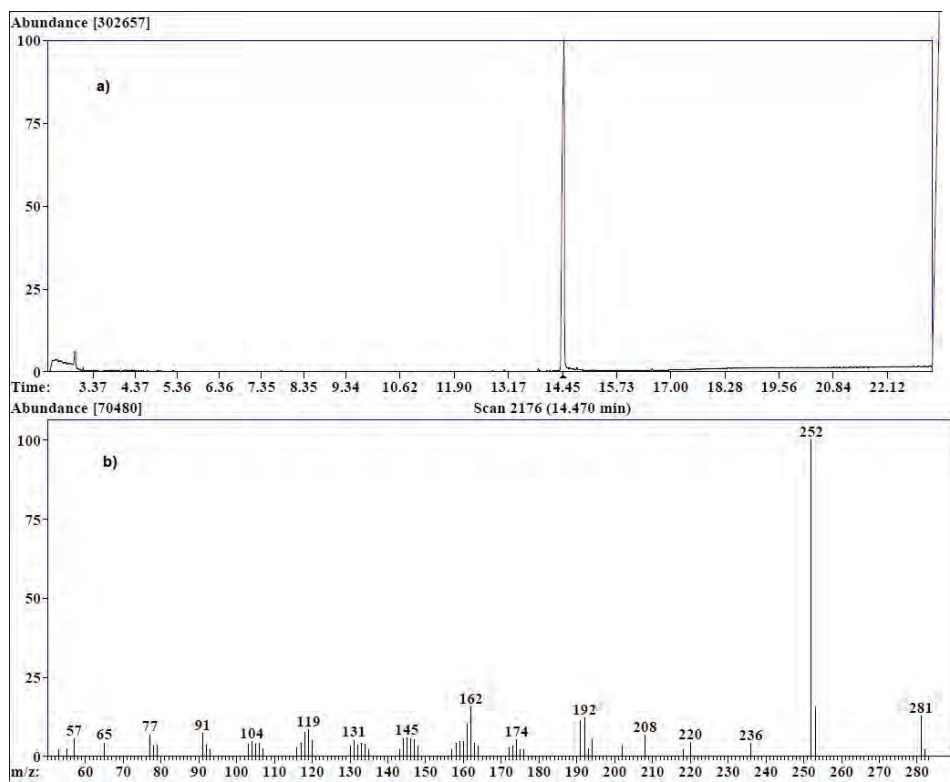
Fig S-2. a) Total-Ion Chromatogram (TIC) of pendimethalin solution, b) Mass spectrum of pendimethalin.
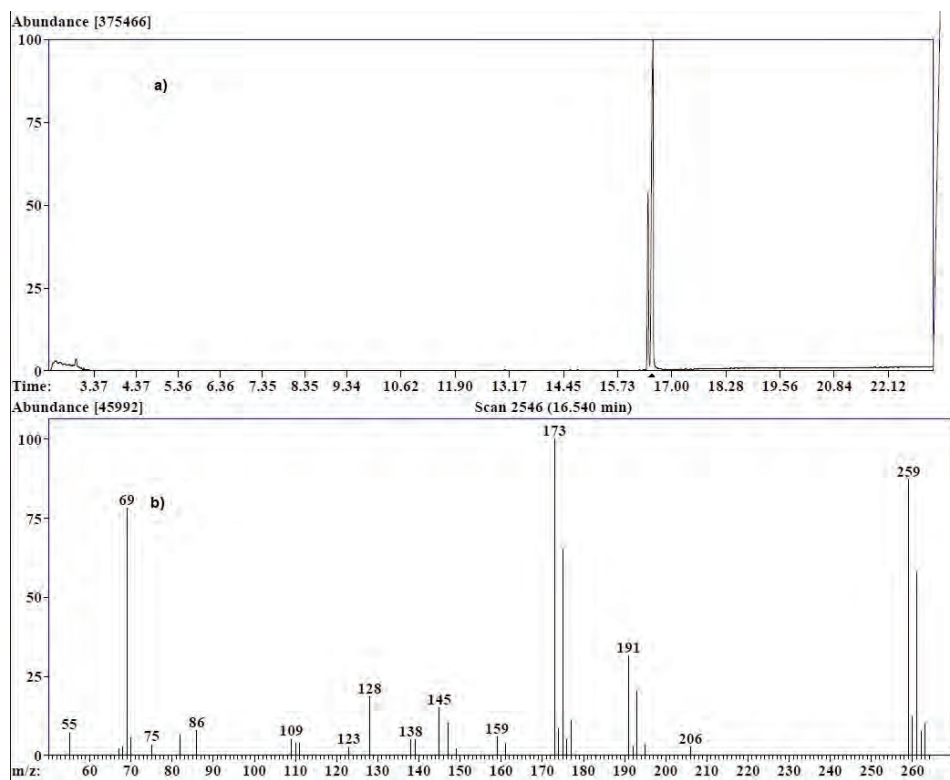
Fig S-3. a) Total-Ion Chromatogram (TIC) of propiconazole solution, b) Mass spectrum of propiconazole.
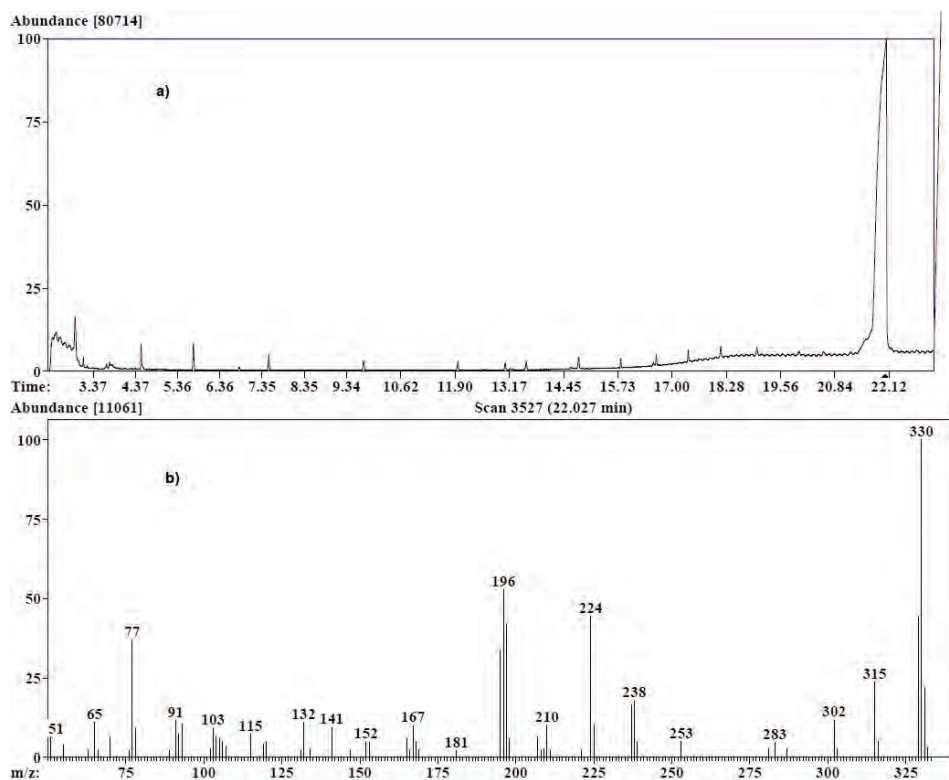
Fig S-4. a) Total-Ion Chromatogram (TIC) of famoxadone solution, b) Mass spectrum of famoxadone.

Table S-I. Calculated absorption, distribution, metabolism, elimination, and toxicity (ADMET) parameters of the compounds using QikProp v7.0.

Compound	MW	DM	MV	DHB	AHB	PSA	logP	logS	PCaco	PM	%HOA	VRF	VRT
Tebuconazole	307.8	3.4	978.7	1	3.7	41.4	4.1	-4.5	2515.3	2	100	0	0
Pendimetalin	281.3	4.6	918.5	1	3	83.8	2.9	-3.8	625.9	6	94	0	0
Pyraclostrobin	387.8	1.5	1194.8	0	5.2	71.6	4.9	-5.9	3362.1	3	100	0	1
Propiconazole	342.2	3.7	1002.8	0	4.5	115.5	3.9	-4.5	3382.5	0	100	0	0
Famoxadone	374.4	7.1	1131.4	2	0	75.6	3.7	-5.4	1523.7	2	100	0	0

MW: Molecular weight; DM: computed dipole moment; MV: total solvent-accessible volume; DHB: estimated number of hydrogen-bond donors; AHB: estimated number of hydrogen-bond acceptors; PSA: van der Waals surface area of polar nitrogen and oxygen atoms and carbonyl carbon atoms; logP: predicted octanol/water partition coefficient; log S: predicted aqueous solubility; PCaco: predicted apparent Caco-2 cell permeability; PM: number of likely metabolic reactions; % HOA: predicted human oral absorption percentage; VRF: number of violations of Lipinski rule of five (the rules are as follows: MW< 500, log P < 5, DHB ≤ 5, AHB ≤ 10, positive PSA value); VRT: number of violations of Jorgensen rule of three (the rules are as follows: log S > -5.7, PCaco > 22 nm s^{-1}, PM < 7).

Table S-II. ADME and drug safety profiling of the selected pesticides using Percepta 14.53.0 (Build 3577).

Pesticides	Caco-2 / cm s^{-1}	PPB /%	CNS	HIA /%	Metabolic stability	p-gp substrate	CYP1A2 inhibitor	CYP2C9 inhibitor	CYP2C19 inhibitor	CYP2D6 inhibitor	CYP3A4 inhibitor	Ames	hERG
Tebuco-nazole	142 x 10^{-6}	91	-2.20	100	0.33	0.48	0.41	0.42	0.45	0.45	0.72	0.19	0.36
Pendi-methalin	79 x 10^{-6}	93	-2.29	100	0.37	0.42	0.52	0.37	0.37	0.47	0.46	0.68	0.42
Pyraclo-strobin	174 x 10^{-6}	97	-2.75	100	0.48	0.43	0.56	0.41	0.51	0.47	0.54	0.52	0.54
Propicon-azole	196 x 10^{-6}	92	-2.24	100	0.43	0.32	0.50	0.40	0.52	0.41	0.72	0.20	0.42
Famox-adone	109 x 10^{-6}	98	-2.80	100	0.40	0.47	0.30	0.45	0.50	0.37	0.59	0.34	0.40

The effects of online learning about the Brønsted–Lowry theory of acids and bases in the first grade of grammar school during the COVID-19 pandemic

ANA-ANDREA J. HOLIK[1]* and DRAGICA D. TRIVIC[2#]

[1]Mihajlo Pupin Grammar School, Nikole Tesle 57, Kovačica, Serbia and [2]University of Belgrade – Faculty of Chemistry, Studentski trg 12–16, Belgrade, Serbia

Abstract: The aim of this paper was to examine the effects of the application of online material on the Brønsted-Lowry theory of acids and bases on the active construction of knowledge in first-grade grammar school students during the COVID-19 pandemic. The online material was designed to enable students: a) to learn the teaching material in smaller parts; b) to assess the acquired knowledge after each part of the teaching material; c) to progress through the lesson at their own pace; d) to visualise and interrelate the macroscopic, submicroscopic and symbolic representations of the contents about acids and bases by using a video recording and illustrations; e) to re-examine the accuracy of the given answers. The research sample consisted of 122 first-grade grammar school students, who learnt about the Brønsted–Lowry theory for the first time. The instruments used in this research study were two tests (a pre-test and a post-test), the validity of which was examined by two university professors and two grammar school chemistry teachers. The applied approach enabled the active construction of knowledge in the majority of students, while it provided the teachers with an insight into the progress and outcomes of the process.

Keywords: online education; first grade of grammar school; acids and bases; COVID-19.

INTRODUCTION

The COVID-19 pandemic has caused major changes in instructional strategies by introducing a considerable amount of online instruction. The popularity of online courses had been increasing even before the pandemic, mainly at higher levels of education, due to greater availability of such instruction, its flexibility and the fact that it enables students to study at their own pace.[1]

---

* Corresponding author. E-mail: a.a.kovacica@gmail.com
\# Serbian Chemical Society member.

275

A comparison of the effects achieved by classroom education and the ones achieved by distance education was the subject of numerous research studies in the previous decades. In a meta-analysis which included 355 research reports and papers published in the period from 1928 to 1998 there were no significant differences between the achievements of the participants taught using traditional classroom instruction and those taught using distance instruction by means of various technologies.[2] Similarly, such differences were not found in some subsequent meta-analyses.[3,4] Furthermore, a significant difference in the participants' level of satisfaction with the quality of teaching was not found.[5,6] Even though these research studies did not show a significant difference in the outcomes achieved by distance and classroom education, a study focusing on the differences between some programmes showed that their outcomes could vary depending on a series of pedagogical and technological factors.[7] In some meta-analyses, somewhat better effects of distance education in comparison with traditional classroom education were determined, but it was pointed out that careful interpretation of the average effect was necessary due to various formats of distance learning.[8,9]

It was established that low-confidence students felt better during online education and that they experienced greater freedom and less pressure in that kind of environment, while the impression of anonymity encouraged them to be more active, ask questions and complete the assignments.[10] However, students did not always assess positively reduced participation of teachers in online courses due to the impression that they had to "teach themselves". As a result, they chose online instruction for easier subjects, while they chose traditional classroom instruction for more difficult subjects.[11]

Flexibility turned out to be a desirable characteristic of online education to many students. However, even though students appreciated the applied format of asynchronous online learning, the ability to access materials at their own pace, at a time and place that suits them, some of them stated that they preferred regular real-time engagement and feedback information they could get in that way, *i.e.*, synchronous instruction in which the teacher and students simultaneously deal with the content of the course through interaction. These students believed that, in various uncertain circumstances, the real-time engagement offered them greater security and consequently greater motivation to learn.[12] A lack of direct teacher–student contact in online instruction and different kind of communication on various online platforms presented a great change for both students and teachers.[10] Therefore, in order to make distance learning more effective, synchronous online instruction and communication are recommended, as well as the use of interactive technologies, and teacher training in planning and realization of online teaching.[13,14]

Programs and applications which support synchronous and asynchronous online learning are constantly improved, enabling and supporting the student interaction with the course content, the teacher and other students.[6,15,16] However, in order to use these applications and to enable the access to various educational resources, certain technical conditions have to be met, primarily Internet access and the availability of devices. Apart from providing the technical conditions, another important issue is the environment in which students can study, *i.e.*, finding a peaceful place in their place of living where they can take the lessons and participate in the activities. In traditional instruction, this environment is provided in the classroom by the teacher, who manages the process of teaching and learning in the school environment.

Teachers' concern regarding online instruction relates to cheating while doing the assignments, *i.e.*, copying, which can occur when students are not under teachers' direct supervision. A solution to this problem might be writing some new and specific questions and problems, which students could solve by using the information found on the Internet, but the information should provide only partial help with formulating their answers. In this way, students are more engaged, they are less inclined to cheat/copy and better effects of learning are achieved.[16]

Research studies which focused on the degree to which online instruction and chemistry learning enabled effective formation of new knowledge and skills compared to traditional instruction also included the skills necessary for experimental work.[17,18] Learning about the chemistry laboratory through distance learning can be a virtual experience through some platforms, but it can also be a hands-on experience, which can be achieved by using mail-order laboratory kits.[19]

While some students are more engaged within online instruction, others tend to exclude themselves for various reasons, which raises the question of how to monitor students' engagement and progress in the online environment. This can be achieved by using discussion platforms, organising a test or a quiz, which can be graded or ungraded, organising a self-quiz and some other activities of formative assessment in order to determine when a student needs some additional support and assistance.[12] Involving students in solving online homework also can contribute to their better achievement.[20]

Engaging students in activities during the COVID-19 pandemic presented a challenge for teachers, particularly in the situation of a sudden switch to online instruction. This paper presents an attempt to find a way to improve student interaction with the course content in order to enable active knowledge construction in the online environment.

EXPERIMENTAL

The aim of this research study was to examine the effects of the application of online material on the Brønsted–Lowry theory of acids and bases on the active construction of know-

ledge in first-grade grammar school students during the COVID-19 pandemic. Based on the established aim the following research questions were formulated:

1. To what extent do students construct the meaning of the concepts related to the Brønsted–Lowry theory of acids and bases using the online learning material?

2. What kind of interaction do students have with the contents of the online material on the Brønsted–Lowry theory of acids and bases?

The Brønsted–Lowry theory of acids and bases was chosen as the teaching content in this research study since it was studied for the first time in the first grade of grammar school. Students' problems with learning the concepts of acids and bases had been pointed out by some research studies,[21] and the cause of the problems with understanding these concepts had also been observed within the explanations in some textbooks.[22]

The research study was conducted in the online environment, in line with the recommended organisation of teaching in Serbia in April 2021. The sample consisted of 122 first--grade grammar school students (14–15 years old). Prior to the beginning of the research study, the consent for the participation in the research study based on the presented aim and the method of research realisation had been obtained from the school, and a contract between the school and the University of Belgrade – the Faculty of Chemistry had been concluded. The students' participation in the research study was voluntary, and their achievement in the tests did not influence their chemistry grade. Through online communication, the aim of the research study and the expected activities were explained to the students. The links to the online material and tests, prepared in the Google Forms application, were forwarded to the school's chemistry teacher, who sent them to the students to work at the time when their chemistry class was supposed to be according to their school timetable. That was the first time they studied Brønsted–Lowry theory of acids and bases (according to the chemistry curriculum, the students in the sample had previously studied the Arrhenius theory of acids and bases in the seventh grade of primary school, at the age of 13). At the beginning of their work, students did a pre-test which tested their knowledge of acids and bases acquired at primary school. Afterwards they learnt about the Brønsted–Lowry theory of acids and bases using the online material. At the end they did a post-test which examined the knowledge gained by working with the online material.

The online material on the Brønsted–Lowry theory of acids and bases was prepared in such a way as to enable students: a) to learn the teaching material in smaller parts; b) to assess the acquired knowledge after each part of the teaching material; c) to progress through the lesson at their own pace; d) to visualise and interrelate the macroscopic, submicroscopic and symbolic representations of the contents about acids and bases by using a video recording and illustrations; e) to re-examine the accuracy of the answers they produced. The teaching material was divided into seven parts. Each part of the lesson was followed by items which checked the student achievement in learning that part of the lesson and student interaction with the contents. Students were also expected to select the information based on which they had formulated their answer to the item, which encouraged them to re-examine the given answer. Based on the students' answers the teacher was able to observe within which part they had had a problem with understanding the contents, which pieces of information they had selected as relevant to formulating the answers and to plan subsequent additional support accordingly. The text of the online material, the illustrations, the video recording and the items were prepared based on the corresponding outcomes defined within the chemistry curriculum for the first grade of grammar school. When formulating the textual part of each segment, special attention was devoted to the length of sentences, the use of terms which were familiar to stu-

dents and the explanation of the meaning of new terms, the number of concepts and clear definition of the new terms.

A pre-test and a post-test were designed according to the research aim and research questions. The pre-test consisted of five open-ended items. In the first and second item students were expected to provide the definitions of acids and bases according to the Arrhenius theory, which they had studied at primary school. In the third and fourth item, they were to provide names and formulae of two acids and two bases respectively, while in the fifth item they were expected to write the term used for a chemical reaction between acids and bases.

The post-test also consisted of five items, three open-ended and two multiple-choice items. In the first and second item students were expected to provide the definitions of acids and bases according to the Brønsted–Lowry theory of acids and bases, which they had studied using the online material. The third item tested students' understanding of the limitations of the Arrhenius theory in explaining acid–base properties of substances. In the fourth item they were to identify amphoteric species among the given examples, while in the fifth item they were supposed to identify conjugate acid-base pairs.

The validity of the instruments was assessed by two university professors of the Department of Chemical Education at the University of Belgrade – the Faculty of Chemistry and two grammar school chemistry teachers. The reliability of the tests was examined by means of Cronbach's Alpha coefficient. The value of Cronbach's Alpha coefficient in the pre-test amounts to 0.688, and in the post-test to 0.600, which indicates a lower level of internal consistency of the instruments. This could be related to the specific circumstances in which the research study was conducted and the newer way of testing students at that time.

To monitor students' voluntary interaction with the content of the online material the Google Forms application had been set in such a way that students had to provide answers only to the items of the post-test.

RESULTS AND DISCUSSION

The characteristics of the distribution of the pre- and post-test scores (the minimum and maximum number of points achieved, the arithmetic mean, the standard deviation, the *skewness* and *kurtosis* values) are presented in Table I. The *skewness* and *kurtosis* values are within ±1 range, so the distribution of the scores in the pre- and post-testing can be considered to be normal.

TABLE I. The characteristics of the distribution of the pre- and post-test scores (the maximum number of points is 7 in the pre-test and 5 in the post-test)

Test	N	Min	Max	M	SD	Skewness	Kurtosis
Pre-test	122	0	7	4.98	1.52	–0.913	0.852
Post-test	122	0	5	3.63	1.25	–0.852	0.354

Table II shows the number and percentage of students who provided correct and incorrect answers to the pre-test requirements.

A larger number of students gave a correct definition of acids compared to bases according to the Arrhenius theory. Furthermore, a larger number of students provided the names and formulae of acids in comparison to bases. Students' answers showed that, even though over 40 % of them could not provide a

definition of acids and bases, they were familiar with the formulae and names of some acids and bases. Also, a high percentage of students were familiar with the term neutralization.

TABLE II. The frequency of correct and incorrect answers to the pre-test items

Item	Correct answers		Incorrect answers	
	N	%	N	%
1. Definition of acids	73	59.8	49	40.2
2. Definition of bases	61	50.0	59	48.4
3. Names and formulae of two acids	110	90.2	8	6.6
4. Names and formulae of two bases	72	59.0	42.5	34.8
5. Neutralisation	109	89.3	8	6.6

The second research question related to student interaction with the contents of the online material on the Brønsted–Lowry theory of acids and bases. It can be examined based on their answers to the items following each part of the online material. The frequencies of students' correct and incorrect answers to these items are given below (Table III).

Within the first part of the online material, students had an opportunity to recall the definitions of acids and bases according to the Arrhenius theory. In the item which followed, they were expected to identify acids and bases based on the given chemical formulae as well as the ions in the aqueous solution due to which those compounds exhibit acidic or base properties. The percentage of correct answers to eight such requirements was high (73–96 %), particularly for the formulae of inorganic bases and inorganic acids, while it was somewhat lower for the formula of the organic acid. In addition to this, it was observed that a smaller number of students (between three and nine), who had correctly identified inorganic compounds, did not relate the ion in the solution to the acid–base properties of that solution. Even though they identified an acid or a base based on its formula, these students had not understood the information given in the first part of the online material on the electrolytic dissociation and ions due to which solutions exhibit acidic or basic properties, *i.e.*, they had not interrelated the symbolic and submicroscopic level. The highest percentage of incorrect answers (20.5 %) related to the example of an organic acid (methanoic acid), while the percentage of incorrect answers for other examples was below 10 %.

In order to examine the student interaction with the content and the comprehension of the text they had read, Table IV presents the frequencies of students' assessments as to which pieces of information in the first part of the material were relevant to formulating the answers. They could choose more than one piece of information. This item referred the students back to the text in the first part of the online material and offered them an opportunity to re-examine the answer they produced.

TABLE III. The frequencies of correct and incorrect answers to the items in the online material on the Brønsted–Lowry theory of acids and bases

Items following each part of the online material – the description of the requirements	Correct answers		Incorrect answers	
	N	$\%$	N	$\%$
1a. Identifying to which class the compound KOH belongs[a]	111	91.0	7	5.7
1b. Identifying the ions due to which KOH solution has basic properties	98	80.3	7	5.7
1c. Identifying to which class the compound HNO_3 belongs	117	95.9	3	2.4
1d. Identifying the ions due to which HNO_3 has acidic properties	98	80.3	3	2.4
1e. Identifying to which class the compound $Mg(OH)_2$ belongs	105	86.1	7	5.7
1f. Identifying the ions due to which $Mg(OH)_2$ solution has basic properties	97	79.5	10	8.2
1d. Identifying to which class the compound HCOOH belongs	89	73.0	16	13.1
1f. Identifying the ions due to which HCOOH solution has acidic properties	91	74.6	25	20.5
2a. Recognising reaction products	99	81.1	22	18.0
2b. Describing observations regarding the chemical reaction	9	7.4	72	59.0
3a. Identification of acids according to the Brønsted-Lowry theory of acids and bases	61	50.0	59	48.4
3b. Identification of bases according to the Brønsted-Lowry theory of acids and bases	72	59.0	49	40.2
4a. Recognising ammonia as a proton acceptor	110	90.2	12	9.8
4b. Recognising hydrogen chloride as a proton donor	109	89.3	13	10.7
5a. Identification of the conjugate base	87	71.3	34	27.9
5b. Identification of the conjugate acid	85	69.7	35	28.7
6. Explaining the acidic properties of HCl according to the two theories	36	29.5[b]	54	44.3
7. Explaining the basic properties of NH_3 according to the two theories	11	9.0[b]	87	71.3

[a]Within item 1 students were expected to identify acids and bases according to the Arrhenius theory; [b]the percentage of correct explanations according to both theories. There were also partially correct answers to the items following the sixth and seventh part of the online material (32 % of students provided a correct explanation for item 6 according to the Arrhenius theory and 54 % according to the Brønsted–Lowry theory of acids and bases, while 10.7 % of students provided a correct answers for item 7 according to the Arrhenius theory and 37.7 % according to the Brønsted–Lowry theory of acids and bases)

The majority of students based their answers on the definitions of acids and bases in the text, while less than half of the students also based their answers on the examples of the dissociation of acid and base, given at the symbolic level. The higher percentage of students who marked the pieces of information relevant to formulating the answers was in line with the percentages of correct answers to

the first item. However, less than 11 % of students assessed as relevant some pieces of information based on which they could not provide answers to the first item. These students required some additional support in order to understand the information given in the text and at the symbolic level. It is important that chemistry teachers have this in mind when planning the material for learning in the online environment.

TABLE IV. The frequencies of the pieces of information from the first part of the online material on the Brønsted–Lowry theory of acids and bases used to formulate the answer

Information	N	$\%$
The first theory which described acids and bases was the theory of electrolytic dissociation. The theory was proposed by a Swedish chemist, Svante August Arrhenius (1859–1927) in 1887.	10	8.2
According to the theory of electrolytic dissociation, acids are substances which dissociate in water to give hydrogen ions H^+ as positive ions.	105	86.1
For example: $HCl \xrightarrow{H_2O} H^+ + Cl^-$	51	41.8
Hydroxides (bases) are substances which dissociate in water to produce hydroxide ions OH^- as negative ions.	96	78.7
For example: $NaOH \xrightarrow{H_2O} Na^+ + OH^-$	51	41.8
The Arrhenius theory of electrolytic dissociation can explain acids and bases to a limited extent since it refers only to aqueous solutions.	8	6.6
It can be used to explain the formation of a salt when aqueous solutions of an acid and a base are mixed (for example, when hydrochloric acid and the aqueous solution of sodium hydroxide react, water and sodium chloride, a salt dissolved in water, are produced).	13	10.6

In the second part of the online material, information was conveyed to students using a video recording which showed a reaction between hydrogen chloride and ammonia and a text which contained an explanation regarding the formation of NH_4^+, *i.e.*, the formation of ammonium chloride. Students' understanding of the information explained through the video and the text was checked by a multiple-choice item in which students were expected to identify symbolically represented ions formed in the reaction and by an open-ended item, in which they were expected to describe what in the experiment indicated that hydrogen chloride and ammonia reacted. The percentage of correct answers to the multiple--choice item was high (81 %). However, out of the two thirds of the students who answered the open-ended item, only 7 % correctly described the indicator of the chemical reaction in the experiment they had observed. This indicates that a large number of students did not relate the information from the text regarding the submicroscopic level of the chemical reaction between hydrogen chloride and ammonia to the information from the video, in which the reaction is presented at the macroscopic level. Therefore, students need some additional support with collecting data on the properties and changes of substances by observation, inter-

preting the observations at the submicroscopic level and relating them to the symbolic representations of substances and their changes.

In the third part of the online material, it was explained how the limitations of the Arrhenius theory in defining acids and bases can be overcome with the help of the Brønsted–Lowry theory of acids and bases and new definitions of these concepts were given. In the item which followed students were expected to identify among the options offered which species, represented at the symbolic level, can act as acids and which as bases. Half of the students correctly identified the examples of acids, while slightly more than half of them correctly identified the examples of bases. The fact that a charged particle such as, for example the NH_4^+ ion, can act as an acid was new to the students, which explains a somewhat lower percentage of correct answers to this item. The frequencies of students' answers as to the pieces of information from the text based on which they answered the items are presented in Table V (they could choose more than one piece of information).

TABLE V. The frequencies of the pieces of information from the third part of the online material on the Brønsted–Lowry theory of acids and bases used for formulating answers

Information	N	$\%$
The Brønsted–Lowry theory of acids and bases is broader than the theory of electrolytic dissociation and also provides explanations for acid-base properties of substances in non-aqueous solutions.	6	4.9
The theory was proposed independently by two scientists in 1923, the Danish scientist Johannes Brønsted (1879–1947) and the English scientist Thomas Lowry (1874–1936).	9	7.4
According to the Brønsted–Lowry theory of acids and bases acids donate H^+ (it means that they are proton donors) to other ions or molecules, and bases accept H^+ (it means that they are proton acceptors).	108	88.5
A substance can act as an acid (HA) and donate protons, only if there is another substance which acts as a base (B) and accepts protons.	38	31.1
This can be represented by the following general equation: $HA + B \rightleftharpoons BH^+ + A^-$	47	38.5

The majority of students based their answers regarding the third part of the online material on the definitions of acids and bases according to the Brønsted––Lowry theory of acids and bases, while slightly more than a third of students considered the general symbolic representation of the reaction between acids and bases to be relevant. Less than a third of students used the information when, according to the Brønsted–Lowry theory of acids and bases, a substance can act as an acid or a base. The three pieces of information mentioned are indeed relevant to formulating the required answer. At the same time, it was observed that less than 8 % of students selected some pieces of information which were not relevant to the item.

In the fourth part of the online material, the reaction between hydrogen chloride and ammonia was presented in light of the Brønsted–Lowry theory of acids and bases using the drawings of the models of molecules and ions (the submicroscopic level), and a chemical equation (the symbolic level). In the item which referred to this part, students were expected to identify which species is a proton donor and which species is a proton acceptor. Approximately 90 % of students provided a correct answer to this item, and the frequency of the answers as to which piece of information they used to answer this item is presented in Table VI.

TABLE VI. The frequencies of the pieces of information from the fourth part of the online material on the Brønsted–Lowry theory of acids and bases used for formulating the answers

Information	N	%
The drawings of the models of molecules and ions.	13	10.6
The equation showing the chemical reaction.	14	11.5
The drawings of the models of molecules and ions, and the equation showing the chemical reaction.	95	77.9

The majority of students based their answer regarding the fourth part of the online material on the combination of the submicroscopic and symbolic representation. Approximately 11 % of students used one or the other form of representation for formulating their answer.

In the fifth part of the online material the concepts of a conjugate acid and a conjugate base, *i.e.*, conjugate pairs, were explained using a text and symbolic representations. In the item which followed, students were expected to identify conjugate acid-base pairs in the previously considered chemical reaction. Approximately 70 % of students provided a correct answer, primarily based on the textual description of a conjugate acid and a conjugate base (Table VII). Less than half of the students used the symbolic representation for formulating their answers.

In the sixth part of the online material, the change which is caused by introducing hydrogen chloride into water was considered in the light of the Brønsted––Lowry theory of acids and bases. In the open-ended item which followed this part the students were expected to explain the acidic properties of HCl based on the Arrhenius theory and the Brønsted–Lowry theory of acids and bases. Approximately 30 % of the students provided a correct explanation according to both theories. In addition to this, a correct explanation, but only according to the Arrhenius theory, was provided by 32 % of students, while 54 % of students provided a correct explanation only according to the Brønsted–Lowry theory of acids and bases. Table VIII shows the frequency of their answers as to which part of the online material they considered to be relevant to formulating their answers (they could choose more than one part).

TABLE VII. The frequencies of the pieces of information from the fifth part of the online material on the Brønsted–Lowry theory of acids and bases used for formulating answers

Information	N	%
A reaction in which a positive hydrogen ion, i.e. a proton, is exchanged is called a protolytic reaction or protolysis.	15	12.3
When an acid releases a proton, it becomes a species (an ion or a molecule) which is referred to as a conjugate base.	70	57.4
A base which accepts a proton becomes a conjugate acid.	76	62.3
Protolytic reactions in which protons are accepted and donated can be shown using the following general representation: acid 1 + base 2 $\rightleftharpoons$ base 1 + acid 2 $HA + B \rightleftharpoons A^- + BH^+$	49	40.2
The pairs acid 1 and base 1, and acid 2 and base 2 are called conjugate pairs, *i.e.*, such pairs consist of two mutually related substances.	30	24.6
This means that, according to the Brønsted–Lowry theory of acids and bases, each acid has its conjugate base and each base has it conjugate acid.	5	4.1
BH^+ is the conjugate acid of the base B, while A^- is the conjugate base of the acid HA.	39	32.0
The stronger an acid is, the weaker its conjugate base is, and the stronger a base is, the weaker its conjugate acid is.	24	19.7
These relationships influence the equilibrium composition of the system in which the protolytic reaction takes place.	17	13.9

TABLE VIII. The frequencies of the parts of the online material on the Brønsted-Lowry theory of acids and bases used for formulating the answers to items 6 and 7

The part of the online material	Item 6		Item 7	
	N	%	N	%
1	69	56.6	72	59.0
2	17	13.9	12	9.8
3	23	18.8	17	13.9
4	17	13.9	14	11.5
5	20	16.4	22	18.0
6	77	63.1	0	0
7	–	–	88	72.1

The most frequent answers of the students referred to the first part, which is about the Arrhenius theory, and to the sixth part. These two parts were indeed relevant to giving the answers.

In the seventh part of the online material, it was explained, in the light of the Brønsted–Lowry theory of acids and bases, what happens when ammonia is introduced into water. In addition to this, the concept of an amphoteric substance was explained and illustrated with examples. In the item which followed, students were expected to explain the basic properties of NH_3 according to the Arrhenius theory and the Brønsted–Lowry theory of acids and bases. Approximately 9 % of students provided an accurate explanation based on both theories,

10.7 % provided a correct answer based on the Arrhenius theory, and 37.7 % based on the Brønsted–Lowry theory of acids and bases. The most frequent answers of the students as to which parts of the material helped them formulate their answers and they could choose more than one answer (Table VIII), correspond to the parts of the online material which were relevant to formulating the answers.

The frequencies of correct and incorrect answers to the requirements of the post-test are shown in Table IX.

TABLE IX. The frequencies of correct and incorrect answers to the requirements of the post-test

Item	Correct answers		Incorrect answers	
	N	%	N	%
1. Definition of acids	113	92.6	8	6.6
2. Definition of bases	110	90.2	8	6.6
3. The explanation of the difference between the two theories	71	58.2	23	18.8
4. Identification of ampholyte (correct answer: HCO_3^-)	95	77.9	27	22.1
5. Identification of conjugate pairs (correct answers: HCO_3^-/CO_3^{2-}; HPO_4^{2-}/PO_4^{3-}; HS^-/S^{2-})	54	44.3	61[a]	50.0

[a]Students who provided an incorrect answer, who opted for both correct and incorrect answers (13.9 %), or who did not mark all correct answers (23.8 %)

By using the online material, a high percentage of students learnt what acids and bases are according to the Brønsted–Lowry theory of acids and bases (but some students were still more successful at defining acids than bases). After working with the online material more than half of the students could explain the limitations of the Arrhenius theory. More than three quarters of students could identify the species which is an ampholyte based on the symbolic representation, while less than half of them could identify conjugate acid–base pairs. The percentage of correct answers to the last item (Table IX) refers to the students who correctly chose all conjugate pairs, while the percentage of incorrect answers includes the students who chose both correct and incorrect answers or whose choice was incomplete.

CONCLUSION

The results of the conducted research study show positive effects of the application of the online material for studying the Brønsted–Lowry theory of acids and bases in slightly more than 70 % of the first-grade grammar school students. This is particularly significant in the light of the circumstances in which the instructional strategies were suddenly changed due to the COVID-19 pandemic and the fact that problems with understanding acids and bases, which are basic chemical concepts, were observed even in regular teaching circumstances.[21]

Based on the post-test results the first research question can be answered by stating that, working under changed circumstances, the majority of students learnt the definition of acids and bases according to the Brønsted–Lowry theory of acids and bases (over 90 %) by using the online material and that over half of them understood the limitations of the Arrhenius theory in explaining the acid––base properties of substances in comparison to the Brønsted–Lowry theory of acids and bases. While doing this, students learnt about the new theory autonomously, without their teacher's help.

Students' answers to the items which followed each part of the online material provide a response to the second research question about student interaction with the teaching contents. Based on the total number of the answers given (correct and incorrect), the majority of students were engaged (the average percentage of answers per item used to check the acquired knowledge was 91 %). This result is important since the application the students used to study and do assignments had been adjusted in such a way that they were obliged to answer only the items of the post-test, and they did not have to answer the items which followed each part of the online material. Such adjustment was made in order to examine the student interaction with the content of the online material. The examination into what pieces of information students had used to formulate their answers showed that a certain number of students had had difficulty with choosing the relevant pieces of information. These students needed some additional support in order to improve the comprehension of the text they had read. In the applied method of work the teacher can have a full insight into which students need additional support to what extent and with which contents. The problem which arose with the video recording in the online material (approximately 7 % of the students explained what indicated a chemical reaction between hydrogen chloride and ammonia) also occurs in the traditional classroom during demonstration experiments. Therefore, students need support with learning how to gather data about the properties and changes of substances by observing and with relating the macroscopic, submicroscopic and symbolic level.

The conducted research study showed that students could learn chemistry using online material, even for the teaching contents for which the regular teaching practice and research studies had shown to be difficult for students to understand. When preparing the online learning material, it turned out that dividing a lesson into smaller segments and checking the acquired knowledge after each segment was beneficial. The research study examined the student interaction with the content and for that purpose questions regarding the pieces of information based on which the students had formulated their answers were asked, but at the same time this step caused them to re-examine their answers by reading certain parts again. In regular practice, it would be useful to offer students some feedback information, to encourage them to re-examine the accuracy of the pre-

viously given answer and to refer them back to the parts which they had not well mastered. In the applied method of work students progressed through the teaching material at their own pace, but they all worked using the same contents. Online material which would enable students to use different contents, depending on how successfully they form their knowledge, can be designed.

И З В О Д

ЕФЕКТИ ОНЛАЈН УЧЕЊА О ПРОТОЛИТИЧКОЈ ТЕОРИЈИ КИСЕЛИНА И БАЗА У ПРВОМ РАЗРЕДУ ГИМНАЗИЈЕ ТОКОМ ПАНДЕМИЈЕ COVID-19

АНА-АНДРЕА Ј. ХОЛИК[1] и ДРАГИЦА Д. ТРИВИЋ[2]

[1]Гимназија Михајло Пупин, Nikole Tesle 57, Ковачица и [2]Универзитет у Београду – Хемијски факултет, Studentski trg 12–16, Beograd

Циљ рада био је да се истраже ефекти примене онлајн материјала о протолитичкој теорији на активну конструкцију знања код ученика првог разреда гимназије током пандемије COVID-19. Припремљени онлајн материјал требало је да омогући ученицима: а) учење градива у мањим деловима; б) проверу стеченог знања након сваког дела градива; в) напредовање кроз лекцију сопственим темпом; г) визуализацију помоћу видео снимка и илустрација у циљу повезивања макроскопског, субмикроскопског и симболичког представљања садржаја о киселинама и базама; д) преиспитивање тачности датих одговора. Узорак у истраживању чинило је 122 ученика првог разреда гимназије који први пут уче о протолитичкој теорији киселина и база. Инструменти у истраживању су два теста (пре-тест и пост-тест), чију су валидност проверила два универзитетска и два гимназијска професора хемије. Примењени приступ омогућава већини ученика активну конструкцију знања, а наставницима увид у ток и исходе тог процеса.

(Примљено 30. марта, ревидирано 3. маја, прихваћено 8. септембра 2023)

REFERENCES

1. A. Pardino, I. Gleyzer, I. Javed, J. Reid-Hector, A. Heuer, *Creat. Educ.* **9** (2018) 1123 (https://doi.org/10.4236/ce.2018.97083)
2. T. Russell, *The No Significant Difference Phenomenon: As reported in 355 research reports, summaries, and papers*, 5th ed., IDECC, North Carolina State University, 2001
3. C. Cavanaugh, K. J. Gillan, J. Kromrey, M. Hess, R. Blomeyer, *The effects of distance education on K-12 student outcomes: a meta-analysis*, Learning Point Associates/North Central Regional Educational Laboratory, 2004
4. N. Jahng, D. H. Krug, Z. Zhang, *Eur. J. Open, Dist. E-Learn.* **10** (2007) (https://old.eurodl.org/materials/contrib/2007/Jahng_Krug_Zhang.pdf)
5. M. Allen, J. Bourhis, N. Burrell, E. Mabry, *Am. J. Distance Educ.* **16** (2002) 83 (https://doi.org/10.1207/S15389286AJDE1602_3)
6. A. Driscoll, K. Jicha, A. N. Hunt, L. Tichavsky, G. Thompson, *Teach. Sociol.* **40** (2012) 312 (https://doi.org/10.1177/0092055X12446624)
7. Y. Zhao, J. Lei, B. Y. C. Lai, H. S. Tan, *Teach. Coll. Rec.* **107** (2005) 1836 (https://doi.org/10.1111/j.1467-9620.2005.00544.x)

8. M. Shachar, Y. Neumann, *Int. Rev. Res. Open Dis. Learn.* **4** (2003) 1 (https://doi.org/10.19173/irrodl.v4i2.153)
9. M. Allen, E. Mabry, M. Mattrey, J. Bourhis, S. Titsworth, N. Burrell, *J. Commun.* **54** (2004) 402 (https://doi.org/10.1111/j.1460-2466.2004.tb02636.x)
10. R. A. Tigaa, S. L. Sonawane, *J. Chem. Educ.* **97** (2020) 3318 (https://doi.org/10.1021/acs.jchemed.0c00554)
11. S. S. Jaggars, *Am. J. Dist. Educ.* **28** (2014) 27 (https://doi.org/10.1080/08923647.2014.867697)
12. I. J. Rhile, *J. Chem. Educ*. **97** (2020) 2857 (https://doi.org/10.1021/acs.jchemed.0c00618)
13. S. L. Williams, *Am. J. Dist. Educ*. **20** (2006) 127 (https://doi.org/10.1207/s15389286ajde2003_2)
14. R. M. Bernard, P. C. Abrami, Y. Lou, E. Borokhovski, A. Wade, L. Wozney, P. A. Wallet, M. Fiset, B. Huang, *Rev. Educ. Res.* **74** (2004) 379 (https://doi.org/10.3102/00346543074003379)
15. K. Swan, in *Elements of Quality Online Education, Practice and Direction*, J. Bourne, J. C. Moore, Eds., Sloan Center for Online Education, Needham, MA, 2003, pp. 13–45
16. J. G. Nguyen, K. J. Keuseman, J. J. Humston, *J. Chem. Educ.* **97** (2020) 3429 (https://doi.org/10.1021/acs.jchemed.0c00790)
17. H. T. Nennig, K. L. Idárraga, L. D. Salzer, A. Bleske-Rechek, R. M. Theisen, *Chem. Educ. Res. Pract.* **21** (2020) 168 (https://doi.org/10.1039/C9RP00112C)
18. Z. Qiang, A. G. Obando, Y. Chen, C. Ye, *J. Chem. Educ.* **97** (2020) 3446 (https://doi.org/10.1021/acs.jchemed.0c00609)
19. E. K. Faulconer, J. C. Griffith, B. L. Wood, S. Acharyya, D. L. Roberts, *Chem. Educ. Res. Prac*. **19** (2018) 392 (https://doi.org/10.1039/C7RP00173H)
20. J. F. Eichler, J. Peeples, *J. Chem. Educ.* **90** (2013) 1137. (https://doi.org/10.1021/ed3006264)
21. D. Šišović, S. Bojović, *Nastava i vaspitanje* **50** (2001) 185 (https://scindeks.ceon.rs/article.aspx?artid=0547-33300102185S) (in Serbian)
22. S. H. Paik, *J. Chem. Educ*. **92** (2015) 1484 (https://doi.org/10.1021/ed500891w).